Conference Proceedings of the Society for Experimental Mechanics Series

Christopher Niezrecki · Javad Baqersad *Editors*

Structural Health Monitoring, Photogrammetry & DIC, Volume 6

Proceedings of the 36th IMAC, A Conference and Exposition on Structural Dynamics 2018

SEM

Springer

Conference Proceedings of the Society for Experimental Mechanics Series

Series Editor

Kristin B. Zimmerman, Ph.D.
Society for Experimental Mechanics, Inc.,
Bethel, CT, USA

More information about this series at http://www.springer.com/series/8922

Christopher Niezrecki • Javad Baqersad
Editors

Structural Health Monitoring, Photogrammetry & DIC, Volume 6

Proceedings of the 36th IMAC, A Conference and Exposition on Structural Dynamics 2018

Springer

Editors
Christopher Niezrecki
Department of Mechanical Engineering
University of Massachusetts
Lowell, MA, USA

Javad Baqersad
Kettering University
Flint, MI, USA

ISSN 2191-5644 ISSN 2191-5652 (electronic)
Conference Proceedings of the Society for Experimental Mechanics Series
ISBN 978-3-319-74475-9 ISBN 978-3-319-74476-6 (eBook)
https://doi.org/10.1007/978-3-319-74476-6

Library of Congress Control Number: 2018939784

Printed on acid-free paper

This Springer imprint is published by the registered company Springer International Publishing AG part of Springer Nature.
The registered company address is: Gewerbestrasse 11, 6330 Cham, Switzerland

Preface

Structural Health Monitoring, Photogrammetry & DIC represents one of nine volumes of technical papers presented at the 36th IMAC, A Conference and Exposition on Structural Dynamics, organized by the Society for Experimental Mechanics, and held in Orlando, Florida, February 12–15, 2018. The full proceedings also include volumes on Nonlinear Dynamics; Dynamics of Civil Structures; Model Validation and Uncertainty Quantification; Dynamics of Coupled Structures; Special Topics in Structural Dynamics; Rotating Machinery, Vibro-Acoustics and Laser Vibrometry; Sensors and Instrumentation, Aircraft/Aerospace and Energy Harvesting; and Topics in Modal Analysis and Testing.

Each collection presents early findings from experimental and computational investigations on an important area within structural dynamics.

The organizers would like to thank the authors, presenters, session organizers, and session chairs for their participation in this track.

University of Massachusetts at Lowell, Lowell, MA, USA — Christopher Niezrecki
Kettering University, Flint, MI, USA — Javad Baqersad

Contents

Chapter 1
A Modification to Unified Matrix Polynomial Approach (UMPA) for Modal Parameter Identification

Seyed Ehsan Haji Agha Mohammad Zarbaf and Randall Allemang

Abstract In this paper, a modification to Unified Matrix Polynomial Approach (UMPA) for modal parameter identification of mechanical systems is suggested. Following the proposed modification, the measured Frequency Response Functions (FRF)/Impulse Response Functions (IRF) matrices of the system are manipulated so that the vibrational modes of the system can be identified at smaller model orders. A multi degree of freedom numerical case study and the experimental data of a circular plate are then employed to investigate the enhancement in performance of UMPA framework due to the proposed modification. It will be shown that following the proposed data manipulation, matrices with large values of condition number can be avoided in modal parameter estimation.

Keywords Unified matrix polynomial approach (UMPA) · High-order modal parameter identification · Condition number · Rational fraction polynomial method · Polyreference time domain method

1.1 Introduction

Modal parameter estimation is a branch of system identification where experimentally measured response of the system is used to identify the modal parameters of the system employing a model in terms of modal parameters. There are several types of system responses in time/frequency domain that can be used to extract the modal properties like Impulse Response Functions (IRF) and Frequency Response Function (FRF). The system can be excited using different excitation methods [1, 2] or it can be left to be excited by working/environmental conditions [3–8]. The system responses measured at different points on the structure can be processed individually or simultaneously [9]. Consequently, there are many system identification methods developed to identify the modal properties of systems using several types of systems responses [10–15]. In 1998, Allemang and Brown reformulated different modal parameter identification methods into a consistent mathematical formulation and named it Unified Matrix Polynomial Approach (UMPA) [16]. In UMPA framework, a polynomial of a generalized frequency variable with matrix coefficients is considered as the characteristic equation of the system where the model order is the highest order of the generalized frequency variable. The methods in which there is no limitation on the value of model order such as Complex Exponential (CE) [17], Least Squares Complex Exponential (LSCE) [18], Polyreference Time Domain (PTD) [19], and Rational Fraction Polynomial (RFP) [20] are called high-order methods while the methods with model order 1 (Ibrahim Time Domain (ITD) [21] and Eigensystem Realization Algorithm (ERA) [22]) or 2 (Polyreference Frequency Domain (PFD) [23]) are called low-order methods. For each modal parameter identification method, data matrices in time/frequency domain are manipulated accordingly to calculate the unknown coefficient matrices of matrix polynomial equation. Employing acquired coefficient matrices in a two-stage linear procedure, complex-valued natural frequencies, modal participation vectors, modal vectors, and modal scaling factors (modal A/modal mass) are identified [16].

Large condition number of data matrices involved in high order modal parameter identification methods is a challenge especially for frequency domain method RFP where the data matrix is of Vandermonde form [24] and hence, the condition number of data matrix increases with model order and makes the identification method more sensitive to noise in data. Minimizing the frequency range of the data and the order of the model [25], scaling the frequencies [26], and using

S. E. Haji Agha Mohammad Zarbaf (✉) · R. Allemang
Structural Dynamics Research Laboratory, School of Dynamic Systems, College of Engineering and Applied Science, University of Cincinnati, Cincinnati, OH, USA
e-mail: hajiagsn@mail.uc.edu

C. Niezrecki, J. Baqersad (eds.), *Structural Health Monitoring, Photogrammetry & DIC, Volume 6*,
Conference Proceedings of the Society for Experimental Mechanics Series, https://doi.org/10.1007/978-3-319-74476-6_1

orthogonal polynomials like Forsythe polynomials [27, 28] and Chebyshev polynomials [29] instead of power polynomials in the formulation of RFP have been proposed over the years to deal with ill-conditioning of data matrix in high-order modal parameter identification methods.

In this paper, a data manipulation based on UMPA framework is suggested so that smaller model orders are required to identify the vibrational modes of a system. First, UMPA framework for modal parameter identification of mechanical systems is reviewed. Second, a modification to UMPA framework is suggested to reduce the model order required to identify the vibrational modes of the system and hence, matrices with large condition numbers can be avoided. Finally, two high-order modal parameter identification methods PTD and RFP are implemented in UMPA framework to investigate the enhancement in performance of high order modal parameter identification methods in UMPA framework due to the proposed modification.

1.2 UMPA

The governing differential equation of motion of a system with N Degrees of Freedom (DOFs) can be written as Eq. (1.1),

$$[M]\{\ddot{x}(t)\} + [C]\{\dot{x}(t)\} + [K]\{x(t)\} = \{f(t)\} \tag{1.1}$$

where [M], [C], and [K] ϵ $R^{N \times N}$ are the mass, damping, and stiffness matrices of the system and {x(t)} and {f(t)} are the system response vector and excitation vector. Taking the Laplace transform of both sides of Eq. (1.1) results in,

$$\left([M]s^2 + [C]s + [K]\right)\{X(s)\} = \{F(s)\} \tag{1.2}$$

where s is a general frequency variable and {X(s)} and {F(s)} are the Laplace transforms of {x(t)} and {f(t)} respectively. Assuming the free vibration condition for Eq. (1.1), {f(t)} = 0, the characteristic equation of the system is calculated as Eq. (1.3):

$$\det\left([M]s^2 + [C]s + [K]\right) = 0 \tag{1.3}$$

Partitioning [M], [C], and [K] into sub-matrices $[M_{ij}]$, $[C_{ij}]$, and $[K_{ij}]$, i, j = 1, 2, 3, ..., n, Eq. (1.3) can be expanded as below,

$$\det\left(\begin{bmatrix} [M_{11}] & [M_{12}] & \cdots & [M_{1n}] \\ [M_{21}] & [M_{22}] & \cdots & [M_{2n}] \\ \vdots & \vdots & \ddots & \vdots \\ [M_{n1}] & [M_{n2}] & \cdots & [M_{nn}] \end{bmatrix} s^2 + \begin{bmatrix} [C_{11}] & [C_{12}] & \cdots & [C_{1n}] \\ [C_{21}] & [C_{22}] & \cdots & [C_{2n}] \\ \vdots & \vdots & \ddots & \vdots \\ [C_{n1}] & [C_{n2}] & \cdots & [C_{nn}] \end{bmatrix} s + \begin{bmatrix} [K_{11}] & [K_{12}] & \cdots & [K_{1n}] \\ [K_{21}] & [K_{22}] & \cdots & [K_{2n}] \\ \vdots & \vdots & \ddots & \vdots \\ [K_{n1}] & [K_{n2}] & \cdots & [K_{nn}] \end{bmatrix}\right) = 0 \tag{1.4}$$

The second-order matrix polynomial of Eq. (1.4) can also be written as a higher order matrix polynomial with the same roots:

$$[\alpha_{2n}]s^{2n} + [\alpha_{2n-1}]s^{2n-1} + \cdots + [\alpha_1]s + [\alpha_0] = 0 \tag{1.5}$$

In UMPA framework, the polynomial model of Eq. (1.6) is employed to calculate the unknown coefficient matrices [α] in Eq. (1.5):

$$H_{pq}(\omega) = \frac{\beta_n(j\omega)^n + \beta_{n-1}(j\omega)^{n-1} + \cdots + \beta_1(j\omega)^1 + \beta_0}{\alpha_m(j\omega)^m + \alpha_{m-1}(j\omega)^{m-1} + \cdots + \alpha_1(j\omega)^1 + \alpha_0} = \frac{\sum_{k=0}^{n}\beta_k(j\omega)^k}{\sum_{k=0}^{m}\alpha_k(j\omega)^k} \tag{1.6}$$

where $H_{pq}(\omega)$ is the FRF of the system measured at DOF p while the system is being excited at DOF q, ω is the angular frequency in rad/sec, and m is the model order. Eq. (1.6) can be rewritten as,

$$\sum_{k=0}^{m}\alpha_k(j\omega)^k H_{pq}(\omega) = \sum_{k=0}^{n}\beta_k(j\omega)^k \tag{1.7}$$

For a general multi-input multi-output (MIMO) case, Eq. (1.7) can be written as,

$$\sum_{k=0}^{m}\left[[\alpha_k](j\omega)^k\right][H(\omega)] = \sum_{k=0}^{n}\left[[\beta_k](j\omega)^k\right][I] \tag{1.8}$$

Equation (1.8) is valid for each frequency of the measured frequency response function matrix $[H(\omega)] \in R^{No \times Ni}$ where N_o is the number of DOFs where the response of the system is measured and N_i is the number of DOFs where the system is excited. The time-domain equivalent of Eq. (1.8) is:

$$\sum_{k=0}^{m}[\alpha_k][h(t)] = [0] \tag{1.9}$$

where $[h(t)] \in R^{No \times Ni}$ is the IRF matrix of the system. The size of unknown coefficient matrices $[\alpha_k]$, k = 0, 1, 2, ..., m in Eqs. (1.8) and (1.9) is $N_o \times N_o$ and the coefficient matrices $[\beta_k]$, k = 0, 1, 2, ..., n are $N_o \times N_i$ (Eq. (1.8) only). Assuming that the system is reciprocal ($H_{pq} = H_{qp}$), the transposed FRF/IRF matrices can also be used in Eqs. (1.8) and (1.9):

$$\sum_{k=0}^{m}\left[[\alpha_k](j\omega)^k\right][H(\omega)]^T = \sum_{k=0}^{n}\left[[\beta_k](j\omega)^k\right][I] \tag{1.10}$$

$$\sum_{k=0}^{m}[\alpha_k][h(t)]^T = [0] \tag{1.11}$$

Using Eqs. (1.10) and (1.11), the size of unknown matrix coefficients $[\alpha_k]$, k = 0, 1, 2, ..., m and $[\beta_k]$, k = 0, 1, 2, ..., n will be $N_i \times N_i$ and $N_i \times N_o$ respectively. Following UMPA framework, experimentally measured data matrices of the system (with the size $N_o \times N_i$) are directly used to identify the modal properties of the system employing low-order methods. Consequently, the coefficient matrices $[\alpha_k]$, k = 0, 1, 2, ..., m and $[\beta_k]$, k = 0, 1, 2, ..., n corresponding to low-order methods are always $N_o \times N_o$ and $N_o \times N_i$ respectively. On the other hand, the transpose of measured data matrices of the system is used for implementing high-order methods in UMPA framework and hence, the coefficient matrices $[\alpha_k]$, k = 1, 2, ..., m and $[\beta_k]$, k = 1, 2, ..., n have the size of $N_i \times N_i$ and $N_i \times N_o$ for high-order methods. Table 1.1, shows the manipulation of data matrices in UMPA framework to calculate the unknown coefficient matrices $[\alpha_k]$, k = 0, 1, 2, ..., m and $[\beta_k]$, k = 0, 1, 2, ..., n employing Eqs. (1.8) and (1.9) or Eqs. (1.10) and (1.11) [16]:

Having the coefficient matrices $[\alpha_k]$, k = 0, 1, 2, ..., m, the complex-valued natural frequencies of the system are the eigenvalues of the companion matrix [C]:

$$[C] = \begin{bmatrix} -[\alpha_{m-1}] & -[\alpha_{m-2}] & \cdots & -[\alpha_0] \\ [I] & [0] & \cdots & [0] \\ \vdots & \vdots & \ddots & \vdots \\ [0] & [0] & [I] & [0] \end{bmatrix} \tag{1.12}$$

Modal participation vectors, modal vectors, and modal scaling factors (modal A or modal mass) can also be calculated using the eigenvectors of the companion matrix [C] [16]. Based on Eq. (1.12), the number of identified modes at each model order, m, is equal to the size of coefficient matrices [α] times the model order m (mN_i for high-order methods and mN_o for low order methods). According to the Table 1.1, measured data matrices in UMPA framework is manipulated so that the number of identified modes at each model order m is equal to $m \times Min(N_o,N_i)$. In this paper, it is suggested that the measured data is manipulated according to the Table 1.2.

Table 1.1 Manipulation of data matrices in UMPA framework

$N_i > N_o$ (Roving hammer test)		$N_i < N_o$ (Multi-exciter test)	
High order	Low order	High order	Low order
[H(ω)]/[h(t)] should be transposed	No need to change data matrix	No need to change data matrix	[H(ω)]/[h(t)] should be transposed

Manipulation of data matrices according to Table 1.2, the number of modes identified at each model order m is equal to $m \times Max(N_o,N_i)$. Consequently, in consistency diagrams that are usually employed to identify the modes of structures using varying model orders [7, 30, 31], smaller model orders are required to identify the vibrational modes of the structure and hence, ill-conditioned data matrices (with large values of condition number) can be avoided.

1.3 Numerical Case Study

Figure 1.1 shows the 15-DOF lumped-mass system used to investigate the proposed data manipulation of Table 1.2. The system is excited at DOFs 1 to 5 ($N_i = 5$) and the response is measured at all DOFs ($No = 15$).

Stability diagrams of the system shown in Fig. 1.1, calculated by high-order modal parameter identification methods PTD and RFP implemented in UMPA framework (over frequency range 0–200 Hz) are shown in Figs. 1.2 and 1.3. The curves in Figs. 1.2 and 1.3 represent Complex Mode Indicator Functions (CMIFs) [32, 33]. Both the frequency and mode shape stability criteria were used to eliminate the spurious modes in stability diagrams [34]. Circles correspond to the poles that

Table 1.2 Proposed manipulation of data matrices

$N_i > N_o$ (Roving hammer test)		$N_i < N_o$ (Multi-exciter test)	
High order	Low order	High order	Low order
No need to change data matrix	[H(ω)]/[h(t)] should be transposed	[H(ω)]/[h(t)] should be transposed	No need to change data matrix

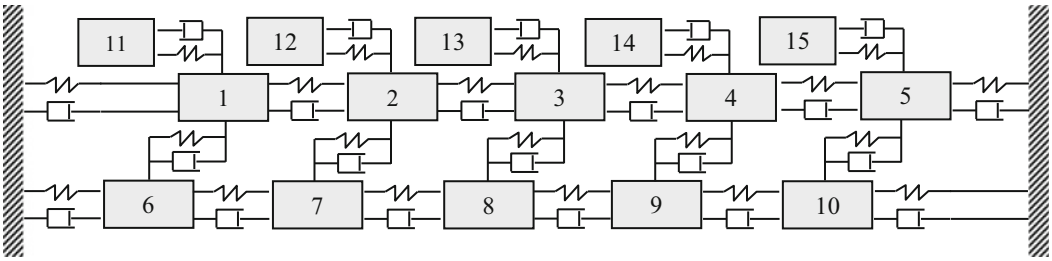

Fig. 1.1 15-DOF Numerical model

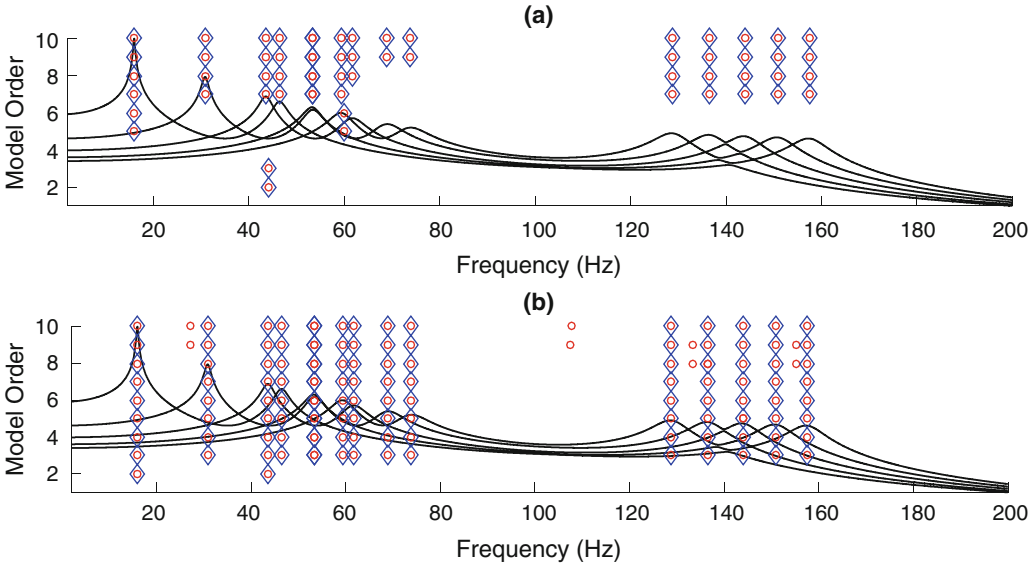

Fig. 1.2 Stability diagrams of 15 DOF analytical model calculated by PTD, (**a**) data manipulation of UMPA framework (Table 1.1), (**b**) proposed data manipulation (Table 1.2)

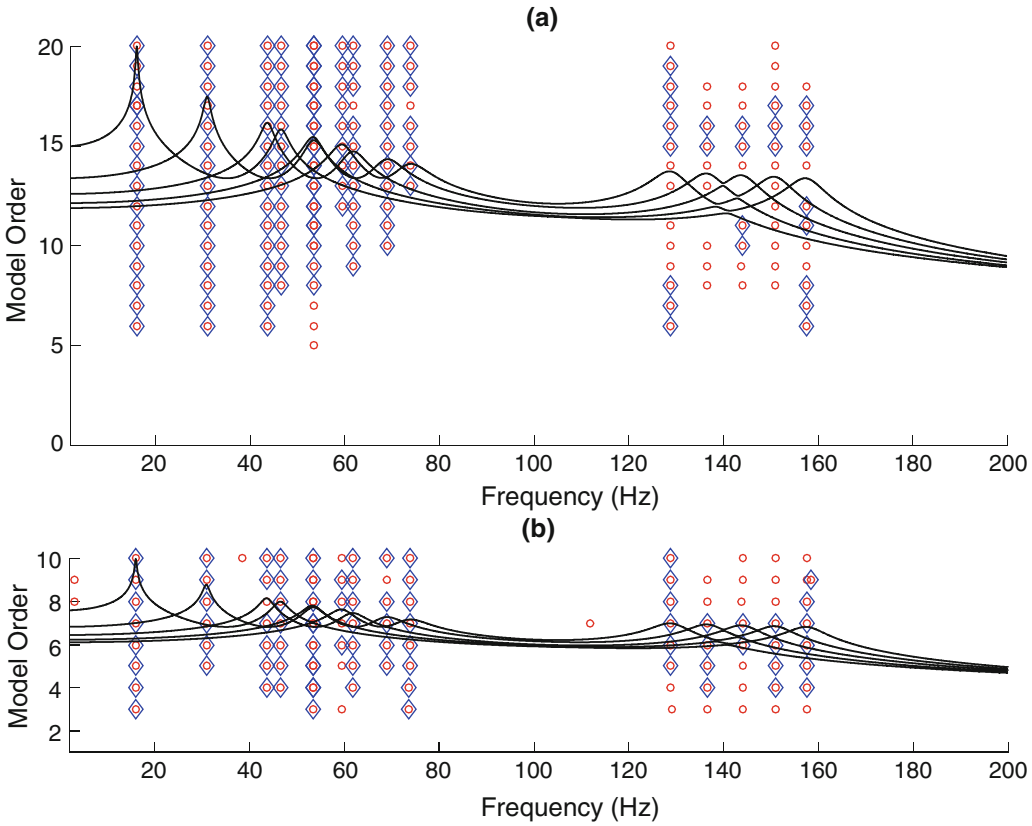

Fig. 1.3 Stability diagrams of 15 DOF analytical model calculated by RFP, (**a**) data manipulation of UMPA framework (Table 1.1), (**b**) proposed data manipulation (Table 1.2)

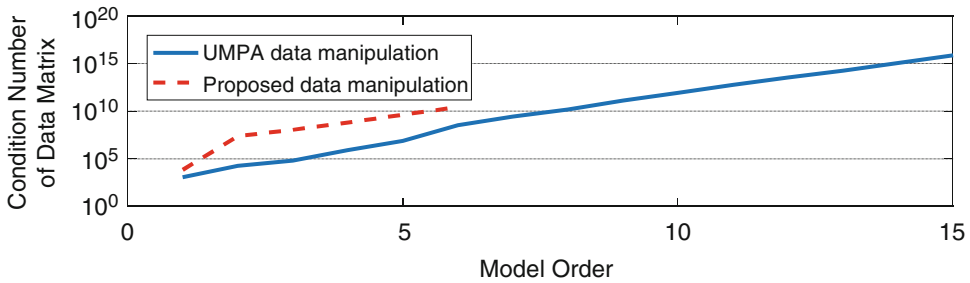

Fig. 1.4 Condition number of data matrices in RFP method corresponding to 15 DOF system

satisfy the consistency in damped natural frequency with differences less than 0.05% and the diamonds are the poles that meet the damped natural frequency consistency criteria and modal vector consistency criteria with Modal Assurance Criteria (MAC) [35] values bigger than 0.95. According to Fig. 1.2, following the data manipulation of UMPA (Table 1.1), all 15 modes of the numerical system can be identified using PTD by increasing the model order up to 9 while employing the proposed data manipulation (Table 1.2), model order needs to be increased to 3 for capturing all the vibrational modes of the system. Investigating the stability diagrams calculated by RFP (Fig. 1.3), the minimum model order at which all modes can be identified is equal to 15 when the data manipulation is performed according to Table 1.1 whereas following the proposed data manipulation (Table 1.2), all the modes can be identified using model order 6. Figure 1.4 shows the condition number of data matrices in RFP method as a function of model order. As it is seen, following the proposed data manipulation, vibrational modes of the system can be identified using data matrices with lower values of condition number (In comparison with traditional UMPA).

1.4 Experimental Case Study

In this section, modal properties of an aluminum circular plate (Fig. 1.5) are identified using high-order modal parameter identification methods PTD and RFP implemented in UMPA and the results are shown in Figs. 1.6 and 1.7. The plate is excited at 3 DOFs and the response is measured at 30 DOFs (Multi-exciter test setup).

Based on Fig. 1.6, Implementing PTD in UMPA framework, all vibrational modes of circular plate can be identified under model order 21 (following data manipulation of Table 1.1) and 3 (following data manipulation of Table 1.2). Figure 1.7a shows that model order 20 is not big enough for identification of modes beyond 300 Hz using RFP if the measured FRF matrices of the system is treated according to the Table 1.1. However, following the proposed data manipulation shown in

Fig. 1.5 Multi exciter test setup for circular plate

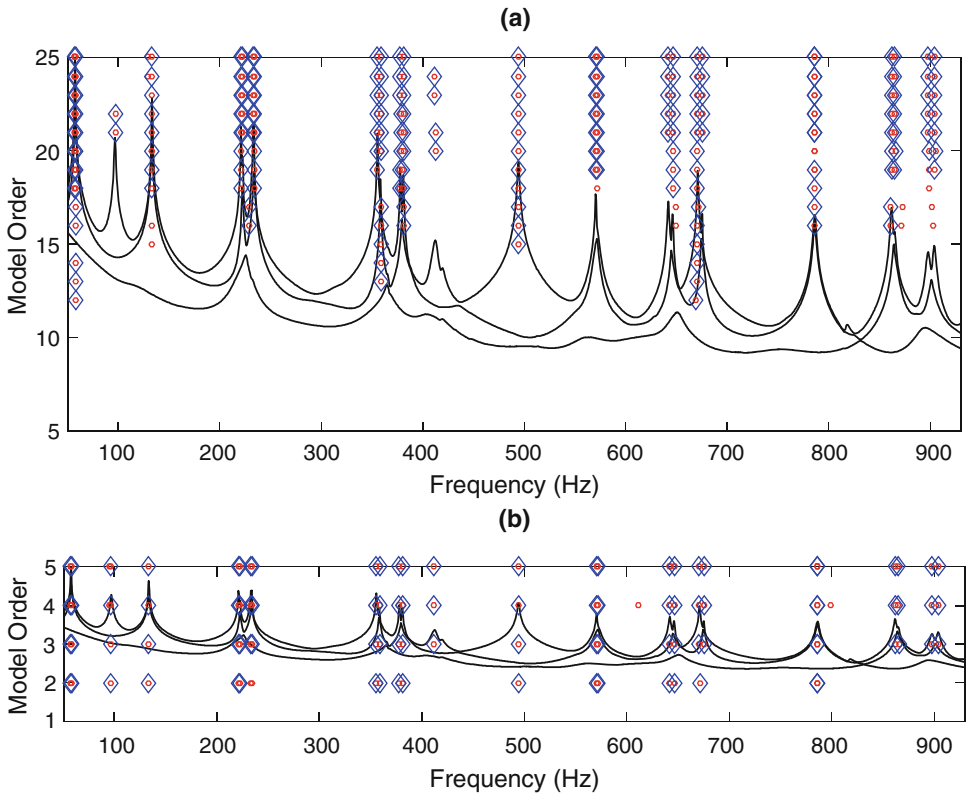

Fig. 1.6 Stability diagrams of the circular plate calculated by PTD, (**a**) data manipulation of UMPA framework (Table 1.1), (**b**) proposed data manipulation (Table 1.2)

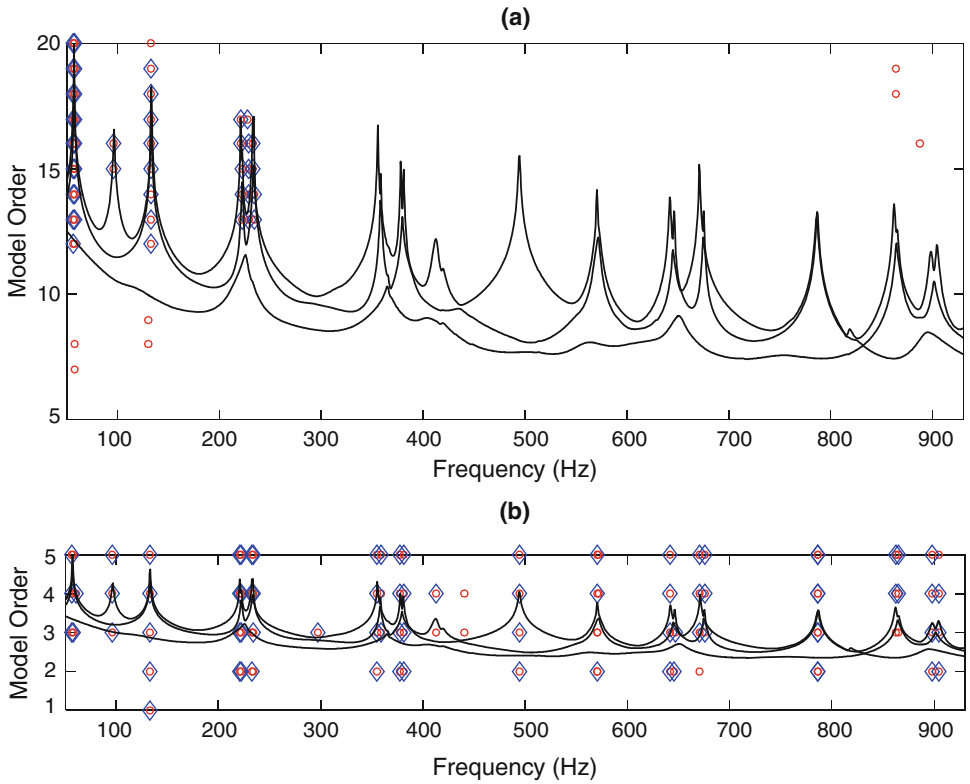

Fig. 1.7 Stability diagrams of the circular plate calculated by RFP, (**a**) data manipulation of UMPA framework (Table 1.1), (**b**) proposed data manipulation (Table 1.2)

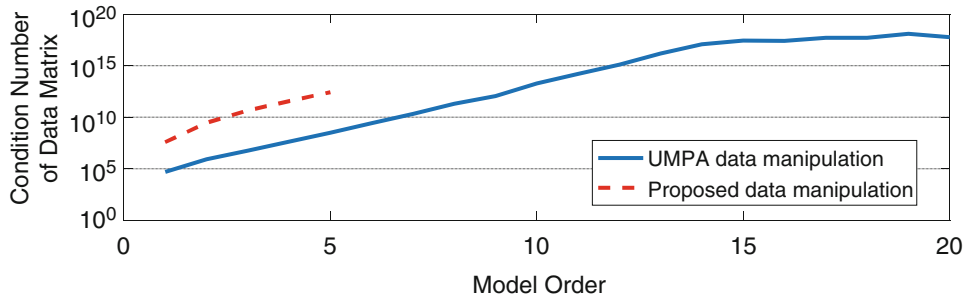

Fig. 1.8 Condition number of data matrices in RFP method corresponding to circular plate

Table 1.2, all vibrational modes of the plate are identified at model order 4 (see Fig. 1.7b). Figure 1.8 shows the condition number of data matrices in RFP method as a function of model order.

1.5 Conclusions

In this paper, a data manipulation in conjunction with Unified Matrix Polynomial Approach (UMPA) was proposed to decrease the condition number of data matrices involved in modal parameter identification process by decreasing the model orders required to identify the vibrational modes of the system. Two high order modal parameter identification methods PTD and RFP were implemented in UMPA framework following the proposed data manipulation to identify the modes of vibration of a numerical case study and a circular plate. The results demonstrated that the suggested modification enhances the performance of high order modal parameter identification methods through decreasing the minimum model order required to identify vibrational modes of the system and the consequent reduction of condition number of data matrices involved in modal parameter identification process.

References

1. Allemang, R.J.: Experimental modal analysis. [for vibrating structures] (1983)
2. Ewins, D.J.: Modal Testing: Theory and Practice, vol. 15. Research Studies Press, Letchworth (1984)
3. Ren, W.-X., Zong, Z.-H.: Output-only modal parameter identification of civil engineering structures. Struct. Eng. Mech. **17**(3-4), 429–444 (2004)
4. Peeters, B., De Roeck, G.: Reference-based stochastic subspace identification for output-only modal analysis. Mech. Syst. Signal Process. **13**(6), 855–878 (1999)
5. Ma, Z.-S., et al.: Parametric output-only identification of time-varying structures using a kernel recursive extended least squares TARMA approach. Mech. Syst. Signal Process. **98**, 684–701 (2018)
6. Asadollahi, P., Li, J.: Statistical analysis of modal properties of a cable-stayed bridge through long-term wireless structural health monitoring. J. Bridg. Eng. **22**(9), 04017051 (2017)
7. Haji Agha Mohammad Zarbaf, S.E., et al.: Stay force estimation in cable-stayed bridges using stochastic subspace identification methods. J. Bridg. Eng. **22**(9), 04017055 (2017)
8. Haji Agha Mohammad Zarbaf, S.E., et al.: Stay cable tension estimation of cable-stayed bridges using genetic algorithm and particle swarm optimization. J. Bridg. Eng. **22**(10), 05017008 (2017)
9. Fassois, S.: MIMO LMS-ARMAX identification of vibrating structures—part I: the method. Mech. Syst. Signal Process. **15**(4), 723–735 (2001)
10. Richardson, M., Schwarz, B.: Modal parameter estimation from operating data. Sound Vib. **37**(1), 28–39 (2003)
11. Allemang, R.J., Brown, D.L.: Experimental Modal Analysis and Dynamic Component Synthesis, vol. 6. Software User's Guide, DTIC Document (1987)
12. Brown, D., Allemang, R.: Review of spatial domain modal parameter estimation procedures and testing methods. In: International Modal Analysis Conference (IMAC) XXVII (2009)
13. Peeters, B., De Roeck, G.: Stochastic system identification for operational modal analysis: a review. J. Dyn. Syst. Meas. Control. **123**(4), 659–667 (2001)
14. Maia, N.M.M.: Extraction of valid modal properties from measured data in structural vibrations, Imperial College London (University of London) (1988)
15. Brown, D.L., Witter, M.C.: Review of recent developments in multiple reference impact testing (MRIT). In: Structural Dynamics, vol. 3, pp. 97–114. Springer, New York, NY (2011)
16. Allemang, R.J., Brown, D.: A unified matrix polynomial approach to modal identification. J. Sound Vib. **211**(3), 301–322 (1998)
17. Spitznogle, F.R., et al.: Representation and Analysis of Sonar Signals. Volume I. Improvements in the Complex Exponential Signal Analysis Computational Algorithm. No. TI-U1-829401-5. TEXAS INSTRUMENTS INC DALLAS EQUIPMENT GROUP (1971)
18. Brown, D., et al.: Parameter estimation techniques for modal analysis, SAE Technical Paper (1979)
19. Vold, H., et al.: A multi-input modal estimation algorithm for mini-computers, SAE Technical Paper (1982)
20. Van der Auweraer, H., Snoeys, R., Leuridan, J.: A global frequency domain modal parameter estimation technique for mini-computers. J. Vib. Acoustics-Trans. ASME (1986)
21. Ibrahim, S.R.: A time domain vibration test technique (1973)
22. Juang, J.-N., Pappa, R.S.: An eigensystem realization algorithm for modal parameter identification and model reduction. J. Guidance. **8**(5), 620–627 (1985)
23. Lembregts, F., Leuridan, J., Van Brussel, H.: Frequency domain direct parameter identification for modal analysis: state space formulation. Mech. Syst. Signal Process. **4**(1), 65–75 (1990)
24. Allemang, R., Phillips, A.: The unified matrix polynomial approach to understanding modal parameter estimation: an update. In: Proceedings of ISMA International Conference on Noise and Vibration Engineering, Katholieke Universiteit Leuven, Belgium (2004)
25. Allemang, R.J., Brown, D.L.: Experimental modal analysis. In: Harris, C.M., Piersol, A.G. (eds.) Harris' Shock and Vibration Handbook. McGraw-Hill, New York (2002)
26. Pintelon, R., Schoukens, J.: System Identification: A Frequency Domain Approach. Wiley, New York (2012)
27. Rolain, Y., et al.: Best conditioned parametric identification of transfer function models in the frequency domain. IEEE Trans. Autom. Control. **40**(11), 1954–1960 (1995)
28. Shih, C., et al.: A frequency domain global parameter estimation method for multiple reference frequency response measurements. Mech. Syst. Signal Process. **2**(4), 349–365 (1988)
29. Vold, H.: Numerically robust frequency domain modal parameter estimation. Sound Vib. **24**(1), 38–40 (1990)
30. Neu, E., et al.: Fully automated operational modal analysis using multi-stage clustering. Mech. Syst. Signal Process. **84**, 308–323 (2017)
31. Javh, J., Slavič, J., Boltežar, M.: High frequency modal identification on noisy high-speed camera data. Mech. Syst. Signal Process. **98**, 344–351 (2018)
32. Allemang, R., Brown, D.: A complete review of the complex mode indicator function (CMIF) with applications. In: Proceedings of the International Conference on Noise and Vibration Engineering (ISMA), Katholieke Universiteit Leuven, Belgium (2006)
33. Shih, C., et al.: Complex mode indication function and its applications to spatial domain parameter estimation. Mech. Syst. Signal Process. **2**(4), 367–377 (1988)
34. Phillips, A., Allemang, R.: Additional mechanisms for providing clear stabilization (consistency) diagrams. In: Proceedings of the ISMA International Conference on Noise and Vibration Engineering, Katholieke Universiteit Leuven, Belgium (2008)
35. Allemang, R.J.: The modal assurance criterion–twenty years of use and abuse. Sound Vib. **37**(8), 14–23 (2003)

Chapter 2
Orthogonal Projection-Based Harmonic Signal Removal for Operational Modal Analysis

S. Gres, P. Andersen, C. Hoen, and L. Damkilde

Abstract A presence of a high amplitude periodic signals in the output responses from operating structures often pose a challenge for output-only system identification and, in case of health monitoring, damage detection/localization methods. This paper introduces a pre-processing approach that removes the harmonic part from the output signals directly in the time domain. The new method uses orthogonal projections of the harmonic realization of the signal onto the raw time series within the stochastic subspace framework. Proposed algorithm is tested on two experimental examples. First, an aluminum plate excited with both random white and periodic excitations. Second, a full-scale industrial case of a ferry excited by a random environmental load with harmonic interference from a rotating machinery on-board. In both cases the proposed method removes the harmonics from the structural responses while leaving the random part of the output signal.

Keywords Operational modal analysis · Stochastic subspace identification · Rotating machinery · Harmonic removal · Non-stationary harmonics

2.1 Introduction

Subspace-based system identification methods became practical tools for identification of the eigenstructure of linear vibrating systems, notably for capacity of solving large models and for the consistency in parameter estimates under non-stationary noise excitations [1]. A family of output-only stochastic subspace-based algorithms (SSI) is deployed for Operational Modal Analysis (OMA) in fields such as aeronautic, mechanical and biomedical engineering, for examples see [2], and formulates basis for a number of Structural Health Monitoring (SHM) methods like in [3, 4]. However, using subspace-based algorithms for OMA and SHM is problematic when applied to structures with rotating machinery, like wind turbines, diesel engines or helicopters, due to the presence of harmonic inputs. In context of a system subjected to a random load combined with steady state signal, the subspace-based methods identify the harmonics as very lightly damped modes that one can filter in the mode selection process. Difficulties emerge when the harmonic excitations are non-stationary, coincide with the structural modes or are of high energy that masks the system response to the random part of the input. In that case, a desirable solution is to discard the harmonic influence over the output signal prior to system identification and without additional knowledge of such, e.g. tachometer measurements. A development of such harmonic removal method in SSI framework is the focus of the present paper.

In context of reducing the harmonic peaks from the response of the system prior to OMA a number of methods exists. Time-synchronous-averaging (TSA) is a signal processing technique that extracts periodic waveforms from signals by averaging synchronized blocks of the signal in the angular domain. In application to harmonic removal the averaged signal is subtracted from the raw measurements, what results in removal of the frequencies depicted to synchronize the blocks, for examples see [5]. Angle matching is often achieved via measurements of a signal with a frequency equivalent to harmonic excitation, which is not always available in some of the real-life applications and was attempted to overcome in [6]. A family of methods that does not require tachometer measurements are based on cepstrum (an inverse Fourier transform of

S. Gres (✉) · L. Damkilde
Department of Civil and Structural Engineering, Aalborg University, Aalborg, Denmark
e-mail: sg@civil.aau.dk

P. Andersen
Structural Vibration Solutions A/S, NOVI Science Park, Aalborg, Denmark

C. Hoen
Kongsberg Digital AS, Asker, Norway

C. Niezrecki, J. Baqersad (eds.), *Structural Health Monitoring, Photogrammetry & DIC, Volume 6*,
Conference Proceedings of the Society for Experimental Mechanics Series, https://doi.org/10.1007/978-3-319-74476-6_2

the logarithm of the spectrum). A number of applications of the cepstral lifters to harmonic removal can be found in [7]. A relatively new group of methods is based on estimating a parametric harmonic signal model fitted via e.g. numerical Gauss-Newton algorithm, see [8], or non-parametric methods, see [9], which estimate is later subtracted from the measurements.

The method proposed in this paper computes a harmonic realization of a modal state space model that is fitted to the recorded responses and projected orthogonally onto the raw signals. The paper is organized as follows: the next section contains derivation of the method, subsequently both the experimental and full-scale results are presented in Sects. 2.3 and 2.4 concludes the paper.

2.2 Theoretical Framework

First paragraph of this section recalls the main principles of the SSI algorithm, in particular the concept of orthogonal projections and innovation component of the data that lead to proposed harmonic reduction method, which description follows in the next paragraph.

2.2.1 State Space Modeling

Consider a second order differential equation of motion (2.1) to model a behavior of a d degree of freedom, viscously damped, linear time-invariant (LTI) structural system,

$$\begin{cases} M\ddot{u}(t) + D\dot{u}(t) + Ku(t) = v(t) \\ y(t) = C_a\ddot{u} + C_v\dot{u}(t) + C_d u(t) \end{cases} \tag{2.1}$$

where $M, D, K \in \mathbb{R}^{dxd}$ are mass, damping and stiffness matrices respectively; $C_a, C_v, C_d \in \mathbb{R}^{rxd}$ are selection matrices for accelerations, velocities and displacements where r is a number of sensors; $u(t), v(t) \in \mathbb{R}^{dx1}$ denote a vector of displacements and a vector of external forces respectively; $y(t) \in \mathbb{R}^{rx1}$ is a output vector; dot expresses a derivative with respect to time t. Providing that input $v(t)$ is unmeasured, transform (2.1) to a stochastic state-space form and sample it with k discrete time steps Δt, what writes,

$$\begin{cases} x_{k+1} = Ax_k + v_k \\ y_k = Cx_k + w_k \end{cases} \tag{2.2}$$

where the system states $x_k = [u(k\Delta t)^T \ \dot{u}(k\Delta t)^T]^T$; zero mean white noise vectors v_k and w_k denote the process and output noise respectively; $A \in \mathbb{R}^{nxn}$, $C \in \mathbb{R}^{rxn}$ are the state and observation matrices with,

$$A = exp\left(\begin{bmatrix} 0 & I \\ -M^{-1}K & -M^{-1}D \end{bmatrix} \Delta t\right), \quad C = \begin{bmatrix} C_d & 0 \\ 0 & C_v \\ -{C_a}^{-1}M^{-1}K & -{C_a}^{-1}M^{-1}D \end{bmatrix}$$

where n is a model order.

While the system matrices $\{A, C\}$ and subsequently the modal parameters- natural frequencies f, damping ratios ζ and mode shapes ϕ can be identified from (2.2) with covariance driven SSI (SSI-cov), see [10], we pursue data driven algorithm (SSI-data), see [11], with associated construction of Kalman filter to formulate the optimal prediction of the states and the output itself.

Let $z_k = E(x_k|y_{k-1})$ be the approximation of x_k given the past data vector y_{k-1} where $E(x_k|y_{k-1})$ denotes the image of x_k orthogonally projected onto the subspace spanned by the stacked vector of past observations y_{k-1} with,

$$E(x|y) = E(xy^T)E(yy^T)^{-1}y \tag{2.3}$$

where $E(\cdot)$ denotes the expectation operator. Provided that both x_k and y_{k-1} are jointly normally distributed the expression $E(x_k|y_{k-1})$ is the conditional expectation, see [12], and yields the best linear (least square) prediction of x_k given y_{k-1}. A step forward predictor of z_k writes $z_{k+1} = E(x_{k+1}|y_k)$ which, combined with the innovation component of the data $e_k = y_k - y_{k|k-1,k-2,\ldots,1}$, gives $z_{k+1} = E(x_{k+1}|y_{k-1}) + E(x_{k+1}|e_k)$. By definition, the residual e_k and the past data sequence $y_{k-1,k-2,\ldots1}$ are not correlated. Substitute z_{k+1} with (2.2) to formulate the innovation state space model,

$$z_{k+1} = Az_k + Ke_k \tag{2.4a}$$

$$y_k = Cz_k + e_k \tag{2.4b}$$

where $K = E(x_k e_k)E(e_k e_k)^{-1}$ is the steady state Kalman filter sequence. To predict a time response of the LTI system from the matrices $\{A, C, K\}$ given inputs y_k insert (2.4b) into (2.4a) to obtain,

$$z_{k+1} = (A - KC)z_k + Ky_k \tag{2.5a}$$

$$\hat{y}_k = Cz_k \tag{2.5b}$$

where $\hat{y}_k$ is the realization of the response and the innovations $e_k = y_k - \hat{y}_k$ are the prediction errors.

2.2.2 Harmonic Reduction

The procedure that follows consists of three steps: first a similarity transform of the innovation state space to a modal state space, second, a prediction of modes that correspond to the harmonic frequencies- selected prior to the reduction or detected with automated methods such as in [13] and last an orthogonal projection of raw time series onto the harmonic realization of the output.

A linear transformation of the Kalman states (2.4a) to modal coordinates, for reference see [14], is given by,

$$\hat{z}_t = Vz_t \tag{2.6}$$

where V denotes a transformation matrix and yields right eigenvectors of A,

$$AV = \lambda V, \quad \lambda \in \mathbb{C}^{nxn}, \quad V \in \mathbb{C}^{rxn}$$

Substituting the Kalman states from (2.4a) and (2.4b) with its similarity transforms, the innovation state space model takes a modal form and is represented by,

$$\begin{cases} \hat{z}_{t+1} = V^{-1}AV\hat{z}_t + V^{-1}Ke_t \\ y_t = CV\hat{z}_t + e_t \end{cases} \tag{2.7}$$

where the transformed state matrices can be written as $A_0 = V^{-1}AV \in \mathbb{C}^{nxn}$, $C_0 = CV \in \mathbb{C}^{rxn}$, $K_0 = V^{-1}K \in \mathbb{C}^{nxr}$. Notice that $A_0 = \lambda$ and $C_0 = \phi$, where the latter implies that a realization of the output in the modal form will render the response of the model due to identified modes. That manifests with,

$$\hat{z}_{t+1} = (A_0 - K_0C_0)\hat{z}_t + K_0y_t \tag{2.8a}$$

$$\hat{y}_t = C_0I_m\hat{z}_t \tag{2.8b}$$

where $I_m \in \mathbb{R}^{nxn}$ is a diagonal selection matrix with ones on the diagonal entries that corresponds to the pairs of complex conjugate eigenvalues of A reflecting the response from selected modes.

Suppose that the state space system from (2.4a) is completely controllable and observable, that is $CV_n \neq 0 \ \forall \ n$ and $V_n^{-1}K \neq 0 \ \forall \ n$ and i_{har} being a Boolean vector mapping the complex conjugate eigenvalues of A to the frequency of harmonic input. To remove the harmonic modes from the system response, first consider a prediction of the harmonic part given by,

$$\hat{y}_{har} = C_0\text{diag}(i_{har})\hat{z}_t \tag{2.9}$$

Subsequently, one can decouple the true response of the system from the harmonic-affected response by projecting the latter orthogonally onto harmonic realization $\hat{y}_{har}$, what writes,

$$E(y_t|\hat{y}_{har}) = y_t - E(y_t\hat{y}_{har}^T)E(\hat{y}_{har}\hat{y}_{har}^T)^{-1}\hat{y}_{har} \tag{2.10}$$

where the resultant residual is orthogonal to the subspace spanned by $\hat{y}_{har}$ and, given a complete identification of the harmonic modes, yields a reduced matrix,

$$\hat{y}_{red} = E(y_t|\hat{y}_{har}) \tag{2.11}$$

with the harmonics removed.

2.3 Results

The efficiency of the orthogonal projection-based harmonic removal is investigated with two laboratory tests of a plate and a full-scale, in-operation, dynamic test of a ship. The performance of the method is assessed based on its capacity to remove the harmonic poles from the measurements while maintaining the natural modal properties of the structure unaffected. A variation of the method is implemented in *ARTeMIS Modal Pro 5.2*, for reference see [15], which is used here for signal processing and presentation of results.

2.3.1 Experimental Results

The measurements were collected from a rectangular aluminum plate subjected to both random and harmonic excitation and equipped with a 16-channel acquisition system recording accelerations normal to the plate surface. The experimental tests were carried out by Niels-Jørgen Jacobsen from B&K Nærum in Denmark. The plate model and the experimental setup are illustrated on Figs. 2.1 and 2.2. The signals were sampled with 4096 Hz over 120 s intervals.

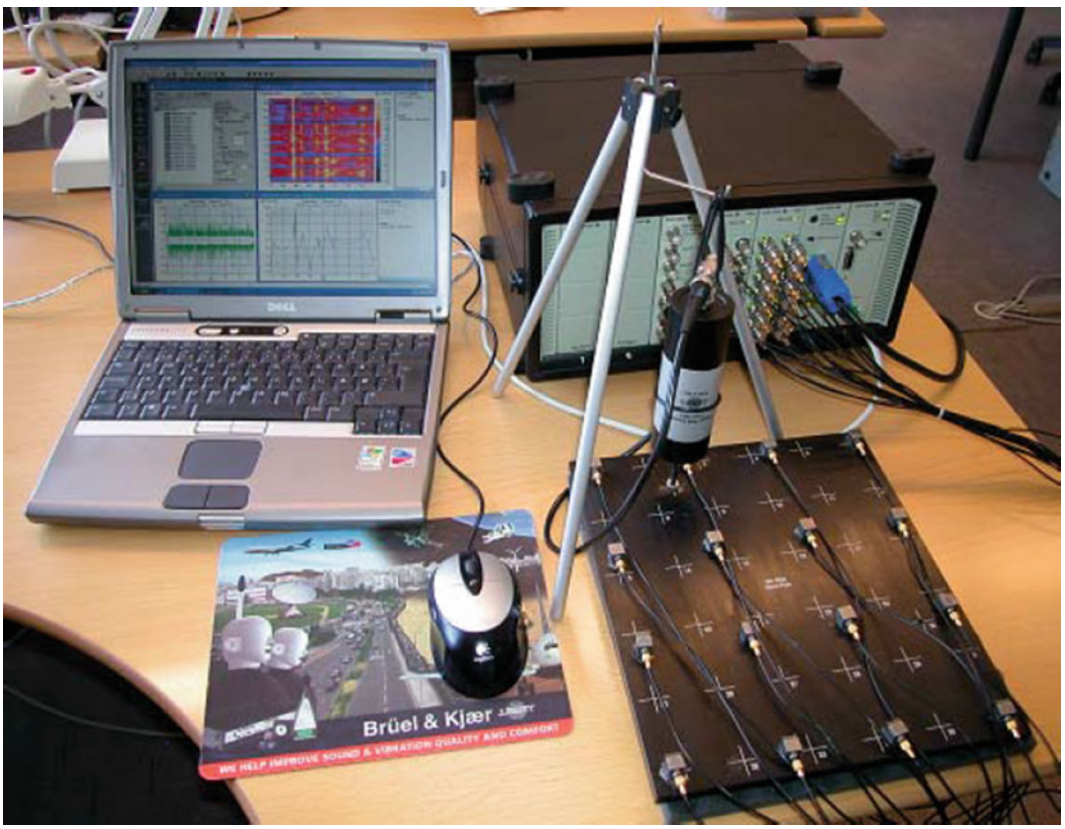

Fig. 2.1 The experimental setup: test plate with 16 acceleration channels, shaker, acquisition system

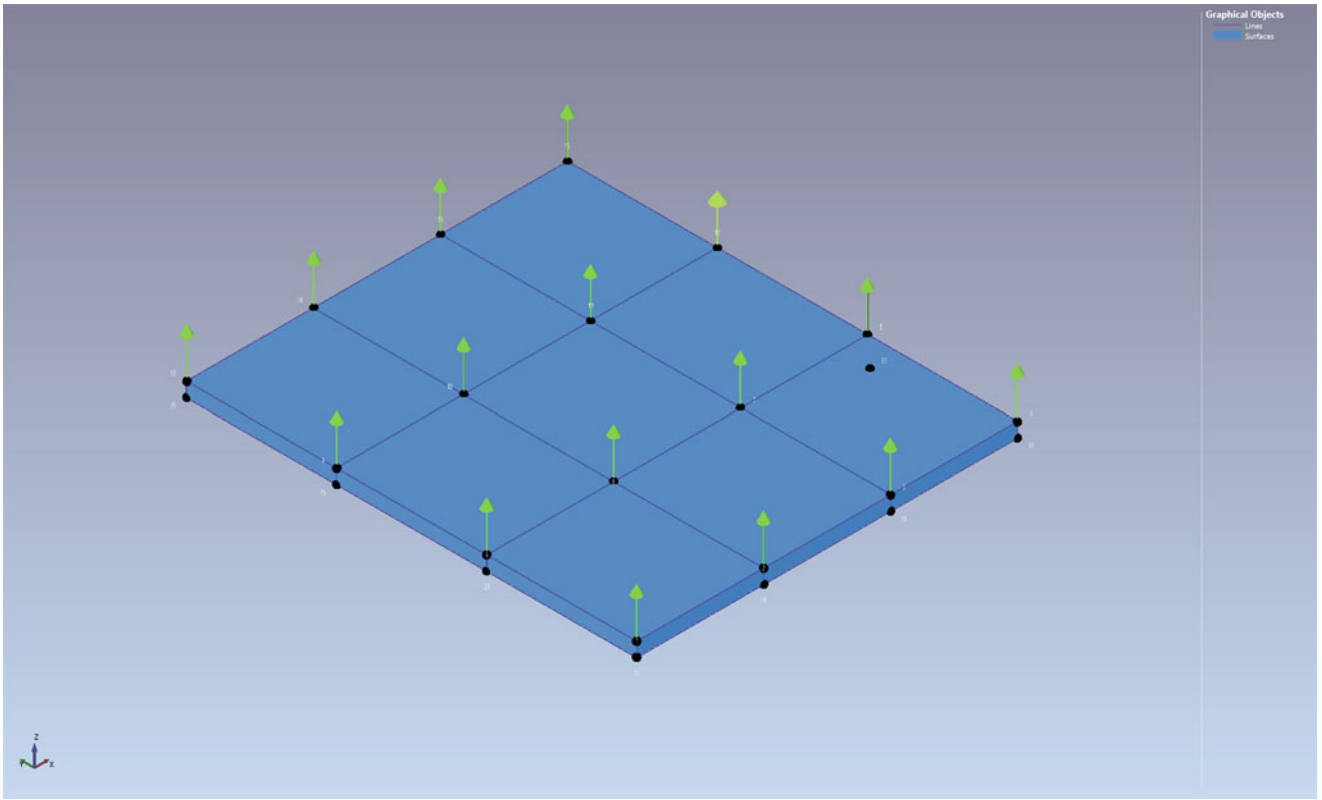

Fig. 2.2 The test plate model with 16 acceleration channels attached

To challenge the harmonic reduction algorithm two non-trivial input schemes are considered, namely:

- Random combined with swept sine of frequency varying in between 340 and 342 Hz and a sweep rate of 10 Hz/s,
- Random combined with burst sine of frequency of 370 Hz and 10 s burst intervals.

A short-time Fourier transforms (STFT) of the recorded accelerations for the two scenarios are depicted on Figs. 2.3 and 2.4.

The non-stationary harmonic frequencies in the measured accelerations are represented as a 5 dB dash red line in Fig. 2.3 and 20 dB bold red line in Fig. 2.4. A power difference between the steady state and the system response is 10–25 dB, Figs. 2.3 and 2.4. Small fluctuations (2 Hz) of the swept sine will become visible after zooming in Fig. 2.4. In both cases harmonics are in the vicinity, for the swept sine directly on top, of the 1st natural frequency of the plate, where the latter is 341 Hz, see Table 2.1. In context of OMA, performing the system identification on the two tested data sets even with the harmonic-robust methods is ineffective (high model orders, multiple spurious modes and unstable stabilization diagrams), hereby the reduction attempt is fully justified.

The analysis requires several user-defined parameters. First, the algorithm proposed in (2.9) and (2.10) operates in the premise that the harmonic frequencies are selected prior to the analysis and as such, we pick a sharp peak of the first singular values (SVs) of the power spectral densities (PSD) of the measured accelerations yielding the frequency of the harmonic input. Second, we define a number of block rows in the data Hankel matrix and a range of damping ratios to navigate the identification algorithm towards a state space model that predicts the harmonic modes in a optimal way. The subject of the optimum is not discussed in this work.

Both experimental tests are processed with one set of the user-defined inputs, namely: 45 block-rows of data Hankel matrix and 0.00–0.1% range of the harmonic mode damping ratios. The manually picked frequency of the harmonic response is 370 and 341 Hz respectively for burst sine and swept sine. The example of a graphical user interface containing the input parameters and SVs of PSD from the data before and after the harmonic reduction, for the burst sine case, is illustrated on Fig. 2.5.

A visual inspection of Fig. 2.5 shows a successful removal of harmonics at 370 Hz, what is in agreement with the STFT of the modified data, see Fig. 2.6, and confirmed by the comparison of the modal properties of the plate subjected to random

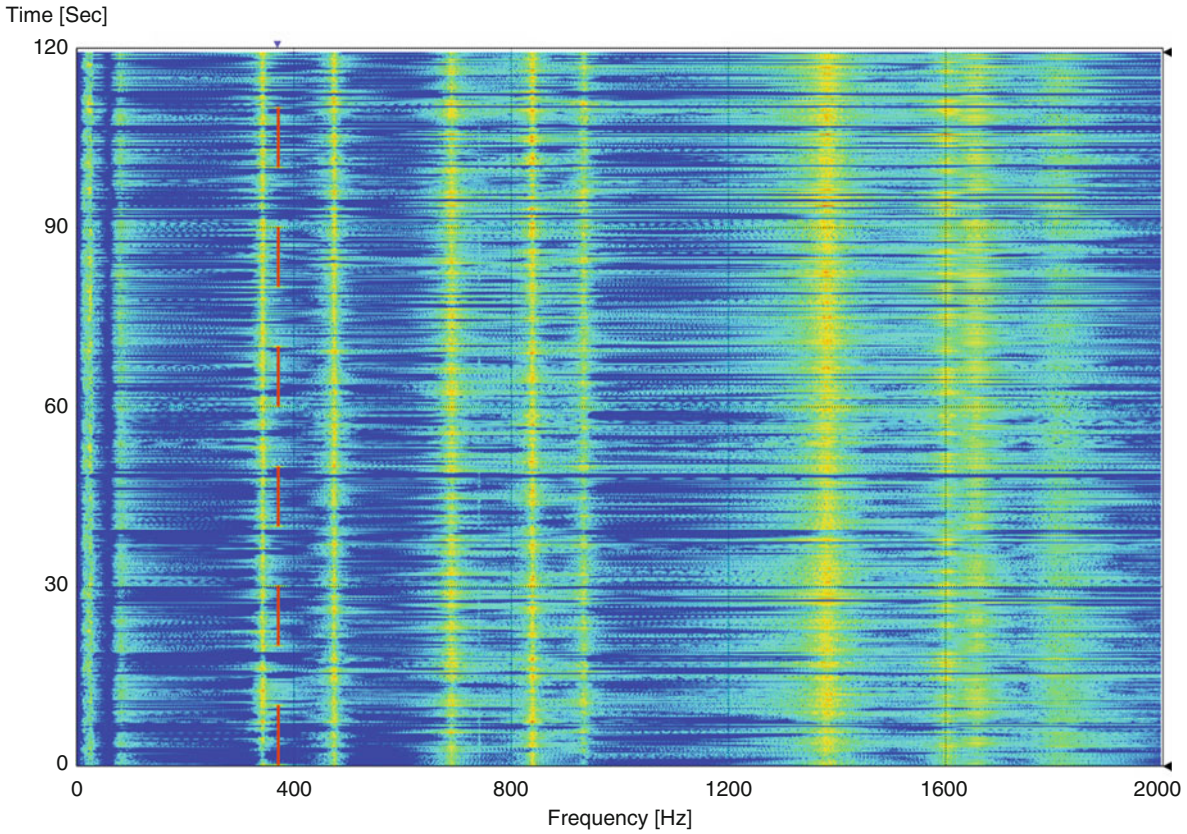

Fig. 2.3 STFT channel 1–3 before the harmonic reduction. Burst sine: 370 Hz, 10 s

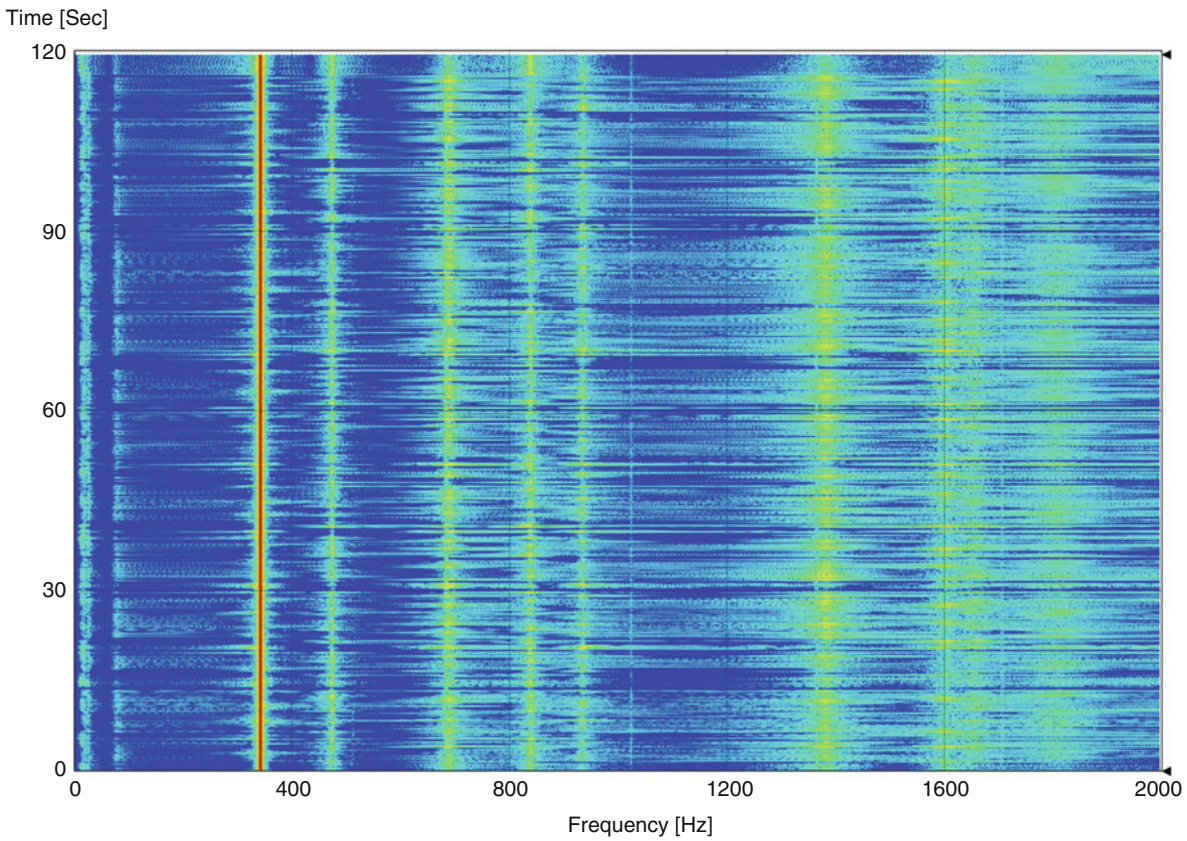

Fig. 2.4 STFT channel 1–3 before the harmonic reduction. Swept sine: 340–342 Hz, 10 Hz/s

Table 2.1 Three first natural frequencies and damping ratios of the plate estimated with SSI-UPCX

Test [-]	f_1[Hz]	f_2[Hz]	f_3[Hz]	ζ_1[%]	ζ_2[%]	ζ_3[%]
Random vibration	341.01	472.10	688.60	0.56	0.49	0.88
Random + swept sine	341.33	472.62	688.50	0.57	0.45	0.84
Random + burst sine	341.18	472.89	688.88	0.59	0.47	0.81

Fig. 2.5 Removal harmonic at 370 Hz. Burst sine: 370 Hz, 10 s

vibrations and the OMA of the measurements after harmonic removal, see Table 2.1. In case of swept sine, harmonics are removed recursively in a second trial run with the same input parameters; the results are depicted on Fig. 2.7 and Table 2.1.

Figure 2.6 illustrates that the response of the plate to the burst sine input (dashed red line on Fig. 2.3) is removed without leaving any additional harmonic artifacts in the modified signals. As for the swept sine test, Fig. 2.7 indicates that after the harmonic reduction the magnitude of the power spectrum in the 340–342 Hz range dropped from 20 to 6 dB, although, since the frequency of the harmonics coincide with the 1st natural frequency of the plate, it is not a direct sign that the harmonics are completely removed. To verify both cases, we refer to Table 2.1 containing an overview of the modal properties of the plate extracted both from random vibration measurements and the modified signals after the harmonic removal. The influence of the shaker weight has been included. Modal properties are estimated with an output-only SSI with Extended Unweighted Principal Component (UPCX) method, for reference see [16].

Considering that the results of the random vibrations test are the *true* modal parameters of the plate, the natural frequency of the first three modes exhibits a marginal deviation of max. 0.5% between the different data sets. That is not the case for the damping ratio. For the swept sine test: the smallest error yields 1.42% in the 1st mode and the highest error yields 9.92% in the 2nd mode. For the burst sine test: the smallest error writes 4.25% in the 2nd mode and the highest error writes 4.97% in the 1st mode. The highest errors are significant, in particular when recalling that e.g. the swept sine (340–342 Hz) input is mixed with the 1st mode (341.01 Hz) instead of the 2nd (472.10 Hz), see Fig. 2.5. One possible reason for that bias can be a non-linear damping behavior of the plate while loaded by a high amplitude period input; other might be a non-optimal choice of the state space model to predict the harmonic response of the signal.

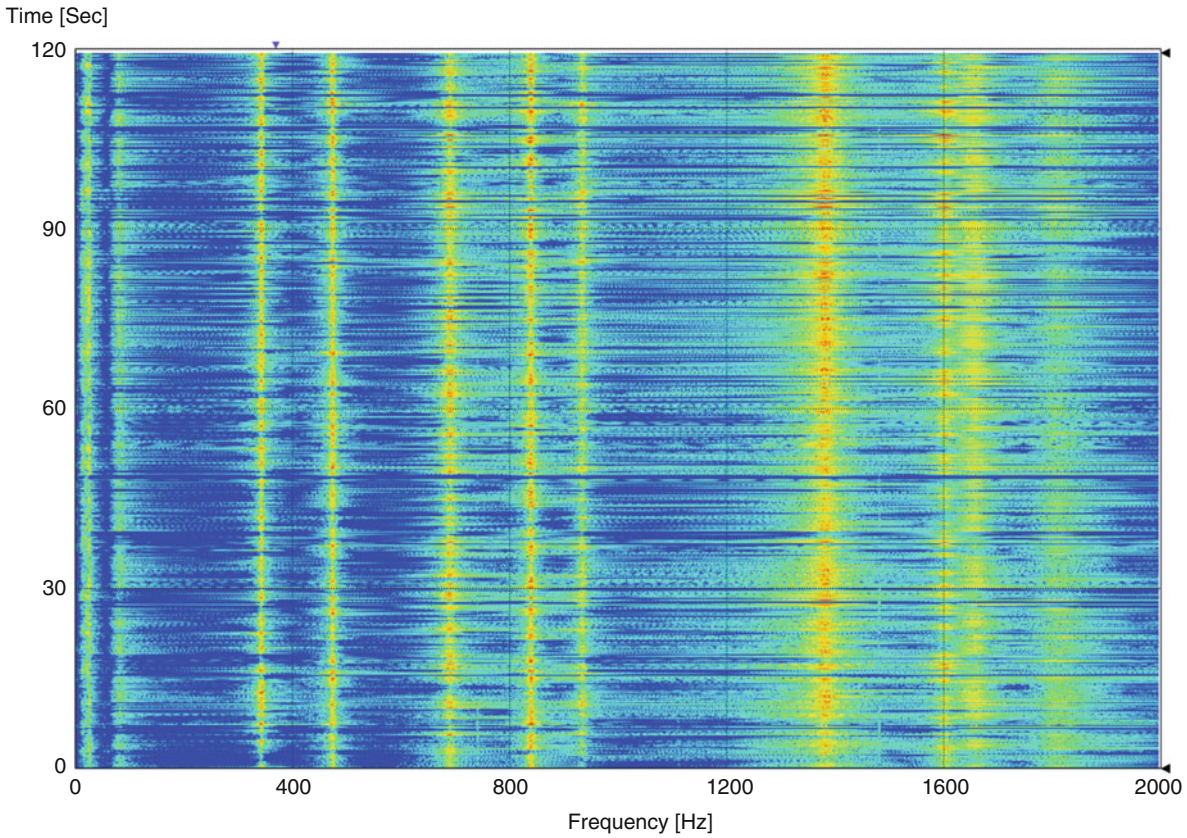

Fig. 2.6 STFT channel 1–3 after the harmonic reduction. Burst sine: 370 Hz, 10 s

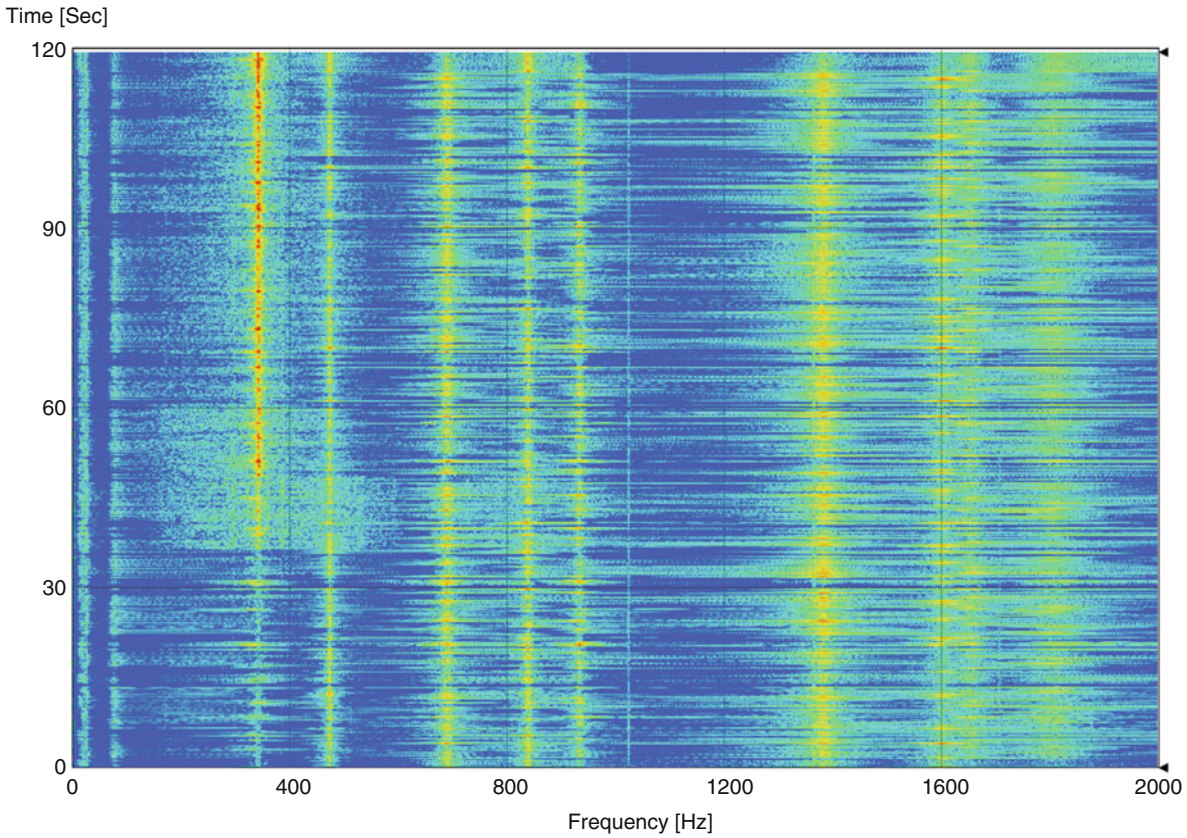

Fig. 2.7 STFT channel 1–3 after the harmonic reduction. Swept sine: 340–342 Hz, 10 Hz

2.3.2 Full-Scale Test

The ferry is excited by a random environmental load (wind and waves) with a harmonic interference from a rotating machinery on-board. The ferry docks at Flensburg shipyard, is 199.8 m long and powered by 20 MW 9 cylinder MAN B&W engine with nominal rotation speed of 123 rpm. The dynamic test is undergone under fully operational conditions; the responses are recorded using a 16-channel acquisition system and sampled with 128 Hz. The measurements were carried out by Dr. Sven-Erik Rosenow, Santiago Uhlenbrock and Prof. Günter Schlottmann from University of Rostock in Germany and made available to analysis by Structural Vibration Solutions A/S from Aalborg, Denmark. The same data set was analyzed in [17] and [18] with respect to harmonic detection. Model of the ship with the measured degrees of freedom is illustrated on Figs. 2.8 and 2.9. Prior to harmonic reduction measurements are decimated to 16 Hz.

During the test the rotational frequency of the engine is 2.05 Hz, hence a family of four harmonic frequencies: 2.05, 4.1, 6.15 and 7.8 Hz is present in the decimated response signals, see Fig. 2.10. The harmonic reduction is prepared with user-defined parameters depicted on Fig. 2.10, with two harmonic peaks at 2.05 and 4.1 Hz selected to reduce.

Figure 2.10 illustrates that along with peaks at 2.05 and 4.1 Hz the algorithm automatically reduced the harmonics at 6.15 and 7.8 Hz. A marginal remanence of the harmonic mode at 4.1Hz is still present in the second largest SV as well as an artifact of the 6.15 Hz peak. That fact, however, is not expected to have influence on the system identification of the modified signals. For more graphic overview Figs. 2.11 and 2.12 show the STFTs of the measurements before and after the harmonic reduction.

Comparing the Figs. 2.11 and 2.12 it is clear that the three solid red lines representing the response of the ferry towards the harmonic excitation, visible on Fig. 2.11, are removed on Fig. 2.12. No information regarding the modal properties of the ferry without the influence of the harmonic inputs is available hence instead of the tabular comparison of modal parameters a stabilization diagram with corresponding natural frequencies estimated from the data is presented on Fig. 2.13.

Multiple stable modes are depicted on Fig. 2.13. The harmonic modes previously present in the measurements are not detected nor they influence the identification algorithm after the harmonic reduction.

Fig. 2.8 The ferry at the Flensburg shipyard

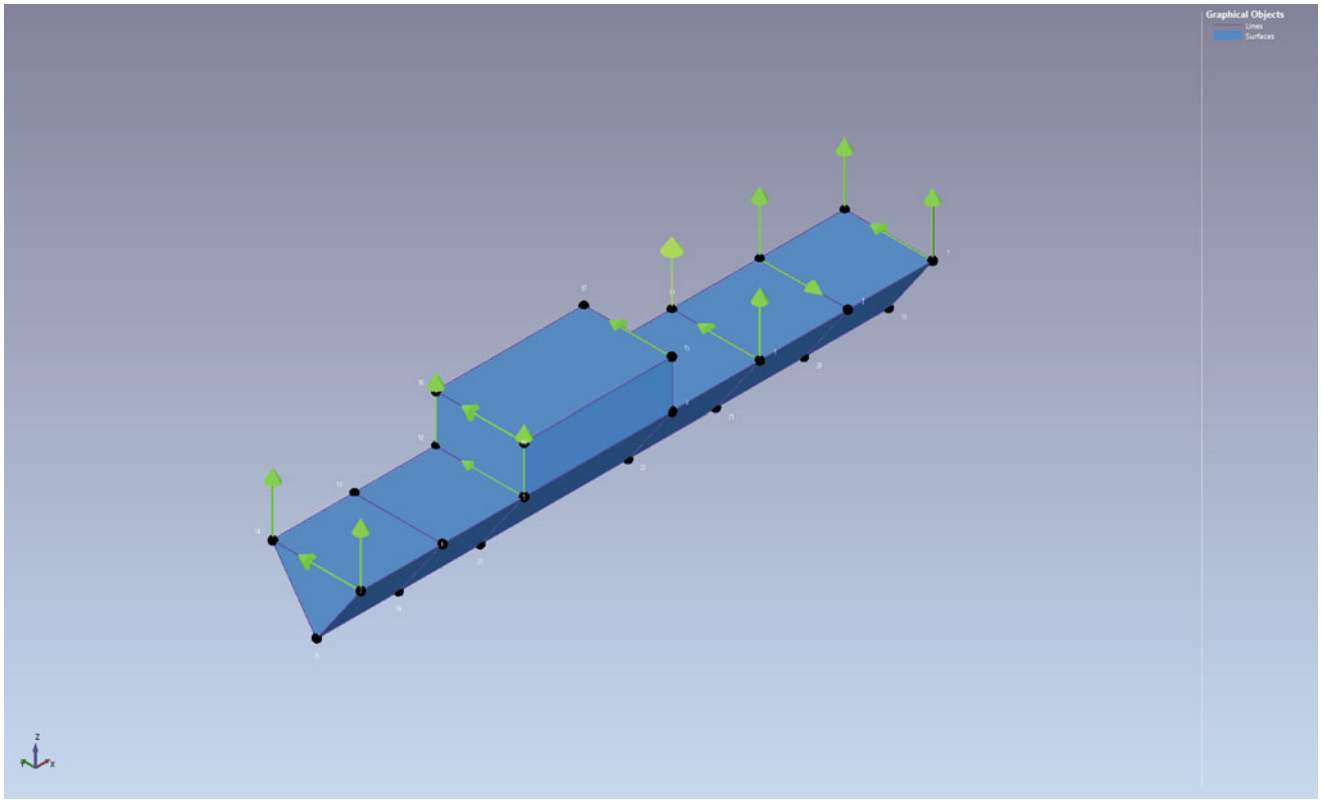

Fig. 2.9 The ferry model with 16 acceleration channels attached

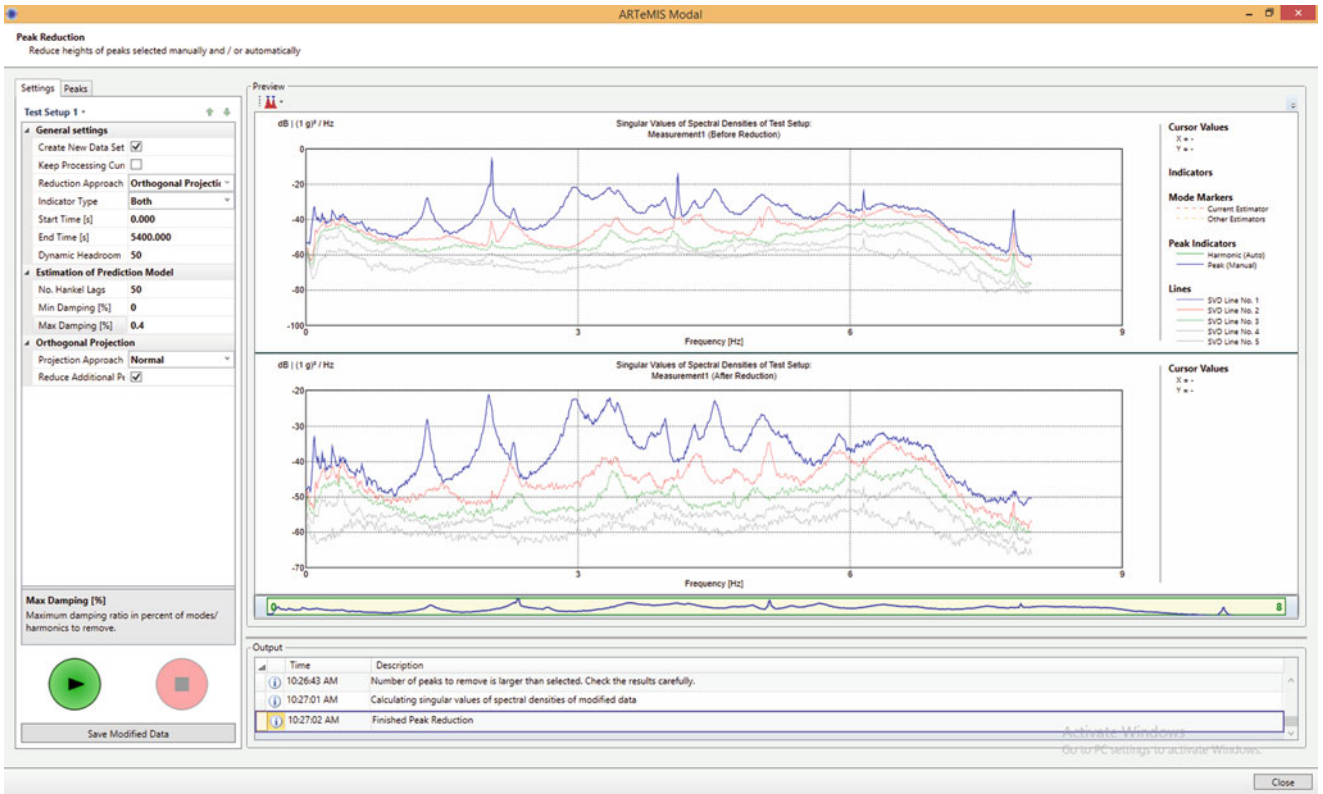

Fig. 2.10 Removal of predefined harmonics at 2.05 and 4.1 Hz. Harmonics at 6.15 and 7.8 Hz removed automatically

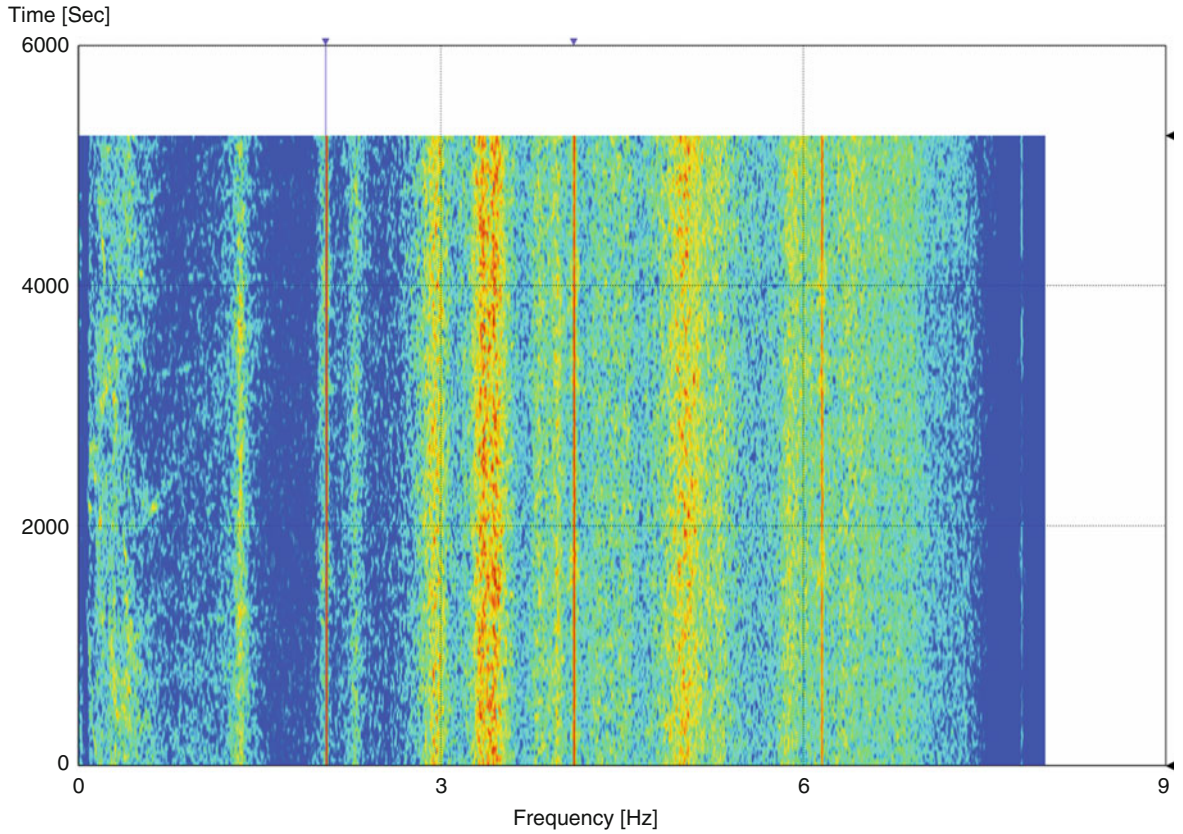

Fig. 2.11 STFT channel 5–9 before the harmonic reduction. Harmonics at 2.05, 4.1, 6.15 and 7.8 Hz

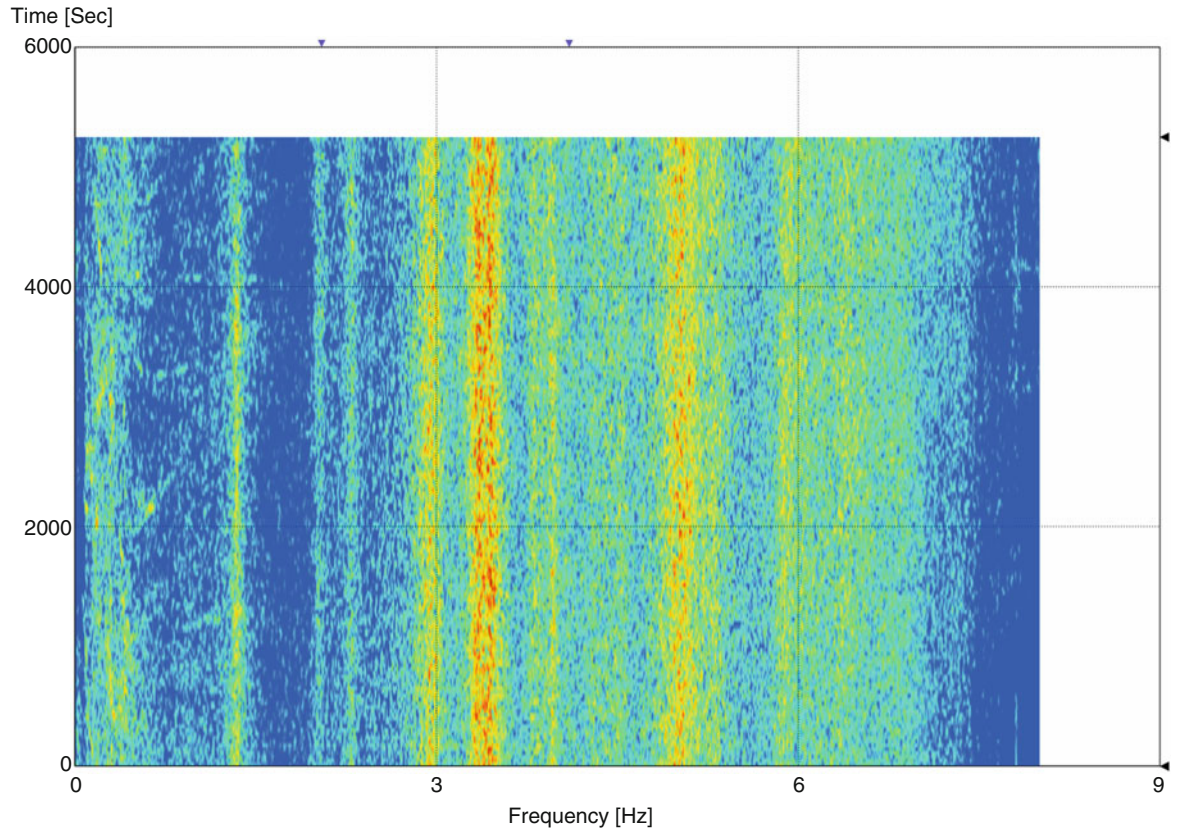

Fig. 2.12 STFT channel 5–9 after the harmonic reduction. Harmonics at 2.05, 4.1, 6.15 and 7.8 Hz removed

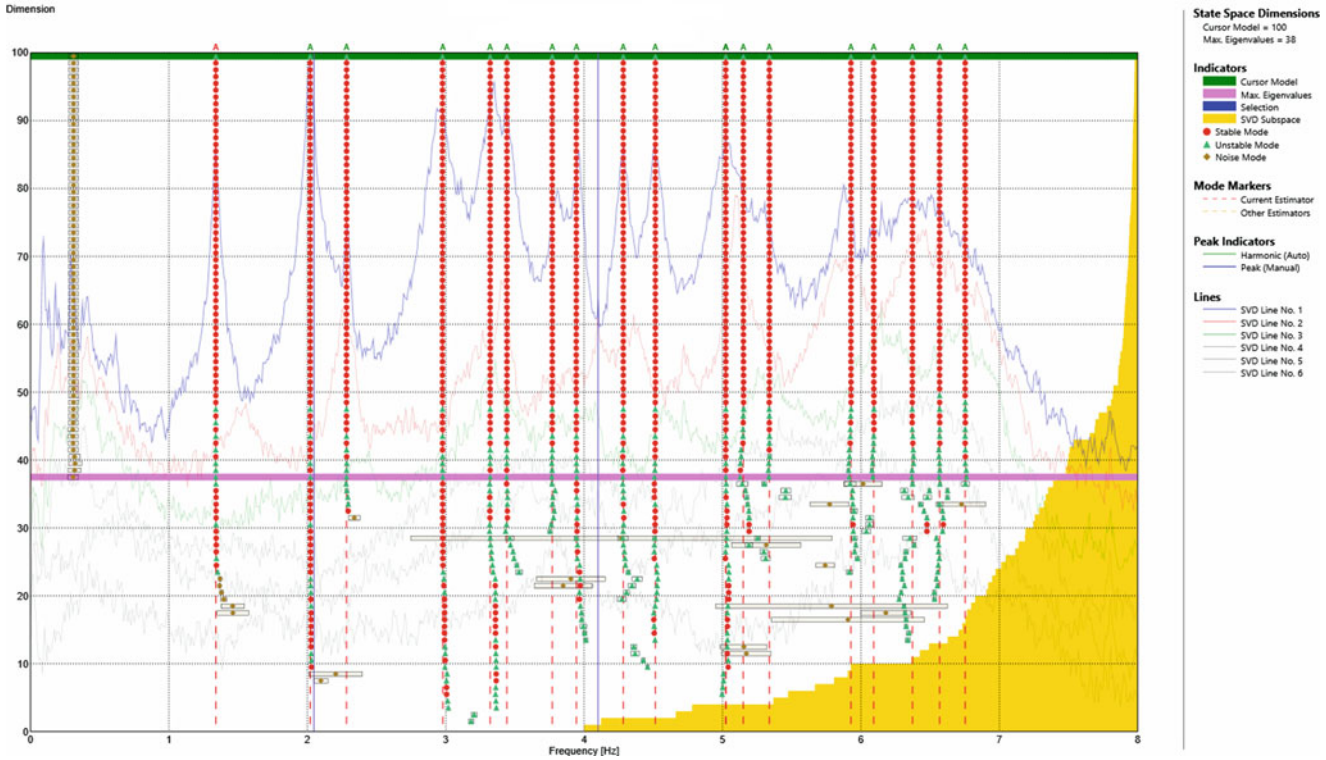

Fig. 2.13 Stabilization diagram of the estimated state space models from the signals after the harmonic removal. SSI-UPCX

2.4 Conclusion

In this paper we presented both the theory and the application of the orthogonal projection-based harmonic reduction method. Proposed algorithm successfully removed the harmonics from the experimental response signals albeit introducing a bias varying in range 1.42–9.92% between the different modal damping ratios. The source of the error can be explained by a non-linear damping behavior of the plate while excited with strong periodic signals, thus larger than from the random vibration test or a suboptimal choice of a the state space model order for predicting the harmonic realization of the response.

Similar results for the harmonic removal were achieved in context of a real-life application. Developed method removed the harmonic frequencies propagated from the engine of an operating ferry and enabled efficient OMA of the modified response signals.

The application of the method can be extended not only to harmonic reduction\removal but also to removing any arbitrary mode of the system. That might be useful to remove high energy modes present, for instance, in forced excitation during structural testing.

The bottleneck of the method is the choice of the state space model order such that it solely predicts the modal response that corresponds to selected harmonic frequencies. That, along with conducting more tests on a real measurements with strong non-stationary harmonic excitations and large number of channels will be the subject of our future work.

Acknowledgements The authors would like to thank Niels-Jørgen Jacobsen from B&K Nærum in Denmark for conducting the experimental tests and for sharing its results.

References

1. Benveniste, A., Mevel, L.: Nonstationary consistency of subspace methods. IEEE Trans. Autom. Control **52**(6), 974–984 (2007)
2. Basseville, M., Benveniste, A., Goursat, M., Hermans, L., Mevel, L., Van der Auweraer, H.: Output-only subspace-based structural identification: from theory to industrial testing practice. J. Dyn. Syst. Meas. Control **123**(4), 668–676 (2001)
3. Balmés, E., Basseville, M., Mevel, L., Nasser, H., Zhou, W.: Statistical model-based damage localization: a combined subspace-based and substructuring approach. Struct. Control. Health Monit. **15**(6), 857–875 (2008)

4. Döhler, M., Mevel, L., Hille, F.: Subspace-based damage detection under changes in the ambient excitation statistics. Mech. Syst. Signal Process. **45**(1), 207–224 (2014)
5. Peeters, B., Cornelis, B., Janssens, K., Van der Auweraer, H.: Removing disturbing harmonics in operational modal analysis. In: Proceedings of the International Operational Modal Analysis Conference (2007)
6. Combet, F., Gelman, L.: An automated methodology for performing time synchronous averaging of a gearbox signal without speed sensor. Mech. Syst. Signal Process. **21**(6), 2590–2606 (2007)
7. Randall, R., Smith, W.: New cepstral techniques for operational modal analysis. In: Proceedings of the First World Congress on Condition Monitoring (2017)
8. Bienert, J., Andersen, P., Aguirre, R.: A harmonic peak reduction technique for operational modal analysis of rotating machinery. In: Proceedings of the International Operational Modal Analysis Conference (2015)
9. Pintelon, R., Peeters, B., Guillaume, P.: Continuous-time operational modal analysis in the presence of harmonic disturbances the multivariate case. Mech. Syst. Signal Process. **24**(1), 90–105 (2010)
10. Peeters, B., de Roeck, G.: Reference-based stochastic subspace identification for output-only modal analysis. Mech. Syst. Signal Process. **13**(6), 855–878 (1999)
11. van Overschee, P., de Moor, B.: Subspace identification for linear systems, 1st edn. Springer, Boston (1996)
12. Aoki, M.: State space modeling of time series, 3rd edn. Springer, New York (1990)
13. Jacobsen, N.-J., Andersen, P., Brincker, R.: Eliminating the influence of harmonic components in operational modal analysis. In: Conference Proceedings, Society for Experimental Mechanics (2007)
14. Hoen, C.: Subspace identification of modal coordinate time series. In: Proceedings of the 24th International Modal Analysis Conference (IMAC) (2006)
15. Structural-Vibration-Solutions: ARTeMIS Modal Pro 5.2 (2017)
16. Döhler, M., Andersen, P., Mevel, L.: Variance computation of modal parameter estimates from UPC subspace identification. In: IOMAC – 7th International Operational Modal Analysis Conference, Ingolstadt (2017)
17. Rosenow, S.-E., Uhlenbrock, S., Schlottmann, G.: Parameter extraction of ship structures in presence of stochastic and harmonic excitations. In: Proceedings of the International Operational Modal Analysis Conference (IOMAC 2007), vol. 4, p. 01 (2007)
18. Jacobsen, N.-J., Andersen, P.: Operational modal analysis on structures with rotating parts. In: Proceedings of the International Conference on Noise and Vibration Engineering, KU Leuven (2008)

Chapter 3
Identifying Mode Shapes of Turbo-Machinery Blades Using Principal Component Analysis and Support Vector Machines

Alex La, John Salmon, and Jaron Ellingson

Abstract Manually identifying mode shapes generated from finite element solvers images is an expensive task. This paper proposes an automated process to identify mode shapes from gray-scale images of compressor blades within a jet-engine. This work introduces mode shape identification using principal component analysis (PCA), similar to approaches in facial and other recognition tasks in computer vision. This technique calculates the projected values of potentially linearly correlated values onto P-linearly orthogonal axes, where P is the number of principal axes that define a subset space. Classification was done using support vector machines (SVM). Using the PCA and SVM algorithm, approximately 5300 training images representative of 16 different modes were used to create a classifier. The classifier achieved on average 98% accuracy when tested using a test set of approximately 2000 images given P = 70. The results suggest that using digital images to perform mode shape identification can be achieved with high accuracy. Potential generalization of this method could be applied to other engineering design and analysis applications.

Keywords Mode Shape Identification · Computer Vision · Machine Learning · PCA · Image processing

3.1 Introduction and Background

Modal analysis is often executed inside a *design of experiments* loop to explore turbomachinery blade geometry. Design of experiments (DOE) is a method that allows a designer to iteratively traverse a design space to explore many designs and eventually find a satisfactory solution [1, 2]. When hundreds to thousands of designs are computationally generated, each design's modal displacements shapes and natural frequencies must be evaluated. To prevent a human user from doing simple mode shape classifications repeatedly, computer automated mode shape classification is often implemented [1, 2]. This work contributes a method to combining image processing, pattern recognition, machine vision, and machine learning techniques to develop a method to automatically identify mode shapes as part of the post-processing of a DOE loop for engineering design and analysis.

3.2 Method

This work used Mechanical ANSYS to generate mode shape images like those shown in Fig. 3.1. After the training and test images are gathered, each image is preprocessed prior to feature extraction. Preprocessing is used scale each image to a common size for feature extraction and to remove as much white space as possible, making the modal displacement data the focus of each image. First, the corners of the mode shape are found using the Shi-Tomasi corner detector [3]. Given a maximum of four corners per image, this facilitates a projective transform from a 4-cornered quadrilateral to a 100 × 100-pixel size square using the *Bilinear Warping Algorithm* [4]. After the image has been transformed to a square, the matrix is flattened into a vector to facilitate principal component extraction (Fig. 3.2).

After preprocessing, principal component analysis can be used to extract the eigenvalues and eigenvectors of a covariance matrix of a set of images [5]. Here, these eigenvectors are referred to as the 'blade-space'. After performing PCA on the training images, the original training images are projected back onto the 'blade-space' by an inner product. The number of principal components, P, is chosen to represent the smaller subspace created by the training set. When a projection is

A. La · J. Salmon (✉) · J. Ellingson
Brigham Young University, Department of Mechanical Engineering, Provo, UT, USA
e-mail: johnsalmon@byu.edu

C. Niezrecki, J. Baqersad (eds.), *Structural Health Monitoring, Photogrammetry & DIC, Volume 6*,
Conference Proceedings of the Society for Experimental Mechanics Series, https://doi.org/10.1007/978-3-319-74476-6_3

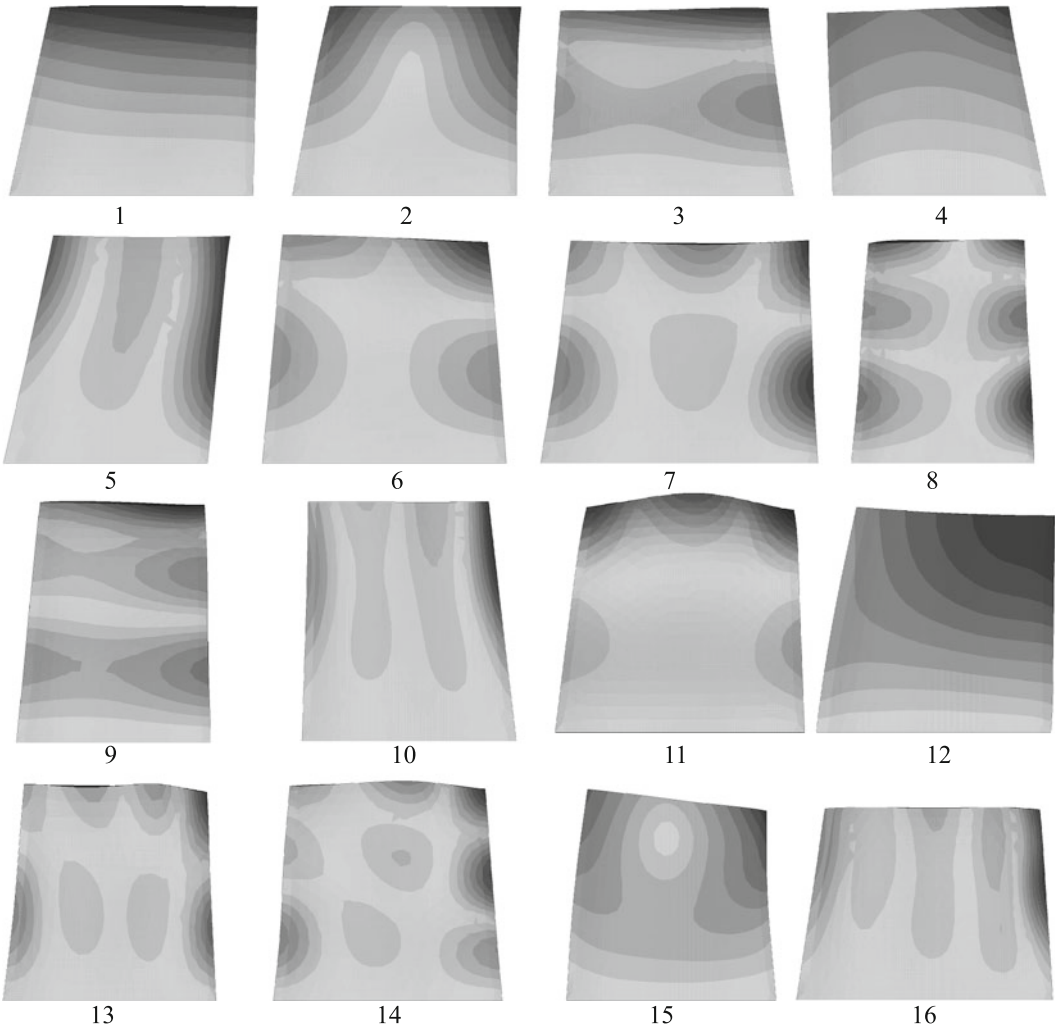

Fig. 3.1 Dominant mode shapes up to the 16th order. These mode shapes show the possible 2D deflections of an example compressor blade due to dynamics cyclic loading

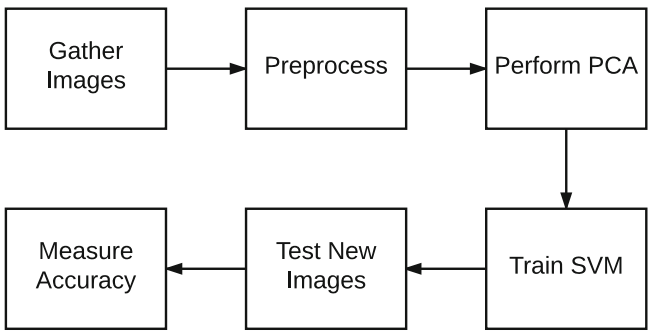

Fig. 3.2 High-level view of the "Eigenblades" classification method. The process begins with gathering the training and testing images, then each image is preprocessed, and featured extracted with PCA. After, a SVM classifier learns the feature vectors of the training set. This classifier is a function that maps a feature vector to a mode shape label

performed, an array of length P is returned and is called the PC-Scores for an image. This array is a unique descriptor used to describe an image, called the feature vector. Now, each training image can be uniquely defined by a list of values.

The PC-Scores (feature vector) and label for each training mode image is then used to train a machine learning classifier to determine how the different modes are separated by hyper-planes. In this work, support vector machines (SVM) were used

after an empirical study of other classifiers, including k-Nearest-Neighbor and decision trees. A one-vs-one approach is used to create multiple classifiers for 16 different mode shapes trained. In this work, the Python implementation of SVM through scikit learn is used [6].

After training the SVM classifier, the test images are ready to be classified. Each test image goes through the same preprocessing as the training images, to transform them into squares. After preprocess, each image is projected into the eigenspace of the training set images using PCA. This projection returns a vector of length P that is the feature vector, or the PC-Score of the test image. This feature vector is input into the SVM classifier and a predicted label is output for the unknown mode image.

3.3 Results and Conclusion

The accuracy, precision, recall scores shown in Table 3.1 demonstrates the excellent results of using PCA and SVM to identify mode shapes. As shown in Table 3.1, modes 1, 4, 11, and 13 scored a perfect classification for the test set. Most mode's accuracy measured greater than 90% except mode 12. Further inspection of the confusion matrix for modes 5 and 6 showed one reason for the inaccuracy was because ten images that were supposed to be classified as mode 6 were misclassified as mode 5. Looking at the images directly, we noticed that the errors were due to image conflation, as seen in Fig. 3.3. All mode

Table 3.1 Accuracy, precision, and recall for the mode shapes that were in the test set. This classifier extracted 70 principal components and was deemed the best of all other cases

Mode	Accuracy	Precision	Recall
1	1.0000	1.0000	1.0000
2	0.9965	1.0000	0.9965
3	0.9900	0.9900	1.0000
4	1.0000	1.0000	1.0000
5	0.9372	1.0000	0.9372
6	0.9324	0.9415	0.9897
7	0.9949	0.9945	1.0000
8	0.9474	0.9934	0.9558
9	0.9286	1.0000	0.9286
10	0.9876	0.9937	0.9937
11	1.0000	1.0000	1.0000
12	0.8696	0.9756	0.8889
13	1.0000	1.0000	1.0000
Average	1.9844	0.9906	0.9937

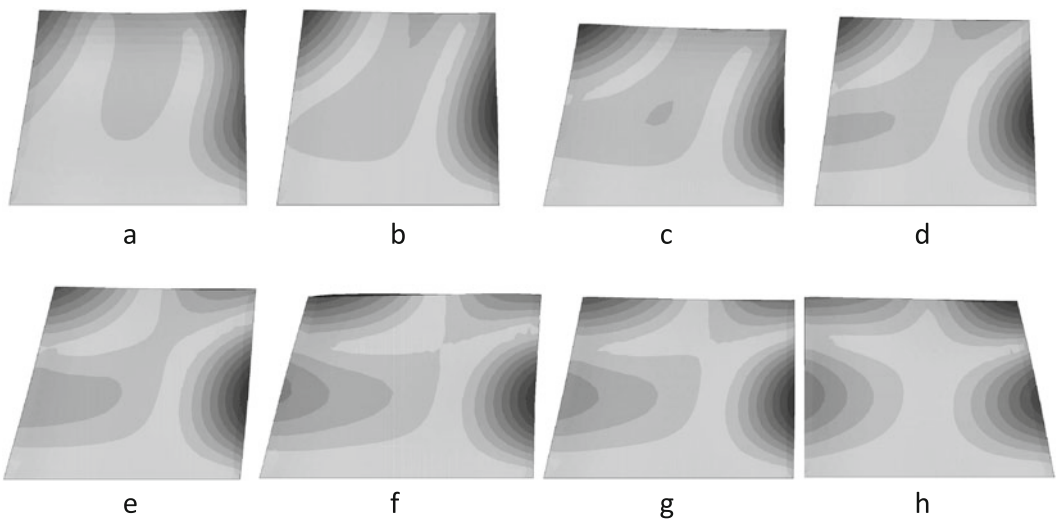

Fig. 3.3 Conflation of mode 5 to mode 6. Mode 5 is seen in image a and mode 6 is image h. These two images are distinct mode shapes. However, conflation can be seen in the images as different geometries are considered. These images are difficult even for human experts to classify and that is why they were incorrectly labeled

shapes in this figure are either mode 5 or 6, where mode 5 is labeled as **a** and mode 6 is labeled as **h**. The images labeled **a** and **h** are very distinct mode shapes. However, the distinction begins to weaken as the image chain progresses.

Another factor that improved the accuracy of this work, was removing the need for NURBS interpolation. As discussed before, the NURBS interpolation method found it was difficult to choose common point for interpolation between two modal displacement vectors as shown in Selin's [1] and Porter's et al. [2] methods. Because the "Eigenblades" method does not use any interpolation of the data, rather it uses dimensionality reduction through PCA, the main components of the data are kept intact. In addition to good accuracy, this method showed that it could correctly classify more modes than prior research. In both [1, 2], they classified only 5 mode shapes. In this work, 13 were achieved. A larger training set, could increase the number of different mode shapes that could be classified.

References

1. Selin, E.D.: Application of parametric NURBS geometry to mode shape identification and the modal assurance criterione (2012)
2. Porter, R., Hepworth, A., Jensen, C.G.: Application of machine learning and parametric NURBS geometry to mode shape identification. Comput. Aided Des. Appl. **13**(2), 184–198 (2016)
3. Shi, J.: Good features to track. Computer Vision and Pattern Recognition, 1994. Proceedings CVPR'94., 1994 IEEE Computer Society Conference on. IEEE (1994)
4. Wolberg, G.: Digital Image Warping, vol. 10662. IEEE Computer Society Press, Los Alamitos (1990)
5. Turk, M.A., Pentland, A.P.: Face recognition using eigenfaces. In: Computer Vision and Pattern Recognition, 1991. Proceedings CVPR'91., IEEE Computer Society Conference on. IEEE, pp. 586–591 (1991)
6. Pedregosa, Fabian, et al.: Scikit-learn: machine learning in Python. J. Mach. Learn. Res. **12**, 2825–2830 (2011)

Chapter 4
Full-Field Modal Analysis Using a DSLR Camera

Jaka Javh, Janko Slavič, and Miha Boltežar

Abstract High-speed camera measurements are increasingly being used in modal analysis to measure full-field response measurements using Digital image correlation and other Optical Flow methods. High-speed cameras can be very expensive, this is why this paper aims at measuring and identifying the full-field response using cheaper still-frame cameras, such as DSLR and mirrorless cameras. Using Spectral Optical Flow Imaging (SOFI) full-field operational shapes can be acquired using still-frame cameras. This study demonstrates a hybrid modal parameter identification of full-field mode shapes using an accelerometer and a DSLR camera, for responses far above the DSLR camera frame-rate (demonstrated up to 1 kHz).

Keywords SOFI · DSLR camera · Modal parameter identification · Optical flow · LSCF · LSFD · Photogrammetry

4.1 Introduction

High-speed cameras are increasingly being used in modal analysis, because of their ability to instantaneously measure a full-field of displacements. Digital cameras nowadays are affordable, boast high resolutions and large bit depths, this is why there has been a tendency to perform modal analysis with such cheaper, lower-speed cameras. One such example is the use of a mobile phone camera to measure the stay cable's natural frequency and in turn it's tension [1]. The problem with lower-speed cameras is the limited sampling rate. To overcome the low sampling rate techniques such as under-sampling and remapping the time instances to measure above the Nyquist frequency have been implemented [2], similar can be done by using frequency zooming and allowing for aliasing [3], or by filming at different frame-rates and combining the information to produce the aliased spectrum [4], also the rolling-shutter effect has been used to sample high frequencies from a normal DSLR camera video [5]. Fast motion can also be filmed using strobe lights, which produce an intense but short pulse of light producing an image with little-to-no blur [6].

It was recently shown that images indicating individual displacement spectral components can be produced by harmonically varying the illumination, thereby producing an analogue Fourier transform [7]. The said method, known as Spectral Optical Flow Imaging (SOFI), can obtain operational displacement shapes using still-frame cameras such as DSLR or mirrorless cameras, by acquiring a reference image, an image with sine phase and an image with cosine phase and combining the information into a full-field complex displacement field for a chosen frequency, determined by the harmonic of the blinking lights.

This research implements Spectral Optical Flow Imaging to acquire high-frequency (up to 1 kHz) full-field displacement fields for selected frequencies and combines this data in a hybrid modal parameter estimation [8] by using the Least Squares Complex Frequency method (LSCF) [9] to identify the eigenvalues from a single point sensor (accelerometer and/or laser vibrometer) and using the Least-Squares Frequency Domain method (LSFD) [10] to produce the full-field mode shapes.

4.2 Spectral Optical Flow Imaging

Spectral Optical Flow (SOFI) [7] produces individual spectral components by capturing an image of a vibrating structure illuminated with a harmonically varying light (blinking & vibrations image) and a reference motionless image at constant illumination. The difference is scaled with illumination scaling and the reference image gradient to produce the displacement spectral component $S_s\big((x, y), \omega_l\big)$ of frequency equal to the frequency of the varying light ω_l for every pixel (x, y):

J. Javh · J. Slavič (✉) · M. Boltežar
Faculty of Mechanical Engineering, University of Ljubljana, Ljubljana, Slovenia
e-mail: jaka.javh@fs.uni-lj.si; Janko.slavic@fs.uni-lj.si

C. Niezrecki, J. Baqersad (eds.), *Structural Health Monitoring, Photogrammetry & DIC, Volume 6*,
Conference Proceedings of the Society for Experimental Mechanics Series, https://doi.org/10.1007/978-3-319-74476-6_4

$$\underbrace{S_s\big((x,y),\omega_l\big)}_{\substack{\text{displacement}\\ \text{spectral}\\ \text{component}}} = \frac{\underbrace{I\Big((x,y)+s\big((x,y),t\big),L(t)\Big)}_{\text{blinking \& vibrations image}} - \underbrace{I\big((x,y),L_0\big)}_{\text{reference image}}}{\frac{1}{2}\underbrace{\frac{L_A}{L_0}}_{\text{illumination}}\underbrace{\nabla I\big((x,y),L_0\big)}_{\substack{\text{referenceimage}\\ \text{gradient}}}} \tag{4.1}$$

By using different frequencies of the blinking lights, different spectral components can be measured. Also, by changing the phase of the lights from $\sin(\omega_l t)$ to $\cos(\omega_l t)$ the cosine amplitudes $S_c((x,y),\omega_l)$ can be measured. The frequency of interest is not limited by the camera and can be very high (in the range of kHz) as long as the displacements are significant enough to be identified.

The displacement amplitudes from Eq. (4.1) $S_s((x,y),\omega_n)$ and $S_c((x,y),\omega_n)$ are displacements in the direction of the image gradient only. The 2D displacements can be obtained using Lucas-Kanade by solving the system of equations for a $H \times H$ subset containing various gradient directions and scaling the results according to the illumination $1/(L_A/L_0)$.

For more on Spectral Optical Flow Imaging see [7].

4.3 Hybrid Modal Parameter Identification

A structure's dynamic response is composed from different mode shapes, each with it's own eigenvalue (eigenfrequency & damping). Modal parameter identification methods typically identify the eigenvalues and the mode shapes separately.

Precise sensors, such as an accelerometer or a laser vibrometer can be used to determine the eigenvalues from a single point measurement ($\hat{\lambda}_r$ for $r = 1, 2, \ldots, N$), because the eigenvalues are a global parameter and only one location has to be measured to obtain them.

When the eigenvalues are known, selected full-field frequencies of interest can be measured using SOFI and the full-field mode shapes identified with the LSFD method. LSFD identifies the modal constants ${}_rA_{jk}$, which form the scaled mode shapes, based on the response model [11]:

$$\alpha_{jk}(\omega) = \sum_{r=1}^{N}\left(\frac{{}_rA_{jk}}{\mathrm{i}\,\omega - \lambda_r} + \frac{{}_rA^*_{jk}}{\mathrm{i}\,\omega - \lambda^*_r}\right) \tag{4.2}$$

Using measured full-field (SOFI) frequency responses $\hat{\alpha}_{jk}(\Omega_n)$, where Ω_n are the selected measured angular frequencies of interest, a system of linear equations can be produced using Eq. (4.2):

$$\begin{Bmatrix} \hat{\alpha}_{jk}(\Omega_1) \\ \hat{\alpha}_{jk}(\Omega_2) \\ \vdots \\ \hat{\alpha}_{jk}(\Omega_L) \end{Bmatrix} = \begin{bmatrix} \frac{1}{\mathrm{i}\,\Omega_1-\hat{\lambda}_1} & \frac{1}{\mathrm{i}\,\Omega_1-\hat{\lambda}_2} & \cdots & \frac{1}{\mathrm{i}\,\Omega_1-\hat{\lambda}_{2N}} & -\frac{1}{\Omega_1^2} & 1 \\ \frac{1}{\mathrm{i}\,\Omega_2-\hat{\lambda}_1} & \frac{1}{\mathrm{i}\,\Omega_2-\hat{\lambda}_2} & \cdots & \frac{1}{\mathrm{i}\,\Omega_2-\hat{\lambda}_{2N}} & -\frac{1}{\Omega_2^2} & 1 \\ \vdots & \vdots & \ddots & \vdots & \vdots & \\ \frac{1}{\mathrm{i}\,\Omega_L-\hat{\lambda}_1} & \frac{1}{\mathrm{i}\,\Omega_L-\hat{\lambda}_2} & \cdots & \frac{1}{\mathrm{i}\,\Omega_L-\hat{\lambda}_{2N}} & -\frac{1}{\Omega_L^2} & 1 \end{bmatrix} \begin{Bmatrix} {}_1A_{jk} \\ {}_2A_{jk} \\ \vdots \\ {}_{2N}A_{jk} \end{Bmatrix} \tag{4.3}$$

The solution of the above system produces the modal constants ${}_rA_{jk}$ (mode shapes).

4.4 Experiment and Results

An experiment using a cymbal as the test structure was performed. The cymbal was chosen because it has a wide dynamic response and has been measured extensively in previous experiments.

Since SOFI only works for small displacements and is sensitive to large rigid body motions, the cymbal was rigidly fixed at it's centre hole and a stinger for saker excitation was attached close to the ridge of the cymbals inner indentation (see Fig. 4.1).

A simple light regulating circuit was used to harmonically regulate the light intensity and the experiment was performed in a dark (anechoic) chamber to avoid outside interference, such as ambient light. The excitation was measured by a force transducer attached between the shaker and the cymbal and the response was measured by an accelerometer and the DSLR camera.

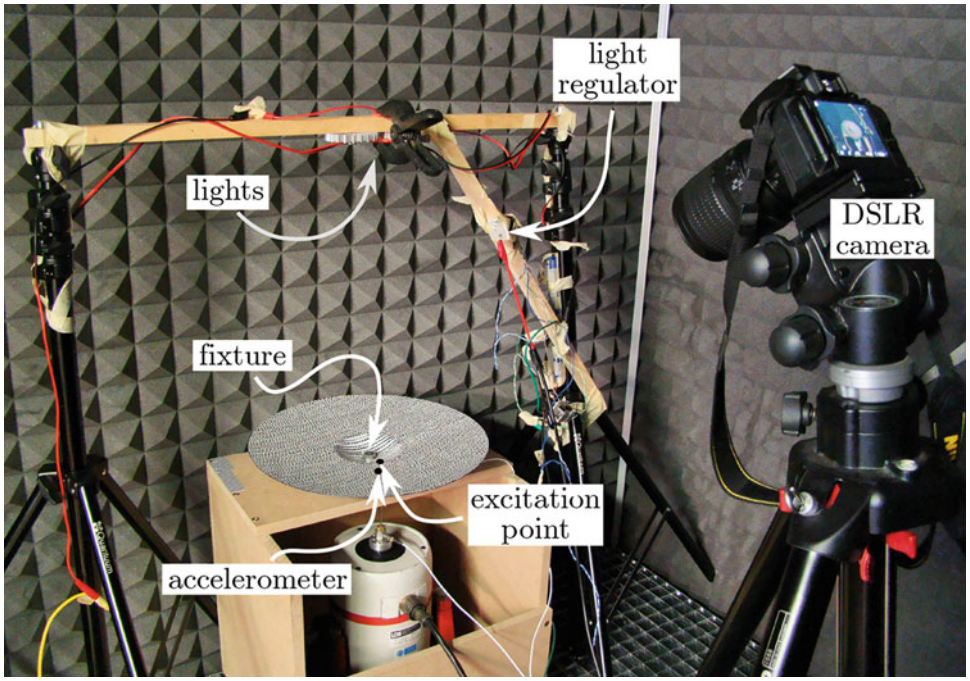

Fig. 4.1 The SOFI experimental set-up

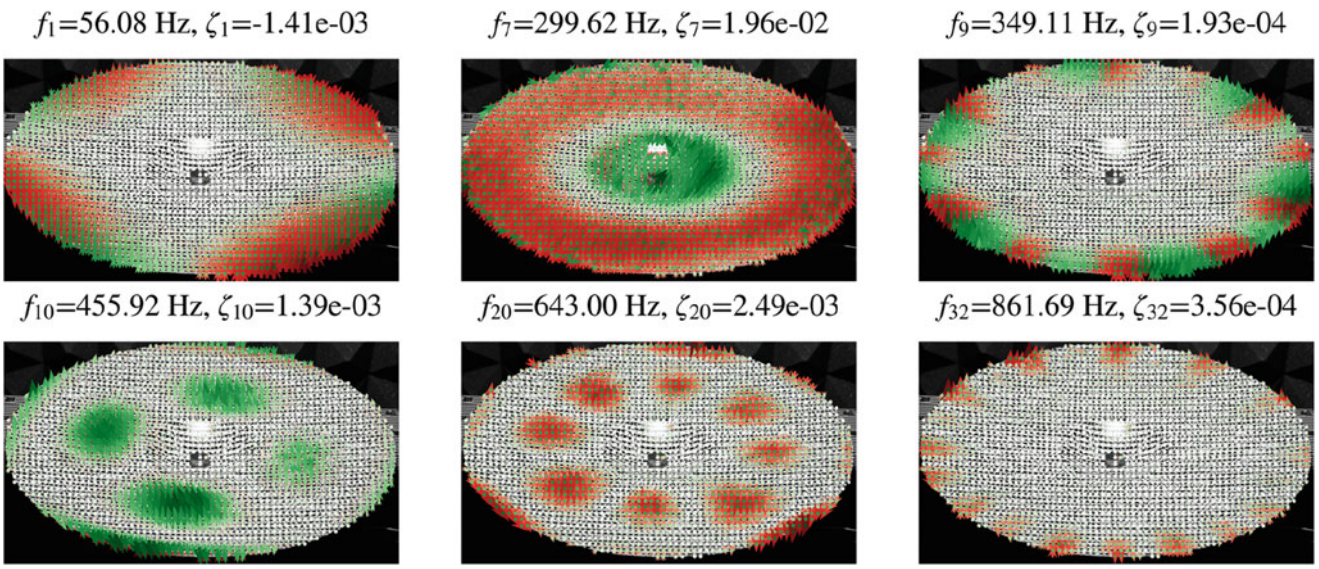

Fig. 4.2 A few identified mode shapes using the DSLR camera and SOFI in the hybrid modal parameter identification (green – real values, red – imaginary values)

The eigenvalue identification was performed for a regulated pseudo-random (multi-sine) excitation of a 2 s window 30–1000 Hz frequency band. Thirty nine eigenfrequencies were identified in the specified frequency range. The full-field spectral response measurements were later performed using SOFI on a Nikon D5300 DSLR camera during single harmonic excitation for frequencies close to the eigenfrequencies. The excitation used was single harmonic, however SOFI can work with broad-band vibrations as well.

Figure 4.2 shows 6 of all 39 successfully identified full-field mode shapes obtained using SOFI in the hybrid modal parameter identification.

4.5 Conclusion

Full-field modal analysis can be performed using an affordable still-frame camera and SOFI in combination with an additional single point sensor for the eigenvalue identification. The obtained results are comparable to the results obtained by using high-speed cameras, however attention has to be given to the experimental set-up which should prohibit large motions and assure appropriate light control and repeatability.

Acknowledgements The authors acknowledge the partial financial support from the Slovenian Research Agency (research core funding No. P2-0263 and J2-6763).

References

1. Zhao, X., Ri, K., Wang, N.: Experimental verification for cable force estimation using handheld shooting of smartphones. J. Sens. **2017**(5625396) (2017). https://www.hindawi.com/journals/js/2017/5625396/
2. Liu, Y., Gao, H., Zhuge, J., Zhao, J.: Research of under-sampling technique for digital image correlation in vibration measurement. Shock. Vib. Aircr./Aerosp. Energy Harvest. Acoust. Opt. **9**, 49–58 (2017)
3. Javh, J., Brumat, M., Slavič, J., Boltežar, M.: A high-speed camera measurement set-up for deflection shape analysis. In: Proceeding of ISMA2016-USD2016, pp. 1043–1050 (2016)
4. Yang, Y., Dorn, C., Mancini, T., Talken, Z., Nagarajaiah, S., Kenyon, G., Farrar, C., Mascarenas, D.: Blind identification of full-field vibration modes of output-only structures from uniformly-sampled, possibly temporally-aliased (sub-Nyquist), video measurements. J. Sound Vib. **390**, 232–256 (2017)
5. Davis, A., Rubinstein, M., Wadhwa, N., Mysore, G., Durand, F., Freeman, W.T.: The visual microphone: passive recovery of sound from video. ACM Trans. Graph. (Proc. SIGGRAPH) **33**(4), 1–10 (2014)
6. Stampfer, S.: Die stroboscopischen Scheiben; oder, Optischen Zauberscheiben: Deren Theorie und wissenschaftliche Anwendung, Trentsensky & Vieweg (1833)
7. Javh, J., Slavič, J., Boltežar, M.: Measuring full-field displacement spectral components using photographs taken with a DSLR camera via an analogue fourier integral. Mech. Syst. Signal Process. **100**, 17–27 (2018)
8. Javh, J., Slavič, J., Boltežar, M.: High frequency modal identification on noisy high-speed camera data. Mech. Syst. Signal Process. **98**, 344–351 (2018)
9. Guillaume, P., Verboven, P., Vanlanduit, S.: Frequency-domain maximum likelihood identification of modal parameters with confidence intervals. In: Proceedings of ISMA 23, pp. 16–18 (1998)
10. Auweraer, H.V., Leurs, W., Mas, P., Hermans, L.: Modal parameter estimation from inconsistent data sets. In: Proceeding of IMAC XVIII, pp. 763–771 (2000)
11. Cauberghe, B.: Applied frequency-domain system identification in the field of experimental and operational modal analysis, Ph.D. thesis, Vrije Universiteit Brussel (2004)

Chapter 5
Enhancing Standard GVT Measurements with Digital Image Correlation

S. Manzato, E. Di Lorenzo, and P. Mäckel

Abstract In recent years, high-speed cameras permit to record high-resolution images at several thousand frames-per-second. In addition to this, Digital Image Correlation (DIC) measures full-field displacements and strains in 3D from stereo camera images and perform Operational Deflection Shape and Modal Analysis on the data. Several papers have demonstrated the validity of the approach on laboratory cases, comparing and validating the results with those obtained using more standard measurement techniques (accelerometers, strain gauges, lasers). Very limited cases have been however investigated on the possibility to combine high-speed DIC and standard accelerometer-based measurement to fully exploit the advantages of both techniques. In this paper, the possibility to combine global acceleration measurements on an F16 during a classical Ground Vibration Test with local full-field camera measurement is investigated. The advantages of the combined approach are clear, as the standard measurement will provide the global mode shapes of the aircraft, which can be used for certification and modal validation, while the local high-speed camera measurement system can provide displacement and strain field data with an unmatchable spatial resolution. In particular, the paper will focus on the possibility of using the local displacement measurements to better characterize the non-linear behavior of the connection between the wing and the payload.

Keywords Ground Vibration Testing · Digital Image Correlation · Modal Analysis · non-linearities

5.1 Introduction

Over the last two decades, there has been a growing research and industrial interest in contactless measurement technologies. This has mostly been driven by the increasing usage of lightweight materials and topologically optimized structures (thanks to Additive Manufacturing and 3D printing), but also by scenarios were standard sensor cannot deliver high quality results. While Laser Doppler Vibrometry is a quite establish solution to achieve contactless measurement with high spatial resolution, image-based techniques are now attracting more and more attention, as they can achieve an incredibly high spatial resolution. Without the need or repeating the measurement multiple time. While in the past this technology was mostly used in static and quasi static testing, it was also proven that it was similarly possible to apply it to dynamic problems as well. In parallel, the quality of high-speed cameras has also drastically improved, not only in terms of frame rates, but also Signal to Noise Ratio, linearity and resolution, which are essential requirements for DC. Also size and weight have been significantly reduced, so that stereo high speed camera systems are easier to handle. Furthermore the computational power and memory available on modern Laptop and Desktop PCs is able to handle the high amount of space and time domain data generated by the stereo high speed system for FFT processing.

A thorough overview of photogrammetry and optical methods, with application to structural dynamics, is available in [1]. In [2], a detailed comparison between Digital Image Correlation (DIC), Laser Doppler Vibrometry (LDV), Electronic Speckle Pattern Interferometry (ESPI) and accelerometer-based measurement is performed, with a specific focus on the identification of the dynamic response. Many other similar publications have been published and presented in recent years, but most of the time on dedicated test cases, often in lab conditions. Some examples of operational measurements on rotors are reported in [1, 3].

S. Manzato (✉) · E. Di Lorenzo
Siemens Industry Software NV, Leuven, Belgium
e-mail: simone.manzato@siemens.com

P. Mäckel
isi-sys GmbH, Kassel, Germany

C. Niezrecki, J. Baqersad (eds.), *Structural Health Monitoring, Photogrammetry & DIC, Volume 6*,
Conference Proceedings of the Society for Experimental Mechanics Series, https://doi.org/10.1007/978-3-319-74476-6_5

In this paper, the objective is to use a stereo high-speed camera systems to measure the displacement field of the wing end of an F16 during a GVT campaign. The measurement where performed under a limited time window of 2 days by two experienced users, who however had never had the chance to perform such a measurement in a comparable combined scenario, with the goal of integrating the DIC measurements and results with those from a standard GVT system (which uses accelerometers). A theoretical overview of DIC measurement and analysis is outside the scope of the paper, but a detailed and thorough description can be found in [4], which also describes the software VIC3D of Correlated Solutions applied here.

5.2 F16 Ground Vibration Test

Every 2 years, Siemens Industry Software organizes for its customers, as well as anybody interested, a Master Class to share best practices on how to perform successfully a GVT, covering all topics from instrumentation, to test setup, data analysis, validation and verification of numerical models and finally covering also the fundamentals of flutter testing [5]. The theory is of course applied on the fly on a real F16 aircraft, shown in Fig. 5.1.

The standard instrumentation used on the aircraft includes:

- A combination of single axis and triaxial ICP accelerometers, measuring a total of 109 Degrees-of-Freedom (see Fig. 5.2)
- Two electro-dynamic shakers exciting each wing tip in the vertical direction;
- Two load cells or impedance heads at the interface between the shaker stinger and the structure to measure the applied forces.

In order to facilitate interpreting the results and visualize the mode shapes, it is highly recommended to build a geometry with the location of the transducer (Fig. 5.2). This process can be quite time consuming and prone to errors, which are particularly important when the results are used to validate a numerical model.

Figure 5.3 show the results obtained by applying modal analysis on the 109 $\times$ 2 FRF matrix measured using a Pseudo Random excitation profile. On the left, the measured FRFs at 1 DOF are compared with those synthesized using the identified modal model. On the right, the AutoMAC allows to verify that the modeshapes are orthogonal and there is no spatial aliasing.

In the occasion of the Master Class, we generally have the opportunity to keep the aircraft instrumented for some extra time for research purposes. In the past, for example, we tested the applicability of photogrammetry to generate a geometry of the text object that could be used for mode shapes expansion when a CAD or FE model is not available [5] (Fig. 5.4), or to collect data on a representative structure to develop/validate engineering approaches to deal with non-linearities in structural dynamics [6] (Fig. 5.5).

Fig. 5.1 The tested F16 aircraft

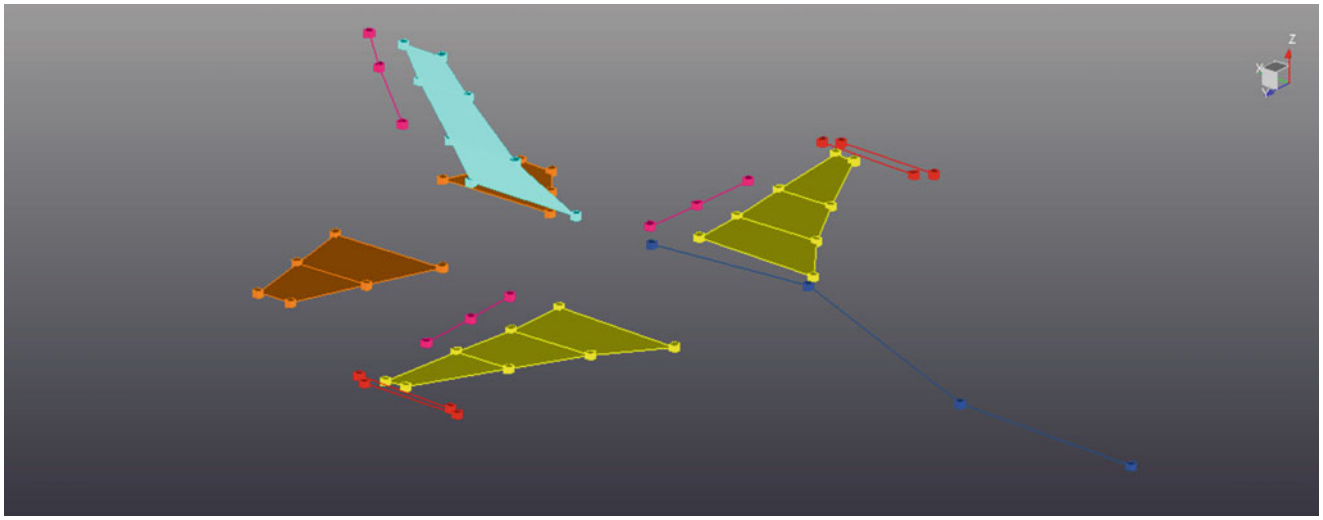

Fig. 5.2 Standard GVT test geometry with measurement points

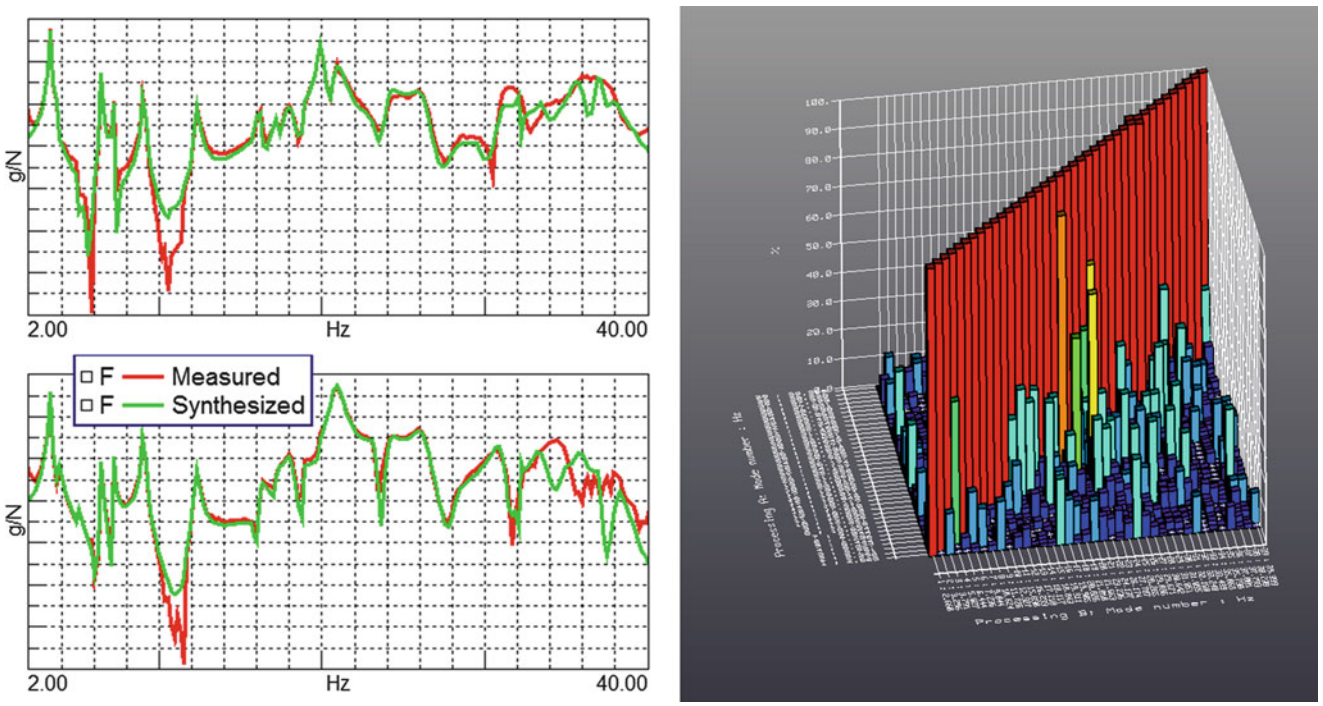

Fig. 5.3 Modal analysis results. Left: measured vs. synthesized FRFs. Right: autoMAC matrix for the identified mode set

For the more recent master class, organized in September 2016, it was decided to further focus on optical techniques, and in particular on full-field dynamic DIC. The test campaign was planned and designed to get a clear answer to the following questions:

- Can High-Speed Camera with Digital Image Correlation be used in a GVT context?
- Can it be used in combination with a standard GVT measurement setup and what is the added value of combining the two systems?
- What is the best way to combine the results from the two systems together?

In order to keep the complexity of the setup to a minimum and to fit the measurements in the limited time frame available, the DIC analysis was focused on a local area of the aircraft, namely the wing tip, the payload support and the payload itself. In particular, this area was chosen as the connections between these three components showed a non-linear response when

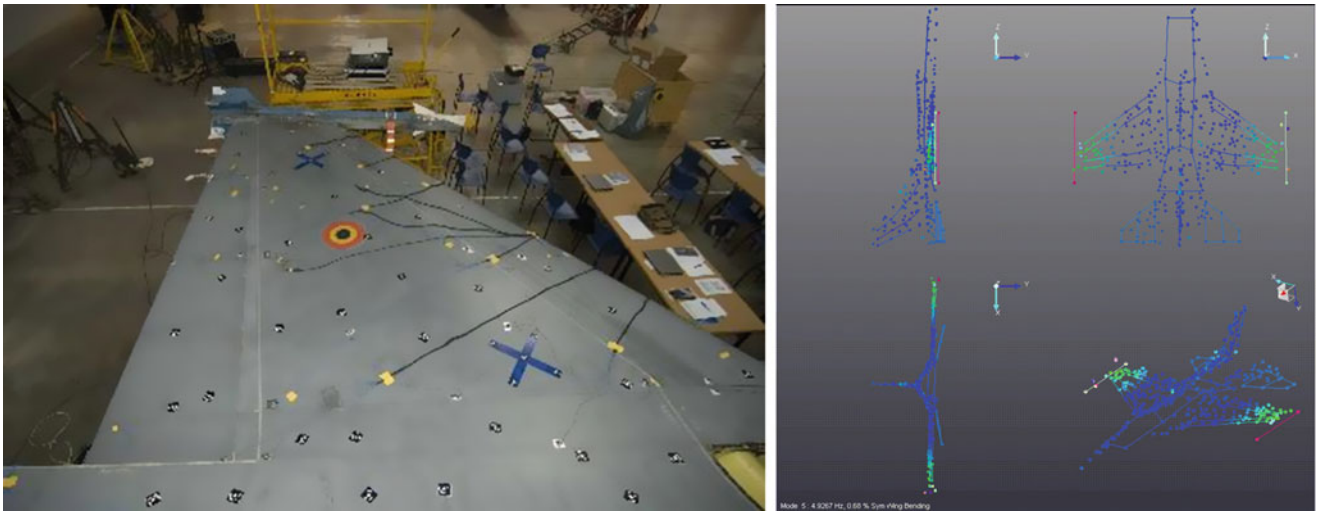

Fig. 5.4 Left: left wing with markers for photogrammetry. Right: Measured point cloud used for mode shape expansion

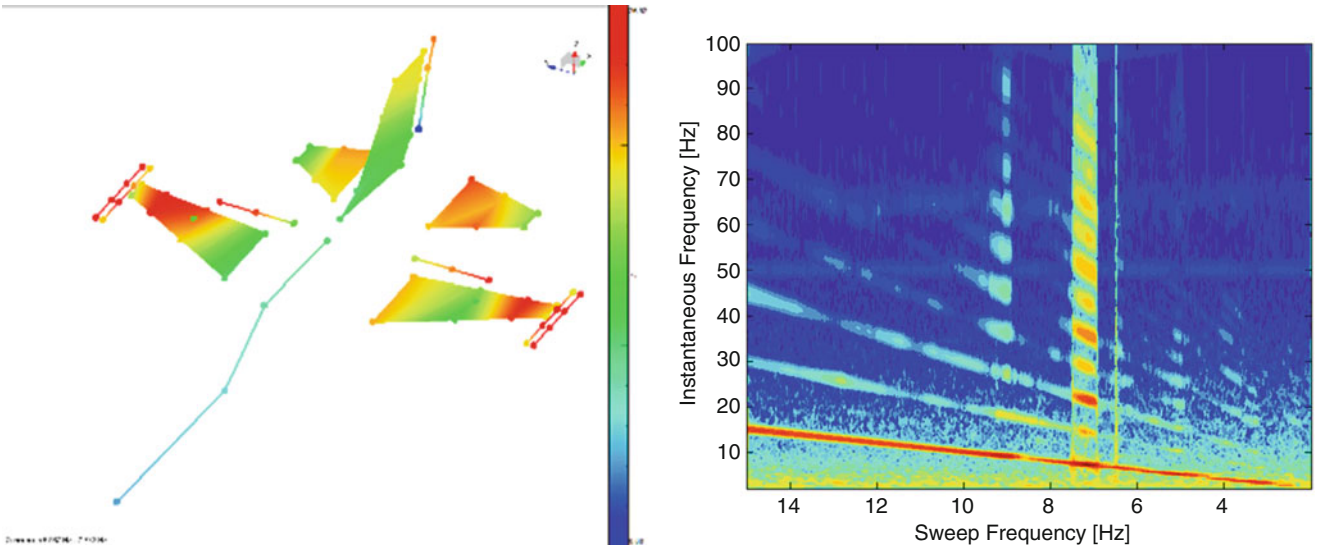

Fig. 5.5 Nonlinear dynamics assessment: Left: linearity map. Right: time frequency analysis

exciting one of the low frequency modes. The availability of the full field displacement field can provide more accurate information on the non-linearity than the use of few accelerometers.

In Fig. 5.6 the system used for measurement is shown. Two Photron FASTCAM AX100 cameras with were used in a stereo system arrangement of isi-sys GmbH. Lenses with a comparable short focal length of 20 mm have been selected in order to allow 3D measurements from below the wing. To simplify the setup, the speckle pattern was obtained by attaching printed stickers to the lower side of the wing, Finally, artificial lighting was used to allow sufficiently short exposure times to reduce motion blurring. An example of the two frames captured by the stereo camera pair of the system is shown in Fig. 5.7.

To calibrate the 3D stereo camera system and record and process the images, the VIC-3D software, with the special FFT-Module, was used. The FFT-Module of VIC-3D was developed by Correlated Solutions INC, USA in 2009/2010 for vibration and running mode analysis using the phase separation method. Due to the instantaneous full field recording principle in combination with High Speed Cameras this principle is one of the only method which can be applied for full field operation mode analysis. In parallel, to drive the shakers and measure accelerometers, LMS SCADAS with LMS Test.Lab software were used.

However, streaming data synchronously on a PC from the two setups is not possible, as pictures are collected on an internal storage device and then need to be transferred to a PC after the measurement is finished. Also, synchronization between the

Fig. 5.6 Camera Instrumentation overview with the stereo system on the left and the whole setup with the extra lights on the right

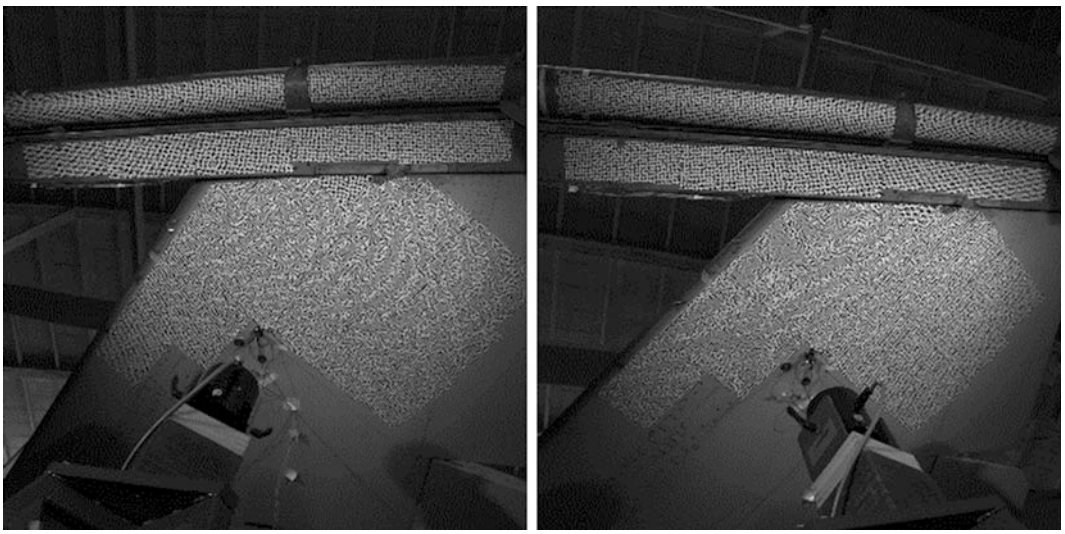

Fig. 5.7 Example of a stereo image pair of the F16 wing tips from below. The payload support and the payload itself. On the center of the lower part the electrodynamic shaker and the connection to the wind is seen

two systems can be an issue if data are to be processed simultaneously, as the internal clocks might be slightly different. Thus other means of combining the data from the two systems were investigated, and will be discussed in next section.

To excite the aircraft, standard random and burst random excitation profiles were used first. In the VIC-3D FFT module, time data can be converted to the frequency domain and Operational Deflection Shapes (or Running Mode analysis) performed. However, no averaging process is foreseen and consequently broad band random spectra will be quite noisy and the shapes might not be extremely clear (also considering displacements are calculated from the measurements). Consequently, sine sweep excitation was used, which yielded a much higher signal to noise ratio. To keep the sweep speed low enough and comply with the storage space available in the cameras, the frequency range had however to be limited between 5 Hz and max 30 Hz. To analyze the non-linear response, excitation was applied at two different levels. Finally, in order to limit the amount of data to be stored and the processing time, the displacement outputs are calculated on a reduced grid than the one on which the DIC is performed. Example of the calculated Operational Deflection Shapes from the image processinareis shown in Fig. 5.8.

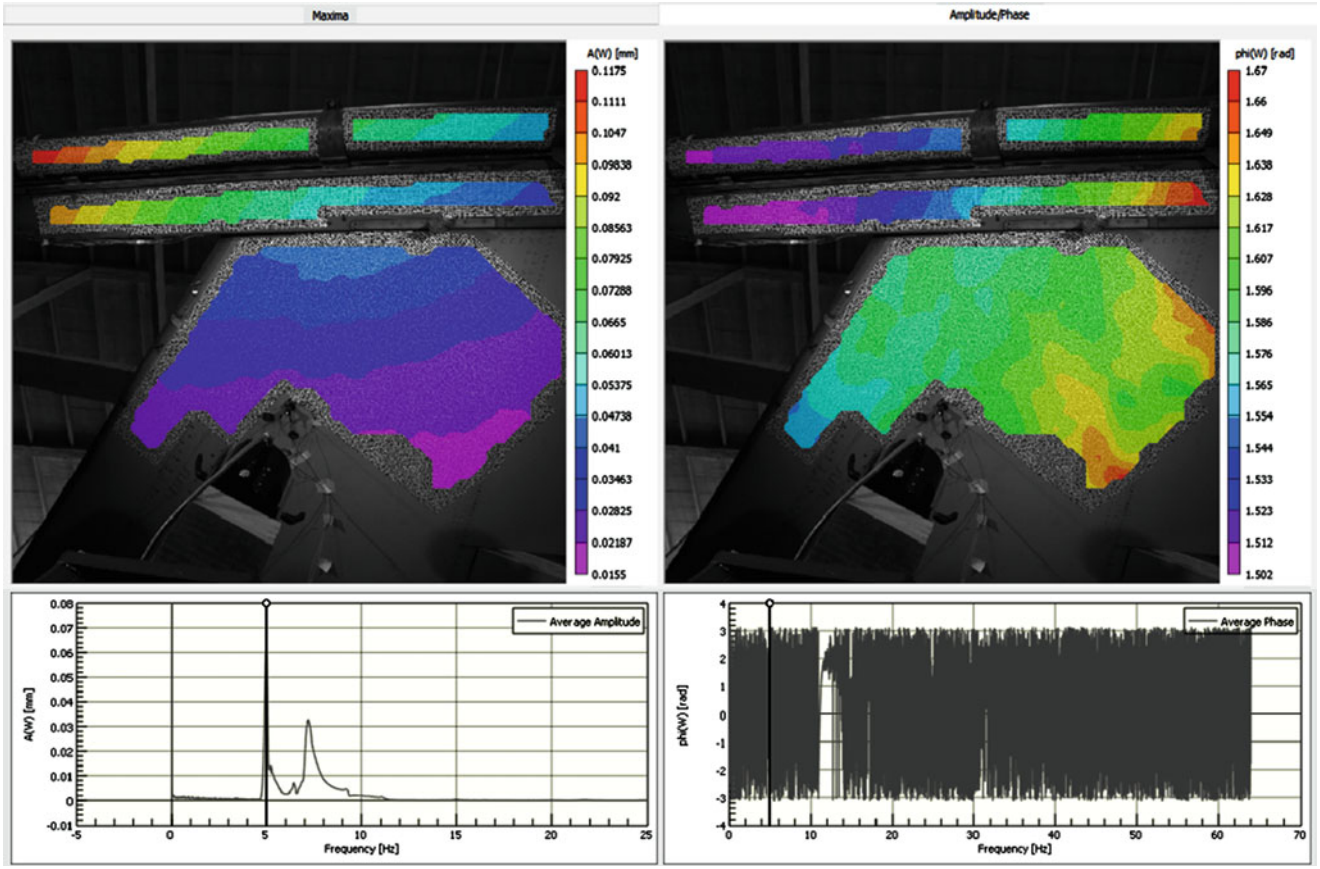

Fig. 5.8 DIC processing in the CIV3D software. Example of an Operational Deflection Shape

5.3 Combining Standard and Full-Field Measurements

As mentioned above, one of the objectives of the work was the identification of the most practical ways to combine the data and results from the two systems.

The most obvious approach would be to align the time histories based on reference signals prior to perform any further processing. This would have the advantage of allowing calculating the Frequency Response Functions (FRFs) from the DIC displacements, but it would also require a perfect synchronization. As it was not possible to use a reference clock (i.e. GPS based) for both systems, this accurate alignment cannot be achieved.

An alternative possibility is to process time data into half auto and crosspowers, identify the modal parameters using operational modal analysis and then combine the mode sets using a common reference. Although sine tests were performed, the excitation profiles in the frequency range of interest is equivalent to a white noise (Fig. 5.9) and Operational Modal Analysis can then be reliably applied.

One of the big advantages of DIC is that geometry is automatically calculated by the system. The point coordinates can then be added in Test.Lab to the original F16 geometry and the two geometries be aligned (Fig. 5.10). As a consequence of the alignment, a common reference point can be determined, which will be useful to merge the mode shapes. Figure 5.11 shows first a comparison of the displacements obtained from DIC on the same point for the two levels. In the 30 N test, the excitation spanned from 5 to 30 Hz, with a sweep speed of 0.25 Hz/s. In the 75 N test, it was decided to decrease the sweep speed to 0.1 Hz/s to better characterize the non-linear response of the mode at 7.4 Hz. This however required to limit the max frequency to 12 Hz.

For the selected reference point, the spectra from the acceleration signal (integrated to displacement) are compared with those directly obtained from the DIC. The dominant peaks match very well, with the main difference, as expected, being the better Signal-to-Noise Ratio achieved with accelerometers. This could be caused by the fact that raw time data were processed, without using any of the available filters in VIC3D.

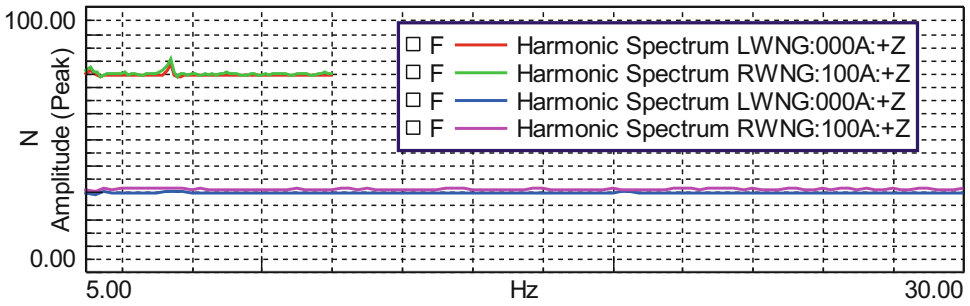

Fig. 5.9 Reference input force spectra for the two excitation levels

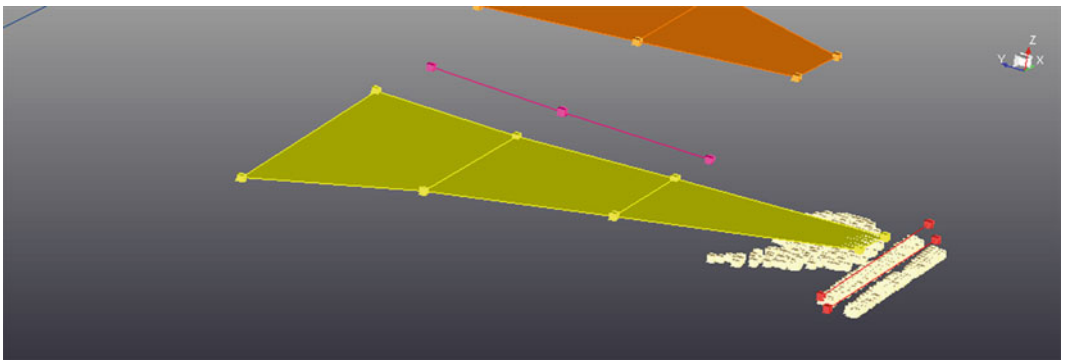

Fig. 5.10 DIC geometry overlaid to the standard one

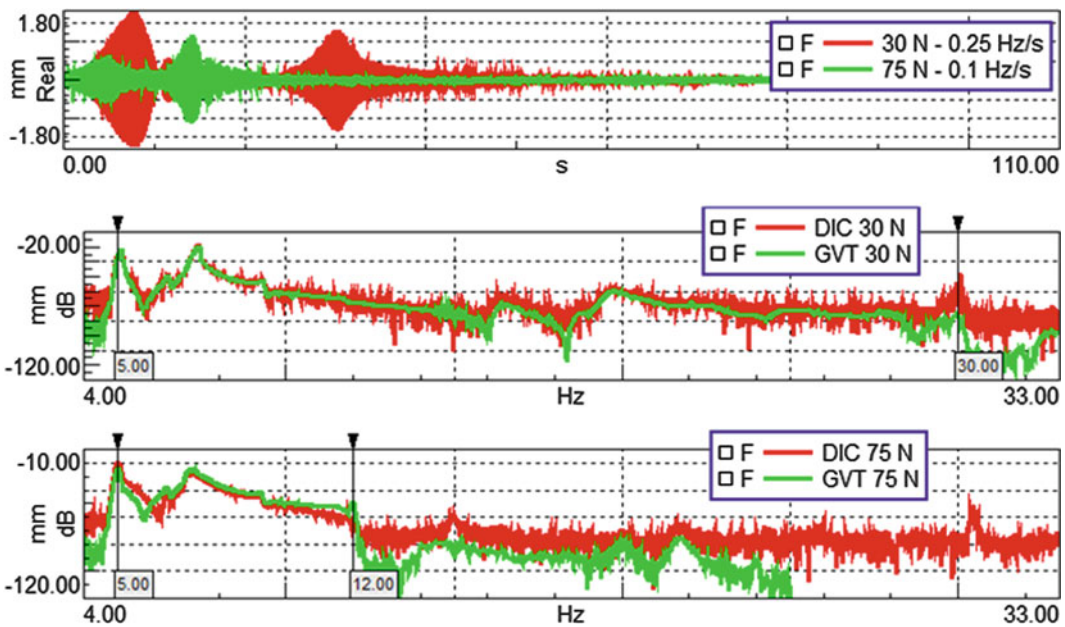

Fig. 5.11 Comparison between DIC and standard measured data on the same reference point

First, the data from the standard GVT system will be measured. As two shakers are used, FRFs need to be calculated using two sweeps with different phases between the shakers to have uncorrelated forces. To compute the Operational Modal Analysis (OMA) modes, the complete time histories are considered. However, the second sweep is not available in the DIC system, as the internal memory didn't allow to store all data. Only the symmetric modes are then expected to be found in that case. Also, as the DIC focused on the left wing tip area, only dominant wing modes will be considered and up to 12 Hz to allow a comparison between all runs.

Table 5.1 Reference GVT modes for random excitation and comparison to OMA results on Sine Sweep data

	Freq. Rand	Freq. 30 N	Freq. 75 N	Damp Rand	Damp. 30 N	Damp. 75 N
Mode 1	5.121	5.076	5.003	0.66	0.79	0.81
Mode 2	6.503	6.537	6.401	0.41	1.08	1.536
Mode 3	7.417	7.369	7.205	0.41	0.809	2.665
Mode 4	9.334	9.314	9.221	0.8	0.729	1.144
Mode 5	11.919	11.756	11.618	0.65	1.067	1.161

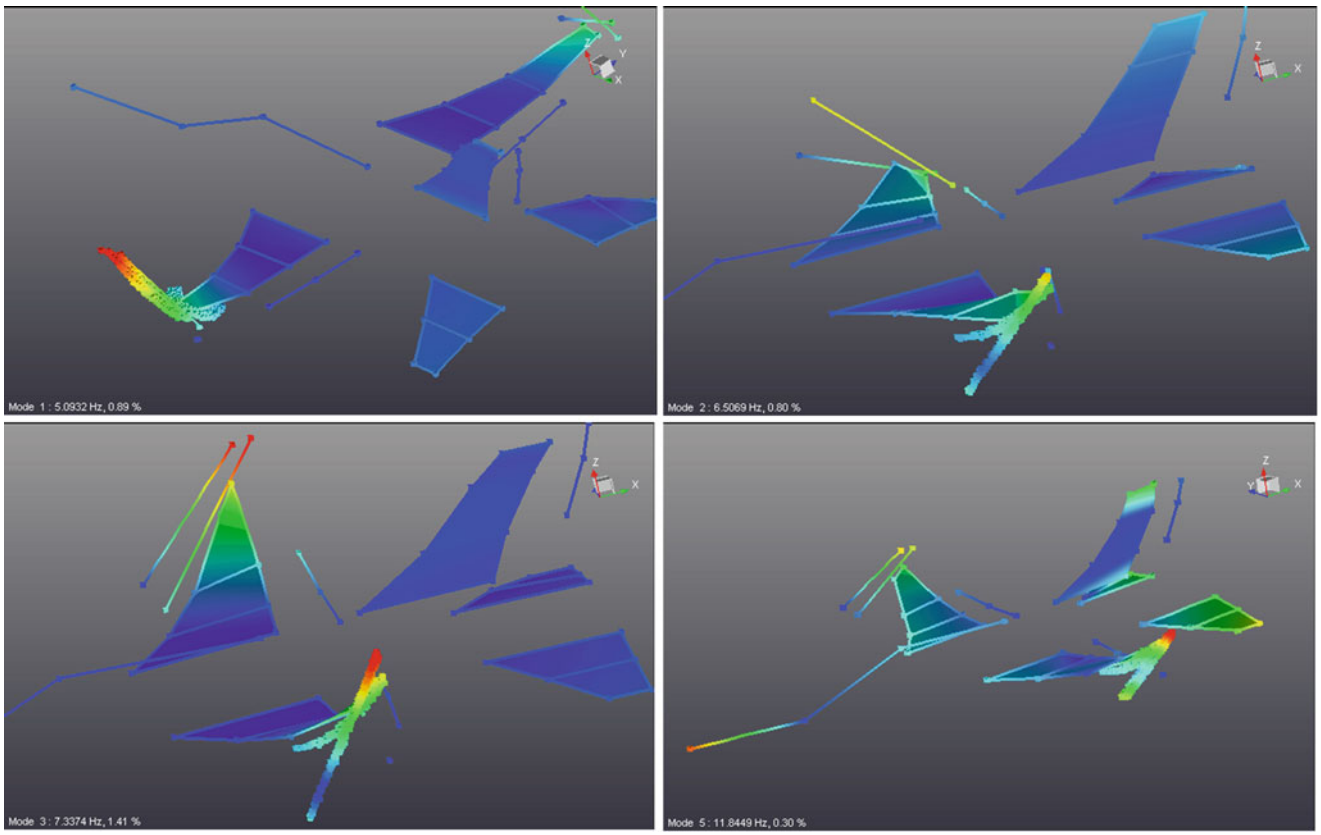

Fig. 5.12 Examples of identified mode shapes with GVT and DIC modes combined

The same processing is repeated also for the data collected at the higher excitation level. In Table 5.1, the results obtained with OMA are compared to those from standard random excitation and FRF modal analysis. It can be observed that, as the excitation level increases, the frequencies decrease while damping increase. This will be further investigated in the next section.

Modes will be now calculated applying OMA on the DIC time histories. Similar settings are used to compute the cross-powers and calculate the modal parameters. To merge the modes, the standard procedure available in the LMS Test.Lab software is used:

- The same DOF Id is used for the common points between the two datasets
- The point is selected as reference for the Crosspowers calculation.
- The two modesets are loaded in the Multi Run Modal worksheet;
- The software looks for pairs of modes to merge based on the natural frequency.
- The two modesets are rescaled and merged assuming the modal component on the reference DOF need to be the same.
- As modal components are always computed as displacements, there is no need to integrate acceleration before merging.

The merged modes are displayed in Fig. 5.12. The displacement output of VIC measurements are superposed on the left wing tip (in flight direction). In the left top image the bending of the wing tip, the payload support and the payload itself can be seen, as well as in the above Fig. 5.8.

The results show that the modes obtained with the two systems and then merged are compatible and the processing applied can be considered correct. These results allow then to give a clear reply to some of the initial questions:

- High-Speed Cameras measurements and DIC processing can be used in a GVT context and can be very useful and practical if limited to a specific area in this application, although e. g. gas and steam turbine blade up to wind turbines can be monitored in full scale (although full scale is possible, but technically more challenging).
- Measuring wider areas at equivalent pixel resolution comes with lower displacement measurement sensitivity and spatial resolutions, thus a compromise is needed.
- Combining standard measurement with local DIC can then be considered as an optimal solution.
- Using OMA to combine the modal results can be considered as a viable and more practical alternative than recombining time data, in particular when an accurate synchronization signal is not available.
- However, synchronizing the measurement systems remains the only solution if FRF calculation is required.
- In general, it is suggested, if possible, to use sine excitation as is the one that will compensate for the lower signal to noise ratio (related to the measurement of displacements) for spectral analysis using camera-based systems. In other cases (lighter structures), broadband random excitation might still suffice.

5.4 Preliminary Analysis of Non-linear Response

As mentioned and already reported in [6], non-linear response was identified at the connection between the wing and the payload. From the results summarized in Table 5.1, it can be already observed that in general the wing modes have a softening effect, with natural frequencies decreasing with increasing load, while damping increase (normally because of friction). This can be also observed in the Autopowers in Fig. 5.13. For a linear system, the FRFs scale the response to the input. However, if we try to scale the measured Autopowers either from acceleration measurement or the DIC to the force levels in Fig. 5.13, we can observed they don't really match and we can observe s general shift of the peaks to lower frequencies and a decrease of amplitude response at resonance because of damping. This is mostly evident in the 7.4 Hz resonance corresponding to the symmetric wing torsion.

Similarly, if we perform a time-frequency analysis using a Short-Time Fourier Transform on the DIC data, we see in the response not only the excitation frequency, but also its higher harmonics excited. However, the low signal-to-noise ratio of the camera based measurements in this scenario makes the detection of higher order harmonics more difficult than when

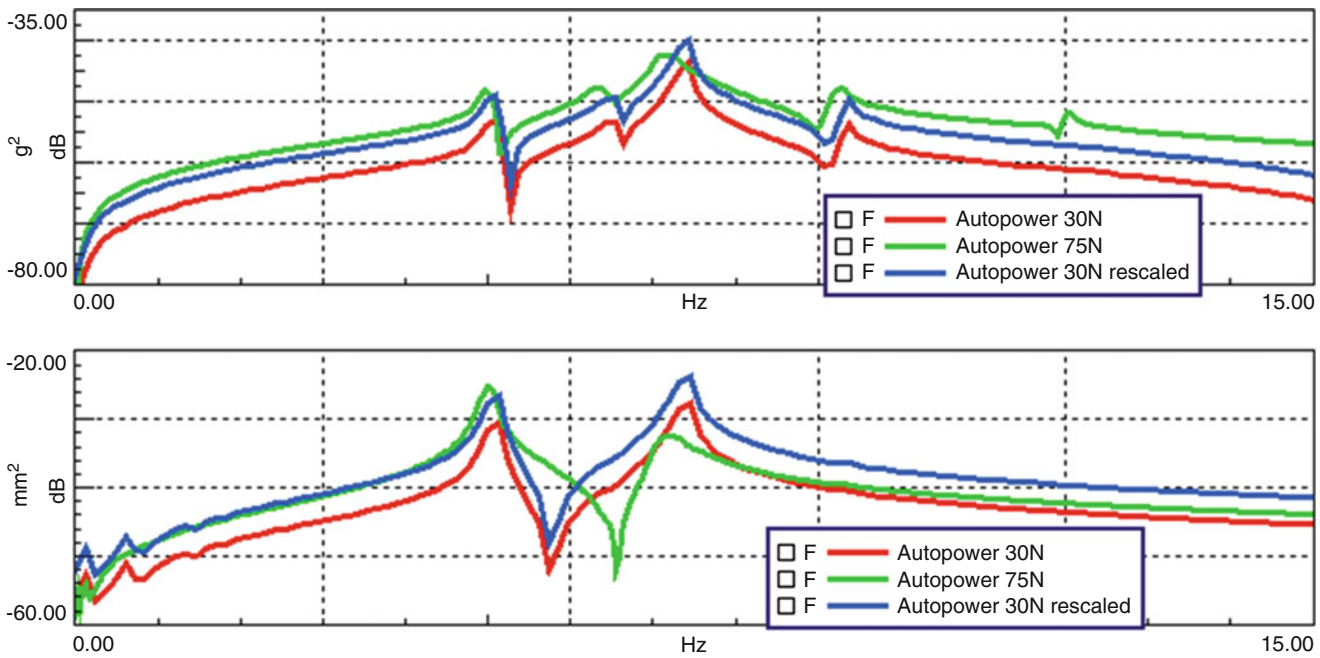

Fig. 5.13 Response linearity plots: autopower comparison

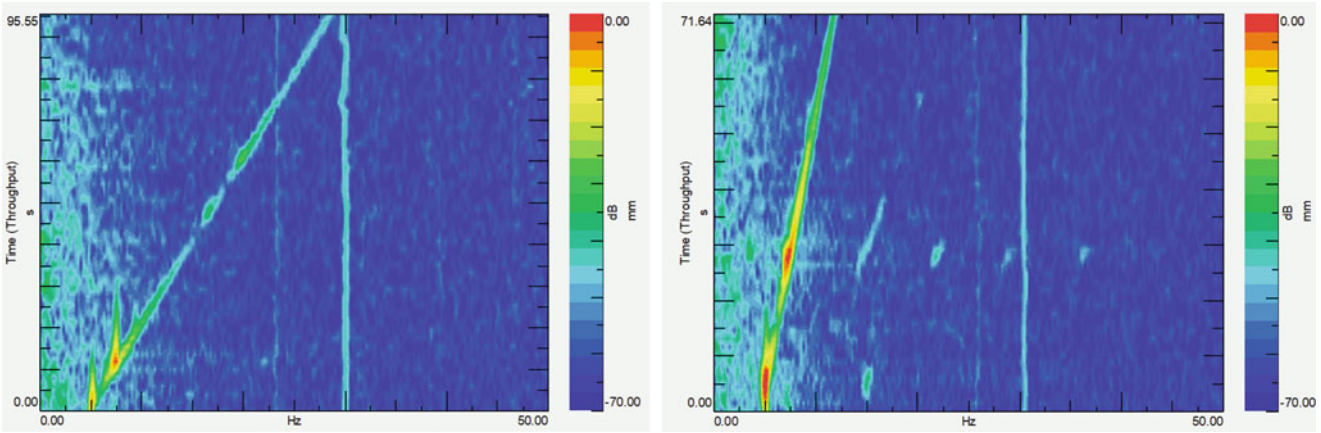

Fig. 5.14 Low (left) vs high (right) time-frequency analysis plot for DIC data

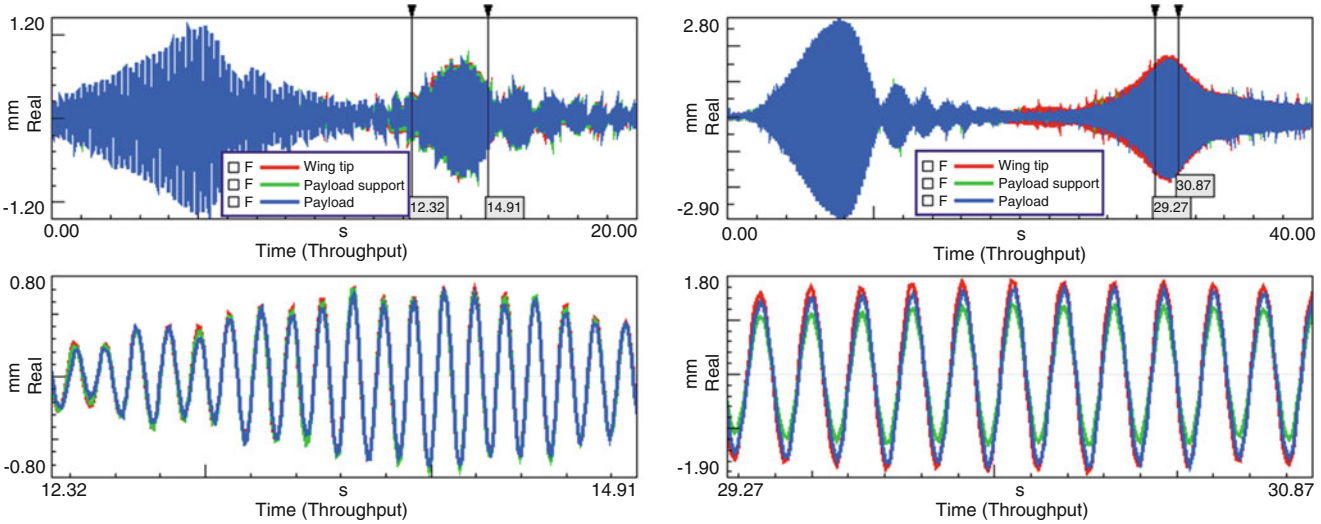

Fig. 5.15 Linearity analysis on time histories. Left: 30 N. Right: 75 N

using accelerometers (Fig. 5.14). The same limitations can also be observed in the time histories. Normally, for increasing load, higher harmonic distortion is observed using accelerometers. Here, however, the limited acquisition bandwidth and the low SNR make these distortions difficult to visualize (Fig. 5.15).

5.5 Conclusions

In this paper, an application combining standard acceleration measurement with high-speed camera and DIC analysis is presented. The test object is a full F16, fully instrumented for a GVT, with the DIC focusing on a limited area at the left wing tip, including the payload and its connection to the wing. The test was performed using industrial solution (LMS Test.Lab with LMS SCADAS and a DIC system of isi-sys based on FASTCAM AX100 cameras of Photron in combination with 3D software of Correlated Solutions.

The activity was considered successful, as it could be proven data:

- DIC can be used for dynamic analysis on a full scale structure, although the limited sensitivity relate to the measurement of displacements can become an issue at higher frequencies
- Even though the systems might be difficult to synchronize at the moment of the measurement, modal analysis, and in this case operational modal analysis, provides a simple mean of combining the modal results.

- The great advantage over other measurement techniques is that DIC provides a very high spatial resolution without the need of repeating the measurement multiple times.

On the other hand, some limitations were also identified. First of all, the internal memory of the camera limited the total amount of data that can be acquired. The OMA results on DIC are then biased by fact that only one sweep was considered and thus input are uncorrelated. It was decided to measure a relatively wide area of approx.. 2 m $\times$ 1 m, which obviously causes the sensitivity at higher frequency to decrease. This makes non-linear investigations a bit difficult, since higher harmonics are difficult to distinguish. This can be dangerous since DIC results improve when the force is higher and non-linear response can be activated.

It should be also taken into account that this is maybe not the optimal scenario for using DIC, but it anyhow proves the validity of the method and the possibility to combine it with more traditional techniques to further enrich the information we can derive from our data.

References

1. Baqersad, J., Poozesh, P., Niezrecki, C., Avitabile, P.: Photogrammetry and optical methods in structural dynamics – a review. Mech. Syst. Signal Process. **86**, 17–34 (2017)
2. Zanarini, A.: Broad frequency band full field measurements for advanced applications: point-wise comparisons between optical technologies. Mech. Syst. Signal Process. **98**, 968–999 (2018)
3. Ozbek, M., Rixen, R.J.: Operational modal analysis of a 2.5 MW wind turbine using optical measurement techniques and strain gauges. Wind Energy. **16**(3), 367–381 (2013)
4. Suttom, M.A., Orteu, J.-J., Schreier, H.W.: Image Correlation for Shape, Motion and Deformation Measurements. Springer, New York (2009.) ISBN: 978–387-78746-6
5. Lau, J., Peeters, B., Debille, J., Guzek, Q., Flynn, W., Lange, D.L., Kahlmann, T.: Ground Vibration Testing Master Class: modern testing and analysis concepts applied to an F16e. In: Advanced Aerospace Applications, Conference Proceedings of the Society for Experimental Mechanics Series, vol. 1. Springer, New York (2011)
6. Noël, J.-P., Renson, L., Kerschen, G., Peeters, B., Manzato, S., Debille, J.: Nonlinear dynamics analysis of an F-16 aircraft using GVT Data. In: Proceedings of the International Forum on Aeroelasticity and Structural Dynamics, Bristol (2013)

Chapter 6
A Multi-view DIC Approach to Extract Operating Mode Shapes of Structures

Vanshaj Srivastava, Kiran Patil, Javad Baqersad, and James Zhang

Abstract Accelerometers have been conventionally used to measure the response of structures for modal analysis. These pointwise sensors only provide information at a few discrete locations being measured. Additionally, the use of accelerometers to capture the response at discrete locations can mass-load the structure. Thus, the obtained results may not predict the true dynamics of the structure. Stereo-photogrammetry and Three-Dimensional Digital Image Correlation (3D DIC) have recently been adopted to collect operating data for vibration analysis. These non-contact optical techniques provide a wealth of distributed data over the entire structure. One of the limitations of a stereo-camera system is its line of sight, which limits the field of view; a single pair of DIC cameras may not be able to provide deformation data for the entire structure. Several pairs of cameras may be coupled simultaneously to perform DIC measurement on large complex structures. However, the use of multiple cameras involves huge costs and may not be a viable choice. In this paper, a multi-view 3D DIC approach is used to predict the dynamic characteristics of a cantilever beam as a sample structure. A pair of DIC cameras is roved over the entire structure to capture the deformation data of each field of view. Each measured data includes the geometry and displacement data which is later mapped into a universal coordinate system. The measured data is stitched in the frequency domain to extract the operating shapes of the entire structure.

Keywords Modal analysis · DIC · Stitching · Vibration analysis · Operating deflection shapes

6.1 Introduction

Recently, there has been an increase in applications of lightweight materials in the aerospace and automotive industries. That makes test engineers seek for non-contact measurement techniques that can be used for these applications. The conventional modal analysis approach needs an array of accelerometers, an impulse hammer, and a data acquisition system. This technique is based on exciting the structure with an impulse hammer or a mechanical shaker and measuring the response using axial or multi-axial accelerometers. However, accelerometers may mass-load the structure and can only provide measurements at discrete locations. Thus, it is very desirable to develop a non-contact technique that can measure the full-field response of structures.

Optical methods as non-contact measurement techniques have received attention in the field of structural dynamics. Laser Doppler vibrometry, digital speckle shearography, Electronic Speckle Pattern Interferometry (ESPI), holographic interferometry, photogrammetry, and Digital Image Correlation (DIC) are some common optical techniques that are used to measure vibrations. Digital image correlation has recently received special attention in the field of structural dynamics [1, 2] because it can be used to obtain the full-field data in a very short acquisition time. This approach has been used for measuring vibrations of wind turbine blades [3–5], helicopter rotors [6–9], automotive components [10], bridges [11, 12], and infrastructure [13, 14]. Researchers have also used motion magnification [15, 16] and blind source separation techniques [17] to extract the vibration characteristics of structures. However, a pair of DIC cameras may have a limited line of sights only on a certain part of a large complex structure. This makes it very difficult to use DIC technique for the vibration measurement of large structures. To resolve this issue, researchers have used multiple pairs of cameras coupled simultaneously to measure the deformation of large structures [18]. The use of multiple pairs of cameras involves excessive cost which may not be feasible. Patil, Baqersad et al. proposed a new technique to scale the mode shapes using measured force and stitch the mode shapes in the frequency domain [10]. However, it might not always be feasible to measure the excitation force.

V. Srivastava · K. Patil · J. Baqersad (✉) · J. Zhang
NVH & Experimental Mechanics Laboratory (NVHEM Lab), Kettering University, Flint, MI, USA
e-mail: jbaqersad@kettering.edu

C. Niezrecki, J. Baqersad (eds.), *Structural Health Monitoring, Photogrammetry & DIC, Volume 6*,
Conference Proceedings of the Society for Experimental Mechanics Series, https://doi.org/10.1007/978-3-319-74476-6_6

In this paper, an approach is proposed to stitch the operating mode shapes of a structure and obtain the full-field response for a complex structure. In this approach, there is no need to scale the mode shapes. The DIC cameras are roved over the structure to obtain the response of the structure in multi-views. Furthermore, the deformations in the time domain obtained using DIC technique is filtered and transformed into the frequency domain. This frequency domain data is then used to extract the natural frequencies and operating deflection shapes of each section of the structure. Later, the obtained operating mode shapes of each section are scaled and stitched together to obtain the operating mode shapes of the entire structure.

6.2 Methodology

A way of evaluating the vibration pattern is through operational mode shapes also defined as unscaled mode shapes. At times, it becomes difficult to measure the excitation force of the structure, and only the response of the structure is captured. The measured response of the structure can be used to obtain the operating mode shapes. Operating mode shapes of the structure are defined as the deflection patterns of the structure at its natural frequencies. They depend upon the operating force of the structure and are not inherent properties of the structure.

An innovative approach is being proposed in the current paper to extract the operating mode shapes of the structure using stereophotogrammetry. The structure is excited with an impact hammer, and the response is measured using a pair of DIC cameras. Figure 6.1 illustrates a flowchart of the proposed approach to extract the operating mode shapes of a 44-inch long aluminum beam using the digital image correlation technique. Due to the limited field of view for a pair of DIC cameras, the entire length of the cantilever beam cannot be captured in a single view. Therefore, the cantilever beam is divided into two sections with an overlap area of 8-inches. A Fast Fourier Transform (FFT) algorithm converts the obtained time domain

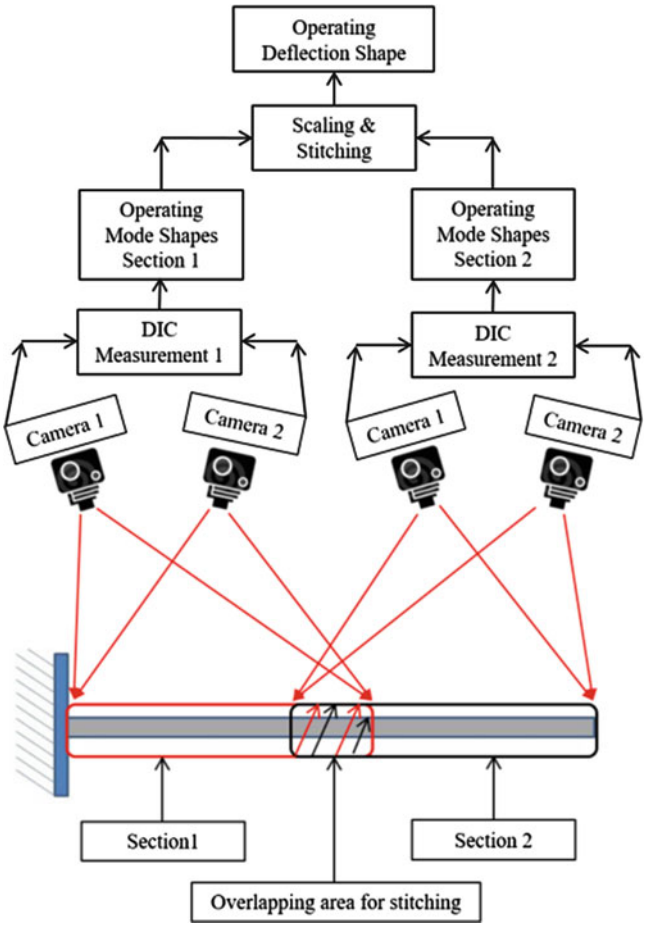

Fig. 6.1 A flowchart showing the proposed technique for extracting operating mode shapes of a beam using multiple views

data into the frequency domain for each section. The obtained operating mode shapes for each section are then scaled and stitched together to obtain the operating mode shapes of entire beam.

6.3 Experimental Setup

The first step to carry out a DIC measurement is to create a speckle pattern on the structure's area of interest. In this experiment, because the entire beam cannot be captured in one section, the entire length of the beam was divided into two sections of 26 inches each. To obtain better results, the speckle size should be at least 3–5 pixels in diameter and with a density of more than 50%. Hence, the size of the speckle pattern was chosen to be a minimum of 1 mm. The beam was set in a cantilever condition by fixing its one end on a workbench (see Fig. 6.2). The beam was excited using an impulse hammer, and the response was captured using a pair of DIC cameras. The beam was excited at a point approximately 1/3rd length from the fixed end. This ensured that the higher order modes of the beam were excited as well.

6.4 Results from DIC

The deformation data for each section was captured using a pair of Photron high-speed cameras. The captured images were further analyzed and processed to obtain the natural frequencies and operating mode shapes using VIC-3D by Correlated Solutions. Figure 6.3 shows the obtained operating mode shapes for both sections of the cantilever beam. Two full-field operating mode shapes, one at 21 Hz and second at 127 Hz were obtained using the DIC.

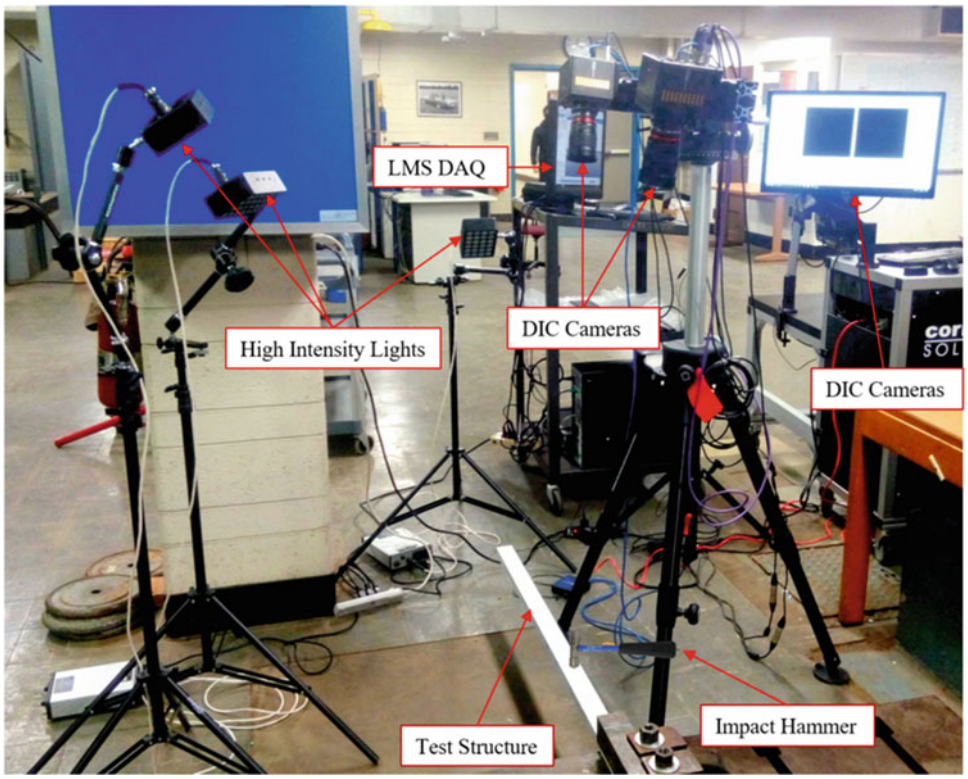

Fig. 6.2 A photograph showing the experimental setup including the test structure and cameras

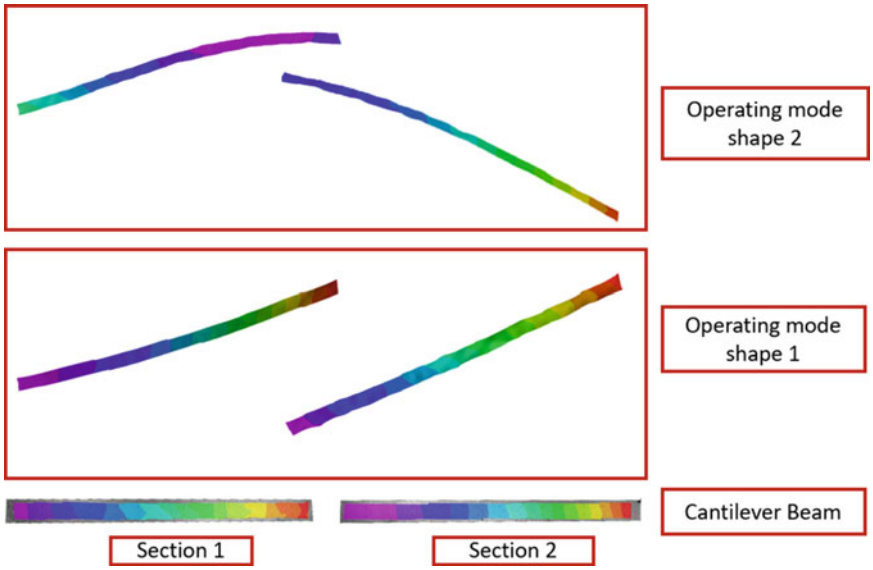

Fig. 6.3 Operating Mode Shapes of two sections of cantilever beam from DIC

6.5 Stitching

A dynamic stitching of the two sections is to be performed to extract the operating mode shapes of the entire beam. The orientation of the cameras and the relative distance between the cantilever beam and cameras changed when different sections of the beam were captured. Because the excitation forces for the two sections were different, the amplitudes of the vibration for the sections were different. A least square minimization technique was adopted to normalize the displacement of two sections in the overlapped area. Three reference points were selected in the overlap region in section one to redefine the coordinates of points in section one and to stitch the two sections. The same three points were selected in section two to redefine the coordinates of each point in section two. A 3D translation and rotation matrix was used to precisely overlap these reference points which stitched the two sections.

6.6 Results

The two operating mode shapes of the cantilever beam occur at resonant frequencies of 21 Hz and 127 Hz (see Fig. 6.4). Figure 6.5 shows the mode shapes obtained from DIC and LMS.test lab. As can be seen, the mode shapes obtained using DIC show a strong correlation to the mode shapes obtained using conventional modal analysis (LMS Test.lab).

6.7 Conclusion

3D digital image correlation technique not only eliminates the mass loading effect of the accelerometers but also provides the full-field response of the structure. A successful attempt was made to overcome the limitations of the 3D DIC technique for predicting the dynamics of structures. In the proposed technique, the operating shapes of a test structure are stitched together to obtain the mode shapes of the entire structure. The multi-view 3D digital image correlation technique was used for vibration measurement on a cantilever beam as a sample structure. The proposed technique further expands the use of 3D DIC technique for predicting the dynamics of large complex structures.

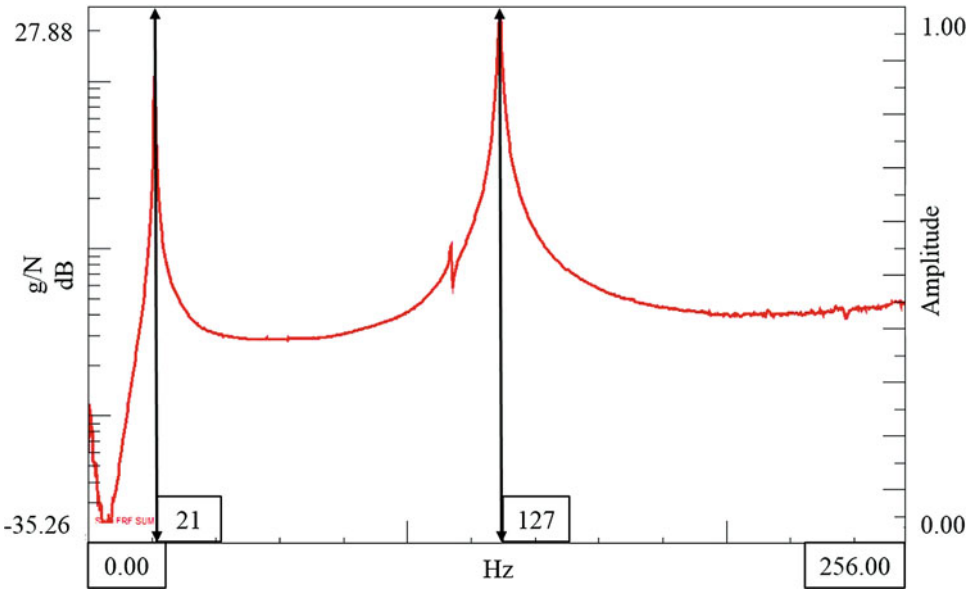

Fig. 6.4 The summation of Frequency Response Functions for all the measurement points on the cantilever beam obtained using LMS Test.Lab

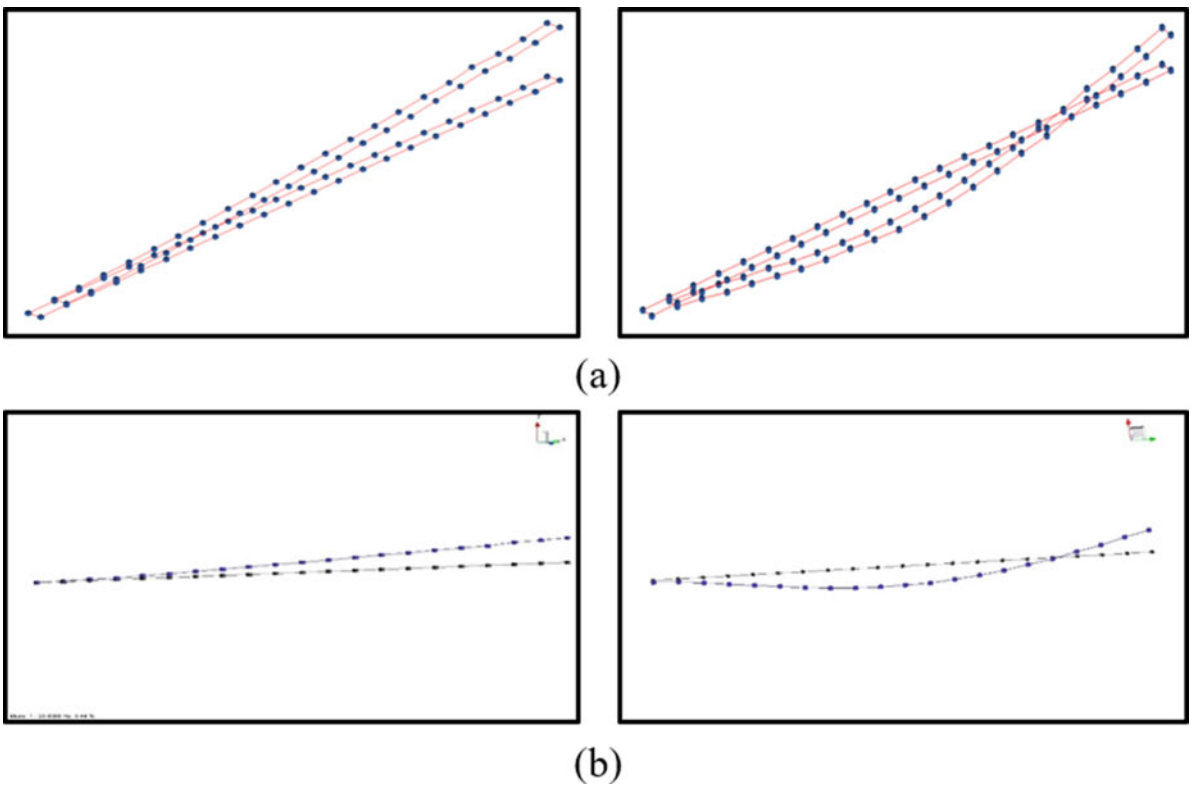

Fig. 6.5 Mode shapes of the cantilever beam obtained with (**a**) the stitching approach using DIC and (**b**) conventional modal analysis using LMS Test.lab

Acknowledgement This research presented in this paper is partly supported by the National Science Foundation under Grant Number 1625987 (Acquisition of a 3D Digital Image Correlation System to Enhance Research and Teaching at Kettering University). Any opinions, findings, and conclusions or recommendations expressed in this material are those of the author(s) and do not necessarily reflect the views of the sponsoring organizations.

References

1. Sarrafi, A., Poozesh, P., Mao, Z.: A comparison of computer-vision-based structural dynamics characterizations. In: Barthorpe, R., Platz, R., Lopez, I., Moaveni, B., Papadimitriou, C. (eds.) Model Validation and Uncertainty Quantification, Volume 3: Proceedings of the 35th IMAC, A Conference and Exposition on Structural Dynamics 2017, pp. 295–301. Springer International Publishing, Cham (2017). https://doi.org/10.1007/978-3-319-54858-6_29
2. Baqersad, J., Poozesh, P., Niezrecki, C., Avitabile, P.: Photogrammetry and optical methods in structural dynamics – a review. Mech. Syst. Signal Process. **86**(1), 17–34 (2017.) https://doi.org/10.1016/j.ymssp.2016.02.011
3. Poozesh, P., Baqersad, J., Niezrecki, C., Avitabile, P., Harvey, E., Yarala, R.: Large-area photogrammetry based testing of wind turbine blades. Mech. Syst. Signal Process. **86**(1), 98–115 (2017.) https://doi.org/10.1016/j.ymssp.2016.07.021
4. Carr, J., Baqersad, J., Niezrecki, C., Avitabile, P.: Full-field dynamic strain on wind turbine blade using digital image correlation techniques and limited sets of measured data from photogrammetric targets. Exp. Tech. (2015). https://doi.org/10.1111/ext.12129
5. LeBlanc, B., Niezrecki, C., Avitabile, P., Chen, J., Sherwood, J.: Damage detection and full surface characterization of a wind turbine blade using three-dimensional digital image correlation. Struct. Health Monit. **12**, 430–439 (2013)
6. Stasicki, B., Boden, F.: In-flight measurements of aircraft propeller deformation by means of an autarkic fast rotating imaging system. In: International Conference on Experimental Mechanics 2014, ICEM 2014, 15 Nov 2014–17 Nov 2014, SPIE, Singapore (2015). https://doi.org/10.1117/12.2081393
7. Stasicki, B., Boden, F.: Application of high-speed videography for in-flight deformation measurements of aircraft propellers. In: 28th International Congress on High-Speed Imaging and Photonics, 9 Nov 2008–14 Nov 2008, SPIE, Canberra (2009). https://doi.org/10.1117/12.822046
8. Sicard, J., Sirohi, J.: Modeling of the large torsional deformation of an extremely flexible rotor in hover. AIAA J. **52**, 1604–1615 (2014)
9. Sicard, J., Sirohi, J.: Measurement of the deformation of an extremely flexible rotor blade using digital image correlation. Meas. Sci. Technol. **24**, 065203 (2013)
10. Patil, K., Baqersad, J., Sheidaei, A.: A Multi-View Digital Image Correlation for Extracting Mode Shapes of a Tire, Shock & Vibration, Aircraft/Aerospace, Energy Harvesting, Acoustics & Optics, vol. 9, pp. 211–217. Springer, Cham (2017)
11. Cigada, A., Mazzoleni, P., Tarabini, M., Zappa, E.: Static and Dynamic Monitoring of Bridges by Means of Vision-Based Measuring System, Topics in Dynamics of Bridges, vol. 3, pp. 83–92. Springer, New York (2013)
12. Busca, G., Cigada, A., Mazzoleni, P., Zappa, E.: Vibration monitoring of multiple bridge points by means of a unique vision-based measuring system. Exp. Mech. **54**, 255–271 (2014). https://doi.org/10.1007/s11340-013-9784-8
13. Caprioli, A., Manzoni, S., Zappa, E.: People-Induced vibrations of civil structures: Image-Based measurement of crowd motion. Exp. Tech. **35**, 71–79 (2011). https://doi.org/10.1111/j.1747-1567.2009.00574.x
14. Poozesh, P., Sabino, D.D., Baqersad, J., Avitabile, P., Niezrecki, C.: Practical techniques for scaling of optically measured operating deflection shapes. In: De Clerck, J., Epp, D.S. (eds.) Rotating Machinery, Hybrid Test Methods, Vibro-Acoustics & Laser Vibrometry, Volume 8: Proceedings of the 34th IMAC, A Conference and Exposition on Structural Dynamics 2016, pp. 1–17. Springer International Publishing, Cham (2017). https://doi.org/10.1007/978-3-319-30084-9_1
15. Chen, J.G., Wadhwa, N., Cha, Y.-J., Durand, F., Freeman, W.T., Buyukozturk, O.: Modal identification of simple structures with high-speed video using motion magnification. J. Sound Vib. **345**, 58–71 (2015.) https://doi.org/10.1016/j.jsv.2015.01.024
16. Sarrafi, A., Poozesh, P., Niezrecki, C., Mao, Z.: Mode extraction on wind turbine blades via phase-based video motion estimation. In: SPIE Smart Structures and Materials+ Nondestructive Evaluation and Health Monitoring, pp. 101710E–1101712. International Society for Optics and Photonics. Portland, Oregon, United States (2017)
17. Poozesh, P., Sarrafi, A., Mao, Z., Niezrecki, C.: Modal parameter estimation from optically-measured data using a hybrid output-only system identification method. Measurement. **110**, 134–145 (2017)
18. Li, J., Xie, X., Yang, G., Zhang, B., Siebert, T., Yang, L.: Whole-field thickness strain measurement using multiple camera digital image correlation system. Opt. Lasers Eng. **90**, 19–25 (2017.) https://doi.org/10.1016/j.optlaseng.2016.09.012

Chapter 7
Development of a Semi-autonomous Drone for Structural Health Monitoring of Structures Using Digital Image Correlation (DIC)

Sean Catt, Benjamin Fick, Matthew Hoskins, Joseph Praski, and Javad Baqersad

Abstract Digital Image Correlation (DIC) has proven itself to be a highly versatile and accurate method to measure 2D and 3D displacement, deformation, and strain in a wide range of structures and objects. A major advantage is that it is a non-contact, full-field measurement technique; it measures phenomena across the entire target object without having to attach sensors directly to the object. Despite the ability to measure many static and dynamic phenomena, the cameras and data acquisition equipment are almost exclusively set up in a static configuration. The cameras are often mounted on tripods and remain positioned in the same location while taking measurements. Such an immobile measurement platform prevents DIC from being employed to measure objects in inaccessible locations, such as bridges and tall buildings. An unmanned aerial vehicle carrying digital image correlation cameras has high mobility and can easily access regions on structures that would otherwise be too expensive or dangerous to measure with conventional static camera setups. This paper presents the development and testing of a prototype mobile digital image correlation platform. The resulting platform carries all of the necessary equipment on-board the drone and can be controlled by a single user with a remote control. It is shown that the prototype drone platform is capable of taking accurate and repeatable measurements while airborne. This drone aims to be used for vibration measurement and structural health monitoring of structures such as wind turbines and bridges.

Keywords UAV · DIC · Drone · Bridges · Structural health monitoring

7.1 Introduction

The goal of this project is to develop a mobile digital image correlation (DIC) platform that is mounted to an unmanned aerial vehicle (UAV) in order to capture data wirelessly while airborne. Current DIC systems do not have the versatility to readily capture data in many field applications. These field applications include measuring inaccessible structures such as bridges, tall buildings, or other objects where conventional camera equipment cannot be easily mounted or monitored. In order for crews to capture images to examine the structural integrity of various types of infrastructure, they must spend excessive time and money to construct adequate rigging for each application. A DIC system mounted on a UAV would allow for data to be collected in nearly any application without any additional fixturing or setup. This would allow for structural engineers to inspect bridges, wind turbines, or other inaccessible structures to measure vibrations and to monitor damages. This allows for more active preventive maintenance to occur as needed. In order for this system to function with relative ease and reliability, the UAV must be capable of carrying a load including a mobile computer processing unit, DIC camera(s), and all associated fixturing with a minimum flight time of 20 min. The camera mount rigging must be capable of reducing vibration enough to allow stable image capturing, and the design must also be robust enough to have the capability to add or change equipment for future projects.

The use of unmanned drones has gained popularity in recent decades. While still mainly utilized in a military reconnaissance role, various designs have been produced for use by civilians as well. Civilian drones are classified by size: large, medium, small/mini, and micro/nano, as well as take-off and landing techniques; horizontal or vertical [1] . Unmanned Aerial Vehicles (UAV) have become an increasingly versatile platform for scientific research. They can carry a wide array of sensor payloads and conduct data acquisition in places inaccessible for conventional equipment. Benefits of

Sean Catt, Benjamin Fick, Matthew Hoskins, and Joseph Praski are contributed equally to this work.

S. Catt · B. Fick · M. Hoskins · J. Praski · J. Baqersad (✉)
NVH & Experimental Mechanics Laboratory (NVHEM Lab), Kettering University, University Avenue, Flint, MI, USA
e-mail: jbaqersad@kettering.edu

C. Niezrecki, J. Baqersad (eds.), *Structural Health Monitoring, Photogrammetry & DIC, Volume 6*,
Conference Proceedings of the Society for Experimental Mechanics Series, https://doi.org/10.1007/978-3-319-74476-6_7

drone remote sensing include low material and operational costs, flexible control of spatial and temporal resolution, high-intensity data collection, and absence of risk for crews. Drones have proven useful in areas such as forestry research, aerial mapping/surveying, emergency/disaster management and structural inspection [2].

Recently, digital image correlation has been used for vibration measurement and structural health monitoring [3–6]. Researchers have used this system for structural health monitoring of bridges [7–10], wind turbines [11–15], and helicopter rotors [16, 17]. There have been previous studies that uses drones for quantitative inspection purposes. A study conducted by the Research and Development Department of Baytech Korea Inc. mounted a camera to an AiBotix X6 drone to photograph cracks and potential cracks in structures [18]. A specialized morphological algorithm (MorphLink-C) was developed to detect and measure cracks in the images taken by the drone. A similar study was done by the University of Massachusetts Lowell; mounting a pair of DIC cameras to an InstantEye Gen 4 drone. This system would be used to monitor the structural integrity of bridges [19]. However, all of the previous efforts are focused on designing a drone for semi-static applications.

For the project, a working prototype of the mobile DIC platform was built, and proof-of-concept testing was performed to aid future use and development of the drone. To perform the proof-of-concept testing, the authors installed all portions of the camera and data acquisition system attached to the drone and fully functional during flight. Due to time/budgetary/regulatory constraints, the authors chose to perform the initial testing on more easily acquired and manipulated objects as opposed to existing infrastructure around the city. Once the images were captured, the authors hoped to perform proper data analysis to show the deformation measured on the object in the test. This aims to be eventually used to measure vibrations of structures such as wind turbines.

7.2 Drone Design

The drone used in this project was developed to be a stand-alone platform. All of the necessary equipment needed to capture images will be on board the drone during flights. All flight inputs of the drone are performed with a single remote control.

7.2.1 Drone Body and Battery

The drone was constructed using a TAROT X8 8-Axis Octocopter FPV Frame TL8X000 Multicopter platform which utilizes eight motors for full flight capabilities. Drones with eight motors are known as octocopters. Octocopters have several advantages over hexacopters (six motors) and quadcopters (four motors). They have much better flight characteristics; namely maneuverability and stability. Stability is especially important when utilizing a drone as a photography platform, so an octocopter is ideal in this application. The additional motors of an octocopter also provide greater lift for the drone, allowing it to carry heavier payloads. The main disadvantages of octocopters are their larger size and limited battery life.

The motors used to provide power for the propellers were included in the drone kit and mounted on collapsible arms which are joined on the main hub of the drone body. On each motor runs a single, 15″ inch propeller to provide adequate lift for the total weight of the drone and the additional payload of the camera equipment. The maximum lift capacity for this motor, propeller, and power combination is twenty (20) kg; however, the recommended maximum flight capacity including the weight of the drone is ten (10) kg. This discrepancy is held so that there is enough variability to control the direction of the drone without overloading any of the motors and to ensure a proper efficiency to sustain flight for an acceptable length of time. Since the direction of the drone is changed by increasing and decreasing the speeds of certain motors, if the drone is operating above half of its maximum lift capabilities, it will not be able to adequately alter these motor speeds while maintaining enough lift for flight.

To provide electrical power for all components, a Tattu Plus LiPo 22000mAh 22.2 V 25C 6S Smart Battery Pack was utilized. With this battery powering all electronics and flight control systems on the drone, the battery is capable of a total flight time of approximately twenty (20) min. This battery must be stored in a fireproof container when not in use and all precautions taken when charging/discharging the battery to prevent catastrophic failure of the battery.

The final configuration of the drone is shown in Fig. 7.1. In the final configuration of the drone, the total payload of the drone was exactly equal to the maximum recommended flight weight, 10.00 kg. The drone body and flight electronics accounted for 5.75 kg while the camera platform and controls accounted for 4.25 kg. The entire payload was comprised of a Surface Pro 3, the two (2) DIC cameras, the battery, the camera mount rigging, all wiring, the flight control electronics, the two (2) LED light strips, and the LIDAR sensor, as seen below.

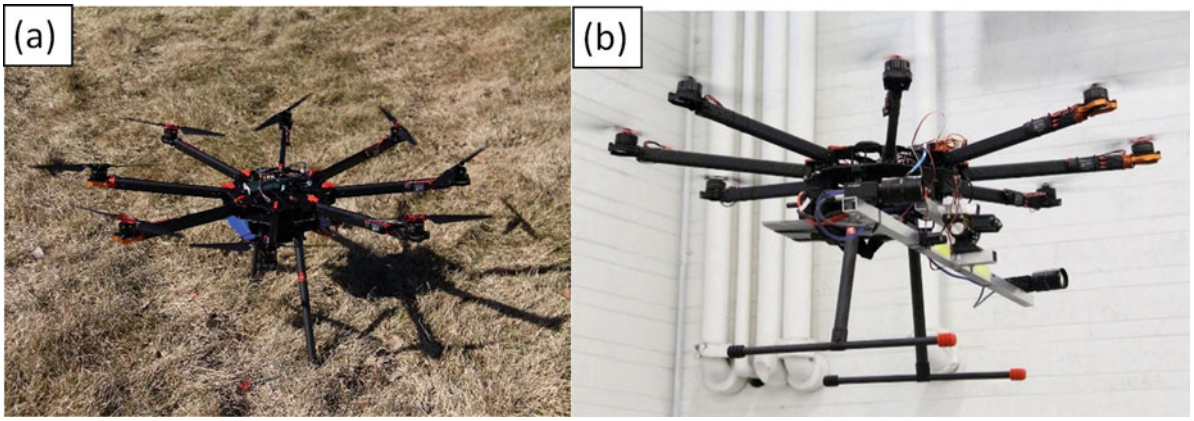

Fig. 7.1 (**a**) Assembled drone without camera equipment (**b**) Total payload of final drone configuration

Fig. 7.2 Point Grey GS3-U3-32S4M-C camera with Fujinon 1:1.4/12.5 mm CF12.5HA-1 lens

7.2.2 Flight Control and GPS

The flight control system that was utilized for the drone was an Arducopter APM 2.8 Flight Controller with Ublox NEO-M8 N GPS Module for a multirotor platform. The flight controller was mounted on top of the drone hub and connected wirelessly through a receiver module to the handheld controller. The handheld controller that was chosen for the project was a RadioLink AT9 9-Channel 9CH 2.4GHz Transmitter + R9D Receiver (with S.Bus) for RC Airplane Quadcopter Helicopter.

7.2.3 Camera Equipment and Camera Mounting Setup

In order to perform 3-dimensional DIC measurements, two cameras are required. The drone uses two Point Grey GS3-U3-32S4M-C cameras with Fujinon 1:1.4/12.5 mm CF12.5HA-1 lenses (see Fig. 7.2). These lenses allow for a wider depth of field to maintain image clarity and compensate for any movement of the drone while taking images. The depth of field for camera lenses is difficult to define as it depends upon the intended resolution, target distance, and definition of clarity.

The camera mounting beam consists of a single $1'' \times 1''$, $1/16''$ thick square aluminum tube. The beam has three holes per side to mount the cameras, creating a separation between the cameras of either 1.00 m, 1.04 m, or 1.08 m. A smaller aluminum beam is attached directly to of the drone via rubber grommet vibration dampers and carbon fiber tubes underneath the central hub. A tilt servo mates the camera mounting beam and the drone allowing the cameras to articulate up 45° and down 90°.

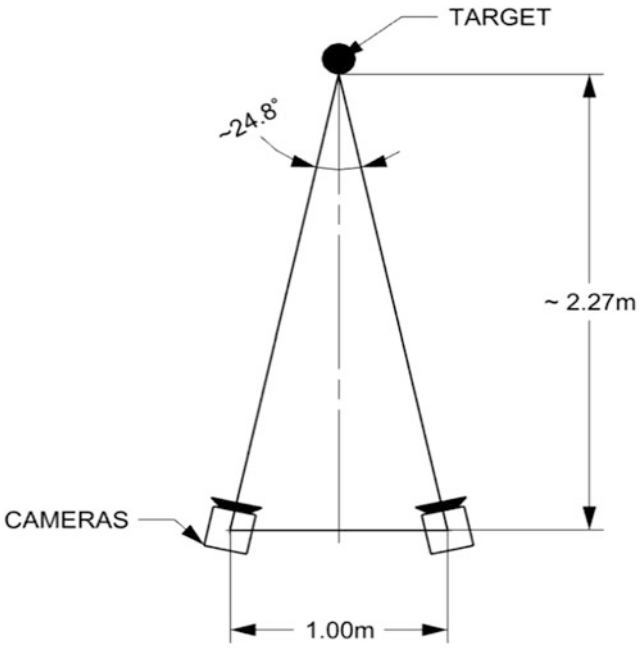

Fig. 7.3 Diagram of camera configuration and focal length

Using trigonometry, the distance between the cameras creates adjustable stereoscopic angles and focal lengths in order to control the operating distance that the drone must be from the target in order to capture acceptable images. Ideally, the cameras would be situated in such a way that they form a 30° angle with the target and would have a focal length that is large enough to eliminate the possibility that the drone could collide with the object it is measuring. The camera configuration for the test measurements is shown in Fig. 7.3. The cameras are 1.00 m (∼39.4″.) apart with a focal length of 2.27 m (∼90″). At this focal length, the cameras form a 24.8° at the target. However, with the mobile platform and variability in the flight envelope, the authors felt it was best to be able to have the adjustability to increase/decrease the focal length and camera angles in order to be able to move the drone away from the area being measured or increase the angle between the cameras.

7.2.4 Camera Triggering Method

Triggering the cameras remotely is essential to the functionality of the DIC drone platform. The cameras have two modes of triggering: manually clicking on a "fire software trigger" icon within the software or using a microcontroller to trigger them remotely in a similar manner. The software trigger works if an accessible ground-based setup exists. However, this is not the case in this application. The cameras have a hardware trigger that accepts a 3.3 volt logic input into one of the four digital I/O channels integrated into the Grasshopper3 cameras.

Using an oscilloscope, the authors were able to create a hardware trigger using a microcontroller that reads from one of the receiver's pulse width modulation (PWM) ports and translates the signal into a discrete I/O at the required 3.3 volt logic level to trigger the cameras. This was done by using a 3.3 volt Arduino Pro Micro. The captured images were then stored in the Point Grey software which was running on the onboard Microsoft Surface Pro 3 throughout the flight and data acquisition process.

The synchronization of the cameras was tested by capturing a set of images with a timer in the field of view. This was done to prove that a single trigger would capture an image from both cameras without excessive signal delays. Theoretically, since both cameras are wired to the same pin on a microcontroller, both receive the exact same signal. The cameras are rated for a signal delay less than one (1) microsecond, so the authors were assured that the cameras were capturing images simultaneously despite the test only having only two (2) decimal place accuracy.

7.3 Experimental Data Collection and Imaging

7.3.1 Data Acquisition System Calibration

Before beginning any data acquisition, it was imperative that calibration images be captured and their quality the software calibration using VIC 3D, the post-processing software. To do this, the complete drone assembly was taken to the testing area and placed the focal length's distance (2.27 m) away from a reference plane. A 0.5 m calibration plate as seen in Fig. 7.4 (provided by Correlated Solutions) was moved throughout the entire field-of-view at the correct focal distance, angling it slightly between images. Approximately 20 photos were taken with the plate in different positions in order to ensure proper target tracking within entire field-of-view. Before capturing test data, these calibration photos were uploaded to the VIC-3D software in order ensure proper calibration before analyzing the target photos.

7.3.2 Data Acquisition

Once sufficient calibration was confirmed, data acquisition on the target of interest could begin. The drone was placed at an arbitrary distance away from the target after all flight control and imaging systems were certified for functionality. From here, the pilot used the controller to accelerate the propellers and lift the drone off the ground. The drone was flown to an altitude where the target was in nearly direct view of the cameras. A video feedback camera mounted to the drone transmitted wirelessly to a monitor, but this does not give indicate how close the drone is to an object. The video feedback system only provides navigation from the point of view of the drone. However, through multiple practice flights, the proper altitude became more apparent and easily achievable. The focal distance was far more challenging to judge. Initially, the cameras were triggered by a switch on the remote controller. This required the pilot to both control the position and movement of the drone and trigger the cameras at the correct distance and location. This proved to be too difficult for one person, so the LIDAR sensor that was originally intended for the obstacle detection was mounted to the camera beam in order to determine the actual distance the cameras were from the target. This simplified the pilot's controls because once at the proper altitude, the drone was flown in and out of the designated focal length. As the drone moved toward and away from the target, photos were captured automatically while the drone was between 2.24 and 2.30 m away from the target using the LIDAR sensor to measure the distance. Ten (10) photos were taken per second while the drone was within this range. For the first few passes through the focal range, images were taken with the board held tightly in a reference position (flat against the cage). Once reference photos were taken, a piece of tape was added to the board to identify the change and a person tasked with deforming the target applied a load to the back side of the board to deform the board a certain distance. A diagram of one of the test flights can be seen in Fig. 7.5.

The test target for this experiment is a 1/8″ (3.175 mm) thick sheet of Masonite. A random, hand-drawn dot pattern was applied to an area of ∼32″ × ∼42″ of the board. The dots range in size from ∼3/8″ to ∼7/16″; at the experimental focal length of the cameras (∼2.27 m), a single dot is about 10 times larger than a single pixel in a camera's resolution.

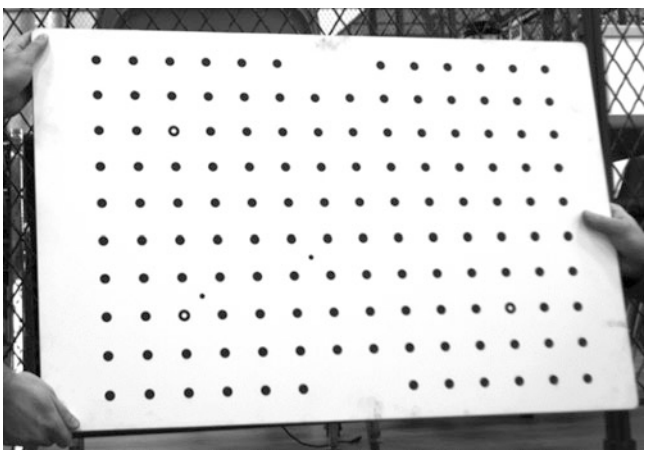

Fig. 7.4 Calibration photo from LH camera

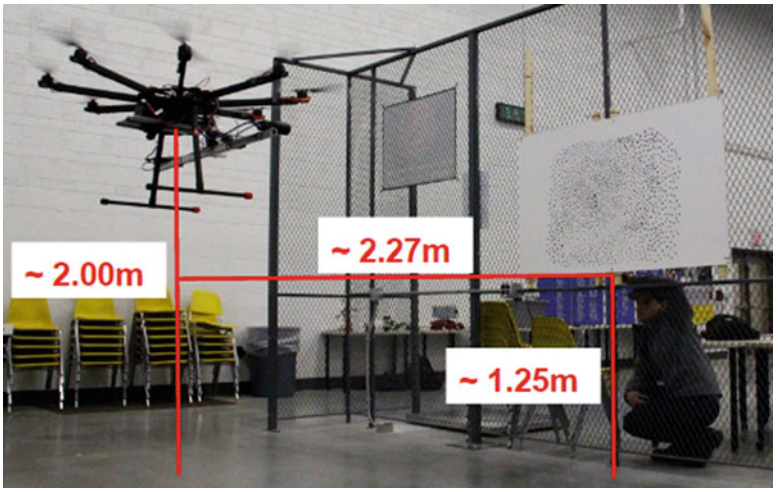

Fig. 7.5 Data acquisition test flight

The target was suspended from a metal fence, and the edges of the target were braced with scrap pieces of wood. Each corner of the target was secured using zip-ties to prevent flutter as a result of the displaced air from the drone's propellers. The Masonite sheet was deformed by simply pushing against the center of the sheet from the back side with a ruler. That said, the total deformation as measured by the ruler was 2.5 in. Ultimately, the ruler was chosen as the tool to provide the load to deform the board due to its inherent ability to provide repeatability. Once the initial deformation was known, this same distance of deformation could be used for all future tests to provide the most uniform measurements as possible.

7.3.3 Post-processing

Since Point Grey serves only as data acquisition software, the image sets must be exported to a separate post-processing software. In this case, VIC 3D was used.

Once the image sets are correctly named, they must be added to the post-processing software as "Speckle Images." A reference image set is then selected to compare all other image sets against. In this way, each image set can be measured as a displacement of the reference image set. In this reference image, an "Area of Interest" (AOI) must be defined. This area of the target must be present in all image sets in order to collect data. The software then tracks the speckle patterns based on an input subset size. Since the drone platform is not fixed relative to the target, the AOI shifts slightly in the field-of-view between image sets; this makes it difficult for the software to accurately track points between images. For this reason, manual tracking of points is used to reduce the software's error as shown. These points are the yellow flags in the AOI in Fig. 7.6.

Once all of the image sets are adequately tracked, the software can calculate the displacement of each image set with respect to the reference image.

7.4 Results

With the images loaded into the VIC 3D software, the analysis could begin following the steps listed in the previous section. Graphical images of the results can be found in Figs. 7.7 and 7.8. From that area of interest, the software tracked the points to calculate the total displacement of the target, as seen in Fig. 7.7. In this figure, it can be seen that the board is flat with no displacement in the direction out of the board across the area of interest. From the scale provided in the image, it can be seen that the color indicates a displacement ranging between −1.77487 and 2.24478 mm. Due to this range containing 0 mm of displacement, it can be stated that the authors' plan to hold the target board flat against the support structure worked well in providing a reference image with minimized displacement across the area of interest.

Here, it is important to note how the characteristics of the drone's flight impacted the analytical results. As previously noted, the movement of the target in the field-of-view makes it difficult for the software to track all of the points in the AOI.

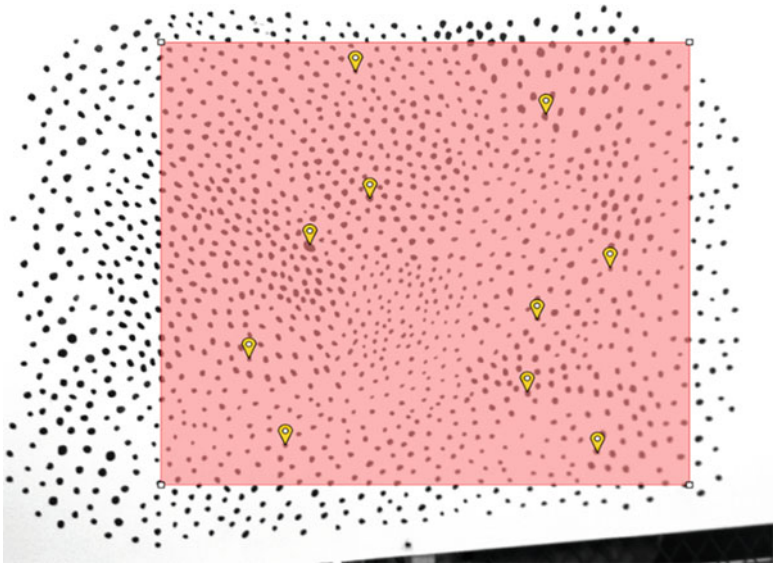

Fig. 7.6 Area of interest and manually tracked points

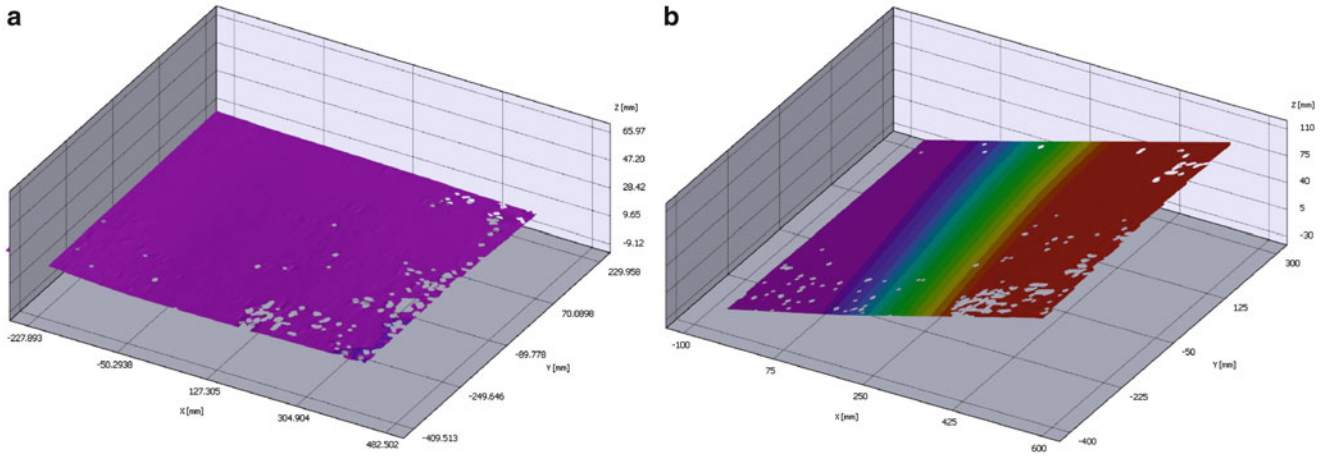

Fig. 7.7 (**a**) Post-processing reference 3D plot, (**b**) Post-processing deflected AOI (poor photo)

This can be seen in the gaps of the mapped area. This movement also causes issues due to platform rotation to the target. As seen in Fig. 7.7b, the target AOI appears to have a large amount of deformation that increases from left to right across the area. However, it can be seen that the target area is flat, similar to that in the reference image in Fig. 7.7a. This indication of false deformation can be attributed to the drone not being positioned in flight to where the cameras were equidistant to the target. This is likely a result of the drone being rotated about its vertical axis (yaw) and/or off the centerline in relation to the target. This problem can be resolved using rigid body correction [20, 21].

Finally, the best results from the analyses performed are shown in Fig. 7.8a, b. Here, the two-dimensional plot is overlaid on top of the image and the deflected three-dimensional plot is shown, illustrating the total deformation of the target. Again, certain portions of the AOI were difficult to track in the software, which are represented by the gaps in the plots. For the rest of the target that could be tracked in the software, though, the results are favorable. As seen in both images, the total deformation is easily seen, especially with the stratified colors that are included in each plot. Ultimately, it can be seen that the area of the maximum deflection of the board, shown in red, had a range of 57.0198–60.9395 mm (2.25″ – 2.39″) with the absolute maximum being the upper bound of the range. Obviously, a discrepancy exists between this deformation and the distance measured by the ruler that was used to deflect the board. This discrepancy could be attributed to the human error or an excessive to capture images. In the process of deflecting the board, it became difficult to hold the ruler in place throughout the duration of the flight and data acquisition process. Due to the operator repositioning the ruler, the total deflection may have been reduced as the images used in this analysis were captured. In future tests, this would be recognized and avoided

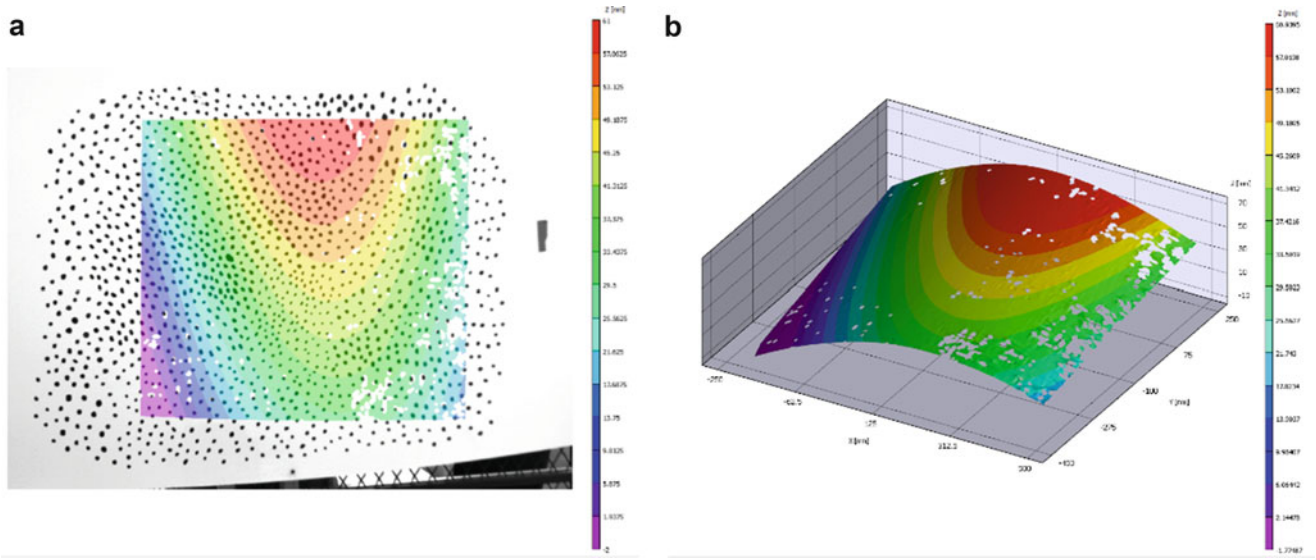

Fig. 7.8 (**a**) Post-processing deflected area of interest 2D plot, (**b**) Post-processing deflected 3D plot

to provide the best possible results. The entire platform may have also been too close to target due to the window used to capture images. Since the cameras were triggered when the platform was within three (3) cm of the target in either direction of the target, all measured deformations have a potential discrepancy of six (6) cm.

7.5 Conclusion

The paper summarizes a successful attempt to develop a drone to carry digital image correlation cameras. The paper shows that the system is able to measure deformations of structures. This method can be used for structural health monitoring of structures and for vibration measurements. As a future work, the authors plan to use this system for structural health monitoring of wind turbines. In order to capture consistent photos in maintenance schedules, the drone can be equipped with a computer vision system to place the drone at the horizontal axis of the turbine and in a specific distance far from the wind turbine. This project can expand the capabilities of the DIC system and provides the test engineers with a robust measurement technique for periodic inspection of wind turbines.

7.6 Acknowledgments

This research presented in this paper is partly supported by the National Science Foundation under Grant Number 1625987 (Acquisition of a 3D Digital Image Correlation System to Enhance Research and Teaching at Kettering University) and Kettering University Sponsored Research Office. Any opinions, findings, and conclusions or recommendations expressed in this material are those of the author(s) and do not necessarily reflect the views of the sponsoring organizations. This project can expand the capabilities of the DIC system and provides the test engineers with a robust measurement technique for periodic inspection of wind turbines.

References

1. Anderson, K., Gaston, K.J.: Lightweight unmanned aerial vehicles will revolutionize spatial ecology. Front. Ecol. Environ. **11**, 138–146 (2013)
2. Tang, L., Shao, G.: Drone remote sensing for forestry research and practices. J. For. Res. **26**, 791–797 (2015)
3. Baqersad, J., Poozesh, P., Niezrecki, C., Avitabile, P.: Photogrammetry and optical methods in structural dynamics – a review. Mech. Syst. Signal Process. **86**(1), 17–34 (2017.) https://doi.org/10.1016/j.ymssp.2016.02.011

4. Sarrafi, A., Poozesh, P., Mao, Z.: A comparison of computer-vision-based structural dynamics characterizations. In: Barthorpe, R., Platz, R., Lopez, I., Moaveni, B., Papadimitriou, C. (eds.) Model Validation and Uncertainty Quantification, Volume 3: Proceedings of the 35th IMAC, a Conference and Exposition on Structural Dynamics 2017, pp. 295–301. Springer International Publishing, Cham (2017). https://doi.org/10.1007/978-3-319-54858-6_29
5. Javh, J., Slavič, J., Boltežar, M.: Measuring full-field displacement spectral components using photographs taken with a DSLR camera via an analogue Fourier integral. Mech. Syst. Signal Process. **100**, 17–27 (2018)
6. Javh, J., Slavič, J., Boltežar, M.: High frequency modal identification on noisy high-speed camera data. Mech. Syst. Signal Process. **98**, 344–351 (2018)
7. Busca, G., Cigada, A., Mazzoleni, P., Tarabini, M., Zappa, E.: Static and dynamic monitoring of bridges by means of vision-based measuring system. In: Cunha, A. (ed.) Topics in Dynamics of Bridges, vol. 3, pp. 83–92. Springer, New York (2013). https://doi.org/10.1007/978-1-4614-6519-5_9
8. Lee, J.J., Shinozuka, M.: A vision-based system for remote sensing of bridge displacement. NDT & E International. **39**, 425–431 (2006.) https://doi.org/10.1016/j.ndteint.2005.12.003
9. Busca, G., Cigada, A., Mazzoleni, P., Zappa, E.: Vibration monitoring of multiple bridge points by means of a unique vision-based measuring system. Exp. Mech. **54**, 255–271 (2014). https://doi.org/10.1007/s11340-013-9784-8
10. Kim, S.-W., Kim, N.-S.: Dynamic characteristics of suspension bridge hanger cables using digital image processing. NDT & E International. **59**, 25–33 (2013.) https://doi.org/10.1016/j.ndteint.2013.05.002
11. Baqersad, J., Poozesh, P., Niezrecki, C., Avitabile, P.: A noncontacting approach for full-field strain monitoring of rotating structures. J. Vib. Acoust. **138**, 031008–031008 (2016). https://doi.org/10.1115/1.4032721
12. Baqersad, J., Niezrecki, C., Avitabile, P.: Full-field dynamic strain prediction on a wind turbine using displacements of optical targets measured by stereophotogrammetry. Mech. Syst. Signal Process. **62**, 284–295 (2015). https://doi.org/10.1016/j.ymssp.2015.03.021
13. Baqersad, J., Niezrecki, C., Avitabile, P.: Extracting full-field dynamic strain on a wind turbine rotor subjected to arbitrary excitations using 3D point tracking and a modal expansion technique. J. Sound Vib. **352**, 16–29 (2015). https://doi.org/10.1016/j.jsv.2015.04.026
14. Sarrafi, A., Poozesh, P., Niezrecki, C., Mao, Z.: Mode extraction on wind turbine blades via phase-based video motion estimation. In: SPIE Smart Structures and Materials+ Nondestructive Evaluation and Health Monitoring, pp. 101710E–1101712. International Society for Optics and Photonics. Portland, Oregon, United States (2017)
15. Poozesh, P., Sarrafi, A., Mao, Z., Avitabile, P., Niezrecki, C.: Feasibility of extracting operating shapes using phase-based motion magnification technique and stereo-photogrammetry. J. Sound Vib. **407**, 350–366 (2017)
16. Lundstrom, T., Baqersad, J., Niezrecki, C.: Monitoring the dynamics of a helicopter main rotor with high-speed Stereophotogrammetry. Exp. Tech. **40**(3), 907–919 (2015). https://doi.org/10.1111/ext.12127
17. Rizo-Patron, S., Sirohi, J.: Operational modal analysis of a helicopter rotor blade using digital image correlation. Exp. Mech. **57**, 367–375 (2017). https://doi.org/10.1007/s11340-016-0230-6
18. Kim, J.-W., Kim, S.-B., Park, J.-C., Nam, J.-W.: The 2015 World Congress on Advances in Structural Engineering and Mechanics (ASEM15), Incheon, Korea, August 25–29 (2015)
19. Reagan, D., Sabato, A., Niezrecki, C., Yu, T., Wilson, R.: An autonomous unmanned aerial vehicle sensing system for structural health monitoring of bridges. Proc. SPIE. **9804**, 980414–980411 (2016)
20. Lundstrom, T., Niezrecki, C., Avitabile, P.: Appropriate rigid body correction of Stereophotogrammetry measurements made on rotating systems. Exp. Tech. **39**(6), 25–34 (2013). https://doi.org/10.1111/ext.12030
21. Lundstrom, T., Baqersad, J., Niezrecki, C., Avitabile, P.: Using high-speed stereophotogrammetry techniques to extract shape information from wind turbine/rotor operating data. In: 30th IMAC, A Conference on Structural Dynamics, 30 Jan 2012–2 Feb 2012, Springer New York, Jacksonville, pp. 269–275 (2012). https://doi.org/10.1007/978-1-4614-2419-2_26

Chapter 8
Experimental Examples for Identification of Structural Systems Using Neural Network and DOF-Based Reduction Method

Heejun Sung and Maenghyo Cho

Abstract Various identification methods have been introduced in many manners using numerical techniques to validate a complicated structures described in FEM by comparing experimentally measured modal data. The objection of this study is to propose a methodology to identify a perturbed structure by comparing measured modal data to the original FEM data. Identified structures will improve the accuracy to the numerical model by minimizing the differences between those two models. Base-line model will be constructed by using FEM and will be compared to perturbed model by solving inverse problem. Measured modal responses, which are eigenvalues and eigenvectors, will be applied to satisfy the equilibrium and to minimize the differences of modal responses between the original model and the perturbed model. In this study, a neural networks-based detection method using modal properties is presented as a method for the identification which can effectively consider the modeling errors. Also experimental examples will be followed. Due to lack of number of the sensors, DOF-based reduction method is used to restore full model. As neural network is used for identification method, detailed schemes will be reported. In the present study, neural networks-based identification method will be proposed and will be verified by experimental examples. Experimental examples will demonstrate that the proposed method have efficiencies in accuracy of identifying structural model.

Keywords Structural system identification · Reduction method · Neural network

8.1 Introduction

As the likelihood of numerical computation continues to increase, the demand for computational technology has increased significantly. The concept of calculation technology starts with a method of minimizing calculation time. The computing power of a computer grows day by day, so you can calculate a model with a complex design. As a result, the requirements of the model have become more complex and difficult, and at the same time have been difficult for engineers. The finite element method (FEM) was one of the most progressive processes in computing technology. However, on the other hand, the FEM was dissipated due to differences between the actual models. Minimizing the difference between an actual model and an analytical model is an important target for engineers. Structural system identification is a method of describing physical models in computer analysis. It can be used for any type of process that needs to compare damage detection or model update methods or analytical models with real models.

In this study, we use structural model identification to update the numerical model with data from the actual model. We used vibration test data to compare the differences. Previous studies on structural system identification were compared only with eigenvalues, so only simple models such as trusses or beam models [1–3] were applied to the identification process. The truss or beam model has a reasonable number of parameters to solve the identification problem [4]. However, in this study, we applied the continuum model to extend the coordinate system. It is important to consider parameter improvements to apply the continuum model. Also, due to the improvement of the parameters, the eigenvalues from each mode shape appeared to be insufficient. The eigenvectors from each mode shape are measured from each sensor point and compared to the corresponding eigenvectors from the numerical model. The concept of the degree of freedom reduction method has been used to restore full eigenvector data from measured data [5–10]. Several methodologies for identifying structural systems have been introduced and utilized [10–13]. Reverse Perturbation (IPM) is used to compare numerical and real models [14–16]. Sensor location selection [16, 17] is one of the most important processes in this study, and the proposed method is provided by comparing

H. Sung (✉) · M. Cho
Department of Mechanical Engineering, Seoul National University, Seoul, Republic of Korea
e-mail: heejunsung@snu.ac.kr

C. Niezrecki, J. Baqersad (eds.), *Structural Health Monitoring, Photogrammetry & DIC, Volume 6*,
Conference Proceedings of the Society for Experimental Mechanics Series, https://doi.org/10.1007/978-3-319-74476-6_8

node energies considering mode shapes. This process allows you to identify structural differences in the actual model and update the analytical model. Verification of the experimental example compared with the numerical model follows.

8.2 Analysis

Because structural system identification is the process of matching a numerical model to an actual model, the meaning of this process will be reduced without experimental data. However, after collecting experiment data, comparing experiment data with numerical data is another important process for identification. Eigenvalues and eigenvectors are used as indicators of this study and geometry (thickness) was chosen as a parameter.

The Inverse Perturbation Method (IPM) was used as a methodology for comparing two models. IPM repeats the numerical model and the experiment data. At every step, the thickness of the numeric model is changed and different eigenvalues and eigenvectors are given. It then calculates the residual error, which is the difference between the two models, compared to the experimental data. While this iteration repeats, this method finds the minimum residual error and provides a response with a thickness value. If the residual error value of these two models is 0, these two models have the same vibration characteristics, which means they are the same model.

To improve the convergence of the problem, some eigenvectors were used for sensor location comparisons. The eigenvectors from the comparative sensor position will be compared to the eigenvectors from the same position restored from the eigenvectors of the other sensor positions. As this comparison increases, residual errors increase and more calculations are repeated. This comparison improves convergence and helps you find more accurate geometric answers to identification problems.

A simple aluminum plate has been proposed as an identification example. One was designed with a CAE program using FEM and the other was modeled with real aluminum, which was designed the same as the CAE model and has some parameters with different parameters. Figure 8.1a shows the experimental and numerical models used to identify structural systems. The verification process was confirmed by the results shown in Fig. 8.1b. The parameters are grouped into 21 different groups of equal thickness. As shown in Fig. 8.1b, a difference in shape was found. The amount of position and thickness is accurately identified (Fig. 8.2). The plate model was divided into 21 sections and each thickness ratio was applied for convergence criteria as parameters. Each section has been selected as a candidate for identification and converged to its perturbed thickness ratio.

A neural network technique was used to reduce computation time while maintaining accuracy in system identification [18]. It is assumed that the deformed structure has a rectangular shape, and the parameters of the deformed region are represented by coordinates of the position and the width, the height and the thickness of the deformed structure, and a total of five are used. The mode with the highest energy was used, and the eigenvector value for each position was also used as the input data of the artificial network technique at regular intervals.

Fig. 8.1 Experimental and numerical model of structural system identification

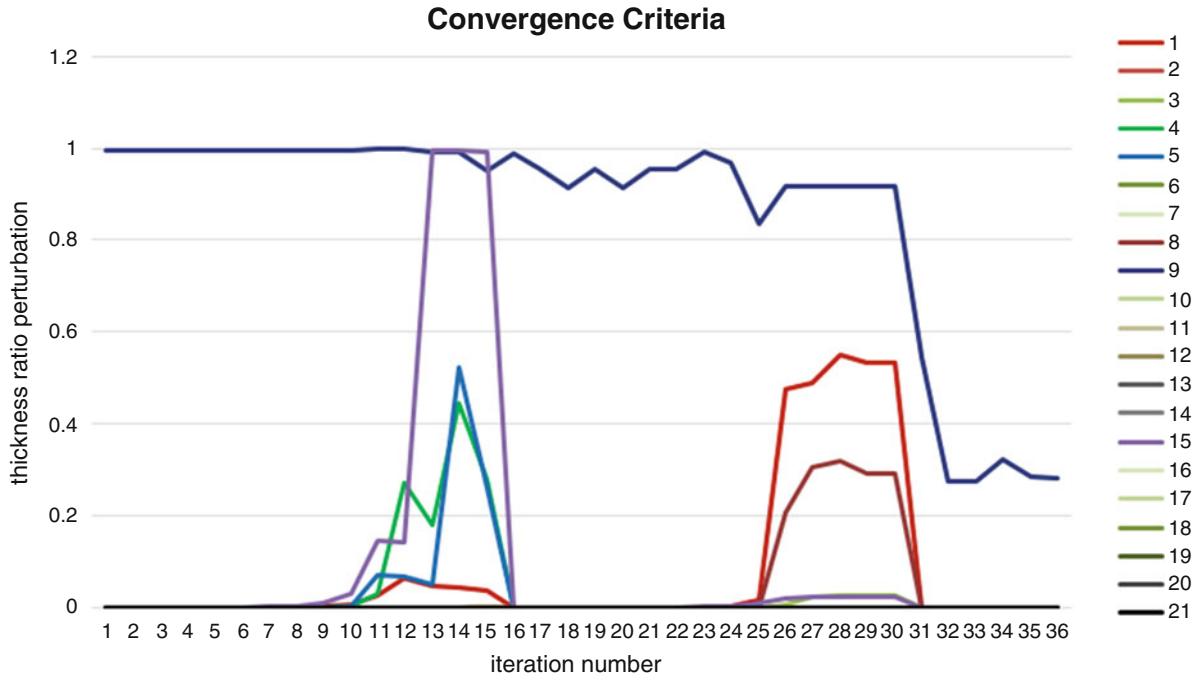

Fig. 8.2 Convergence criteria of identification in plate model

8.3 Summary

In this paper, we propose an identification method of a structural system based on finite element method (FEM). The difficulty of identifying the continuum models was that they had too many parameters to process. A large number of parameters have been processed using the degree-of-freedom reduction method. Decreasing degrees of freedom is a way to accurately represent a full model using only a certain degree of freedom. This study has been verified and the neural network technique has been introduced to reduce calculation time while maintaining the accuracy of the identification result. By building the neural network function through this method, changes in the structure can be identified much faster.

Acknowledgement This work was supported by a grant from the National Research Foundation of Korea (NRF) funded by the Korea government (MSIP) (No. 2012R1A3A2048841).

References

1. Liu, P.: Identification and damage detection of trusses using modal data. J. Struct. Eng. **121**, 599–608 (1995)
2. Hajela, P., Soeiro, F.J.: Structural damage detection based on static and modal analysis. AIAA J. **28**(6), 1110–1115 (1989)
3. Alvin, K.F., Park, K.C.: Second-order structural identification procedure via state-space-based system identification. AIAA J. **2010**, 398621 (2010)
4. Chen, H., Kurt, M., Lee, Y.S., McFarland, D.M., Bergman, L.A., Vakakis, A.F.: Experimental system identification of the dynamics of a vibro-impact beam with a view towards structural health monitoring and damage detection. Mech. Syst. Signal Process. **46**, 91–113 (2014)
5. Guyan, R.: Reduction of stiffness and mass matrices. AIAA J. **3**(2), 380 (1965)
6. Friswell, M., Garvey, S., Penny, J.: Model reduction using dynamic and iterated IRS techniques. J. Sound Vib. **186**(2), 311–323 (1995)
7. Kim, H., Cho, M.: Two-level scheme for selection of primary degree of freedom and semi-analytic sensitivity based on the reduced system. Comput. Methods Appl. Mech. Eng. **195**, 4244–4268 (2006)
8. Kim, K., Choi, Y.: Energy method for selection of degree of freedom in condensation. AIAA J. **38**(7), 1253–1259 (2000)
9. O'Callahan, J., Avitabile, P., Riemer, R.: System equivalent reduction expansion process. In: Seventh International Modal Analysis Conference, Las Vegas (1989)
10. Chang, S., Baek, S., Kim, K., Cho, M.: Structural system identification using degree of freedom-based reduction and hierarchical clustering algorithm. J. Sound Vib. **346**, 139–152 (2015)
11. Robertson, A.N., Park, K.C., Alvin, K.F.: Extraction of impulse response data via wavelet transform for structural system identification. J. Vib. Acoust. **120**(1), 252–260 (1998)

12. Weng, S., Xia, Y., Zhou, X.Q., Xu, Y.L., Zhu, H.P.: Inverse substructure method for model updating structures. J. Sound Vib. **331**, 5449–5468 (2012)
13. Alvin, K.F., Park, K.C.: Extraction of substructural flexibility from global frequencies and mode shapes. AIAA J. **37**, 1444–1451 (1999)
14. Kim, K.O., Anderson, W.J., Sandstorm, R.E.: Nonlinear inverse perturbation method in dynamic analysis. AIAA J. **21**, 1310–1316 (1982)
15. Hoff, C.J., Bernitsas, M.M., Sandatorm, R.E., Anderson, W.J.: Inverse perturbation method for structural redesign with frequency and mode shape constraints. AIAA J. **22**, 1304–1309 (1983)
16. Park, Y.C., Choi, Y.J., Cho, J.Y., Kim, K.O.: Inverse perturbation method and sensor location for structural damage detection. Int. Counc. Aeronaut. Sci. **4**, 31–38 (2003)
17. Kammer, D.C., Tinker, M.L.: Optimal placement of triaxial accelerometers for modal vibration tests. Mech. Syst. Signal Process. **18**, 29–41 (2004)
18. Chen, S., Billings, S.A., Grant, P.M.: Non-linear system identification using neural networks. Int. J. Control. **51**, 1191–1214 (2007)

Chapter 9
Active Control of Flexible Cylinders Undergoing Vortex-Induced Vibrations Using Piezo Stripe Actuators

Ersegun Deniz Gedikli, David Chelidze, and Jason Dahl

Abstract In this study, piezo stripe actuators were used to control the vibrations of a flexible cylinder undergoing underwater flow-induced vibrations. The piezo actuators were attached at the anti-nodes of a rectangular plastic beam and urethane rubber was used to mold the test model to have a circular cylinder shape. Forced base oscillation experiments were first carried out in air to characterize the system and piezo responses. Experiments were then performed in a recirculating water channel with the flexible cylinder in a uniform free stream, where the cylinder undergoes self-excitation due to vortex shedding in the wake and forced excitation due to the piezo actuators. The actuators were oriented to apply an excitation only in the in-line direction of the flow. In the tests, two separate cases were investigated. In the first case, the piezo actuators were activated at a flow speed corresponding to a flow-induced response with a spatial mode change, causing the cylinder to be excited with a higher mode, leading to a significantly smaller amplitude response than without the piezo actuation (vibration suppression). In the second case, piezo actuators were activated at a flow speed corresponding to a significant flow-induced amplitude increase. The interaction of the piezo forcing and the forced response of the cylinder results in a jump to the higher amplitude response regime (vibration enhancement). This study presents two important observations: (1) it is possible that piezo actuators can trip the response frequency to force the cylinder to oscillate with a different mode thus reducing the total response amplitude significantly, (2) it is also possible to prematurely increase the response amplitude for a particular flow speed (i.e. jumping from a lower branch to upper branch response).

Keywords Vortex-induced vibration (VIV) · Active control · Piezo actuator · Flexible · Low-mode

9.1 Introduction

Vortex-induced vibration (VIV) is an inherent problem seen in many engineered structures such as heat exchangers, offshore risers, and underwater cables. Predicting and suppressing these motions is important particularly for offshore structures, where these vibrations can significantly contribute to long-term fatigue damage of the structure.

Active and passive control methods have been previously studied to control VIV. In the active control technique, an external energy input is provided to the structure to give a disturbance to the fluid-structure interaction through the use of open-loop [4] and closed-loop [1, 7] control techniques. Active flow control techniques may also be used to control vibrations by altering the momentum of the fluid around the structure [6]. In passive control methods, no energy input is required, but VIV suppression may be achieved by altering the geometry of the structure with the use of helical strakes, shrouds, or fairings. An extensive review on such structures can be found in [3]. In recent energy harvesting devices, electrical impedance may also be used to passively damp oscillations [2].

In this study, an experimental active control technique has been developed to control VIV motions using piezo stripe actuators that are embedded in the structure. The goal of this study is to demonstrate that excitation of higher mode shapes of the structure may decouple the natural combined in-line (IL) and cross-flow (CF) response of the structure, disrupting the typical VIV response, to result in either significantly smaller amplitude response (VIV suppression) and a premature transition to a higher amplitude dynamic response branch (VIV enhancement).

E. Deniz Gedikli (✉) · J. Dahl
Ocean Engineering Department, University of Rhode Island, Narragansett, RI, USA
e-mail: egedikli@uri.edu

D. Chelidze
Mechanical, Systems and Industrial Engineering Department, University of Rhode Island, Kingston, RI, USA

C. Niezrecki, J. Baqersad (eds.), *Structural Health Monitoring, Photogrammetry & DIC, Volume 6*,
Conference Proceedings of the Society for Experimental Mechanics Series, https://doi.org/10.1007/978-3-319-74476-6_9

9.2 Experimental Approach

Two piezo stripe actuators were attached to a plastic beam at the second mode antinodes of the beam, with the beam embedded in a urethane cylinder to construct the test model. The actuators were oriented to apply a bending excitation in-line with the direction of flow, while the primary excitation due to VIV occurs perpendicular to the direction of flow. Due to the parametric excitation from vortex shedding, the IL direction was expected to be excited with twice the forcing frequency as the CF direction, as is typical in VIV. The plastic beam was chosen to have specific frequency and structural mode characteristics such that it would be excited to oscillate with up to the third mode in the IL direction, while keeping the CF mode shape constant with a first mode shape within the flow speeds tested (see [5]). Characterization experiments were first conducted in air to quantify the dynamic characteristics of the beam with actuators, and then the actuators were tested on the beam in water.

In the air experiments, a varying sinusoidal external base excitation was provided by a shaker apparatus where the test cylinder was attached to the moving shaker. The shaker was controlled using a function generator for a specific range of amplitudes and frequencies. A laser displacement sensor (LDS) was used to measure the displacement of the beam at the center and at $L/4$ from the top where L is the cylinder length. Experiments were conducted with (1) shaker only excitation, (2) piezo only excitation, and (3) combined shaker and piezo excitation. Excitation with the piezos was conducted as open loop, with no feedback to control the frequency excitation of the piezo. Flow channel experiments were conducted in a recirculating water channel, where the cylinder was attached across the flow channel and the flow speed in the channel was varied to determine the response of the cylinder. The piezo actuators were excited with a predetermined frequency to excite the second mode of the cylinder in the IL direction at specific flow speeds. Again, the piezo excitation was performed as open loop with no feedback from the motion of the cylinder. In the experiments, two Phantom V10 high speed cameras were used for motion tracking to measure the IL and CF position of the test cylinder. Tests were conducted for the Reynolds numbers between 900–5200.

9.3 Results and Conclusion

The test cylinder was measured to have a natural frequency of 6 Hz in the CF direction from the pluck tests in air. The left image in Fig. 9.1 shows that when excited purely by the piezo actuators, the cylinder oscillates with the maximum amplitude response when the piezos were actuated with 40 Hz, corresponding to the second mode of the system in the IL direction. The right image in Fig. 9.1 shows the cylinder's amplitude response at two different locations (one at center and the other one at $L/4$ from the top) with the combined shaker and piezo actuation. At first, the system is excited only with the shaker. Once the piezo actuators are turned on with a frequency of 40 Hz, the amplitude response drops significantly. At time t = 30, the piezos are then turned off with the oscillation continuing at the low amplitude state, demonstrating an effective transition to a different dynamic response branch. In air experiments, this shows that piezo controlled vibration suppression is possible if the system's response is carefully identified.

For the water channel experiments, the RMS amplitude response map was first obtained to show the natural IL and CF response of the system for increasing and decreasing flow speeds. Based on the obtained response map, the piezo control was applied at specific flow speeds to try to change the system response. The left image in Fig. 9.2 shows the RMS amplitude response for varying normalized reduced velocities (Vr_n) in CF and IL. Primarily, both the IL and CF responses took on a

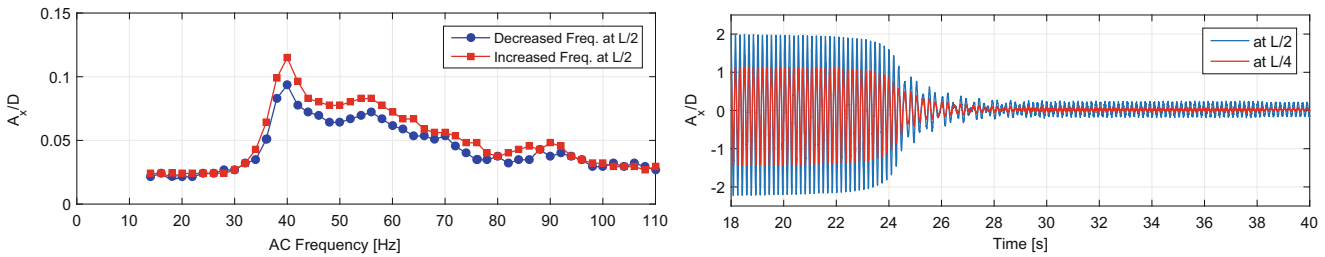

Fig. 9.1 Left: Center point response in air with variation of the piezo excitation frequency. Right: Combined shaker and piezo actuation response in air. Initially, only shaker is providing excitation. Near time t = 20 s, the piezo is turned on with excitation frequency 40 Hz. Near time t = 30 s, piezo is turned off with shaker excitation continuing

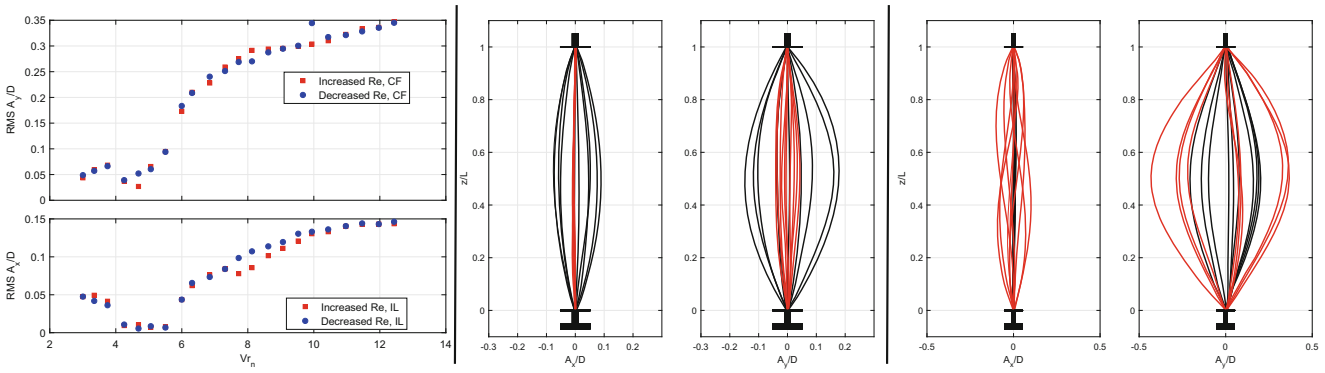

Fig. 9.2 Left: RMS of amplitude response for cross-flow and in-line directions. Center: Spatial response of the cylinder before the piezo actuation (black) and after the piezo actuation (red) at $Vr_n = 3.75$. Right: Cylinder's spatial response before the piezo actuation (black) and after the piezo actuation (red) at $Vr_n = 5.5$

half sinusoid-like shape although this was dependent on flow speed with varying amplitudes of motion. Up to $Vr_n = 4.25$, the cylinder oscillated similar to a first mode (half sinusoidal shape) in both IL and CF, while between the Vr_n values of 4 and 5.9, cylinder oscillated similar to a second mode (full sinusoidal shape) in IL with very small amplitude, and first mode in CF. Between the Vr_n values of 6 and 6.5, a multi-mode (combination of first, second and third mode) response with some traveling wave was observed in IL and a first mode shape was observed in CF. Lastly, a dominant first mode only response was observed in both IL and CF for $Vr_n = 7$–12.5.

Since an apparent mode switch occurred in the IL response between $Vr_n = 3.75 - 4.25$, excitation of the piezos were tested for the motion at $Vr_n = 3.75$. At this flow speed, the cylinder has a comparable IL and CF amplitudes with first mode shape. The center image in Fig. 9.2 shows the original (black) and piezo activated (red) response plots at $Vr_n = 3.75$. In the tests, the piezo was excited at 40 Hz to match the second structural mode of the test cylinder. Experiments showed that with the piezo activated, this resulted in a mode change and significant reduction in both IL and CF motion of the body (75% in CF only), despite the actuation only occurring in IL.

The RMS amplitude plot also showed that there is an apparent amplitude jump after $Vr_n = 5.5$. The piezos were also excited at this flow speed as an example illustration for vibration enhancement. The right image in Fig. 9.2 shows the original (black) and piezo activated (red) response plots at $Vr_n = 5.5$. Similarly, the piezo was excited at 40 Hz resulting in an increase in the response amplitude in both IL and CF directions of the body (100% in CF). The resulting IL response is multi-mode, while the CF response is primarily first mode.

Results show that VIV of a flexible cylinder can be significantly altered through excitation of specific spatial modes. In the tests, only the IL response was selected for applying piezo excitation due to less energy required to alter the smaller IL motions. Applying control in the CF would likely require a significant increase in the forces required to alter the system motion. The observed control in these experiments primarily demonstrates the ability to cause the system to move to a different response state through piezo actuation, rather than forcing the system to cancel motions or oscillate with a particular motion, allowing the system to operate in an open loop state. As a result of this study, the applied control method was observed to work for both high (air) and low (water) mass ratio systems.

References

1. Baz, A., Kim, M.: Active modal control of vortex-induced vibrations of a flexible cylinder. J. Sound. Vib. **165**(1), 69–84 (1993)
2. Bernitsas, M.M., Raghavan, K., Ben-Simon, Y., Garcia, E.: Vivace (vortex induced vibration aquatic clean energy): a new concept in generation of clean and renewable energy from fluid flow. J. Offshore Mech. Arct. Eng. **130**(4), 041101 (2008)
3. Blevins, R.D.: Flow Induced Vibrations, 2nd edn. Van Nostrand Reinhold Company, New York (1990)
4. Cheng, L., Zhou, Y., Zhang, M.: Perturbed interaction between vortex shedding and induced vibration. J. Fluids Struct. **17**(7), 887–901 (2003)
5. Gedikli, E.D.: Dynamic response and active control of flexible cylindrical structures undergoing vortex-induced vibrations. Ph.D. thesis, University of Rhode Island (2017)
6. Rashidi, S., Hayatdavoodi, M., Esfahani, J.A.: Vortex shedding suppression and wake control: a review. Ocean Eng. **126**(Supplement C), 57–80 (2016)
7. Williams, J.F., Zhao, B.: The active control of vortex shedding. J. Fluids Struct. **3**(2), 115–122 (1989)

Chapter 10
Extracting Natural Frequencies of Layered Beams Using a Continuous Variation Model and Modal Analysis

Arnaldo J. Mazzei, Javad Baqersad, and Yaomin Dong

Abstract This study involves the determination of the bending natural frequencies of beams composed by stacked cells of different materials. The focus is on cases with two cells. The analytical model is based on Euler-Bernoulli theory with the variations from one cell to another modeled via logistic functions. This approach leads to a single differential equation with variable coefficients, which is solved numerically using MAPLE® 's differential equation solvers. A forced motion method is used. Forcing frequencies are changed until large motions and sign changes are observed, leading to the resonant frequencies. Of interest is the validation of the analytically obtained frequencies via experimental results. Here, an experiment is set in which a simple two-cell beam is analyzed, via modal analysis, in order to verify the analytically calculated frequencies. The beam is excited using an impact hammer and the response is recorded using accelerometers. Mode shapes are also obtained via digital image correlation. The beam, including distinct materials, is composed of one cell made of steel and another made of aluminum. The joining method is discussed and results for fixed-free beams are obtained.

Keywords Beams with layered cells · Layered structures resonances · Non-homogeneous beams · Modal analysis of layered beams

Nomenclature

A	Area of the beam cross section (A_i, area of i-cell)
E	Young's modulus (E_i, Young's modulus of i-cell)
F	External forcing (spatial function, F_i, acting on i-cell)
f	External transverse force per unit length acting on the beam (f_i, acting on i-cell)
$H(x)$	Logistic function
I	Area moment of inertia of the beam cross section (I_i, moment of inertia of i-cell)
L	Length of the beam (L_i, length of i-cell)
R	Spatial function
S	Non-dimensional beam displacement in the y (transverse) direction
t	Time
ν	Non-dimensional frequency
w	Beam transversal displacement
xyz	Inertial reference system (coordinates x, y, z)
ρ	Mass density (ρ_i, density of i-cell)
ξ	Non-dimensional spatial coordinate
Ω	Frequency of harmonic excitation
Ω_0	Reference frequency

10.1 Introduction

This work is an extension of one given in reference [1] in which forced motions of non-homogeneous elastic beams were investigated. Euler-Bernoulli theory was employed and applied to a two-segment configuration subject to harmonic forcing. The objective was the determination of frequency response functions (FRFs) for the system. An approach was discussed

A. J. Mazzei (✉) · J. Baqersad · Y. Dong
Kettering University, Department of Mechanical Engineering, C. S. Mott Engineering and Science Center, Flint, MI, USA
e-mail: amazzei@kettering.edu

C. Niezrecki, J. Baqersad (eds.), *Structural Health Monitoring, Photogrammetry & DIC, Volume 6*,
Conference Proceedings of the Society for Experimental Mechanics Series, https://doi.org/10.1007/978-3-319-74476-6_10

in which material and geometric discontinuities were modeled by continuously varying functions. That resulted in a single differential equation with variable coefficients, which was tackled numerically using MAPLE®.[1] The resulting FRFs were compared to analytical solutions, for specific spatial loading cases, and compared very well. Here the approach is re-visited. An experimental set up is developed with the goal of validating the numerical results.

Vibrations of layered beams have been discussed in several references. For instance reference [2], where free vibrations of stepped Timoshenko beams were treated via Lagrange multipliers. Results compared well with values obtained using other analytical methods. In reference [3] Euler-Bernoulli stepped beams were studied via exact and Finite Element Method (FEM) approaches. FEM results using non-integer polynomials shape functions [4] compared well with exact solutions. General studies on media with discrete layers have been given, for example, in references [5–8]. Finite difference approaches to the dynamics of non-homogeneous media can be found in reference [9].

10.2 Modeling

As discussed in reference [1], the study uses Euler-Bernoulli beam theory. The equation of motion is given below and Fig. 10.1 exhibits the underlying variables.

$$\frac{\partial^2}{\partial x^2}\left(E(x)I(x)\frac{\partial^2 w\,(x,t)}{\partial x^2}\right)+\rho(x)A(x)\frac{\partial^2 w\,(x,t)}{\partial t^2}=f\,(x,t) \tag{10.1}$$

The configuration studied is a 2-cell beam, which is shown in Fig. 10.2.

Vibration frequencies can be calculated as follows. For harmonic forcing with frequency Ω:

$$f\,(x,t)=F(x)\sin\,(\Omega t) \tag{10.2}$$

Assuming solutions of the form:

$$w\,(x,t)=R(x)\sin\,(\Omega t) \tag{10.3}$$

leads to

$$\frac{d^2}{dx^2}\left(E(x)I(x)\frac{d^2R(x)}{dx^2}\right)-\rho(x)A(x)\Omega^2R(x)=F(x) \tag{10.4}$$

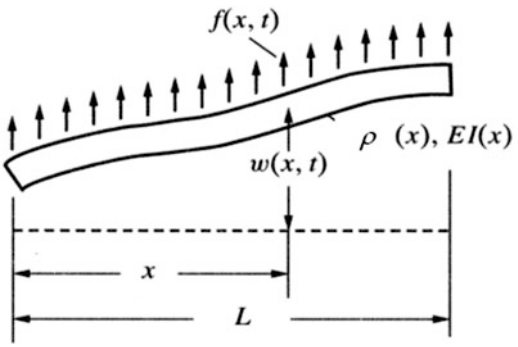

Fig. 10.1 Beam element for Euler-Bernoulli beam theory

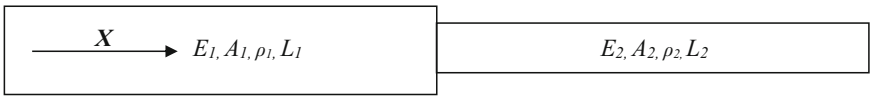

Fig. 10.2 Layered beam

[1] www.maplesoft.com/products/Maple/

The resonant frequencies and steady state response, due to harmonic forcing, are numerically obtained using a forced motion approach and a continuous variation model. This is discussed next.

10.3 Continuous Variation Model

In the continuous variation model, transitions from one material to another are approximated via logistic functions. Solutions are obtained via the forced-motion approach (see reference [10]).

The logistic functions are given by:

$$H(x) \approx \frac{1}{2} + \frac{1}{2}\tanh(Kx) = \frac{1}{1+e^{-2Kx}} \tag{10.5}$$

where a larger K corresponds to a sharper transition at $x = 0$.

A non-dimensional version of Eq. (10.4) can be obtained by taking (H_i, logistic functions):

$$\begin{aligned} &\xi = \frac{x}{L}, S(\xi) = \frac{R(x)}{L}, \nu = \frac{\Omega}{\Omega_0}, E(x) = E_1 H_1(K\xi) = E_1 f_1(\xi), \\ &I(x) = I_1 H_2(K\xi) = I_1 f_2(\xi), \rho(x) = \rho_1 H_3(K\xi) = \rho_1 f_3(\xi), \\ &A(x) = A_1 H_4(K\xi) = A_1 f_4(\xi) \end{aligned} \tag{10.6}$$

Substituting these into Eq. (10.4) leads to:

$$\frac{d^2}{d\xi^2}\left(f_1(\xi) f_2(\xi) \frac{d^2 S(\xi)}{d\xi^2}\right) - \nu^2 f_3(\xi) f_4(\xi) S(\xi) = Q(\xi) \tag{10.7}$$

where Ω_0 is a reference frequency and is set to $\Omega_0 = \sqrt{\frac{E_1 I_1}{\rho_1 A_1 L^4}}$.

In the approach, MAPLE®'s two-point boundary value solver is utilized to solve a forced motion problem. A constant value for the forcing function $Q(\xi)$ is assumed and the frequency ν is varied. Resulting amplitudes are monitored at the center of the beam, which leads to the numerical FRFs. Also, resonant frequencies can be found by observing changes in the signs of the deflections of the beam.

10.4 Numerical Example

Consider the beam shown in Fig. 10.2 and the following materials: Aluminum 6061 ($E_1 = 68.9\ GPa$, $\rho_1 = 2700\ Kg/m^3$) and Low Carbon Steel ($E_2 = 205\ GPa$, $\rho_2 = 7870\ Kg/m^3$).

For this example, a uniform beam with free-fixed boundary conditions and $L = 0.7620\ m$ (30 *in*) is used. In this case, the non-dimensional logistic functions (material and cross-section variations) can be written, for instance, as (see Fig. 10.3):

$$\begin{aligned} f_1(\xi) &= 1 + \frac{E_2 - E_1}{E_1}\left(\alpha + \frac{1}{2}\tanh(500(\xi - \alpha))\right), f_2(\xi) = 1, \\ f_3(\xi) &= 1 + \frac{\rho_2 - \rho_1}{\rho_1}\left(\alpha + \frac{1}{2}\tanh(500(\xi - \alpha))\right), f_4(\xi) = 1 \end{aligned} \tag{10.8}$$

where $\alpha L = L_1$ and $L_1 + L_2 = L$.

Here L_1 is taken to be 0.4572 m (18 *in*) and L_2 0.3048 m (12 *in*), which gives $\alpha = 0.6$.

Assuming a value of *1* for the external forcing and using the approach given in reference [10], the resultant deflections are plotted below for two distinct values of the frequency ν.

The resonance frequencies are taken to occur at $\nu = 5.5$ and $\nu = 23.1$ as seen in Figs. 10.4 and 10.5, respectively.

Amplitudes for the response at the center of the beam can be monitored from Eq. (10.7). This approach leads to the numerical FRF shown in Fig. 10.6, spanning the first two resonances.

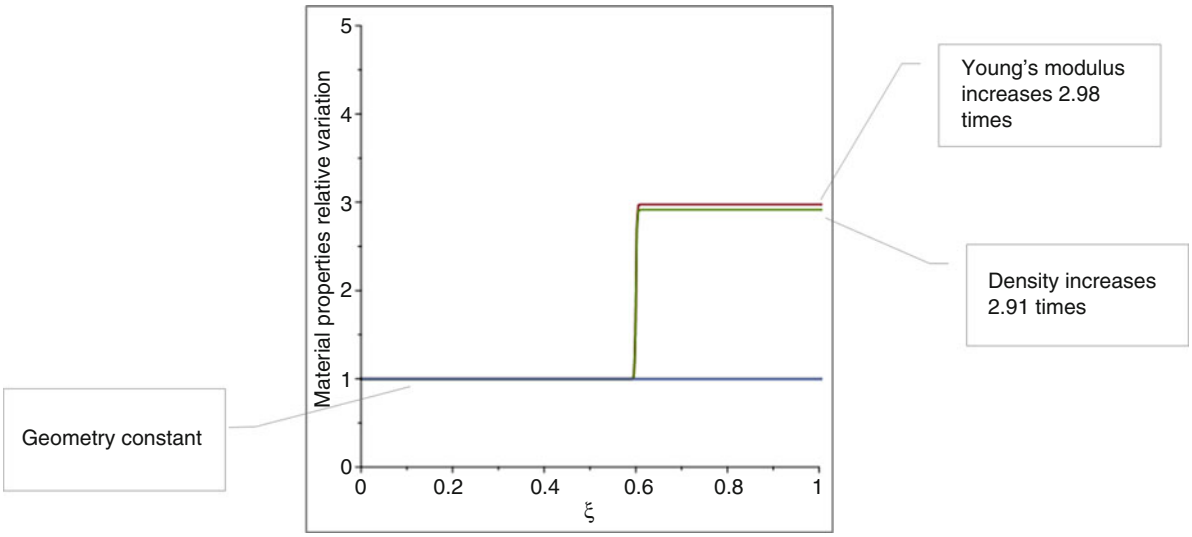

Fig. 10.3 Relative properties variation for the two-cell beam

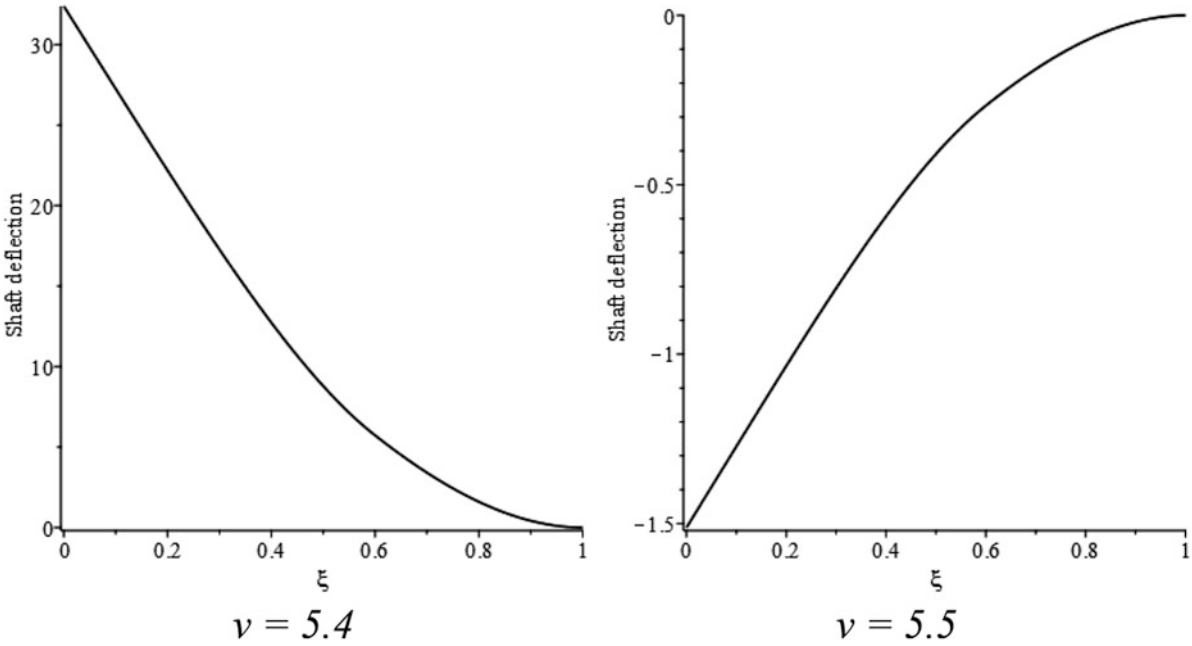

Fig. 10.4 Beam deflections for distinct values of ν – Free-Fixed: first resonance

10.5 Experimental Results

10.5.1 Joints

In order to verify the analytically calculated frequencies, an experiment is designed in which a simple two-cell beam is utilized. The beam, 0.9144 *m* in length (36 *in*), is composed by one cell made of low-carbon steel and another made of aluminum 6061. The cells have square, hollow, cross-sections with lengths L_1 and L_2 as given above. The section dimensions are shown in Fig. 10.7.

Various joining methods are available for joining dissimilar materials (see, for example, references [11, 12]). For the validation purposes of this work, a hybrid joining method of mechanical interlocks (1 *in X* 1 *in*) with adhesive bonding along the whole interface is used. An illustration of this type of joint is shown in Fig. 10.8. When compared to other joining techniques, such a joint design provides high torsional and bending strength, while minimizing the influence of the interfacial geometry.

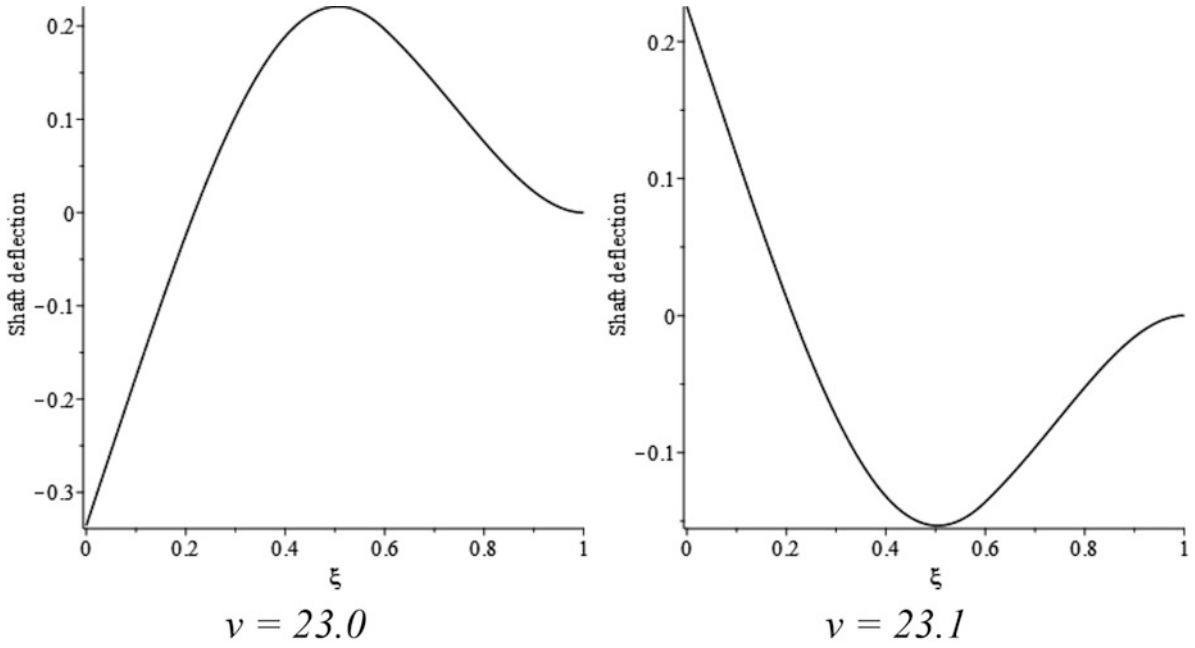

Fig. 10.5 Beam deflections for distinct values of ν – Free-Fixed: second resonance

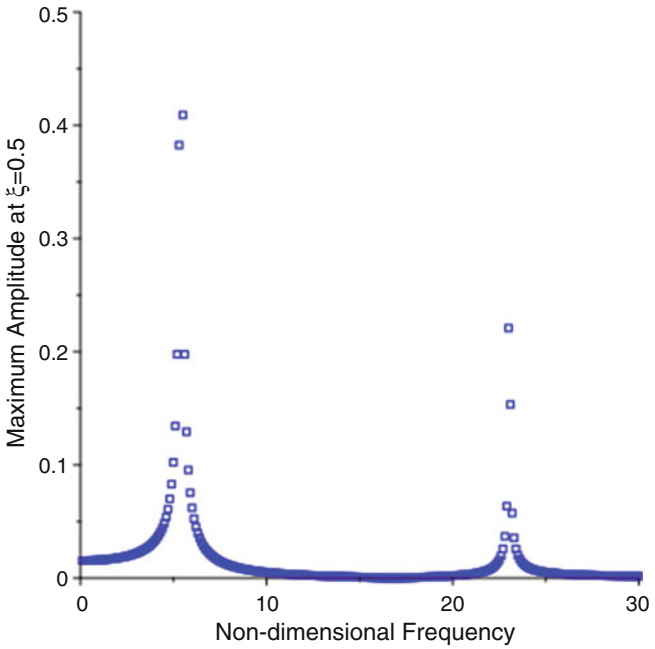

Fig. 10.6 Numerical FRF for non-homogeneous beam – Free/Fixed

Fig. 10.7 Cross-section of square tubes (inches)

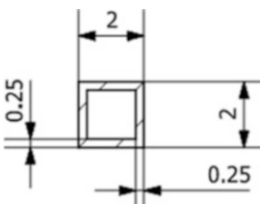

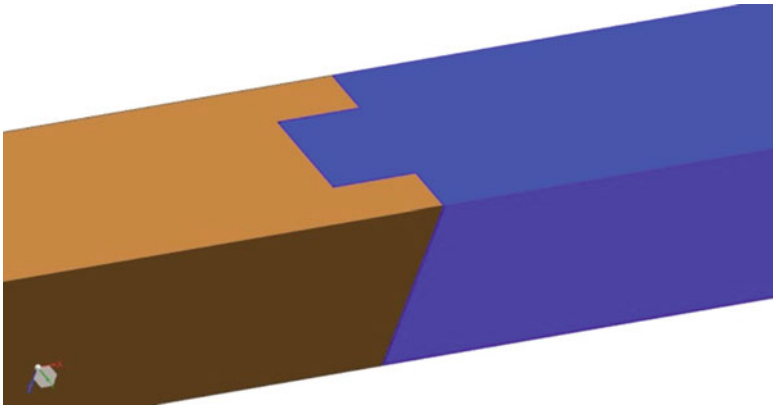

Fig. 10.8 Hybrid joining using mechanical interlocks and adhesive bonding

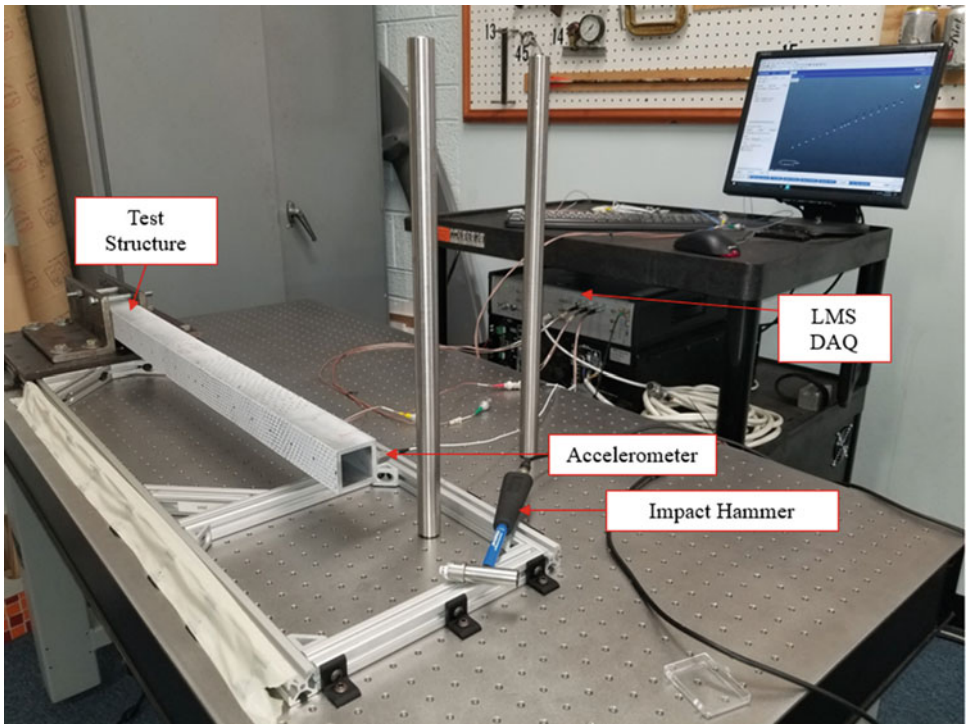

Fig. 10.9 Experimental set up to perform a modal test on a beam in a cantilever condition

10.5.2 Set Up and Results for Conventional Modal Test

In order to verify the numerical results, several experiments were performed on four 3 *ft.* (0.9144 *m*) beams (a steel beam, an aluminum beam, a joined aluminum-aluminum beam and a joined aluminum-steel beam). Modal analysis is conventionally used to validate analytical models. Conventional approaches include using an impact hammer [13] or mechanical shaker [14] to excite the structure and an accelerometer to collect data. Recently, optical measurement techniques such as digital image correlation [15] and computer vision [16] have been used in the field of structural dynamics. These approaches are non-contact and can provide full-filed data. In this paper, both techniques were used to obtain the mode shapes of the beams.

A conventional modal analysis was conducted on the beams in cantilever conditions. In order to provide a "built-in" boundary condition, a 6 *in* (0.1524 *m*) length of the tested beam was clamped in a fixture as shown in Fig. 10.9. In this test, a modal impact hammer was used to apply impact forces at 17 distinct points, on each beam, and the response was measured using an accelerometer located at the tip of the beams. After processing the data, the FRFs for all points were extracted.

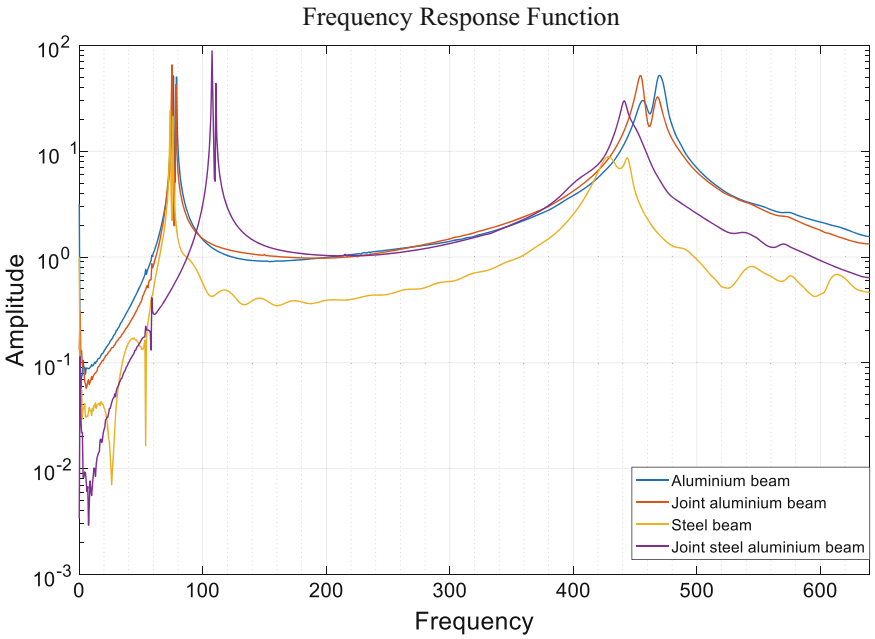

Fig. 10.10 Frequency response functions for the midpoint of the 36 *in* beams (first 6 *in* of the length clamped in the fixture)

Table 10.1 The first two resonant frequencies of the beams

	Aluminum beam (Hz)	Joined aluminum beam (Hz)	Steel beam (Hz)	Joined steel-aluminum beam (Hz)
1st resonant freq.	79	78	76	111
2n resonant freq.	470	468	444	441

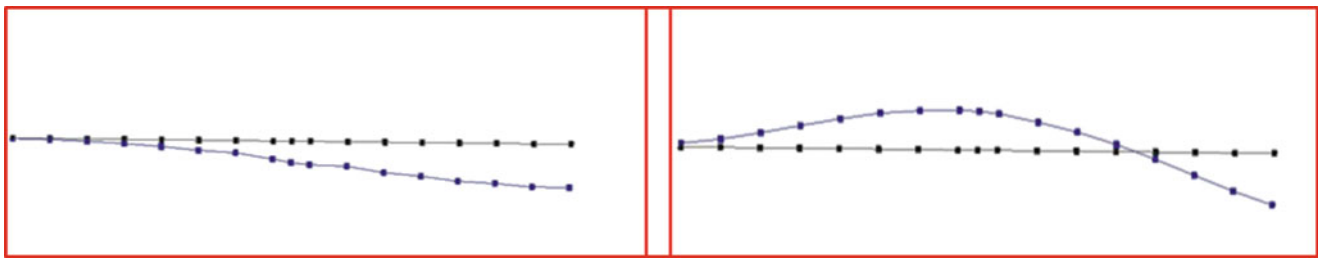

Fig. 10.11 The first mode shape (left) and the second mode shape (right) of the joined beam

The FRFs for the midpoint for all the beams are shown in Fig. 10.10. The peaks of the FRFs plot show the resonant frequencies of the mode shapes. Because no impact was made in edge direction, the edgewise mode shapes cannot be extracted. The first two resonant frequencies for the flapwise bending of beam are listed in Table 10.1. The mode shapes are shown in Fig. 10.11.

10.5.3 Set Up and Results for the Experimental Test Using Digital Image Correlation

In order to extract the mode shapes of the beams, a modal test was also performed using digital image correlation. In the experiment, a speckle pattern was created on the surface of the beams as seen on Fig. 10.12.

The beams were clamped in the fixture and an impact hammer was used for the excitation. A photograph of the test setup is shown in Fig. 10.13. The response of the beams to the excitations was recorded using a pair of high-speed cameras. The recorded images, by the high-speed cameras, were processed using the Digital Image Correlation (DIC) technique. Using this technique, full field mode shapes of the beams were extracted (see Fig. 10.14).

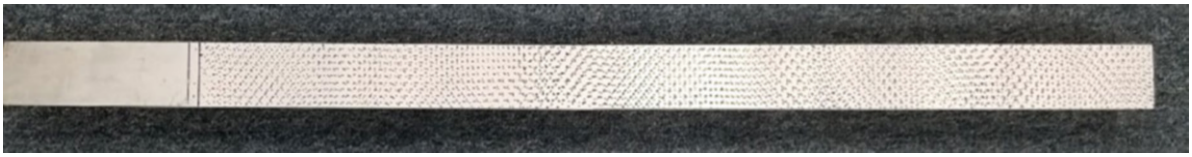

Fig. 10.12 A photograph showing a speckled pattern created on the beam

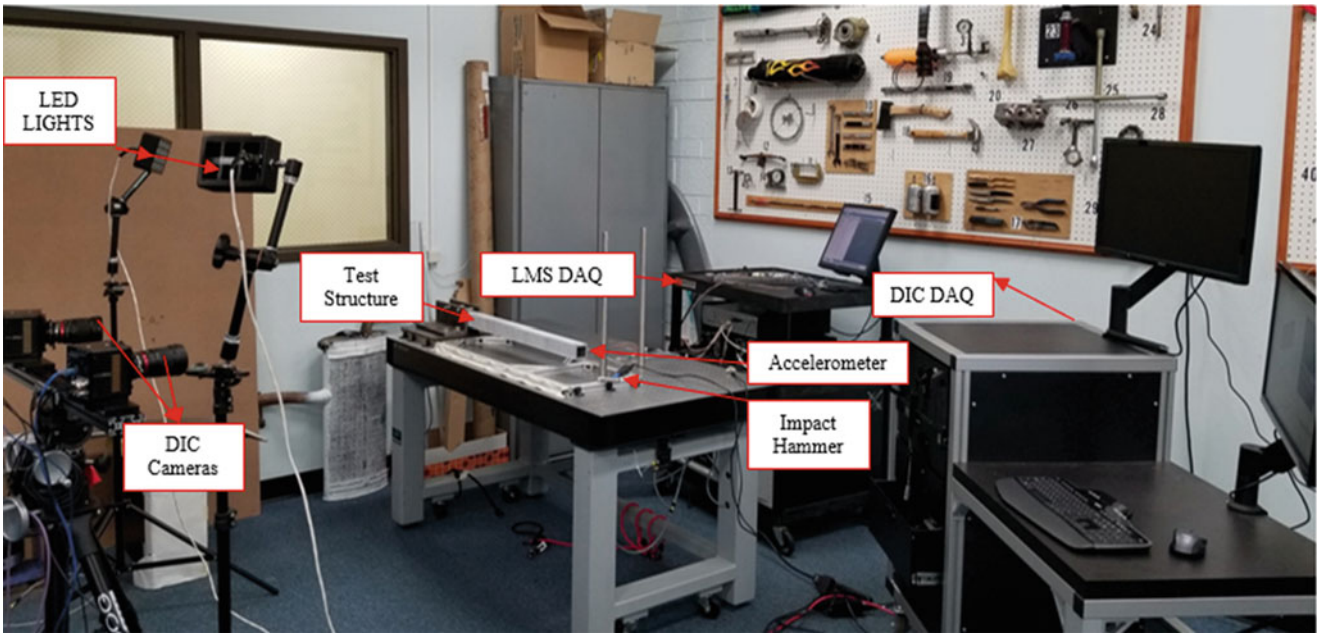

Fig. 10.13 A photograph showing the test setup for DIC measurement

10.6 Results Comparison

Table 10.2 shows the obtained frequencies using both the analytical and experimental approaches. For the single material beams, analytical frequencies were calculated both using Euler-Bernoulli beam theory and the forced motion approach. The analytical frequencies for the stacked beams were calculated using the forced motion approach.

Note that for the single material beams, analytical results agree very well. That lends confidence to the forced motion method.

Comparing the experimental results for the single material aluminum beam to the joined aluminum beam, it is seen that agreement is also very good. The joining of the sections does not significantly affect the resonant frequencies.

As for the experimental results compared to the analytical ones, the frequencies fall below the calculated values. The first frequency is about 11% less for the aluminum beam, 16% for the steel and 21% for the aluminum-steel. The variations for the second frequency are similar, with a slight increase (25%) for the stacked beam.

The differences are attributed to the difficulties in reproducing an actual "fixed" boundary condition in the experiment. Nonetheless results compare well.

10.7 Conclusions

A forced motion approach was used to calculate frequencies and FRFs for layered beams composed of different materials. The method produces very good results when compared to analytically calculated values for single material beams.

In order to verify some of the results, an experiment involving modal analysis of several beams was developed. It included testing of single material beams and stacked beams compose of two cells.

It was found that the joining method utilized in the stacked beams construction did not significantly affect the frequencies.

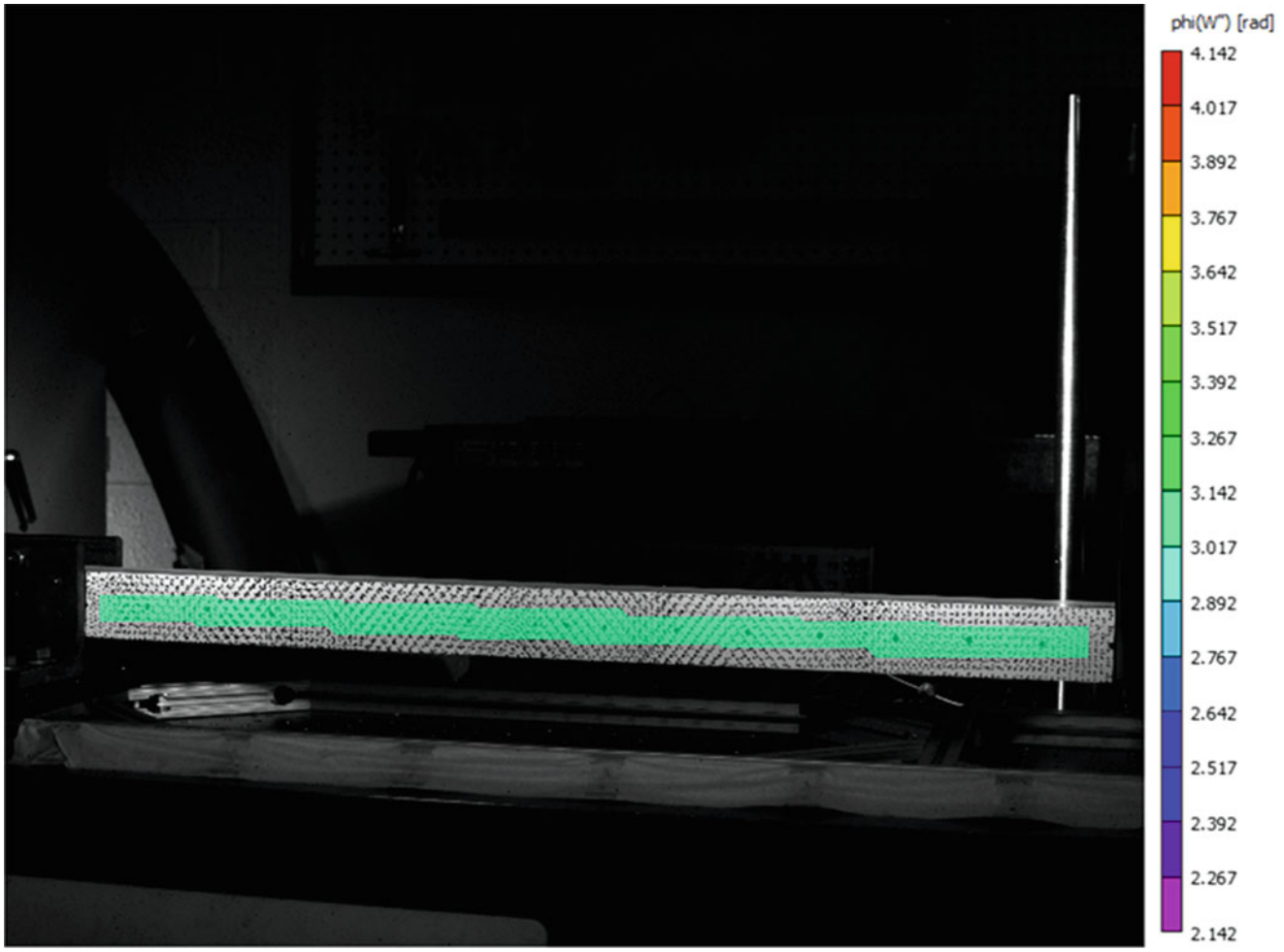

Fig. 10.14 DIC test results showing the first mode of the beam

Table 10.2 Frequency results – analytical and experimental

	Aluminum beam	Joined aluminum beam	Steel beam	Joined steel-aluminum beam
1st resonant freq. experimental	79 Hz (Modal analysis)	78 Hz (Modal analysis)	76 Hz (Modal analysis)	111 Hz (Modal analysis)
2n resonant freq. experimental	470 Hz (Modal analysis)	468 Hz (Modal analysis)	444 Hz (Modal analysis)	441 Hz (Modal analysis)
1st resonant freq. model	89 Hz (Theoretical) 91 Hz (Forced motion)	91 Hz (Forced motion)	90 Hz (Theoretical) 92 Hz (Forced motion)	140 Hz (Forced motion)
2n resonant freq. model	559 Hz (Theoretical) 559 Hz (forced motion)	561 Hz (Forced motion)	565 Hz (Theoretical) 566 Hz (Forced motion)	586 Hz (Forced motion)

Experimental frequency results were found to underestimate the resonances by percentages varying from 11% up to 25%, which was attributed to difficulties in reproducing theoretical boundary conditions in the laboratory environment. Nonetheless results agreed well with the analytical methods used.

References

1. Mazzei, A.J., Scott, R.A.: Harmonic forcing of a two-segment Euler-Bernoulli beam. In: Dervilis, N. (ed.) Special Topics in Structural Dynamics, Proceedings of the 35th IMAC, A Conference and Exposition on Structural Dynamics 2017, vol. 6, pp. 1–15. Springer, Cham (2017)
2. Cekus, D.: Use of lagrange multiplier formalism to solve transverse vibrations problem of stepped beams according to Timoshenko theory. Sci. Res. Inst. Math. Comput. Sci. **2**(10), 49–56 (2011)

3. Jang, S.K., Bert, C.W.: Free vibration of stepped beams: exact and numerical solutions. J. Sound Vib. **130**(2), 342–346 (1989)
4. Bert, C.W., Newberry, A.L.: Improved finite element analysis of beam vibration. J. Sound Vib. **105**, 179–183 (1986)
5. Lee, E.H., Yang, W.H.: On waves in composite materials with periodic structure. SIAM J. Appl. Math. **25**(3), 492–499 (1973)
6. Hussein, M.I., Hulbert, G.M., Scott, R.A.: Dispersive elastodynamics of 1D banded materials and structures: analysis. J. Sound Vib. **289**(4–5), 779–806 (2006)
7. Mazzei Jr., A.J., Scott, R.A.: Vibrations of discretely layered structures using a continuous variation model. In: Allemang, R. (ed.) Topics in Modal Analysis II, vol. 8, pp. 385–396. Springer, Cham (2014)
8. Kang, Y., Shen, Y., Zhang, W., Yang, J.: Stability region of floating intermediate support in a shaft system with multiple universal joints. J. Mech. Sci. Technol. **28**(7), 2733–2742 (2014)
9. Berezovski, A., Engelbrecht, J., Maugin, G.A.: Numerical Simulation of Waves and Fronts in Inhomogeneous Solids. World Scientific, Singapore (2008)
10. Mazzei, A.J., Scott, R.A.: On the effects of non-homogeneous materials on the vibrations and static stability of tapered shafts. J. Vib. Control. **19**(5), 771–786 (2013)
11. Aluminium Automotive Manual [Online]. Available: https://www.european-aluminium.eu/resource-hub/aluminium-automotive-manual/
12. Nicholas, G., Edward, D.: Developments in the friction stir welding of metals. In: Proceedings of the 6th International Conference on Aluminium Alloys, The Japan Institute of Light Metals, Toyohashi, pp. 139–151 (1998)
13. Baqersad, J., Niezrecki, C., Avitabile, P., Slattery, M.: Dynamic characterization of a free-free wind turbine blade assembly. In: Allemang, R., De Clerck, J. Niezrecki, C., Wicks, A. (eds.) Special Topics in Structural Dynamics, Proceedings of the 31st IMAC, A Conference on Structural Dynamics, vol. 6, pp. 303–312. Springer, New York (2013)
14. Baqersad, J., Poozesh, P., Niezrecki, C., Avitabile, P.: Comparison of modal parameters extracted using MIMO, SIMO, and impact hammer tests on a three-bladed wind turbine. In: Allemang, R. (ed.) Topics in Modal Analysis II, Proceedings of the 32nd IMAC, A Conference and Exposition on Structural Dynamics, vol. 8, pp. 185–197. Springer, Cham (2014)
15. Baqersad, J., Poozesh, P., Niezrecki, C., Avitabile, P.: Photogrammetry and optical methods in structural dynamics – a review. Full-Field Non-Contact Vib. Meas. Methods Comp. Appl. **86**(Part B), 17–34 (2017)
16. Sarrafi, A., Poozesh, P., Mao, Z.: A comparison of computer-vision-based structural dynamics characterizations. In: Barthorpe, R., Platz, R., Lopez, I., Moaveni, B., Papadimitriou, C. (eds.) Model Validation and Uncertainty Quantification, Proceedings of the 35th IMAC, A Conference and Exposition on Structural Dynamics 2017, vol. 3, pp. 295–301. Springer, Cham, (2017)

Chapter 11
Extended Abstract: Dynamic Behavior of a Compliant Mechanism Driven by Stacked Piezoelectric Actuators

A. Koyuncu, M. Şahin, and H. N. Özgüven

Abstract Mechanical amplifiers are employed to enhance output displacement of piezoelectric actuators. Dynamic behavior of such an amplified piezoelectric actuator needs to be known accurately in order to verify its suitability for the driven system. The objective of this study is to present a theoretical approach to determine a mathematical model for an amplified piezoelectric actuator (APA) which consists of a stacked piezoelectric actuator (SPA) with rhombus type mechanical amplifier (RPA). Dynamics of the mechanical amplifier is formulated based on distributed-parameter system approach, and Hamilton's principle is used to obtain a reduced order model. The SPA is then dynamically coupled with the reduced order model of a flexural amplifier by employing the constitutive relations between two substructures. The responses of the coupled system are calculated using linear vibration analysis under harmonic voltage input. Finally, the validity of the developed mathematical model is verified by comparing the calculated velocities with that of finite element solutions and experimental measurements in the frequency domain. The finite element (FE) solution is obtained using ANSYS software. Output velocity of the sample RPA is measured with the aid of a laser vibrometer. It is observed that the results obtained from the mathematical model show a very good agreement with those of the finite element analysis and test measurements.

Keywords Amplified piezoelectric actuators · Rhombus type · Strain amplification · Compliant mechanism

11.1 Introduction

Piezoelectric actuators have become widespread in robotics and mechatronics. These actuators are used as positioners, motors and vibration dampers in various applications such as precise positioners in optical devices, small scale ultrasonic motors, and active vibration controllers in space structures. High resolution, large output force, compact size, wide frequency bandwidth and solid-state design are the unique features of the piezoelectric actuators. The major limitation of the piezoelectric actuators, on the other hand, is their small output displacement range. Compliant mechanisms are integrated with multi-layered stacked piezoelectric actuators (SPA) to enhance these output displacements. There are different types of compliant mechanisms in the literature [1]. Amplified piezoelectric actuators (APAs) with flextensional compliant mechanisms are widely used in various engineering fields. Kinematic and dynamic modelling of piezoelectric actuators with compliant mechanisms are required in design and optimization stages of the actuators. Most of the studies in the literature are based on kinematic analysis of the actuators under static loading conditions [1–3]. Statically determined constitutive relations of an actuator may not be valid under dynamic actuation cases [4]. Some of the studies perform dynamic analysis considering only inertial properties of the lumped elements such as the SPA. The inertial effects of the compliant mechanism become important while the piezoelectric actuator is driven by high frequency input voltage. In this study, generalized constitutive equations of an APA with a compliant mechanism are determined based on structural dynamic analysis. A Rhombus type flextensional compliant mechanism (RCM) is formulated in the current study since rhombus type amplified piezoelectric actuators (RPAs) are the most popular and available amplified piezoelectric actuators in the market (Fig. 11.1a).

A. Koyuncu (✉)
Middle East Technical University, Ankara, Turkey

Defense Systems Technologies Business Sector, ASELSAN A.Ş., Ankara, Turkey

M. Şahin · H. N. Özgüven
Middle East Technical University, Ankara, Turkey

C. Niezrecki, J. Baqersad (eds.), *Structural Health Monitoring, Photogrammetry & DIC, Volume 6*,
Conference Proceedings of the Society for Experimental Mechanics Series, https://doi.org/10.1007/978-3-319-74476-6_11

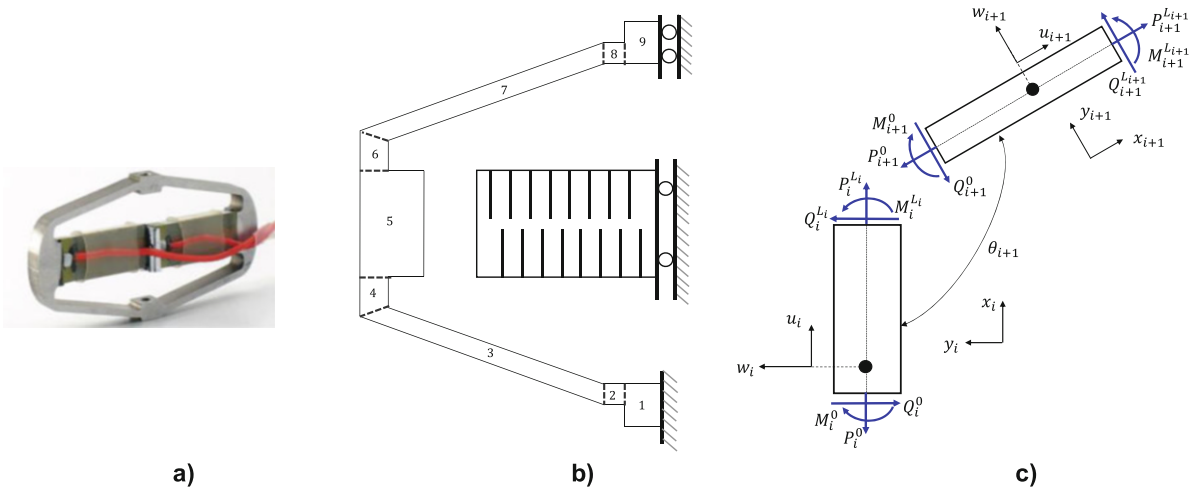

Fig. 11.1 (**a**) Sample RPA (**b**) Half RPA model (**c**) Planar beams connected in series

11.2 Methodology

According to proposed method, the RCM and the SPA are to be analyzed separately. The RPA model can be reduced to a half model by defining appropriate symmetry boundary conditions (Fig. 11.1b). A standard RCM can be decomposed into planar beams connected in series with different angles (Fig. 11.1c). Equations of motions for each beam can be written considering longitudinal and transverse deflections in the beam coordinate systems as shown in Fig. 11.1c. The generalized boundary condition equations are written for intermediate beam connections points. A closed form solution is then obtained in matrix form using eigenfunctions and boundary condition equations. Numerical methods are utilized to determine the eigenvalues and the coefficients of eigenfunctions for each beam. Then, the solution for the dynamic model of the entire RCM is obtained by means of modal superposition. The analytical solution of the half SPA is determined by using a similar approach. Tip displacement of the RCM and coupled degree of freedoms (DOFs) between the RCM and SPA are selected as master DOFs. The half RCM and the half SPA models are reduced to four and three DOF systems respectively based on master coordinates. Then, dynamic coupling methods are utilized to couple the half RCM and the half SPA in modal domain.

11.3 Verification of the Mathematical Model

Mathematical model of the RPA is verified by means of experimental studies and FE analysis. A miniature piezoelectric actuator CEDRAT APA35xs is selected for this purpose. Tip velocity of the actuator is measured by means of laser vibrometer while the actuator is driven by sinusoidal input voltage. Tests are performed by fixing the actuator at the bottom (Fig. 11.2a). The experimental case study is simulated on ANSYS as well. Velocity frequency responses under harmonic voltage inputs are calculated by using ANSYS Multiphysics solver with piezoelectric extension (Fig. 11.2b). Comparison of the calculated velocity response with the experimental one is illustrated in Fig. 11.3.

11.4 Conclusion

In this paper, a new method is proposed to obtain dynamic response of APAs with compliant mechanisms. In order to verify the analytical model, frequency responses calculated by using the mathematical model developed are compared with those obtained with FE analysis, as well as with experimentally measured ones for a sample piezoelectric actuator. It is observed from the comparison of the analytical solutions with the finite element and experimental measurement results that the mathematical model gives promising results, although the analytical response predictions are not as good as those obtained with finite element analysis.

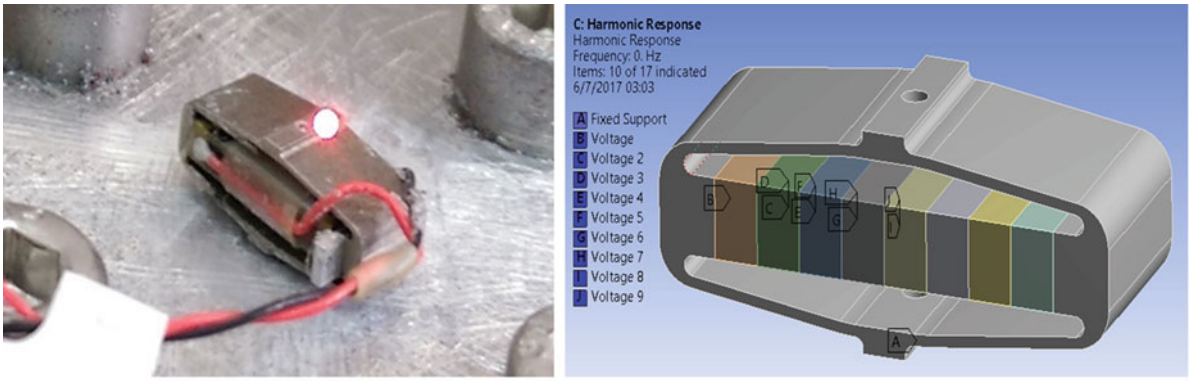

Fig. 11.2 (**a**) Vibration tests measurements with laser vibrometer (APA35xs), (**b**) FE model of APA35xs

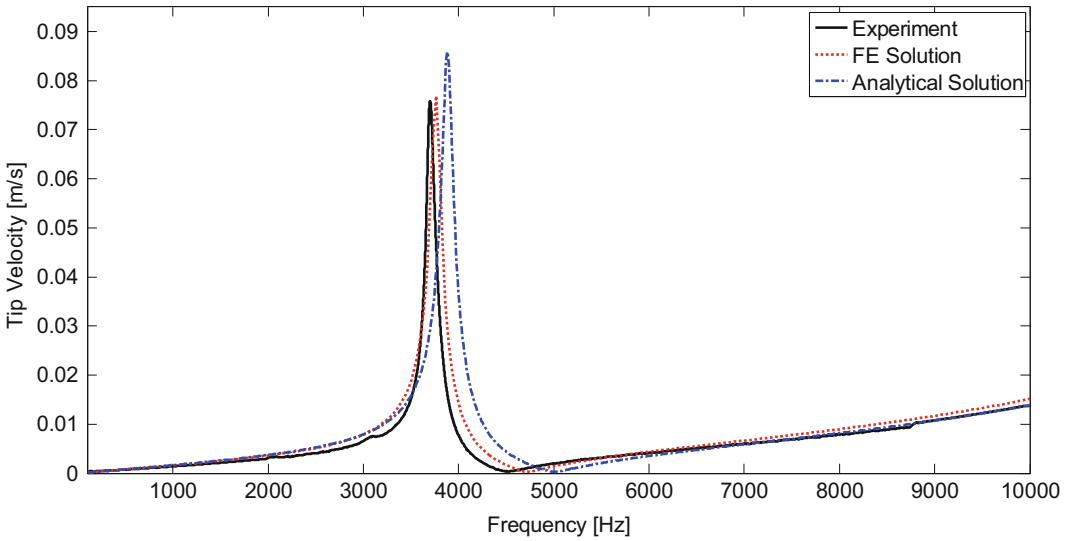

Fig. 11.3 Calculated and measured tip velocity frequency responses

References

1. Ling, M., Cao, J., Zeng, M., Lin, J., Inman, D.J.: Enhanced mathematical modeling of the displacement amplification ratio for piezoelectric compliant mechanisms. Smart Mater. Struct. **25**(7), 1–11 (2016)
2. Ueda, J., Secord, T.W., Asada, H.H.: Large effective-strain piezoelectric actuators using nested cellular architecture with exponential strain amplification mechanisms. IEEE/ASME Trans. Mechatron. **15**(5), 770–782 (2010)
3. Cao, J., Ling, M., Inman, D.J., Lin, J.: Generalized constitutive equations for piezo- actuated compliant mechanism. Smart Mater. Struct. **25**(9), 1–10 (2016)
4. Yeom, T., Simon, T.W., Zhang, M., North, M.T., Cui, T.: Physical high frequency, large displacement, and low power consumption piezoelectric translational actuator based on an oval loop shell. Sensors and Actuators, A: Physical **176**, 99–109 (2012)

Chapter 12
Detection of Natural Frequency and Mode Shape Correspondence Using Phase-Based Video Magnification in Large-Scale Structures

Aral Sarrafi, Peyman Poozesh, Christopher Niezrecki, and Zhu Mao

Abstract Structural dynamics identification is an important part of both the design and certification process for large-scale structures and specifically utility-scale wind turbine blades. Finding the correspondence between the estimated natural frequencies and the mode shapes of interest can be a very challenging due to the sheer size of the structures and the large amount of instrumentation required. The state of the art methods in experimental modal analysis (EMA) and operational modal analysis (OMA) require attachment of numerous accelerometers along the test structure to extract the natural frequencies and the mode shapes. Instrumenting large structures with accelerometers and handling the wiring and the connections can be a very labor-intensive task; therefore, alternative methods should be considered to address this problem. Within this paper, the capabilities of phase-based video magnification and motion estimation are investigated to find the correspondence between the natural frequencies and the mode shapes. The sequence of images (video) is recorded from the vibrating wind turbine blade and then processed using the phase based motion estimation to extract the spectrum of the response of the wind turbine blade to the impact excitation. Afterward based on the obtained spectrum the recorded videos are magnified to visualize the operating deflection shapes. The motion magnified videos represent the visual perception of the operating deflection shapes, which can be used to find the correspondence between the natural frequencies and the mode shapes. The results of this method have also been validated using the benchmark modal data from the accelerometers as well as the point tracking optical measurement method.

Keywords Phase-based motion estimation · Video Magnification · Wind Turbine Blade · Modal Analysis

12.1 Introduction

Structural dynamics identification is an essential procedure in design and certification of brand new structures before being put to operation in the field [1]. This procedure can be considered as the extraction of natural frequencies, mode shapes or operating deflection shapes and the damping ratios associated with each of the modes of the structure [2]. Experimental modal analysis (EMA) and operational modal analysis (OMA) are the most common tools that are being widely used for structural dynamics identification [2]. EMA and OMA have been developed though several decades of research and industrial application.

Based on the safety sensitivity of the application and other considerations, which should be provided by the design and certification standards, several steps and parameters of EMA and OMA could be neglected. For example there are numerous structures in which monitoring of the natural frequencies of the structure is required. Therefore, performing a complete modal analysis on the structure is not necessary and would be a waste of time and energy, since mode shape extraction is much more labor intensive and time consuming than obtaining merely the natural frequencies. As a result, based on the requirements, EMA and OMA can be performed partially to avoid completing the full EMA or OMA test which can be tedious at some points.

This paper aims to propose a technique to perform partial modal analysis on the structures in which the natural frequencies and the correspondence of each natural frequency to a specific mode shape is important. In other words, two separate pieces of information are targeted to be extracted, first the natural frequencies, second which mode a specific natural frequency is

A. Sarrafi · P. Poozesh · C. Niezrecki · Z. Mao (✉)
Structural Dynamics and Acoustic Systems Laboratory, Department of Mechanical Engineering, University of Massachusetts Lowell, Lowell, MA, USA
e-mail: zhu_mao@uml.edu

C. Niezrecki, J. Baqersad (eds.), *Structural Health Monitoring, Photogrammetry & DIC, Volume 6*,
Conference Proceedings of the Society for Experimental Mechanics Series, https://doi.org/10.1007/978-3-319-74476-6_12

corresponding to (for example 5 Hz is corresponding to the first bending etc.). The correspondence problem seems to be trivial to solve if the exact quantified operating deflection shapes (ODS) or mode shapes are available. However, with in this paper we are intending to find this correspondence without extracting the quantified ODS that can be a challenging task, ultimately saving time and effort.

Traditional sensing techniques such as using accelerometers and laser vibro-meters are not readily able to provide the natural frequency and mode shape correspondence without computing the quantified mode shapes. Moreover, for large-scale structures (such as wind turbine blades), instrumentation of the structure with accelerometers is very time consuming [3]. Laser measurements can avoid the instrumentation of the structure, but the measurements should be performed sequentially [4], which will increase the testing time dramatically. On the other hand, digital cameras are able to record the sequence of images from the vibrating structure, which will contain the full field response [3, 5, 6]. Instantaneous full-field measurement capability of digital cameras will decrease the testing time compared to using a laser vibrometer, moreover the measurement is non-contact and the instrumentation of the structure is avoided as well [7, 8]. Therefore, in recent years digital cameras are being more widely used in several engineering applications [9, 10].

Non-contact and full-field measurement capabilities are the most well-known and important features of using digital cameras. Another feature of the camera-based measurements that have not been highlighted vividly in engineering applications is the visual perception that images can provide for the user. Other sensor measurements such as accelerometers and lasers are providing time-series, which are not very meaningful for the user without further processing and advance visualization techniques. In contrast, image and video data can provide useful information because of the similarities between the cameras (image acquisition system) and human vision system without involving intricate processing and visualization techniques. Human vision system can be considered as the primary sensing method for interacting with the environment and receiving and perceiving data. The method provided in this paper, will be taking advantage of the visual perception that images and videos are providing to solve the natural frequency and mode shape correspondence problem.

Speaking of the visual perception, normally the vibrational displacement of the structures are subtle and cannot be easily picked up by a human vision system. Moreover, even if the vibrational displacements are large enough to be perceived with naked eye the videos and the sequence of images will be providing a mixture of several mode shapes and the correspondence of the natural frequencies to the modes will not available. In order to overcome this problem a recently developed computer vision algorithm known as the motion magnification (video magnification) [11–13] is utilized to pre-process the raw videos. The resulting videos will have enlarged motions with in the specific frequency bands, which makes the human vision system pick up the motion pattern easily and detect the frequency to mode shape correspondence based on prior knowledge. The prior knowledge that the user has to know is an approximate intuition of each mode shape, which is trivial for most structural engineers trained in modal analysis. The natural frequencies of the structure can be extracted using a few accelerometers or directly from the captured sequence of images using the phase-based motion estimation technique [14] or other motion estimation methods [15, 16]. Within this paper, the natural frequencies are extracted directly from the images via phase-based motion estimation.

The paper starts with a brief theoretical background on the phase-based motion estimation and motion magnification in order to provide a basic understanding of the procedure for phase-based motion processing. Next, the experimental test-setup is introduced and lastly, the results including the natural frequencies and the inferred natural frequency to mode shape correspondence are presented.

12.2 Theoretical Background on Phase-Based Motion Processing

Within this section a very brief background on the phase-based motion, processing is provided including the phase based motion estimation and motion magnification. The main idea of phase based motion estimation is similar to the shift theorem in Fourier transform. The Fourier transform shift theorem indicates that any shift in the spatial domain of a function would result to variations in phase in the frequency domain representation of the same function.

$$F\left[f\left(x-a, y-b\right)\right] = e^{j2\pi(au+bv)} F\left(u, v\right) \tag{12.1}$$

In Eq. (12.1), it is assumed that the Fourier transformation of function $f(x, y)$ is $F(u, v)$. As it is clear, a shift in spatial domain will represent itself as proportional variations in phase in the frequency domain representation of the function. The same idea can be applied for phase-base motion estimation in 2D images as 2D discrete spatial functions. The major difference between the phase-based motion estimation and the Fourier transform shift theorem is that instead of using sinusoids, Gabor wavelets will be used to map the spatial domain functions to the frequency domain.

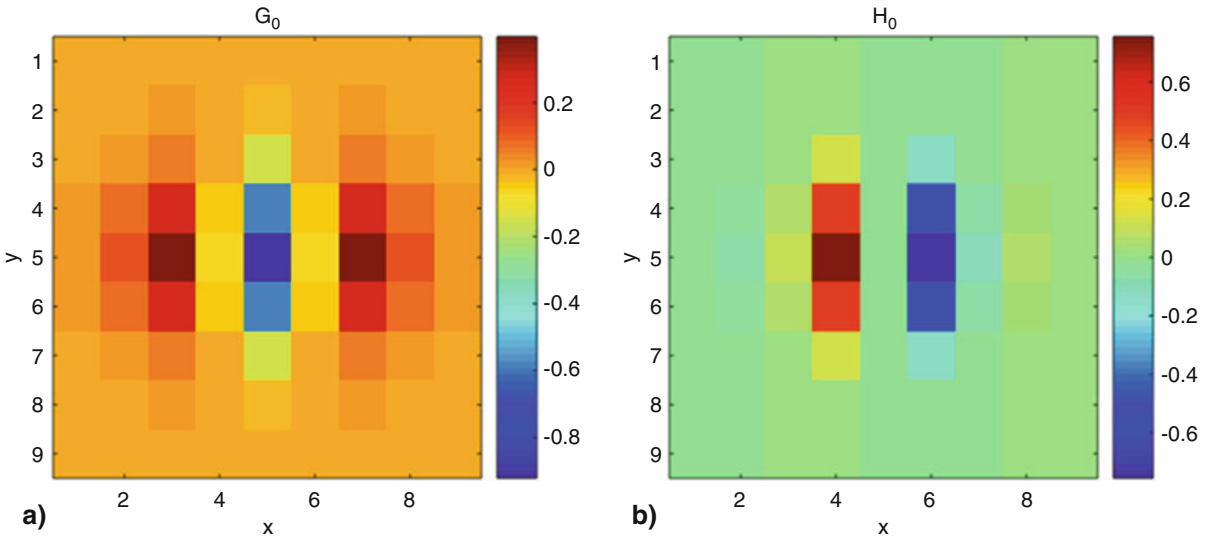

Fig. 12.1 Gabor wavelets oriented in horizontal direction (x-axis). (**a**) Real part of the Gabor wavelet. (**b**) Imaginary part of Gabor wavelet

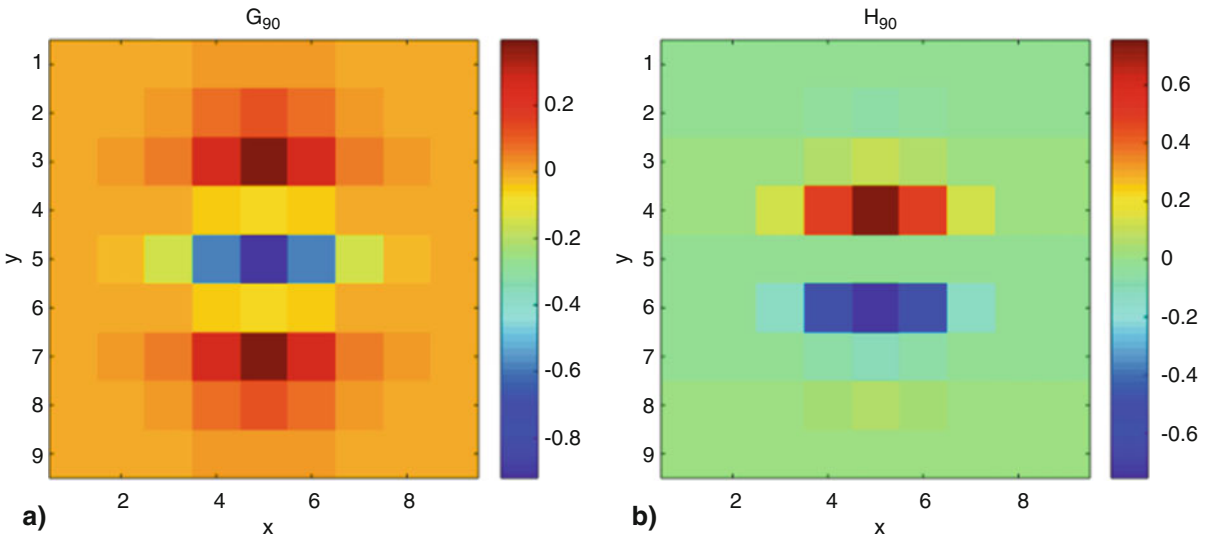

Fig. 12.2 Gabor wavelets oriented in vertical direction (y-axis). (**a**) Real part of the Gabor wavelet. (**b**) Imaginary part of Gabor wavelet

$$g(x,y) = G_\theta + jH_\theta \tag{12.2}$$

Equation (12.2) shows the general form of a complex valued Gabor wavelet. The Gabor wavelets, which are used in this study, are presented in Figs. 12.1 and 12.2 for two different orientations [17].

The orientation of the Gabor wavelet determines the direction of sensitivity for extracting the motion [17]. For example, the Gabor wavelet with orientation having subscript zero, is only sensitive to the motion in x direction and the motions in y-direction will not be extracted using the Gabor wavelet with orientation zero. The sequence of images captured from the vibrating structure will be convolved with a pair of Gabor wavelets based on the direction of the anticipated motion θ. Therefore each frame of the video will be mapped on to a complex valued domain with real and imaginary parts:

$$REAL_\theta(u,v,t) = \sum_x \sum_y I(x,y,t)\, G_\theta(x-u, y-v) \tag{12.3}$$

$$IMAG_\theta(u,v,t) = \sum_x \sum_y I(x,y,t)\, H_\theta(x-u, y-v) \tag{12.4}$$

Convolving images at all frames from the video with Gabor wavelets will map the images on to complex domain and the phase for each of the complex valued numbers can be found:

$$\phi_\theta(u,v,t) = \tan^{-1}\left\{\frac{IMAG_\theta(u,v,t)}{REAL_\theta(u,v,t)}\right\} \tag{12.5}$$

Similar to the Fourier transform shift property any motion in spatial domain will be reflected as variation of phase in the complex domain and the variations will be proportional to the motion. Therefore, the motion from time (t) to($t+1$) can be estimated by subtracting the phase planes as in Eq. (12.6):

$$\delta^{\theta}{}_{t,t+1} = \alpha\left[\phi(u,v,t+1) - \phi(u,v,t)\right] \tag{12.6}$$

In Eq. (12.6) α is a calibration factor, which is not the concern of our study, since the natural frequencies can be extracted from the un-calibrated data as well. Within this paper, the exact same procedure has been implemented in MATLAB to extract the natural frequencies of the structures.

Motion magnification (video magnification) also works based on the fact that the motion information is preserved within the phase variations. In the motion magnification algorithm, the phase plane signals $\phi_\theta(u,v,t)$ are processed with a band-pass filter. In other words, the phase temporal variations in a specific frequency band is amplified and all the other temporal variations out of the selected pass-band are suppressed. Reconstructing a new video using the band-pass filtered phase series will result in a new video with magnified motions with in the selected frequency band. Respectively, if the center frequency of the band-pass filter is selected as one of the natural frequencies of the structure, the resulting video will represent a visual perception of the operating deflection shape corresponding to the selected natural frequency [18–20].

In summary, first the videos will be processed using the phase based motion estimation in order to estimate the natural frequencies of the structure. In the next stage, the extracted natural frequencies will be used as the center frequency for the band-pass filtering of the phase variations in phase-based motion magnification procedure. The operating deflection shapes can be perceived from the motion magnified videos and the natural frequency and mode shape correspondence can be obtained using prior knowledge.

12.3 Experimental Test-Setup

In this section, the experimental test-setup for the proof of concept is studied. Often in large-scale industrial structures such as utility scale wind turbine blades, the full modal analysis in not required and extracting natural frequencies and the correspondence between the natural frequencies and the mode shapes is the only information of interest. Solving this problem can get more complicated for large-scale wind turbine blades because of the concentration of multiple natural frequencies in a narrow frequency band and coupling between the mode shapes. Therefore, it can be very difficult to detect the correspondence between the mode shapes and natural frequencies. Within this study a large scale (approximately 60 m) wind turbine blade is selected as the case study. The wind turbine blade is tested at the Wind Technology Testing Center (WTTC), which is one of the largest wind turbine blade testing centers located at Massachusetts. The wind turbine blade is cantilevered, and was excited at the tip by multiple impacts, and the sequence of the images from the vibrating wind turbine blade was captured using digital video camera at 60 frame per second (fps). Based on the Nyquist criterion the sampling rate is enough to extract natural frequencies up to 30 Hz. (Note: Most of the blade properties and geometries are confidential, therefore the authors are not able to provide detailed information and informative pictures of the wind turbine blade. Moreover, all the natural frequencies are normalized to the first natural frequency).

The camera was mounted on a scissor lift and elevated in order to obtain an acceptable field of view from the side of the wind turbine blade. The captured field of view is suitable to analyze the flap-wise bending mode shapes. Other configurations for the field of view can be selected to study edge-wise and twisting mode shapes which are not in the scope of this study (Fig. 12.3).

The red rectangles show the selected sub-videos for motion processing and extracting the natural frequencies. The green rectangle shows the person on the boom lift while impacting the tip of the wind turbine blade. The sequence of images are captured and the processed using the aforementioned phase-based motion-processing framework.

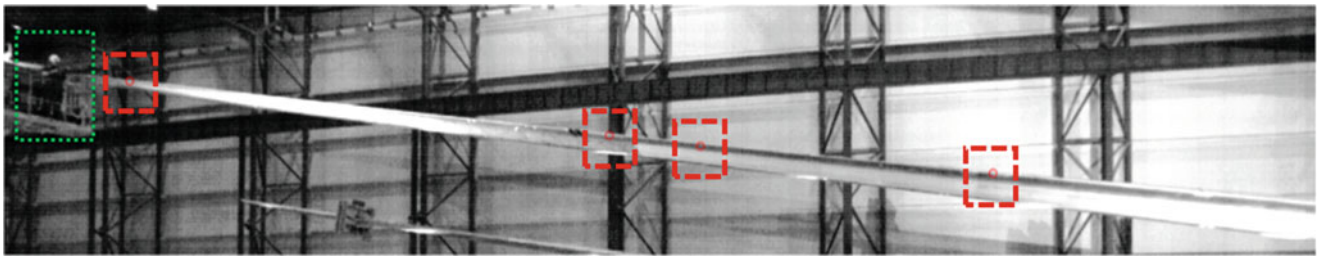

Fig. 12.3 The field of view of the camera along with the excitation location (green box) and the measurement locations (red boxes)

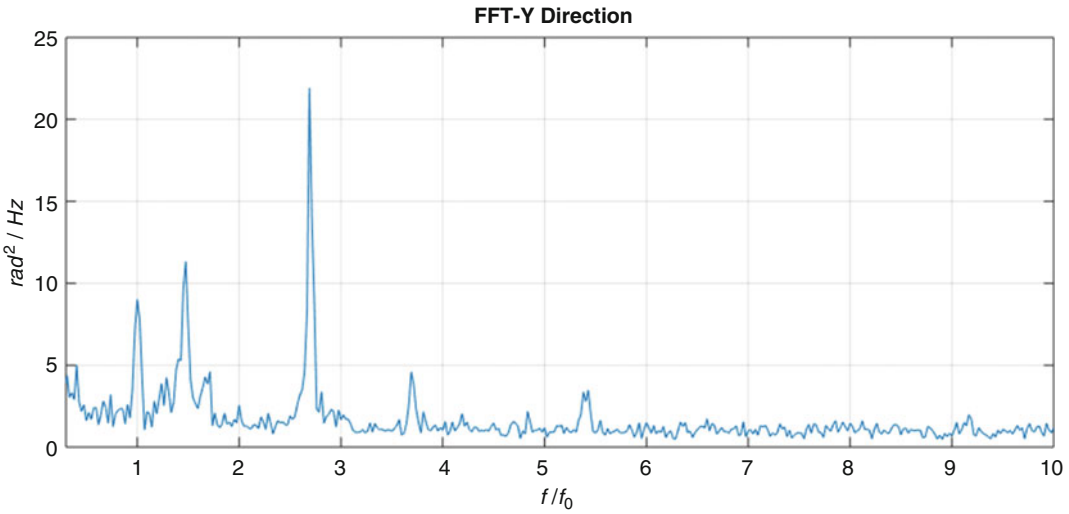

Fig. 12.4 Average FFT of the motion in the four selected sub-videos

12.4 Results and Discussion

Within this section the results of the analysis for the large scale wind turbine blade is presented. After applying the phase-based motion estimation on the captured sequence of images the FTT of the extracted phase variations are computed. A simple peak picking technique on the spectrum of the response can provide an approximation of the natural frequencies of the structure. The frequency axis of the figure is normalized to the lowest natural frequency to maintain confidentiality.

As Fig. 12.4 shows there are a few resonant frequencies identified for the wind turbine blade. However, it is unclear which peaks correspond to which mode. In order to solve this problem without actually performing a full modal test on the structure, phase-based motion magnification has been utilized. The captured video of the vibrating wind turbine blade has been processed at specific frequency bands with the resonant frequency of the wind turbine blade selected as the center frequency of the band-pass filter, and several motion-magnified videos have been obtained. Analyzing the motion pattern in the motion-magnified video can reveal the correspondence to the structural natural frequencies.

In order to process the motion magnified videos in a systematic manner two frames of the motion magnified video at two of its maximum deflection positions with 180 degree phase difference are overlapped. The two frames are color coded as red and green. Therefore, the overlapping areas of the two frames will appear in yellow (Figs. 12.5, 12.6, and 12.7).

Considering Figs. 12.5, 12.6, and 12.7 and the prior knowledge of approximate mode shape, the correspondence between the natural frequencies and the mode shapes can be obtained without performing a rigorous and time consuming modal test. It should be highlighted that prior knowledge regarding the dynamics of this type of structure is straightforward for structural engineers. For example for the second flap-wise bending mode occurrence of one node is anticipated which is clear in Fig. 12.6, and for the third flap-wise bending mode two nodes should be visible in the visual perception of the mode shape. Having an intuition regarding the approximate shape of the first, second and third flap-wise bending mode shapes of the wind turbine blade is very intuitive for the engineers working in the wind turbine blade industry. The frequency and mode shape correspondence is shown in Fig. 12.8. (Note: The edge-wise bending (orange box), correspondence cannot be achieved from this analysis and it has been shown only for the reference).

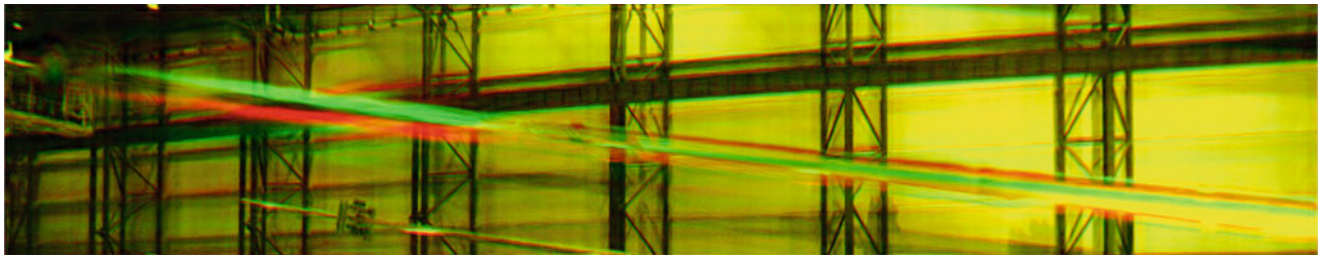

Fig. 12.5 First flap-wise bending mode-selected; frequency ratio for band-pass filtering is 1

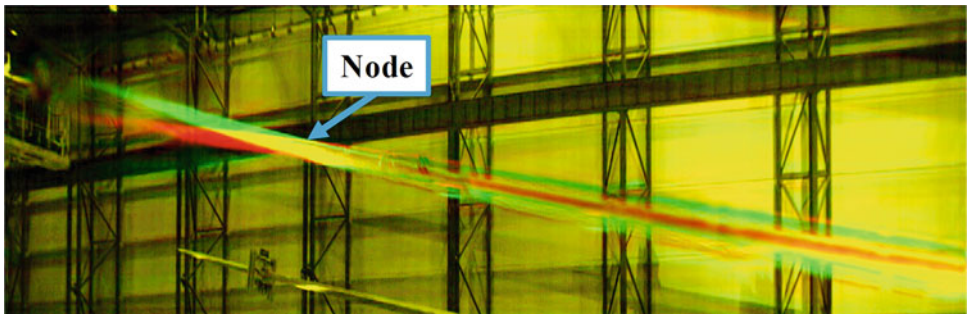

Fig. 12.6 Second flap-wise bending mode-selected; frequency ratio for band-pass filtering is 2.69

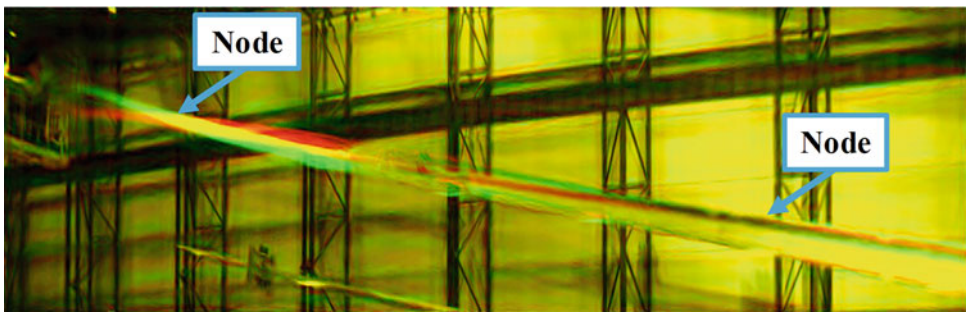

Fig. 12.7 Third flap-wise bending mode-selected; frequency ratio for band-pass filtering is 3.69

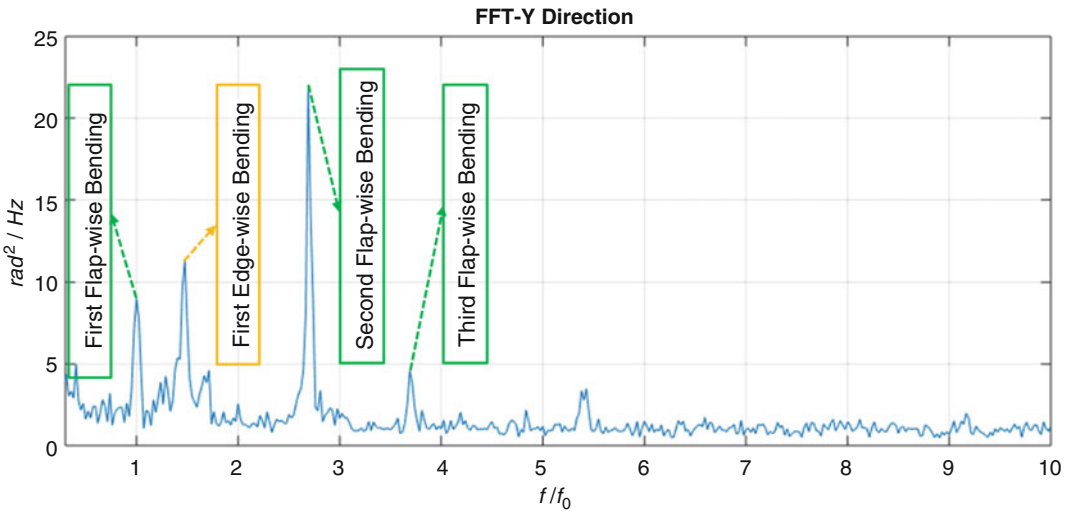

Fig. 12.8 Natural frequency and mode shape correspondence

12.5 Conclusion

Structural dynamics identification can be performed with several levels of detail. The extreme case is obtaining all the modal parameters including natural frequencies, mode shapes and damping ratios. However, based on the application and the requirements, which are provided by the standards, several pieces of information from modal analysis can be neglected. Therefore, other methods should be considered to perform the modal testing partially to avoid labor intensive and time-consuming process compared to a full modal test. Within this paper, a specific case has been studied in which only the natural frequencies and the correspondence of natural frequencies to the mode shapes are required. It has been shown that the natural frequency and mode shape correspondence can be achieved from motion-magnified videos as the visual perception of the mode shapes. Using motion magnification enables the engineers to detect which frequency corresponds to which mode shape without performing a full modal test. This approach can save a lot of time and energy and reduce the cost of certification procedure for large-scale structures such as utility scale wind turbine blades. Moreover, the approach is non-contact and full-field measurement and therefore the testing time can be reduced to just a few seconds (about 40 s). For now, the method has been only studied on the flap-wise bending mode shapes. For future study edge-wise and twisting mode shapes can be studied as well, to better understand the proposed partial modal identification frame work.

References

1. Reynders, E.: System identification methods for (operational) modal analysis: review and comparison. Arch. Comput. Meth. Eng. **19**, 51–124 (2012)
2. Ewins, D.J.: Modal Testing: Theory and Practice, vol. 15. Research Studies Press, Letchworth (1984)
3. Baqersad, J., Poozesh, P., Niezrecki, C., Avitabile, P.: Photogrammetry and optical methods in structural dynamics–a review. Mech. Syst. Signal Process. **86**, 17–34 (2016)
4. Castellini, P., Martarelli, M., Tomasini, E.P.: Laser Doppler Vibrometry: development of advanced solutions answering to technology's needs. Mech. Syst. Signal Process. **20**, 1265–1285 (2006)
5. Baqersad, J., Niezrecki, C., Avitabile, P.: Extracting full-field dynamic strain on a wind turbine rotor subjected to arbitrary excitations using 3D point tracking and a modal expansion technique. J. Sound Vib. **352**, 16–29 (2015)
6. Poozesh, P., Baqersad, J., Niezrecki, C., Avitabile, P., Harvey, E., Yarala, R.: Large-area photogrammetry based testing of wind turbine blades. Mech. Syst. Signal Process. **86**, 98–115 (2016)
7. Ebrahimkhanlou, A., Farhidzadeh, A., Salamone, S.: Multifractal analysis of two-dimensional images for damage assessment of reinforced concrete structures. In: SPIE Smart Structures and Materials+ Nondestructive Evaluation and Health Monitoring, pp. 94351A–94351A-8. SPIE 2015 proceedings, San Diego- California (2015)
8. Ebrahimkhanlou, A., Farhidzadeh, A., Salamone, S.: Multifractal analysis of crack patterns in reinforced concrete shear walls. Struct. Health Monit. **15**, 81–92 (2016)
9. Baqersad, M., Hamedi, A., Mohammadafzali, M., Ali, H.: Asphalt mixture segregation detection: digital image processing approach. Adv. Mater. Sci. Eng. **2017**, (2017)
10. Xie, X., Zeng, D., Li. J., Dahl, J., Zhao, Q., Yang, L.: Tensile test for polymer plastics with extreme large elongation using quad-camera digital image correlation. SAE Technical Paper 0148-7191 (2016)
11. Wadhwa, N., Rubinstein, M., Durand, F., Freeman, W.T.: Phase-based video motion processing. ACM Trans. Graph. (TOG). **32**, 80 (2013)
12. Wadhwa, N., Rubinstein, M., Durand, F., Freeman, W.T.: Riesz pyramids for fast phase-based video magnification, ed: US Patent 9,338,331 (2016)
13. Wadhwa, N., Wu, H.-Y., Davis, A., Rubinstein, M., Shih, E., Mysore, G.J., et al.: Eulerian video magnification and analysis. Commun. ACM. **60**, 87–95 (2016)
14. Fleet, D., Weiss, Y.: Optical Flow Estimation. In: Paragios, N., Chen, Y., Faugeras, O. (eds) Handbook of Mathematical Models in Computer Vision. Springer, Boston, MA (2006)
15. Javh, J., Slavič, J., Boltežar, M.: The subpixel resolution of optical-flow-based modal analysis. Mech. Syst. Signal Process. **88**, 89–99 (2017)
16. Sarrafi, A., Poozesh, P., Mao, Z.: A comparison of computer-vision-based structural dynamics characterizations. In: Model Validation and Uncertainty Quantification, vol. 3, pp. 295–301. Springer, Cham (2017)
17. Freeman, W.T., Adelson, E.H.: The design and use of steerable filters. IEEE Trans. Pattern Anal. Mach. Intell. **13**, 891–906 (1991)
18. Chen, J.G., Wadhwa, N., Cha, Y.-J., Durand, F., Freeman, W.T., Buyukozturk, O.: Modal identification of simple structures with high-speed video using motion magnification. J. Sound Vib. **345**, 58–71 (2015)
19. Poozesh, P., Sarrafi, A., Mao, Z., Avitabile, P., Niezrecki, C.: Feasibility of extracting operating shapes using phase-based motion magnification technique and stereo-photogrammetry. J. Sound Vib. **407**, 350–366 (2017)
20. Sarrafi, A., Poozesh, P., Niezrecki, C., Mao, Z.: Mode extraction on wind turbine blades via phase-based video motion estimation. In: SPIE Smart Structures and Materials+ Nondestructive Evaluation and Health Monitoring, pp. 101710E–101710E-12. SPIE 2017 proceedings, Portland-Oregon (2017)

Chapter 13
Relating Vibration and Thermal Losses Using the Damping Heat Coefficient

Marko Mihalec, Janko Slavič, Jaka Javh, Filippo Cianetti, Michele Moretti, Gianluca Rossi, and Miha Boltežar

Abstract Damping of vibrating systems converts the vibrational energy into other forms, such as heat and sound radiation. Heating of the material is often assumed to be one of the biggest drains of energy; however, it is very hard to experimentally identify how much of the damped energy is converted to heat. This manuscript introduces the damping heat coefficient and via high-speed cameras (optical and thermal) identifies that, for the selected material, approximatelly 30% of the damped energy is converted to heat.

Keywords Damping · Heat · Temperature · Image processing

Damping is a phenomenon present in every real vibrating system. It is a common name for different mechanisms, which dissipate the energy of a vibrating structure by converting it into other forms [1]. Most often, the energy gets dissipated in form of acoustic radiation and heat [2]. This work focuses on the part of the damping, which transforms the vibrational energy into thermal energy and causes change in temperature.

This work builds on theoretical derivation starting with Kelvin-Voigt viscous material model [3] and applying it to the Euler-Bernoulli beam. For such a beam, strain energy density at any position can be written as a function of flexural rigidity EI and the second derivative of an observed modal shape $\phi(x)$ [4].

$$W(x) = \frac{1}{2} EI \left(\frac{\partial^2 \phi}{\partial x^2} \right)^2 \tag{13.1}$$

Damping transforms a portion of mechanical energy into thermal energy, so the spatial distribution of thermal energy should be the similar to the spatial distribution of strain energy given in Eq. (13.1). That means that given a beam's operational deflection shape it is shown that the temperature increase due to the damping is expected to be the highest near surface and on locations where the curvature of the beam is the highest i.e. locations where the absolute value of $\partial^2\phi/\partial x^2$ is the largest.

In order to relate damping to the dissipations in the form of thermal energy, the energy of an entire vibrating beam can be researched concerning the temperature increase at the surface. The amount of energy that gets dissipated in each cycle at a location along the beam can be calculated from Eq. (13.1) using the damping ratio δ.

$$\Delta W(x) = \delta EI \left(\frac{\partial^2 \phi}{\partial x^2} \right)^2 \tag{13.2}$$

Equation (13.2) gives us the amount of energy which gets dissipated by damping at each point on the beam. Some of the energy gets transformed to acoustic radiation while the other part gets transformed to heat. To describe the ratio between those two drains of energy, damping heat coefficient r has been introduced [5]. Damping heat coefficient is a ratio between the energy that gets converted into heat and the total energy lost due to damping. By using this damping heat coefficient it is possible to theoretically predict the temperature increase of a structure, given only the material properties and the damping ratio.

M. Mihalec · J. Slavič (✉) · J. Javh · M. Boltežar
Faculty of Mechanical Engineering, University of Ljubljana, Ljubljana, Slovenia
e-mail: janko.slavic@fs.uni-lj.si

F. Cianetti · M. Moretti · G. Rossi
University of Perugia, Perugia, Italy

C. Niezrecki, J. Baqersad (eds.), *Structural Health Monitoring, Photogrammetry & DIC, Volume 6*,
Conference Proceedings of the Society for Experimental Mechanics Series, https://doi.org/10.1007/978-3-319-74476-6_13

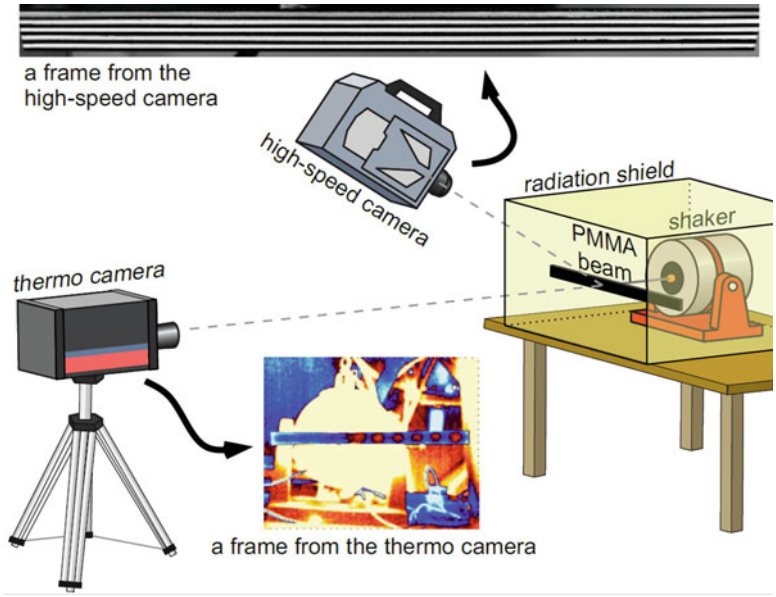

Fig. 13.1 Experimental setup

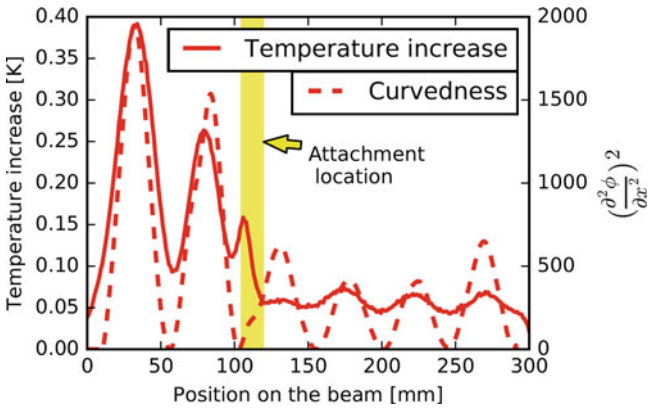

Fig. 13.2 Curvedness and temperature increase on different points on the beam

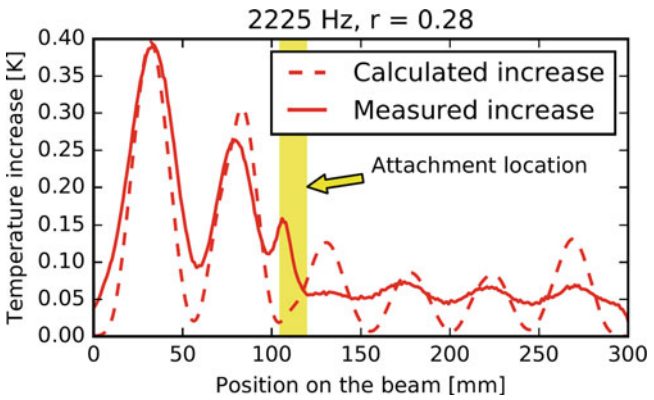

Fig. 13.3 Theoretical and experimental temperature increase

$$\Delta T(x) = \frac{r\delta EI}{c\, m_u}\left(\frac{\partial^2 \phi}{\partial x^2}\right)^2 \tag{13.3}$$

Theoretical relations can be confirmed by measuring the temperature increases of a vibrating structure with a known damping ratio. Such measurements can be challenging because the temperature increases are on the order of hundreds of a Kelvin. The correctness of the derivations is confirmed by experimental data, gathered with high precision near infrared thermal camera and a high speed camera for measuring deflections using procedures described in [6].

Experiments have been conducted using a 300 mm long beam made of PMMA, excited near its resonance frequency. Figure 13.1 shows the experimental setup. Plastic beam is preferable because of its high damping ratio and low temperature capacity and thermal conductivity, but due to its viscoelastic properties, complex modal shapes have to be taken into account when calculating the curvature.

Data shows that the temperature increase measured experimentally coincides well with the predicted increase, both in terms of location as well as in terms of total temperature increases, which is evident from Figs. 13.2 and 13.3 respectively.

References

1. Nashif, A.D., Jones, D.I., Henderson, J.P.: Vibration Damping. Wiley, New York (1985)
2. Puškár, A.: Internal Friction of Materials. Cambridge International Science Publishing, Cambridge (2001)
3. Solecki, R., Conant, R.J.: Advanced Mechanics of Materials. Oxford University Press on Demand, London (2003)
4. Sazonov, E., Klinkhachorn, P.: Optimal spatial sampling interval for damage detection by curvature or strain energy mode shapes. J. Sound Vib. **285**, 783–801 (2005)
5. Mihalec, M., Javh, J., Cianetti, F., Moretti, M., Rossi, G., Slavič, J., Boltežar, M.: Damping heat coefficient – theoretical and experimental research on a vibrating beam. J. Sound Vib. **400**, 13–21 (2017)
6. Javh, J., Slavič, J., Boltežar, M.: The subpixel resolution of optical-flowbased modal analysis. Mech. Syst. Signal Process. **88**, 89–99 (2017)

Chapter 14
Predicting Geometric Tolerance Thresholds in a Five-Axis Machining Centre

T. Rooker, N. Dervilis, J. Stammers, K. Worden, P. Hammond, G. Potts, T. Brown, and K. Kerrigan

Abstract NC-Checker is a software tool used for monitoring and validating the geometric performance in modern machining centres. Threshold settings allow the Manufacturing or Maintenance Engineer to customise the tool based on specific job or industry tolerance requirements. In order to perform effective long-term monitoring, this has the potential to skew the perceived health state of the machining centre as presented in the NC-Checker benchmark reports. This study brings attention to this fact and its relevance in the pursuit of enhanced levels of automation for geometric performance monitoring tools, in preparation for the machine shop's transition to Industry 4.0. A sense-check function is proposed to identify unusual alterations based on historical data, utilising a support vector machine methodology to develop a predictive classifier. The models achieved predictive accuracy scores of 87.5% during validation, acquisition of a suitable testing set is under way and the predictive models will be evaluated upon completion.

Keywords Support vector machine · In-process inspection · CNC machining · Geometric performance · Condition monitoring

14.1 Introduction

Enhancing production through intelligent automation is becoming increasingly important in the advanced manufacturing sector, driven in-part by recent advances in the *Industry 4.0* movement, with its fundamental requirement for data and analytics as a core capability [1]. Of the four design principles set out for implementing Industry 4.0 [2], the two which this research will consider relate to information transparency – analysing the physical system through means of on-line data collection – and providing technical assistance to the Manufacturing or Maintenance Engineer. Application of machine learning to the performance monitoring and optimisation of machining centres provides a unique opportunity to fulfil these principles.

NC-Checker [3] is a software tool developed by metrology software products ltd., for data collection and benchmarking of geometric performance in CNC machining centres. It runs a series of probing cycles on a datum point of a sphere within the machine volume, revealing the errors inherent in the system. It is then possible to compare these errors against both nominal positions and the typical operational conditions, using this data to assess the likelihood of quality part production but also to track any changes in geometric performance over time. Herein, *geometric performance* refers specifically to the level of component error present in the system, as identified in the NC-Checker analysis process, and affecting finished part quality. Due to a variety of error sources [4] present in machining operations, it is not possible to guarantee identical geometric performance at all times, and it is observed that geometric performance tends to drift over time. As such, machining centres undergo regular maintenance to ensure they are performing within the acceptable tolerances.

One key functionality of NC-Checker is the ability to set threshold limits on each tested parameter, providing the operator with a simple system to determine whether the machining centre is in a satisfactory state for operation or not. This is facilitated by the production of a *benchmark report*, the resultant output of the NC-Checker performance monitoring procedure. Generally, the ability to edit these thresholds is restricted to the Manufacturing or Maintenance Engineer and is

T. Rooker (✉) · N. Dervilis · K. Worden
Dynamics Research Group, Department of Mechanical Engineering, University of Sheffield, Sheffield, UK
e-mail: tjrooker1@sheffield.ac.uk

J. Stammers · K. Kerrigan
AMRC with Boeing, Advanced Manufacturing Park, Catcliffe, Rotherham, UK

P. Hammond · G. Potts · T. Brown
Metrology Software Products Ltd., Alnwick, UK

C. Niezrecki, J. Baqersad (eds.), *Structural Health Monitoring, Photogrammetry & DIC, Volume 6*,
Conference Proceedings of the Society for Experimental Mechanics Series, https://doi.org/10.1007/978-3-319-74476-6_14

determined by the required precision of the part in current production. Through interference with the tolerance thresholds, there is the possibility of distorting the actual health state of the machining centre as perceived in the benchmark report. This can have implications for finished part quality if the operator is using NC-Checker as a go/no-go system, as is often the application of the software tool. In order to achieve effective monitoring of machining centre geometric performance with this system, it is pertinent to explore the issue.

An approach to the geometric performance monitoring of five-axis machining centres, utilising NC-Checker as a data acquisition system, is introduced in this paper. Consideration is given to the phenomenon of *threshold bias* (see Sect. 14.2.4) as an immediate application of the research. More holistically, the prospect of automating the fault diagnostic and prognostic processes are discussed, with the greater objective of informing a condition-based maintenance strategy via the synergy of on-line inspection data with contemporary machine learning paradigms.

This paper is structured as follows. Section 14.2 describes the methodology of the study, covering firstly the data collection technique, then the concerns of threshold bias and construction of the predictive models. Section 14.3 describes and presents the results of the support vector machine classifiers. Section 14.4 then discusses these results, the issues outlined in the paper and sets out the prospect for further research.

14.2 Methodology

14.2.1 Data Acquisition

A large gantry head-head five-axis machining centre was investigated in this study. A number of different options were explored in the selection process, but this particular operation was selected due to the high consistency of the data collection being carried out by the team responsible. At the time of contact, six months of legacy data were available, collected at roughly one-week intervals with minimal deviations from this schedule. The individual tests carried out had all been performed and recorded in their entirety, which was a crucial prerequisite for the data analysis procedure.

There are a number of operational factors to consider with respect to the selected machining centre, which have implications for the presented results and comparability with industrial examples. These are described below.

14.2.1.1 Research Environment

Based in a primarily research environment, the studied machining centre does not generally follow the same operational patterns as would be seen with similar systems in industry. Of most concern are trials involving the testing of tools to destruction, which is the primary research application of the machining centre. This involves introducing sustained and excessive levels of force to the system, which is unlikely to occur in an industrial setting under normal conditions. The fatigue process for structural components under loading is well documented [5], and the same principles will apply to the machining centre's structural loop under excessive loading conditions. Thus, the research environment has potential to exacerbate errors incurred in the system, increasing the risk of operational problems such as mechanical breakdown or extensive maintenance requirements.

Due to the relatively small dataset available, this conversely presents some benefit to the study. More extreme variability in the data can be attributed to amplification of the geometric performance deterioration, in essence enhancing the meaningfulness of each measurement in the limited dataset. This characteristic of the data provides worthwhile insight into the machining centre's geometric performance, and is sufficient for preliminary investigations and objectives of the study at this point in the research. Clearly, though, the preference is for an extensive set with a high resolution of data points relative to the observable trends, which will be sought as a priority for future developments of the work.

14.2.1.2 Known Calibration Issues

Throughout the acquisition period of the legacy data, it was apparent to the operator that there were a number of problems with the machining centre requiring extensive maintenance activity. A later investigation, with support from the equipment supplier, diagnosed the issue as a faulty component located in the machine's structural loop, and the issue was rectified. Recent corrections have improved the performance of the machining centre significantly. For the dataset currently applied in this study, however, the fault is still present, and manifests itself in a pronounced effect on the accuracy of the rotary C axis. This is apparent in the results of the benchmark reports, where the measured deviation is observed to be consistently and abnormally higher than the pre-set tolerances.

Throughout the collection period and until the issue was diagnosed, the operational team took a pragmatic approach and continued research whilst applying ongoing maintenance actions to maintain the usability of their machining centre. This was acceptable practice as the trials conducted over the collection period were not adversely affected by the machining centre's geometric performance. As they were distinctly aware of the issue affecting the rotary C axis (see Sect. 14.2.2 for an explanation of the machining centre axes) and monitoring it regularly, they chose to halt updates to the tolerance threshold. This has implications for the analysis methodology employed in this study, and adjustments to compensate are discussed further in Sect. 14.2.3.

14.2.1.3 Extreme Alterations to the Tolerance Thresholds

Due to the calibration issues described above, and the inconsistent mode of application required in a research – as compared to production – environment, the machining centre has undergone a programme of maintenance to correct and enhance its operability. Part of this programme involved extensive alterations to the tolerance thresholds that are saved in NC-Checker and used to determine the pass/fail aspect of the report. Although it must be noted that regular threshold alterations like this are uncommon in industry, it raises a point of interest for exploration, discussion and advice where the practice has the possibility to occur.

14.2.2 The Benchmark Wheel

The standard presentation of the report produced by NC-Checker is the *benchmark wheel*, an example of which can be seen in Fig. 14.1. The wheel is interactive and provides the option to click through individual results, visualised as spokes on the wheel, for detailed reports and data. Each spoke represents an independent feature which directly affects the geometric performance, thus the feature is defined as a measurement of error in a particular aspect of the machining centre. Key features of interest to this study are the probe performance in the linear X, Y and Z axes, and the machine five-axis performance in the rotary C axis. These influence the cutting tool's movements within the machine volume. Probe performance quantifies the ability of the probe to measure accurately in the three linear axes, whilst the machine five-axis performance defines the maximum error incurred when re-orienting the tool relative to the part in the specified rotary axis. The ability to provide rotation in two axes, in addition to the linear movements, is the requirement for a machining centre to be regarded as having five-axis capabilities. Rotary axes are denoted as A, B and C, with the axis of rotation being parallel to the linear X, Y and Z axes, respectively. The position on the spoke indicates the extent of deviation from a given feature's nominal position, always located at 0.0000. Tolerance thresholds are set by the Manufacturing or Maintenance Engineer and provide maximum (always positive) and minimum (can be negative or 0.0000, depending on the test) limits. Should a measurement exceed its tolerance threshold, the software will notify the operator and indicate that the machining centre has failed the geometric performance test, often requiring attention before the operation is permitted to proceed.

14.2.3 Pre-processing

As this study currently represents the initial investigation phase of the overall research project, only the data included on the benchmark wheel was extracted and stored for analysis. This approach allowed the research to present an alternative visualisation procedure to the *trend analysis* tool that comes as part of the NC-Checker package. Contained within the benchmark reports, however, is a much more extensive dataset which will be incorporated into the analysis at a later stage. This provides the opportunity for future expansion of the research, using the methodologies established in this study as the foundation. In particular, incorporating expert knowledge on the report characteristics to pattern recognition tools has promising potential for developing an automated fault diagnosis system, which the research team will will be explored in the near-future.

Damage classifications were assigned to each of the data points. The output of a given parameter is considered a *fail* if the measured value exceeds the engineer-determined threshold *for that particular test instance*; in such a case, the data point receives a classification of damage, encoded as a value of one. Similarly, an output which does not exceed the threshold is considered a *pass*; these data points receive a classification of healthy, encoded as a value of zero.

Here, it is important to again note the effect on the rotary C axis measurements caused by the faulty component, as previously discussed in Sect. 14.2.1.2. A practical solution was employed involving maintaining awareness of the issue,

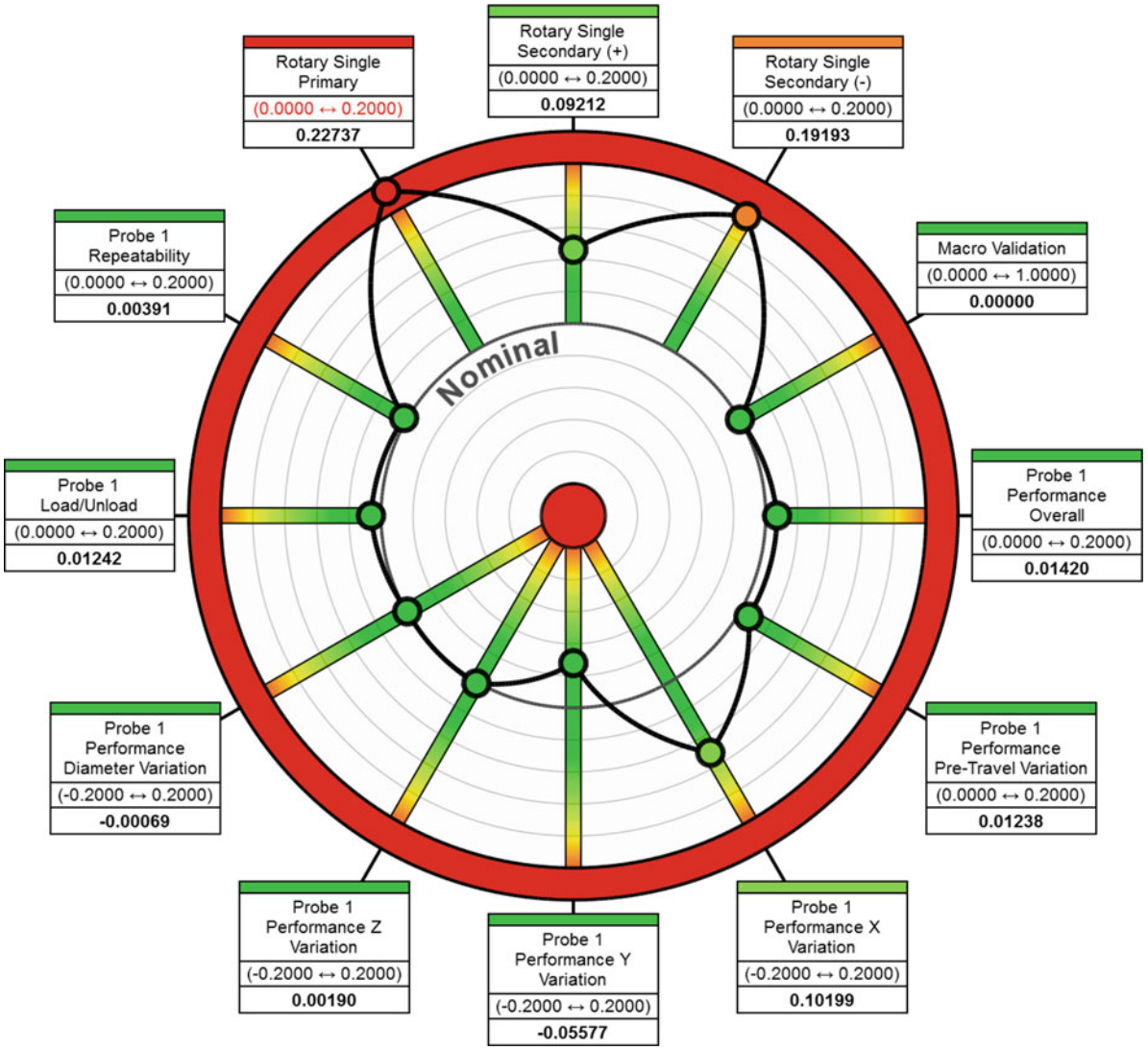

Fig. 14.1 Benchmark report presentation of data used in this study

though in the raw data it is simply presented as persistent failure. As the damage classes have been assigned based on thresholds determined by engineering judgement, this characteristic of the data collection must be considered and accounted for. An amendment was added to raise the threshold for this parameter by 20%, which, given the circumstances, provides a more realistic representation for the operator's judgement of an acceptable limit. It should be noted that this value was estimated based on the point at which the operating team ceased amendments to the tolerance thresholds, and the time-series trend entered the perceived period of stability as observed in Fig. 14.2. Thus, the reader should be aware of a level of uncertainty introduced to the analysis from this action.

14.2.4 Time-Series Graphical Representation

Visualisation of the data as a time-series provides an insight into the effects of altering the tolerance threshold, and the skew it can impart on the perception of the data. Figure 14.2 shows the geometric performance as a function of the tolerance threshold set by engineering judgement. Performance values above 1 indicate a parametric failure in the benchmark report. From this graphical representation, it would not be unreasonable to deduce that the machining centre appears faulty in the months of July and August, but subsequent corrections then led to an extended period of generally stable, healthy operation. From this point, the linear axes plateau close to their nominal positions and the rotary C axis maintains its position around a performance value of 1.

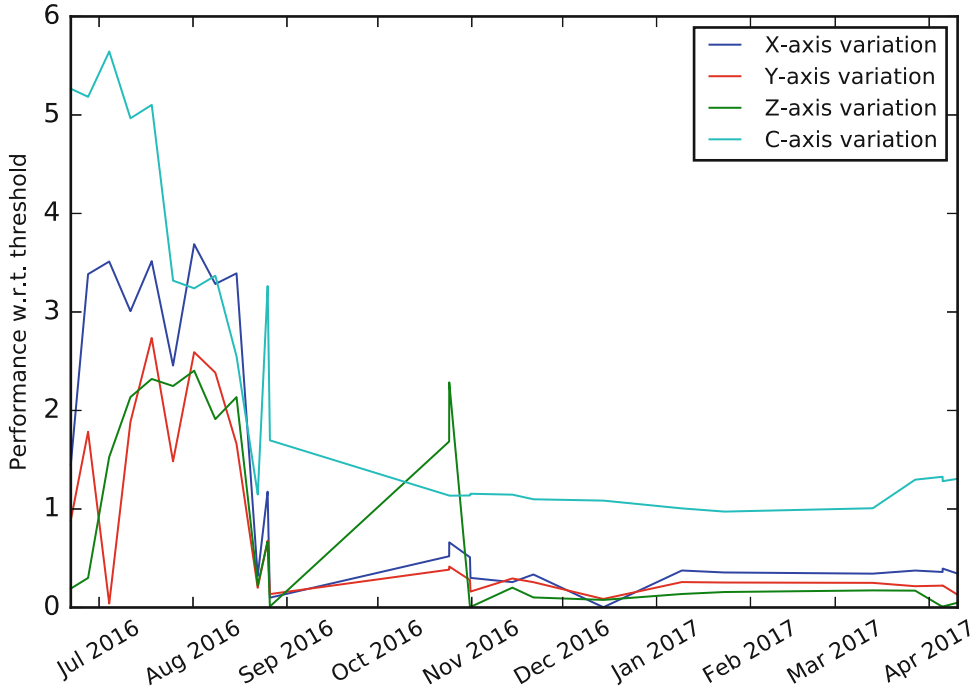

Fig. 14.2 Geometric performance variation over time, as a function of tolerance threshold

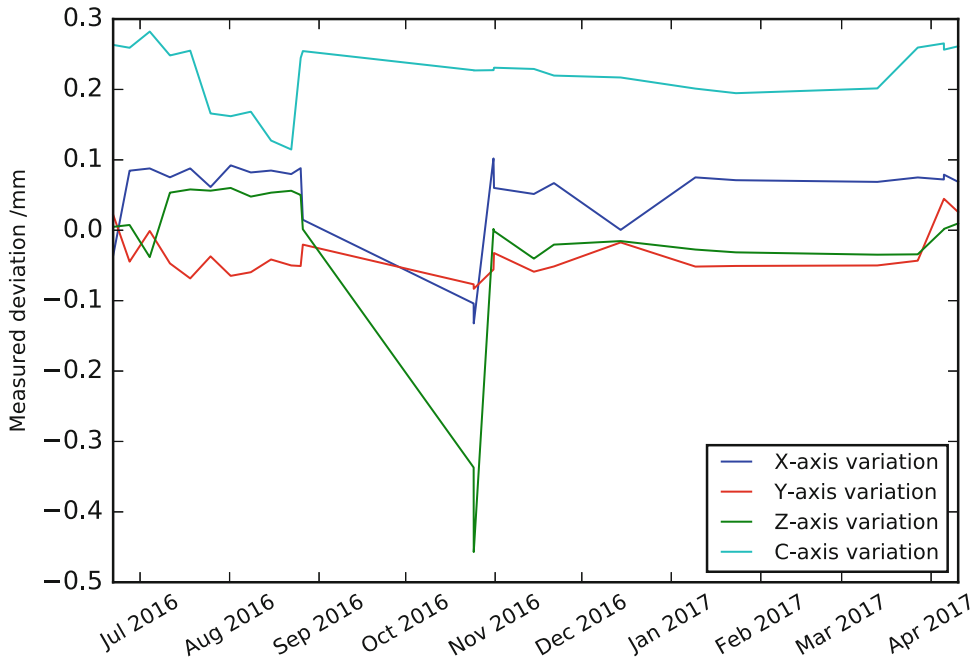

Fig. 14.3 Geometric performance variation over time, absolute measured values

However, different observations are made by comparing these trends with the actual, measured deviations as shown in Fig. 14.3. In the Y axis probe performance, for example, it can be seen that the absolute, measured deviations have a relatively low level of variance throughout the data collection period as a whole. This contrasts sharply with the performance indicated in Fig. 14.2, where there is a clear shift from perceived unacceptable levels in July and August to acceptable in the months that follow. This characteristic is largely apparent in all of the axes, whereby Fig. 14.2 suggests significant performance improvements but similar trends are not observable in the absolute, measure values as seen in Fig. 14.3.

This effect on the graphical representation is caused by the inherently variable nature of the tolerance thresholds. Consider, for example, the C axis deviations as captured in early August, in comparison with those captured in mid November. Figure 14.2 presents considerable failure in August with a performance value of 3.24 and a much more acceptable value of 1.15 in November, suggesting the geometric performance has improved over time. Seen in Fig. 14.3, the absolute, measured deviation for August is 0.16 mm, but in November is 0.23 mm. In absolute terms, then, the interpretation is that geometric performance has worsened.

This contradiction of geometric performance induced by variable tolerance thresholds and human interaction – the phenomenon of threshold bias – is the basis for the argument of this paper. Although it must again be noted that this is not necessarily a common practice in an industrial setting, altering the tolerance thresholds can lead to skewed perceptions of the machine health state which machining centre operators and engineers should be aware of. Moreover, it is a characteristic of the data which must be considered in future research with the intention of increasing levels of automated monitoring. There is no standard threshold setting that is relevant for all parts. For example, parts produced for aerospace applications may require stricter tolerances than those produced for the automotive industry, or indeed certain parts within the same industry may be more critical than others. The intricacy is that the tolerance thresholds must be included to consider the absolute measurements meaningful; ultimately though, it is the absolute measurements alone which provide the necessary information for effective and proper monitoring of overall geometric performance.

14.2.5 Modelling

Four parameters were selected from the dataset for analysis in this study, concerning the measured deviations in probe performance in the X, Y, and Z axes and measured deviations in rotary axis C (representing the rotation potential about the linear Z-axis). Rotary axis A was omitted from this study due to a number of missing data points, which would have adversely affected the analysis and data continuity in the study. The data were split into two sets, one comparing probe X with probe Y and the other probe Z with rotary C, conducted to allow visualisation and direct parametric comparison. Class labels were assigned to all data points, as described in Sect. 14.2.3. The data points were randomly shuffled and split by a three-fold cross validation with stratified sampling, for homegeneity and to ensure adequete representation of the training data [6]. Due to the relatively small dataset, a Bayesian optimisation procedure may be more appropriate for this problem, permitting the use of all training examples for both model fitting and comparison [7]. It must be noted that, for evaluating and confirming the model's predictive capability, an independent test set will always be required, and caution should be exercised with this approach to avoid the possibility of overfitting. This is an element for exploration in further research from this paper and has not been considered at this stage. The training set was then fed into a support vector machine (SVM) for predictive classification, including an optimisation step for the model hyperparameters C (soft margin parameter) and γ (kernel length scale) [8]. Following this, the model score was evaluated against the validation set and discarded if it did not meet a specified minimum threshold of 80% correct classifications. This process was repeated until representative models were found, both X vs. Y and Z vs. C achieving scores of 87.5% correctly classified data points.

14.3 Results

Figures 14.4 and 14.5 present the models to predict the likely classification of a measured data point, based on past events as determined by engineering judgement. Modifications to the engineer-determined thresholds for acceptable performance are represented by the coloured rectangles; whilst the black decision boundary separates the two classification regions predicted by the SVM. Data points for the measured values are visually separated into + and o markers, for a benchmark pass and fail respectively. Note that some measured values with a classification of 'pass' in Fig. 14.5 exceed the maximum engineer-determined threshold. This is the due to the permitted increase in C axis tolerance threshold, discussed in Sect. 14.2.3. A value at the nominal location [0, 0] was also included in the training sets, based on the knowledge that this value will always be deemed acceptable by engineering judgement.

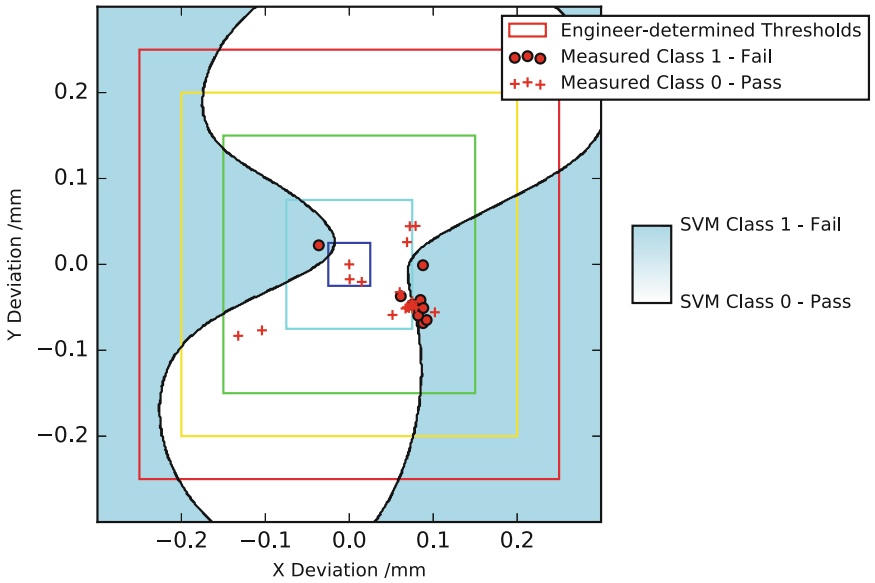

Fig. 14.4 Predictive classification of parametric health states, comparing linear X and Y axes

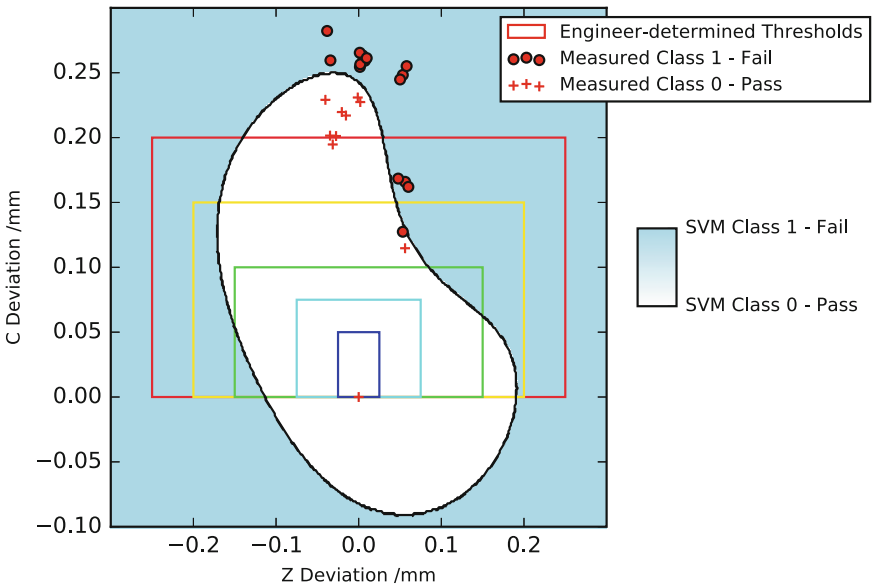

Fig. 14.5 Predictive classification of parametric health states, comparing linear Z and rotary C axes

14.4 Discussion and Further Research

From the analysis, it is reasonable to deduce that modifications to the threshold values can skew perceptions of the machining centre health state. In Fig. 14.4, a cluster of measured data points classified by the engineer as ‘failed‘ is observed, interspersed with three further ‘pass‘-classified data points. The actual operation as observed at these data points is near-identical with respect to the probe performance in the X and Y axes, so in the context of overall machining centre performance it would be more sensible to be grouped into a single class. Furthermore, it would be logical to assume that a tight cluster of data points represents a stable operating condition, as all parts produced in these states are subject to similar conditions.

Clearly, deviation from nominal geometry is of the highest importance when assessing machining centre performance; however, it is also worth considering the stability of the system and the effects that this can have on finished part quality. Figure 14.5 shows a consistent grouping of data points with just one outlier; however, in Fig. 14.4 the data points classified as ‘pass‘ show considerable dispersion. Again, this weakens the argument for relying on engineer-determined thresholds for monitoring the overall system performance.

The SVM models can be used to predict the classification of future measured data points as determined by engineering judgement. Due to applications-based problems out of the researchers' control, a dedicated set of testing data was not available at the time of writing. This will be sought and used to evaluate model performance in the near-future. As abnormal classifications could lead to a reduction in finished part quality and be difficult to interpret at a human level, it is hypothesised that this will have benefits in informing the threshold-setting requirement through automatic identification. The approach provides a means of sense-checking the threshold-setting procedure and the potential for optimising the tolerance requirements based on individual machine-specific characteristics, minimising the requirement for calibration and subsequent machine downtime.

Further to this, the establishment of models describing the normal operating condition of the machining centre is highly relevant to the development of an automated fault diagnostic and prognostic tool. With respect to this objective, the critical aspect raised in this paper is that of threshold bias. As geometric performance monitoring does not entirely conform to the traditional formulation of a damage detection problem, classifications in the training data must be derived from, at least in some part, an engineer's interaction with the system. The primary source of this information is in the legacy data threshold settings. In order to develop an effective monitoring tool, it is imperative to ensure these inputs accurately reflect the genuine health state of the machining centre, and are not adversely affected by threshold bias.

Acknowledgements

1. metrology software products ltd.
   Contribution to research conception, ongoing support and provision of software for data acquisition.

References

1. Reinhard, G., Jesper, V., Stefan, S.: Industry 4.0: building the digital enterprise. In: 2016 Global Industry 4.0 Survey, vol. 1, no. 1, pp. 1–39 (2016)
2. Hermann, M., Pentek, T., Otto, B.: Design principles for industrie 4.0 scenarios. In: Proceedings of the Annual Hawaii International Conference on System Sciences, vol. 1, no. 1, pp. 3928–3937 (2016)
3. Hammond, P., Brown, T.: NC-Checker – metrology software products ltd. [Online]. Available: http://metsoftpro.com/nc-checker/ (2015)
4. Schwenke, H., Knapp, W., Haitjema, H., Weckenmann, A., Schmitt, R., Delbressine, F.: Geometric error measurement and compensation of machines-an update. CIRP Ann. Manuf. Technol. **57**(2), 660–675 (2008)
5. Hahn, G., Iyer, K., Rubin, C.: Fatigue of shear joints, ch. 4,. In: Structural Shear Joints: Analyses, Properties and Design for Repeat Loading, pp. 67–86. ASME, Three Park Avenue New York (2005)
6. May, R.J., Maier, H.R., Dandy, G.C.: Data splitting for artificial neural networks using SOM-based stratified sampling. In: Neural Netw. **23**(2), 283–294 (2010)
7. MacKay, D.J.C.: Information theory, inference, and learning algorithms. Cambridge University Press, Cambridge (2003)
8. Cristianini, N., Shawe-Taylor, J.: An introduction to support vector machines: and other kernel-based learning methods. Cambridge University Press, Cambridge (2000)

Chapter 15
Light Field Imaging of Three-Dimensional Structural Dynamics

Benjamin Chesebrough, Sudeep Dasari, Andre Green, Yongchao Yang, Charles R. Farrar, and David Mascareñas

Abstract Real world structures, such as bridges and skyscrapers, are often subjected to dynamic loading and changing environments. It seems prudent to measure high resolution vibration data, in order to perform accurate damage detection and to validate and update the models and knowledge about the operating structure (aka finite element models). Many existing vibration measurement methods could be either low resolution (e.g., accelerometers or strain gauges), and time and labor consuming to deploy in field (e.g., laser interferometry). Previous work by Yang et al. has shown that low-cost regular digital video cameras enhanced by advanced computer vision and machine learning algorithms can extract very high resolution dynamic information about the structure and perform damage detection at novel scales in an relatively efficient and unsupervised manner. More interestingly this work used a machine learning pipeline that made minimal assumptions about lighting conditions or the nature of the structure in order to perform modal decomposition. The technique is currently limited to two dimensions if only one digital video camera is used. This paper uses light field imagers - a new camera system that captures the direction light entered the camera - to make depth measurements of scenes and extend the modal analysis technique proposed in Yang et al. to three dimensions. The new method is verified experimentally on vibrating cantilever beams with out of plane vibration, whose full-field modal parameters are extracted from the light field measurements. The experimental results are discussed and some limitations are pointed out for future work.

Keywords 3D Structural Dynamics · Modal Analysis · Photogrammetry · Blind Source Separation · Light field imaging

15.1 Introduction

Engineering structures and systems are complex, and could exhibit local dynamics behaviors. It is essential to measure the dynamic responses of the structure at multi-dimensional, high resolution. However, it is a significant challenge using such traditional techniques as accelerometers, strain-gauges, and laser vibrometers. Photogrammetry using digital video cameras is a relatively low-cost alternative providing non-contact, high spatial resolution, simultaneous, measurements. In this paper we propose a novel method of extracting modal information using a single-point light-field imager capable of capturing three-dimensional data at a single time. We discuss the calibration process and application of machine learning techniques we used to extract modal shapes from dynamic structures.

B. Chesebrough
Mechanical Engineering, New Mexico Institute of Mining and Technology, Socorro, NM, USA
e-mail: benjamin.chesebrough@student.nmt

S. Dasari
Electrical Engineering and Computer Science, University of California: Berkeley, Berkeley, CA, USA
e-mail: sdasari@berkeley.edu

A. Green
Computer Science, University of New Mexico, Albuquerque, NM, USA
e-mail: awg@unm.edu

Y. Yang (✉) · C. R. Farrar · D. Mascareñas
Los Alamos National Lab – Engineering Institute, Los Alamos, NM, USA
e-mail: yyang@lanl.gov; farrar@lanl.gov; dmascarenas@lanl.gov

C. Niezrecki, J. Baqersad (eds.), *Structural Health Monitoring, Photogrammetry & DIC, Volume 6*,
Conference Proceedings of the Society for Experimental Mechanics Series, https://doi.org/10.1007/978-3-319-74476-6_15

15.1.1 Modal Analysis with Unconstrained Video

Yang et al. [4] developed a technique to decompose unconstrained video streams of vibrating structures into separate modes at full pixel resolution. The decomposition provided high-resolution information of the vibrating structure that allowed for: verification of finite element models, fine scale damage detection, and reconstruction of the object's individual modes. The technique first passed video through a multi-scale pyramid that encoded motion as the phase response of the filter. These phase values were fed into an unsupervised machine learning pipeline, that first performed dimensionality reduction with PCA and extracted modes using the complexity pursuit algorithm. Unfortunately, a single traditional camera cannot sense depth, which means out of plane modal information is currently out of reach of the algorithm unless multiple cameras are sued. This project's goal is to extend this technique to three dimensions with the use of a single light field camera.

15.1.2 Raytrix Depth Camera Architecture

Light field cameras (also known as plenoptic cameras) are much like other digital cameras but with one crucial modification – a MicroLens Array (MLA) is placed in between the camera's sensor and main lens. This modification allows the light field camera to recover the direction light entered the camera. This added information allows for sundry interesting applications like computational refocusing of images after they have been taken. Loosely speaking, each individual lens in the MLA refocuses light so that the pixels under the lens capture the direction in which light rays passing through the microlens' spatial location enter the camera. Since the interior of a camera has no occlusions each light ray can be parameterized with four dimensions; two of which are provided by the microlens' spatial position, and two directional dimensions provided by the pixels under the microlens. For additional reading on plenoptic cameras refer to Ren Ng's thesis [2].

The Raytrix camera has a relatively unique design that differentiates it from other light field cameras. The Raytrix is a so called "focused" plenoptic camera, which means the MLA is interpreted as being focused on the main lens' imaging plane. As a result, the pixels under each microlens capture overlapping slices of the main image. This allows for higher resolution final image reconstruction, but directional information is now spread across multiple microlenses. Such 'focused' plenoptic cameras are originally proposed by Lumsdaine and Georgiev [1], and in Perwaß and Wietzke [3] the specific optical capabilities of the Raytrix camera are derived.

$$\frac{1}{f} = \frac{1}{i} + \frac{1}{o} \tag{15.1}$$

The Raytrix camera architecture allows for depth calculation by computing pairwise correspondences of the images captured under each microlens. First, let us define a few terms. Object distance – o – is the distance away from the object the main lens is, and image distance – i – is the distance from the main lens (opposite from object side) that the focused image forms. They are related by the thin-lens equation (above) (Eq. 15.1).

Virtual depth – v– is a linear function of image depth and other hardware characteristics of the camera (). The architecture of the Raytrix camera allows for prediction of an object's virtual depth. Figure 15.1 shows how different light rays from the same object would enter the camera, and terminate at the imaging plane of a camera. In a normal camera the direction of the light rays is lost and depth is irrecoverable, but in the Raytrix camera the light rays are focused by different MicroLenses. As a result, the same point is recorded in multiple microlens images, and thanks to similar triangles one could use the ratio of relative shifts of this recorded point to the distance between microlens centers to calculate virtual depth (ratio of image depth to separation of sensor from MLA). In other words:

$$v = \frac{i}{B} = \frac{d}{p_x} \tag{15.2}$$

where: d is the distance between micro-lens centers, and $p_x$is the relative differences between the object's location in each microlens (from figure $p_{x1} - p_{x2}$).

This relationship is the foundation of our implemented depth algorithm. The derivation of these equations and further reading on this topic can be found in Zeller et al. [5].

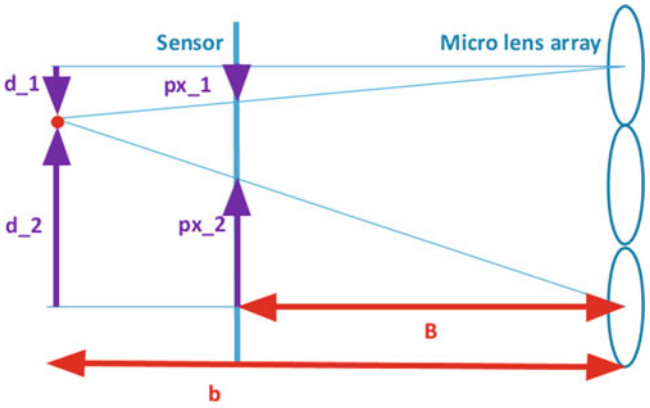

Fig. 15.1 Light enters from the main lens (not pictured) and is focused by micro = lens array onto sensor. In a normal camera the sensor would be placed further back and depth would be lost

15.2 Implementation Details

15.2.1 Overview

Much of the processing pipeline for the depth algorithm was developed in house. There are two distinct phases: first images are captured by the Raytrix camera and point-clouds of the scene are created, and second the point clouds are processed to extract modal information. The above flowchart shows the general pipeline.

15.2.2 Depth Algorithm

The depth algorithm uses the unique optical architecture of the Raytrix camera to calculate depth of objects in the field of view. On a broad level the pipeline works as follows; images are grabbed from the camera, individual microlenses are extracted from raw data, depth is calculated by finding correspondences in micro-lens images, a point-cloud is outputted for modal decomposition.

The specific camera used was a Raytrix R5 camera with specifications as follows: a 2048 by 2048 monochrome digital sensor, 102 by 88 MLA, capability for video capture up to 180 FPS. Unfortunately, much of the camera's out of the box software was non-functional; therefore we built a new processing pipeline. While the data from a light-field camera certainly has to be processed differently, each frame from it is just a normal image (refer to Fig. 15.2) and can be handled accordingly. In our case light field recordings were taken by interfacing the Raytrix camera with a frame grabber, which provided a stream of frames from the camera. The video sequence was saved frame by frame as a sequence of PNG files.

Raw images from the Raytrix camera look like raw images from any other camera sensor, except the micro-lens array positioned in front of the sensor is clearly visible. The next step is to detect the individual micro-lenses, and determine the optical characteristics of the sensor. To assist in this process a series of "whiteshot" images were taken by imaging white light sources while a white-light filter was attached to the end of the camera lens (pictured in Fig. 15.3). Individual microlenses appear as circular regions in the whiteshot. In order to extract them, the whiteshot is first eroded, and then thresholded and filtered. The microlenses now look like white circles, whose centers can be calculated by first passing the image through an edge detector and then computing the centroids of the detected edge contours. These center points give rough estimates of the centers of the microlens, but the estimate is too noisy to use on its own. Thankfully, the Raytrix camera's MLA is laid out in a hexagonal grid pattern, so a simple averaging scheme can be used to find the parameters of the grid. The process from white-shot to hexagonal grid is shown pictorially in Fig. 15.4. Now that the microlens centers are computed, the images formed by each micro-lens can be extracted, optionally white-balanced, and then used for computation later on in the pipeline.

Now that micro-lenses are extracted, calculating depth begins. The goal is to find correspondences between the micro-lens images to estimate parallax, and from there calculate virtual-depth and eventually object depth. Our technique draws heavy

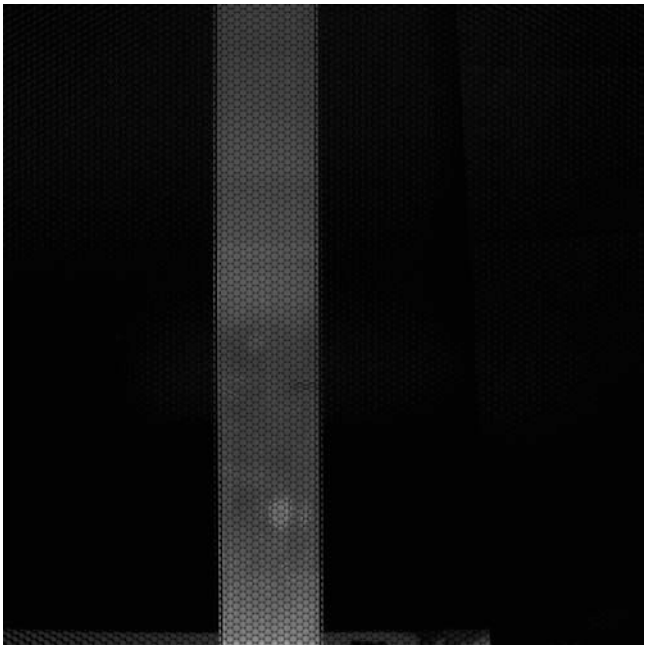

Fig. 15.2 Raw data from the Raytrix Camera

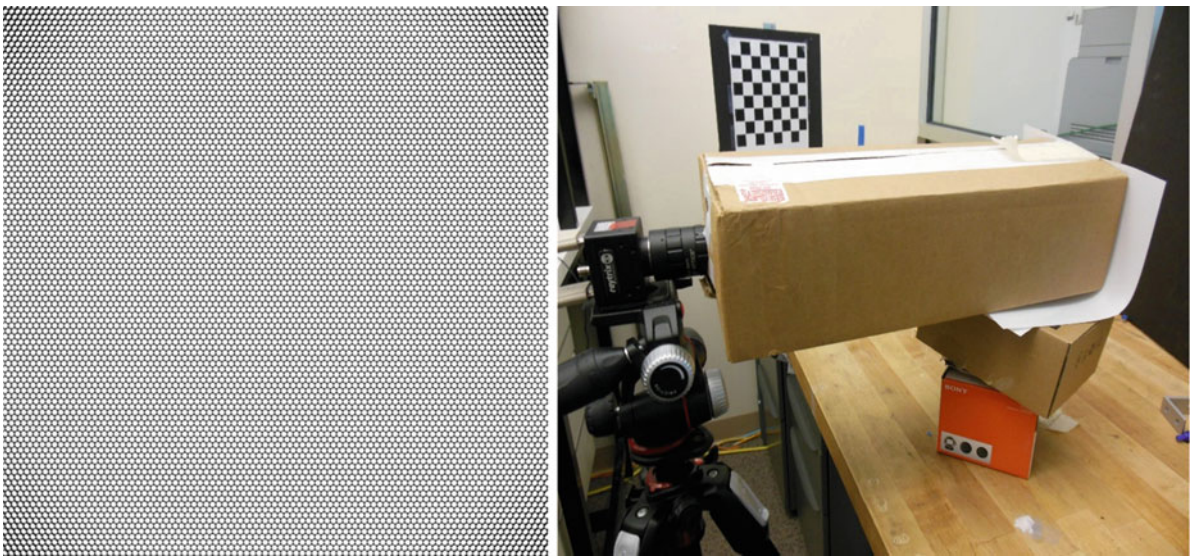

Fig. 15.3 Sample white-shot image and the cardboard setup used to take it

inspiration from the work presented in Zeller et al., but a few modifications were added to repurpose the algorithm for our goals. Specifically, most of the images taken of structures contain edges, so our algorithm specifically attempts to find the same edges in neighboring microlenses.

Virtual depth is a function of image depth (how far image forms from main lens). Once image depth is computed the thin-lens equation (Eq. 15.1) can be used to convert to real world distance from lens (aka depth). Similar to Zeller et al. our technique uses linear regression to estimate the conversion between virtual depth and image depth. After virtual depths are converted to object depths, a point cloud of the scene is outputted. This point cloud encodes the position of various points of the scene, and processing it is the next step to extracting modal information.

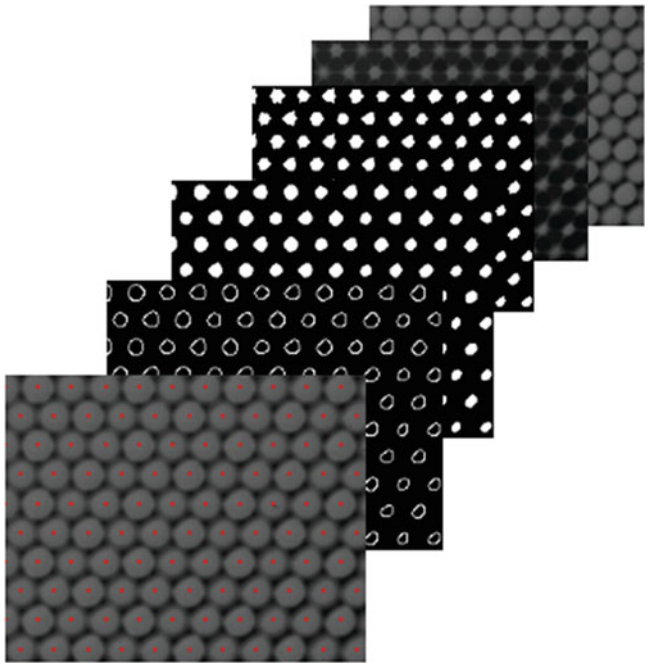

Fig. 15.4 Computer vision pipeline to extract microlenses from white-shot. The images are eroded, thresholded, and filtered, before being passed into an edge detector. Circle centers are detected from the edges, and an average grid is fit

15.2.3 Point-Cloud Processing

The partially populated grid of depth estimates is binned into a coarse, user-defined two-dimensional grid extruded on its z-axis, wherein the set of estimates encapsulated within each region are averaged so as to produce a constant-size vector for use in PCA.

For modal spectral analysis of the structure, we bin all points into a one-dimensional grid extruded along the x-z plane, windowed along y; this simple discretization averaged along the horizontal proved acceptable in our limited testing on a beam experiencing no deformation over the x direction. We perform Fourier analysis on each section so as to ascertain the dominant frequency for that region.

15.3 Results

Experiments were conducted by exciting a cantilever beam so that it vibrated out of plane with respect to the camera's field of view. Above is a picture of the experimental setup, as well as structural response time histories and spectra obtained by exciting the beam and measuring its response with three accelerometers. The out-of-plane motion proved to be irrecoverable using the standard video based decomposition work proposed earlier by Yang et al., because depth is irrecoverable with only one traditional camera. Our project's goal was to extract even out of plane motion with a single Raytrix Camera (Fig. 15.5).

After collecting and processing the light field measurement data on this cantilever beam, out-of-plane motion, the detected frequency (10.26 Hz) is shown to be accurate within 2% of the measurement reported by an accelerometers affixed to the measured structure (10.13 Hz) in the same region. These results are summarized in Fig. 15.6.

In another test (Fig. 15.7), both the first mode and what is presumed to be the aliased second mode are recovered. Note that the real second mode is recorded at 65 HZ, but our camera could only capture at 55 HZ. While the second 20 HZ peak in the recorded data does not line up with an aliased 65 HZ mode captured at 55 FPS, there seems to be a telltale beating pattern in the middle graph where both peaks are apparent. Certainly, more investigation of this phenomena is needed.

Further, combining the depth extraction process proposed within this paper and the BSS/CP technique designed by Yang et al., we algorithmically constructed an amplification matrix for the first mode, which through element-wise multiplication over the collections of depth maps constructed for each frame of the video serves to visually amplify the dominant motion

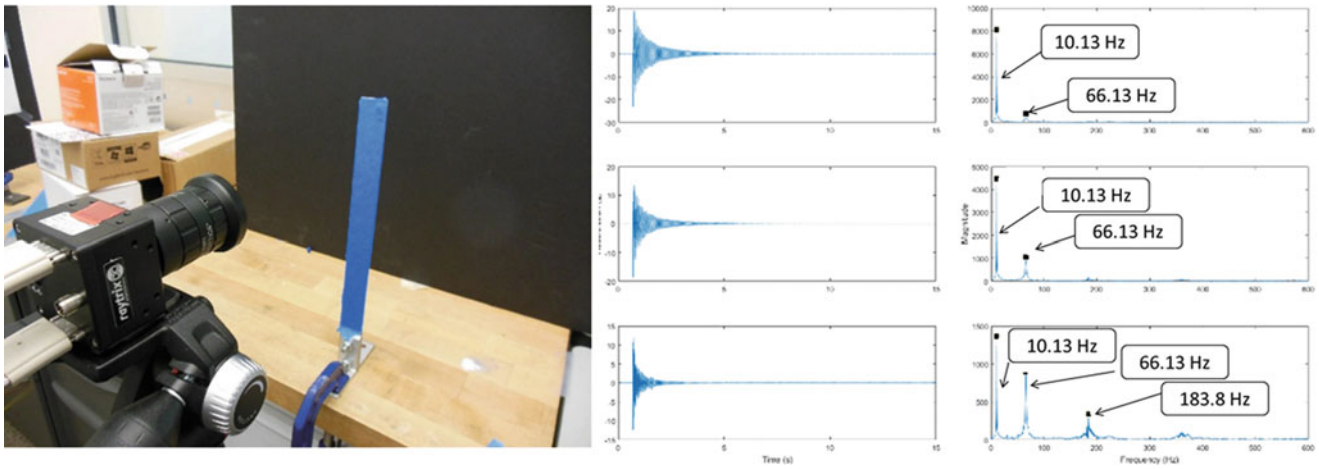

Fig. 15.5 Experimental setup and plot of time/frequency of 10 Hz cantilever beam (measured by accelerometer)

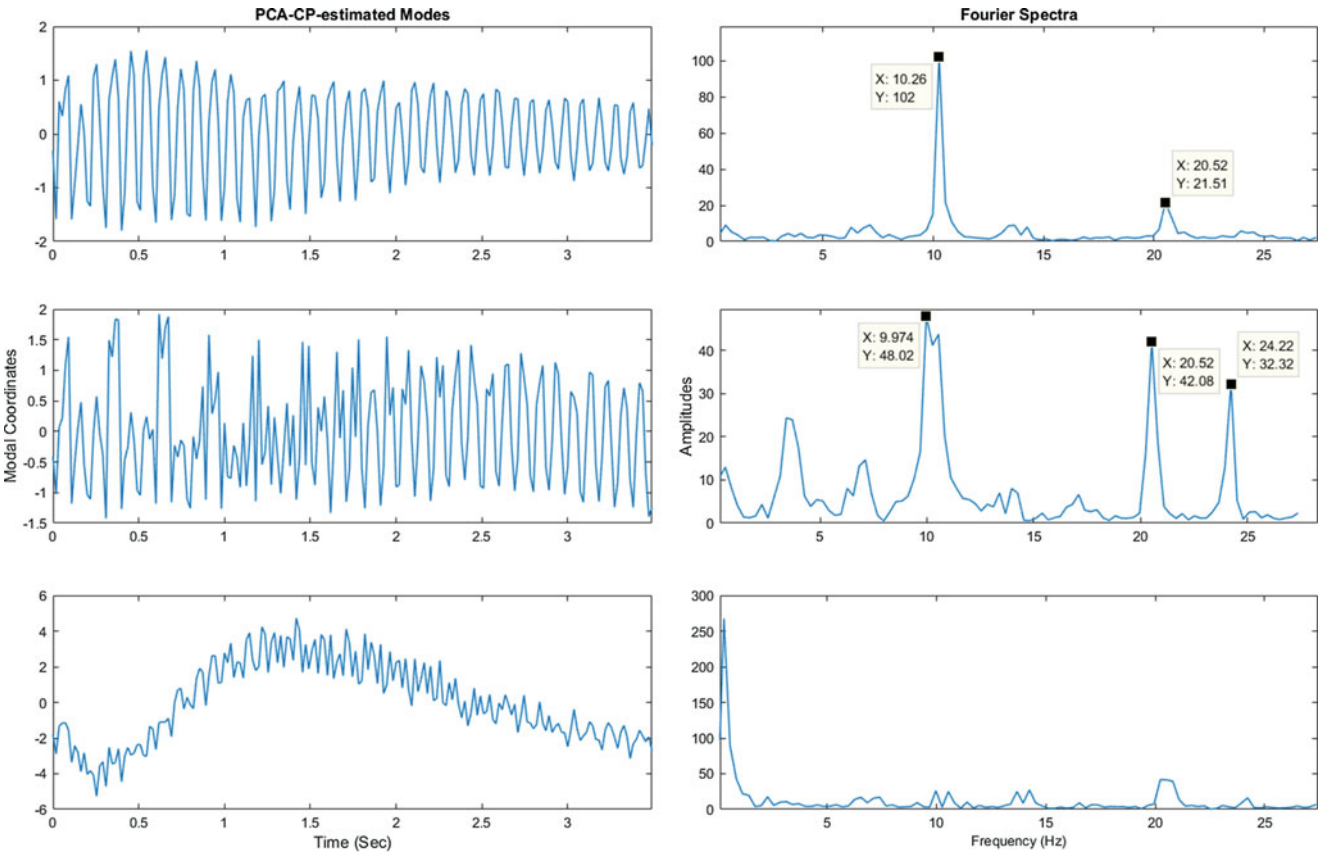

Fig. 15.6 Modal harmonics and frequencies as predicted by blind source separation technique, using light field footage of 10 Hz cantilever beam (pictured above) vibrating

of the first mode. This serves both as a check that the principal component extracted by BSS/CP has physical meaning and as an intuitive method for visualizing the dominant frequencies present in a dynamic structure. Below is a reconstruction of the first mode. The points are from the real data, and a blue line is drawn to assist with visualizing the beam's outline. The behavior of the first mode over time seems to be in line with the physics of a cantilever beam, even though real life depth measurements are quite noisy and the point-clouds are very hard to visualize in an interpretable manner. For future work improved algorithms may be developed to handle the noisy measurements better (Fig. 15.8).

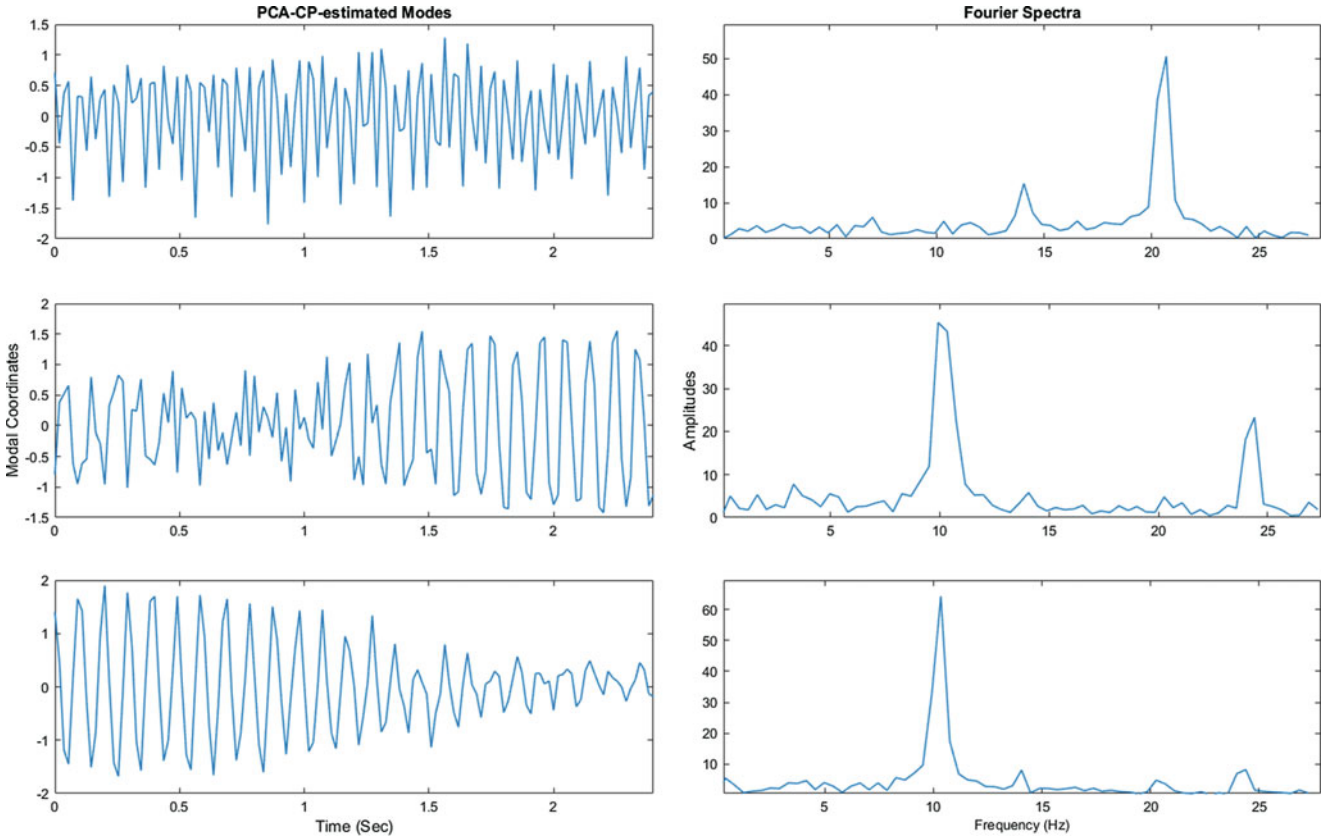

Fig. 15.7 Modal decomposition from experimentally collected light field data using blind source technique. Note the harmonics of the first mode are captured quite well. In the middle plot beating harmonics along with the first and aliased second mode are seemingly observed. Note the frequency spike for the second mode is incorrect

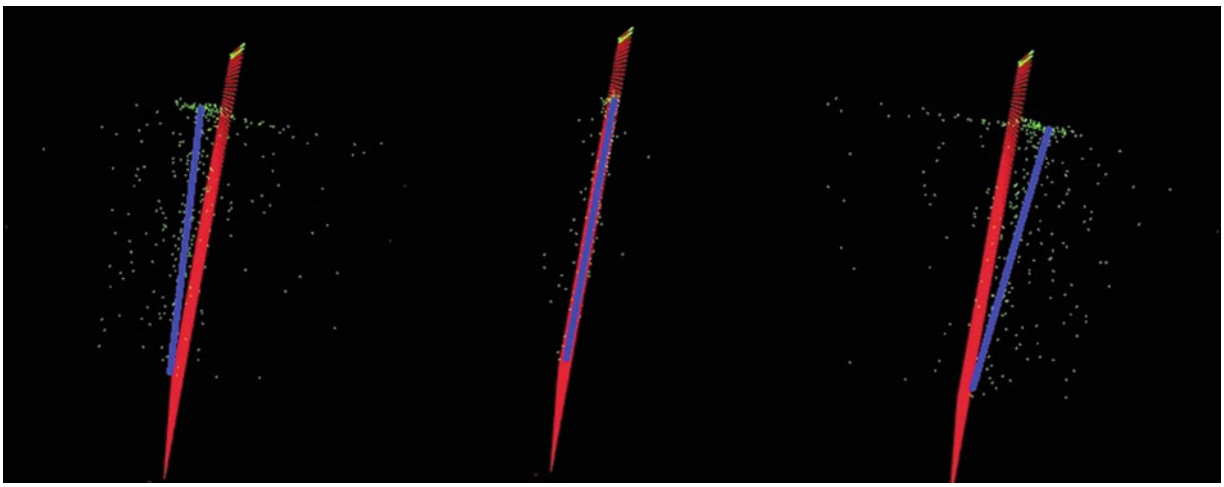

Fig. 15.8 Reconstruction of first mode shape. The average point cloud grid is multiplied element-wise with the generated amplification matrix for the extracted first mode. The point motion (highlighted by blue line) appear in line with expectations for a beam's first mode. More investigation and better visualization of these results is needed

15.4 Conclusions

15.4.1 Discussion

This work explores the application of light field imaging technology to extract three-dimensional structural dynamic information. A depth algorithm and out of plane motion extraction pipeline were developed and tested experimentally. In these tests modal frequency information was extracted, as well as the mode shape of the cantilever beam's first mode with reasonable accuracy.

One challenge is that the provided software for calibration, balancing, and finding depth using the light-field imager was insufficiently supported on the platforms we used. In future we anticipate the developer-built software for reconstructing depth maps will provide greater accuracy and so allows us to further improve upon the work presented in this paper. It would be especially useful to quantify the performance of the depth algorithm with respect to our use case. After all, the noise in the depth measurements is not ignorable - indeed it is quite substantial at times. Additional research on the topic would be required to take this into account. As light field technology becomes more mature, exploring its application will hopefully become more fruitful.

Intrinsic to the nature of the set of point clouds we obtain from the light field imager is the variable number of points in each cloud; although we were able to bin and average these points and obtain useful results, doing so necessarily required exchanging granularity for precision. Although more precise baseline depth estimates would allow for finer granularity and may readily come as usage of light-field imagers and accompanying depth-estimation algorithms becomes more widespread, an approach built about variably sized input would perhaps provide a more faithful representation of the 3-D structure's dynamics.

15.4.2 Promising Results

Having successfully extracted accurate frequency information on and reasonably accurate first mode shape of a simple dynamic structure without many presuppositions nor any models fit to the structure, we believe the technique presented to be more broadly adaptable to more varied structures to attain quantitative and qualitative measures of structural health. Although spectral glare remains a challenge for the imaging device, there exists ongoing research working to address this; as such, we believe that a genuinely non-invasive approach is possible as the technology matures. Overall, this work shreds light on establishing high resolution 3D structural dynamics using the emerging light field imagers.

References

1. Lumsdaine, A., Georgiev, T.: The focused plenoptic camera. IEEE. 1–8, San Francisco, CA (2009)
2. Ng, R.: Digital Light Field Photography. Stanford University (2006). https://www.sciencedirect.com/science/article/pii/S0924271616300508
3. Perwaß, C., Wietzke, L.: Single lens 3D–camera with extended depth-of-field. Proc. SPIE. 8291. 4-. 10.1117/12.909882. (2012). https://www.researchgate.net/publication/258713151_Single_Lens_3D-Camera_with_Extended_Depth-of-Field
4. Yang, Y., et al.: Blind identification of full-field vibration modes from video measurements with phase-based video motion magnification. Mech. Syst. Signal Process. **85**, 567–590 (2017)
5. Zeller, N., Quint, F., Stilla, U.: Depth estimation and camera calibration of a focused plenoptic camera for visual odometry. ISPRS J. Photogramm. Remote Sens. **118**, 83–100 (2016)

Chapter 16
Adaptive Observers for Structural Health Monitoring of High-Rate, Time-Varying Dynamic Systems

B. S. Joyce, J. Hong, J. C. Dodson, J. C. Wolfson, and S. Laflamme

Abstract Safe and reliable operation of hypersonic aircraft, space structures, advanced weapon systems, and other high-rate dynamic systems depends on advances in state estimators and damage detection algorithms. High-rate dynamic systems have rapidly changing input forces, rate-dependent and time-varying structural parameters, and uncertainties in material and structural properties. While current structural health monitoring (SHM) techniques can assess damage on the order of seconds to minutes, complex high-rate structures require SHM methods that detect, locate, and quantify damage or changes in the structure's configuration on the microsecond timescale.

This paper discusses the importance of microsecond structural health monitoring (μSHM) and some of the challenges that occur in development and implementation. Two model-based parameter estimators are examined for estimating the states and parameters of an example time-varying system consisting of a two degree of freedom system with a sudden change in a stiffness value that simulates structural damage. The ability of these estimators to track this stiffness change, the role of measurement noise, and the need for persistent excitation are examined.

Keywords Time-varying systems · Structural health monitoring · SHM · Damage detection · High-rate state estimation · Adaptive observer

16.1 Introduction

There are high-rate dynamic systems, such as hypersonic aircraft, space structures, and advanced weapon systems [1, 2], that experience uncertain and rapidly changing input forces, nonlinearities, time-varying structural parameters, and uncertainties in material and structural parameters. Due to the high rates of change in these systems, damage can quickly propagate through a structure and lead to severe loss of functionally [3, 4]. In order for damage prognosis and mitigation strategies to have enough time to react to a system change, structural health monitoring (SHM) that can detect, locate, and quantify system changes on microsecond timescales is needed.

Researchers are currently developing techniques for microsecond structural health monitoring (μSHM). Some methods under investigation utilize electromagnetic impedance-based methods to detect damage [5]. Other methods utilize adaptive neural-networks to describe the changing dynamics of a system before and after damage [6, 7]. These techniques are able to quickly detect changes in system configuration, but their data-driven nature makes it difficult to link changes in the measured response to a change in a specific system parameter. Therefore adaptive, model-based observers are needed to calculate system parameters and create a useful model for damage prognosis or feedback control schemes. Model-based techniques have been applied previously to civil structures for detecting damage [8–10], however parameter convergence rates in the microsecond to millisecond timescales have not yet been demonstrated with these methods.

B. S. Joyce (✉)
University of Dayton Research Institute (UDRI), Eglin AFB, FL, USA
e-mail: bryan.joyce@udri.udayton.edu

J. Hong
Applied Research Associates (ARA), Niceville, FL, USA

J. C. Dodson · J. C. Wolfson
Air Force Research Laboratory Fuzes Branch (AFRL/RWMF), Eglin AFB, FL, USA

S. Laflamme
Iowa State University, Ames, IA, USA

C. Niezrecki, J. Baqersad (eds.), *Structural Health Monitoring, Photogrammetry & DIC, Volume 6*,
Conference Proceedings of the Society for Experimental Mechanics Series, https://doi.org/10.1007/978-3-319-74476-6_16

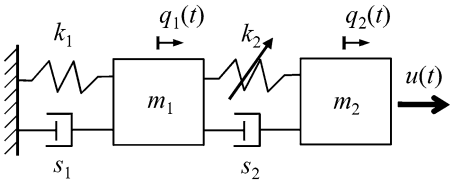

Fig. 16.1 Diagram of a two degree of freedom system with a changing stiffness k_2

This paper investigates the behavior of an example, time-varying system consisting of two masses connected by a spring and damper. The connecting spring undergoes a change in stiffness a few milliseconds into the simulation. Two parameter estimators are examined to estimate this stiffness. The first is a recursive least squares method with a forgetting factor that is based on full state feedback and knowledge of the mass and damping values. This estimator illustrates some of the challenges arising from these time-varying systems, such as the influence of noise, the tradeoff between robustness to noise and convergence speed, and the need for persistently exciting inputs. Next the system states and parameters are estimated using an extended Kalman filter with a forgetting factor. Simulation results show the benefits of using a forgetting factor and ensuring persistent excitation.

16.2 Example: Two Degree of Freedom System

An example system is created to demonstrate the issues that arise when estimating parameters in rapidly-changing system with noisy measurements. Consider the two degree of freedom system shown in Fig. 16.1. The system consists of two connected masses (m_1 and m_2) with displacements $q_1(t)$ and $q_2(t)$. The first mass is connected to a rigid ground with a stiffness k_1 and damper s_1. Connecting the two masses is a damper with a damping coefficient of s_2 and a spring with a time-varying spring stiffness of $k_2(t)$. An input force $u(t)$ is applied to the second mass. For the numerical simulations to follow, both mass are 1 kg, both damper coefficients are 0.1 N-s/m, and both stiffness values are initially 400 N/m. The stiffness of the connecting spring (k_2) is reduced by 5% to 380 N/m at 100 ms into the simulation. While the natural frequencies of this system before the stiffness change are low (1.97 Hz and 5.15 Hz), the results here could be scaled to higher frequency dynamics.

The equation of motion of this system can be written as

$$M\ddot{\mathbf{q}}(t) + S\dot{\mathbf{q}}(t) + K(t)\mathbf{q}(t) = \mathbf{\Gamma}_u u(t), \tag{16.1}$$

where the overdot denotes time differentiation, $\mathbf{q}$(t) is the vector of the displacements of the masses, M is the mass matrix, S is the damping matrix, $K(t)$ is the time-varying stiffness matrix, $\mathbf{\Gamma}_u$ is the force influence vector, and $u(t)$ is the input force. The above vectors and matrices are defined as

$$\mathbf{q}(t) = \begin{bmatrix} q_1(t) \\ q_2(t) \end{bmatrix}, \mathbf{\Gamma}_u = \begin{bmatrix} 0 \\ 1 \end{bmatrix}, \tag{16.2}$$

$$M = \begin{bmatrix} m_1 & 0 \\ 0 & m_2 \end{bmatrix}, S = \begin{bmatrix} s_1 + s_2 & -s_2 \\ -s_2 & s_2 \end{bmatrix}, K(t) = \begin{bmatrix} k_1 + k_2(t) & -k_2(t) \\ -k_2(t) & k_2(t) \end{bmatrix}. \tag{16.3}$$

In state space form, Eq. (16.1) can be written as

$$\dot{\mathbf{x}}(t) = A(t)\mathbf{x}(t) + \mathbf{B}u(t), \tag{16.4}$$

where $\mathbf{x}(t)$ is the state vector, $A(t)$ is the state matrix, and $\mathbf{B}$ is the input matrix defined as

$$\mathbf{x}(t) = \begin{bmatrix} \mathbf{q}(t) \\ \dot{\mathbf{q}}(t) \end{bmatrix}, A(t) = \begin{bmatrix} 0 & I \\ -M^{-1}K(t) & -M^{-1}S \end{bmatrix}, \mathbf{B} = \begin{bmatrix} 0 \\ M^{-1}\mathbf{\Gamma}_u \end{bmatrix}. \tag{16.5}$$

In general, measurements from this system, $\mathbf{y}(t)$, can be written as

$$\mathbf{y}(t) = C(t)\mathbf{x}(t) + \mathbf{D}u(t). \tag{16.6}$$

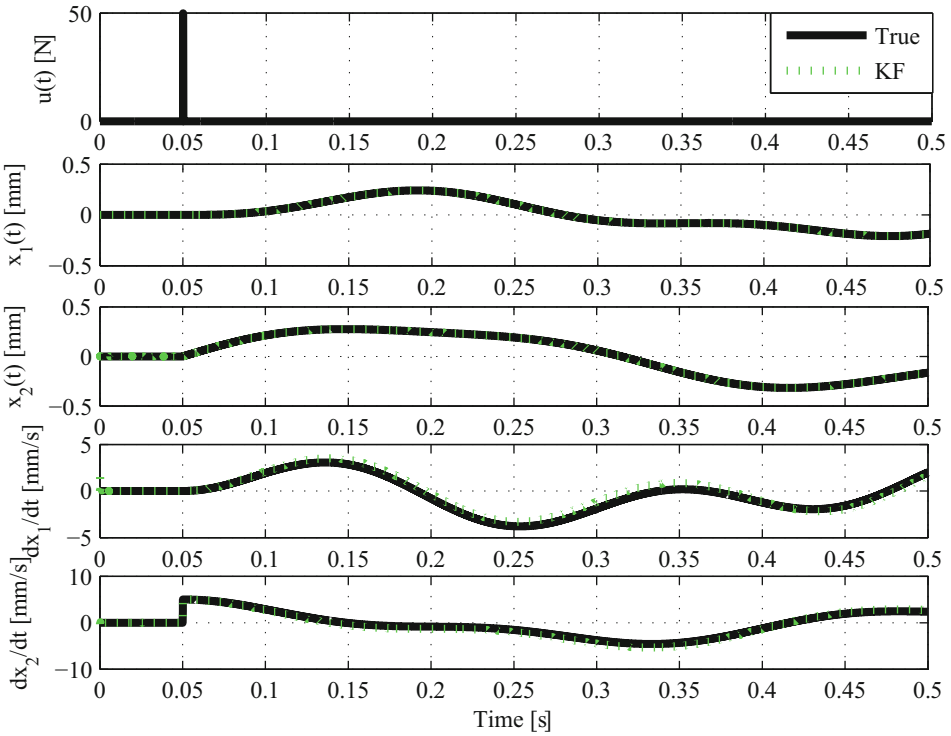

Fig. 16.2 Response of the example two degree of freedom system to an impulse at time 50 ms and a 5% change in stiffness k_2 at 100 ms. The legend in the top plot applies to all lines in this figure. From comparison, estimated states from a standard Kalman filter (KF) are also shown

where $C(t)$ is the output matrix and $\mathbf{D}$ is the direct feedthrough matrix. If the displacements of both masses are measured, then $\mathbf{y}(t)$, $C(t)$, and $\mathbf{D}$ are

$$\mathbf{y}(t) = \mathbf{q}(t), C(t) = [I \ \ 0], \mathbf{D} = \mathbf{0}, \tag{16.7}$$

where the identity matrix I, the zero matrix 0, and the zero vector $\mathbf{0}$ have the appropriate sizes. For velocity measurements from both masses, these take the forms

$$\mathbf{y}(t) = \dot{\mathbf{q}}(t), C(t) = \left[0 \ I\right], \mathbf{D} = \mathbf{0}, \tag{16.8}$$

For acceleration measurements from both masses, these are written as

$$\mathbf{y}(t) = \ddot{\mathbf{q}}(t), C(t) = \left[-M^{-1}K(t) \ -M^{-1}S\right], \mathbf{D} = M^{-1}\mathbf{\Gamma}_u. \tag{16.9}$$

These three different measurement cases (displacements, velocities, or accelerations for both masses) will be considered in the results that follow.

Figure 16.2 shows the response of the two degree of freedom subject to an impulse of amplitude 50 N at 50 ms and a 5% reduction in the connecting spring stiffness k_2 at 100 ms. The simulation sampling rate is 50 kHz. This true system response is plotted beside estimated state values from a standard Kalman filter (KF) with displacement measurements. Here noise is added such that the signal-to-noise ratio for each measured displacement is 60 dB. The observers are given a 10% initial error for k_2 (440 N/m) that remains unchanged over the duration of the simulation. All other parameters in the estimators are their true values. This discrepancy between the true value of k_2 and that used by the state observers results in some error in velocity, but the errors are small over this time interval. Therefore, deviations between the true states and those from a fixed-parameter observer may not be sufficient to detect system damage.

16.3 Methods

To illustrate some of the challenges that arise in high-rate parameter estimation, the stiffness values k_1 and k_2 at each time step are estimated through two methods. The first is a recursive least squares (RLS) method with a forgetting factor. The second is an extended Kalman filter with a forgetting factor. The role of the forgetting factor and other issues faced by these estimators will be discussed in the simulation results that follow.

16.3.1 Recursive Least Squares

First the recursive least squares approach is used to estimate the unknown stiffness values of the two springs in the example system. Here it is assumed that the input force and the displacements, velocities, and accelerations of the two masses are measured, and it is assumed the masses (m_1 and m_2) and damper coefficients (s_1 and s_2) are known. This set of information can be used to derive a recursive least squares estimation of the two stiffness values k_1 and k_2. While difficult to implement directly in practice, this method illustrates the role of state or measurement uncertainties on the estimated parameters and can help tune settings in other adaptive state and parameter estimators.

First, rewrite the equation of motion, Eq. (16.1), as

$$K(t)\mathbf{q}(t) = \mathbf{\Gamma}_u u(t) - M\ddot{\mathbf{q}}(t) + S\dot{\mathbf{q}}(t). \tag{16.10}$$

This can be re-written as a least squares problem of the form

$$\varphi(t)\boldsymbol{\theta}(t) = \mathbf{T}(t), \tag{16.11}$$

where the parameter vector $\boldsymbol{\theta}$ and the other matrices and vectors are defined as

$$\boldsymbol{\theta}(t) = \begin{bmatrix} k_1(t) \\ k_2(t) \end{bmatrix}, \varphi(t) = \begin{bmatrix} q_1(t) & q_1(t) - q_2(t) \\ 0 & q_2(t) - q_1(t) \end{bmatrix}, \text{and } \mathbf{T}(t) = \mathbf{\Gamma}_u u(t) - M\ddot{\mathbf{q}}(t) + S\dot{\mathbf{q}}(t) \tag{16.12}$$

This can be solved using a recursive least squares method (RLS) with an exponential forgetting factor λ. See for example [11]. This algorithm is summarized in Fig. 16.3 below. Here the equations above are written in discrete time with time index k. The forgetting factor λ is a value between 0 and 1 and serves to weight previous data with less importance. Smaller forgetting factors mean that current samples are given more importance over older data. This means that smaller forgetting factors reduce estimation time but make the estimator less robustness to measurement noise.

16.3.2 Extended Kalman Filter

Another method of parameter estimation is the extended Kalman filter. Here a joint extended Kalman filter is used whereby the unknown model parameters are treated as additional states. In this case, the dynamic equations can be written as

Initialize estimated parameters $\hat{\boldsymbol{\theta}}_0$ and error covariance matrix P_0

for $k = 1{:}N$

Assemble φ_k and $\mathbf{T}_k$ as defined in equations (12)

Calculate the Kalman gain: $L_k = P_{k-1}\varphi_k\left[\lambda I + \varphi_k^T P_{k-1}\varphi_k\right]^{-1}$

Update the parameter estimate: $\hat{\boldsymbol{\theta}}_k = \hat{\boldsymbol{\theta}}_{k-1} + L_k\left[\mathbf{T}_k - \varphi_k^T\hat{\boldsymbol{\theta}}_{k-1}\right]$

Update the error covariance estimate: $P_k = \left[I - L_k\varphi_k^T\right]\lambda^{-1}P_{k-1}$

end

Fig. 16.3 Algorithm for the recursive least squares (RLS) with a forgetting factor λ

$$\begin{bmatrix} \dot{\mathbf{x}}(t) \\ \dot{\boldsymbol{\theta}}(t) \end{bmatrix} = \begin{bmatrix} A\left(\boldsymbol{\theta}(t)\right)\mathbf{x}(t) + \mathbf{B}u(t) \\ \mathbf{0} \end{bmatrix}, \tag{16.13}$$

$$\mathbf{y}(t) = C\left(\boldsymbol{\theta}(t)\right)\mathbf{x}(t) + \mathbf{D}u(t). \tag{16.14}$$

For implementation, these continuous time equations will need to be discretized. One method for doing this is to use an Euler approximation for the derivative. This gives

$$\begin{bmatrix} \mathbf{x}_k \\ \boldsymbol{\theta}_k \end{bmatrix} = \begin{bmatrix} \left(I + \Delta t A\left(\boldsymbol{\theta}_{k-1}\right)\right)\mathbf{x}_{k-1} + \Delta t\, \mathbf{B}u_{k-1} \\ \boldsymbol{\theta}_{k-1} \end{bmatrix} + \mathbf{w}_k, \tag{16.15}$$

$$\mathbf{y}_k = C\left(\boldsymbol{\theta}_k\right)\mathbf{x}_k + \mathbf{D}u_k + \mathbf{v}_k, \tag{16.16}$$

where the subscript k is the time index and Δt is the time between samples. In Eqs. (16.17) and (16.18), process and measurement noise are also introduced. The process noise $\mathbf{w}_k$ is assumed Gaussian with zero mean and a covariance $\mathbf{Q}$, and the measurement noise $\mathbf{v}_k$ is also assumed to be Gaussian with zero mean and a covariance $\mathbf{R}$. Next, define the augmented state vector $\mathbf{x}^a$ as the concatenation of the state and parameter vectors, i.e.

$$\mathbf{x}_k^a = \begin{bmatrix} \mathbf{x}_k \\ \boldsymbol{\theta}_k \end{bmatrix}. \tag{16.17}$$

From this, Eqs. (16.15) and (16.16) take the general form

$$\mathbf{x}_k^a = \mathbf{f}\left(k, \mathbf{x}_{k-1}^a, u_{k-1}\right) + \mathbf{w}_k, \tag{16.18}$$

$$\mathbf{y}_k = \mathbf{h}\left(k, \mathbf{x}_k^a, u_k\right) + \mathbf{v}_k. \tag{16.19}$$

From this point, these equations are implemented in an extended Kalman filter (EKF) algorithm. Here the standard EKF algorithm is modified to include a forgetting factor like that of the previous RLS estimator. Figure 16.4 below lists the algorithm for the EKF with forgetting factor. The algorithm is similar to that used by Yang [9] or Xia [12] but with a constant forgetting factor λ. In Fig. 16.4, the subscript "$k|k$-1" denotes predictions of the augmented state vector or the error covariance matrix at time k based on previous data. The procedure is like that of a standard EKF algorithm, but the introduction of the forgetting factor λ has the effect of weighing the previous estimated states with less importance.

16.3.3 Persistent Excitation

Successful parameter convergence depends on having persistently exciting input and measurement signals in order for parameters to converge to a unique solution [11]. One method of quantifying the degree of persistent excitation is to define a persistent excitation metric ρ as

$$\rho(t) = \left\| \varphi(t)\varphi^T(t) \right\|, \tag{16.20}$$

where the matrix 2-norm is used (equivalent to the largest singular value of the matrix), and $\varphi(t)$ is defined in Eq. (16.12). If ρ is close to zero, the RLS algorithm will result in poor parameter estimates due to numerical instabilities.

There are a few methods to overcome this persistent excitation problem. The first is to modify the update law to not estimate states during periods of small measurements. In this approach, if the initial estimates of the parameters are incorrect, then the estimator cannot adjust them to their correct values until a sufficiently large excitation is delivered. This will lead to overall longer converge times. Instead, consider adding an additional, small amplitude forcing term to the original force, i.e. let the input $u(t)$ be

$$u(t) = F\delta\left(t - t_0\right) + \eta(t). \tag{16.21}$$

Initialize estimated augmented state $\hat{\mathbf{x}}_0^a$ and error covariance P_0

for $k = 1{:}N$

Calculate the Jacobians $\hat{A}_k = \left[\frac{\partial \mathbf{f}}{\partial \mathbf{x}^a}\right]_{\mathbf{x}^a=\mathbf{x}_k^a,\mathbf{u}=\mathbf{u}_k}$ and $\hat{C}_k = \left[\frac{\partial \mathbf{h}}{\partial \mathbf{x}^a}\right]_{\mathbf{x}^a=\mathbf{x}_k^a,\mathbf{u}=\mathbf{u}_k}$

Predict state at k: $\hat{\mathbf{x}}_{k|k-1}^a = \mathbf{f}\left(k, \hat{\mathbf{x}}_{k-1}^a, \mathbf{u}_{k-1}\right)$

Predict state error covariance at k: $P_{k|k-1} = \lambda^{-1}\hat{A}_k\ P_{k-1}\ \hat{A}_k^T + Q$

Calculate the Kalman gain: $L_k = P_{k|k-1}\hat{C}_k^T\left(\hat{C}_k P_{k|k-1}\hat{C}_k^T + R\right)^{-1}$

Estimate output: $\hat{\mathbf{y}}_k = \mathbf{h}\left(k, \hat{\mathbf{x}}_{k|k-1}^a, u_k\right)$

Update augmented state estimate: $\hat{\mathbf{x}}_k^a = \hat{\mathbf{x}}_{k|k-1}^a + L_k\left(\mathbf{y}_k - \hat{\mathbf{y}}_k\right)$

Update error covariance: $P_k = \left(I - L_k\hat{C}_k\right)P_{k|k-1}\left(I - L_k\hat{C}_k\right)^T + L_k\ R\ L_k^T$

end

Fig. 16.4 Algorithm for the extended Kalman filter (EKF) with a forgetting factor λ

where F is the amplitude of the impulse, t_0 is the time of the impulse, and $\eta(t)$ is an additional, zero-mean, stochastic force that may be broadband or filtered to a specified frequency band. This additional force excites the system at all times. This allows the estimator to converge to the correct parameter values before the impulse occurs. This is important in many applications where the parameters of the as-built system need to be determined before the system is used in operation. The benefit of this additional force will be demonstrated in the simulation results that follow.

16.3.4 Metrics for Performance Comparison

The performance of the estimators before damage (drop in stiffness value) and after damage can be compared numerically in terms of the settling time and the normalized root-mean-square error (NRMSE). The settling time is taken as the time it takes the stiffness estimate to settle within ± 1 N/m of the true, final stiffness value. Smaller settling times correspond to a faster parameter convergence. The NRMSE is defined as the ratio between the root-mean-square (RMS) value of the error and the RMS value of the true parameter, i.e.

$$NRMSE = \frac{\sqrt{\frac{1}{N}\sum_{k=1}^{N}\left(\widehat{\theta}_k - \theta_k\right)^2}}{\sqrt{\frac{1}{N}\sum_{k=1}^{N}(\theta_k)^2}}, \tag{16.22}$$

where N is the number of points in time considered in the calculation.

16.4 Simulation Results

16.4.1 Recursive Least Squares

First consider the results from the RLS method. Figure 16.5 shows the stiffness estimation results for different forgetting factors (λ). The simulation conditions are the same as those used to generate Fig. 16.2. For the RLS estimator, noise is added to each signal (displacements, velocities, accelerations, and input) such that each has a specified signal-to-noise ratio

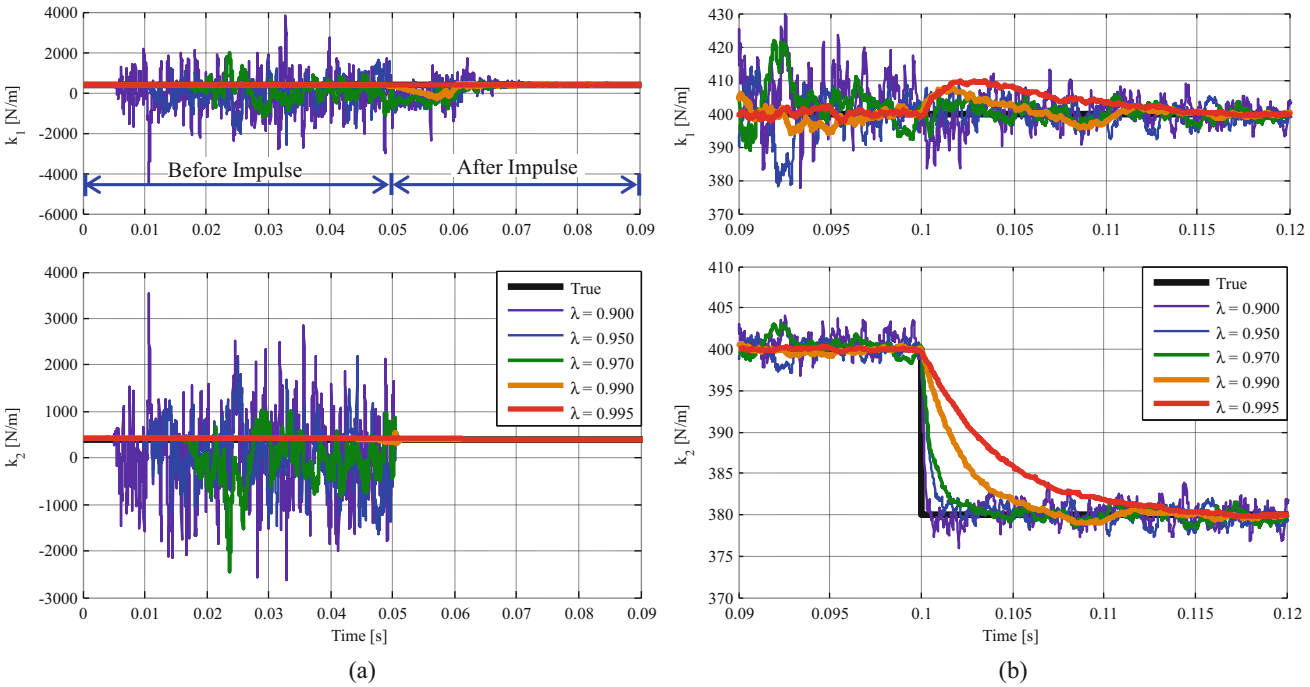

Fig. 16.5 Estimated spring stiffness values for varying values of λ at a fixed 60 dB signal-to-noise ratio on each state and input value. (**a**) Estimations before and after the initial impulse at 0.05 s (50 ms). (**b**) Estimations around the 5% stiffness change at 0.1 s (100 ms)

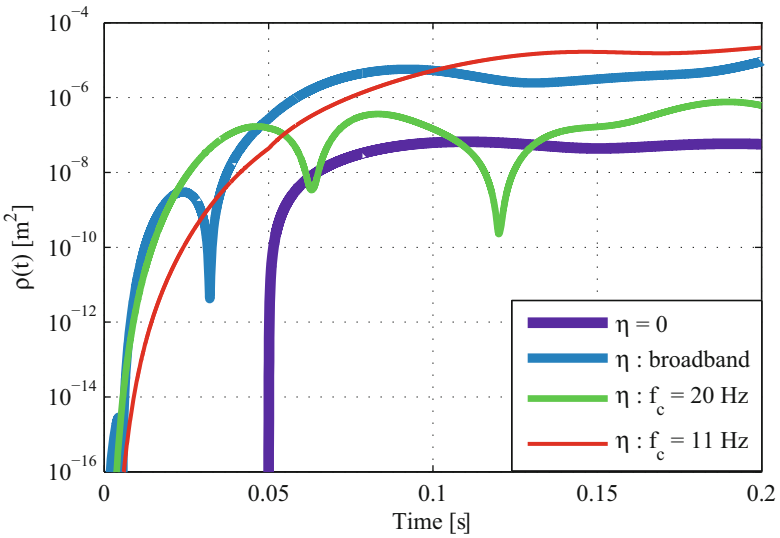

Fig. 16.6 Persistent excitation metric $\rho(t)$ based on the noise-free displacements. The baseline, impulse only condition is shown ($\eta = 0$) alongside using an additional stochastic noise term that is broadband to 25 kHz or filtered at a corner frequency (f_c) of 20 Hz and 11 Hz

of 60 dB. The estimator is given a 10% initial error for k_2 of 440 N/m instead of the correct initial stiffness of 400 N/m. Only measurement noise is provided to the algorithms before the impact at 50 ms, and therefore the stiffness estimates are initially poor in all cases. This lack of excitation can also be illustrated in the persistent excitation metric $\rho(t)$ shown in Fig. 16.6. Before the impulse at 50 ms, the displacements are zero and therefore ρ is zero (the $\eta = 0$ case in Fig. 16.6). When there is not sufficient dynamics to overcome the measurement noise, larger estimation errors can arise. When the system begins to respond with sufficient amplitude, the estimators must now converge to the correct parameter values from the initial large estimation errors. When system motion ceases, this problem will arise again. This initial error can be reduced and overall robustness to noise can be increased by increasing the forgetting factor λ closer to 1. However, increasing λ produces a slower update rate and reduces the time to parameter convergence.

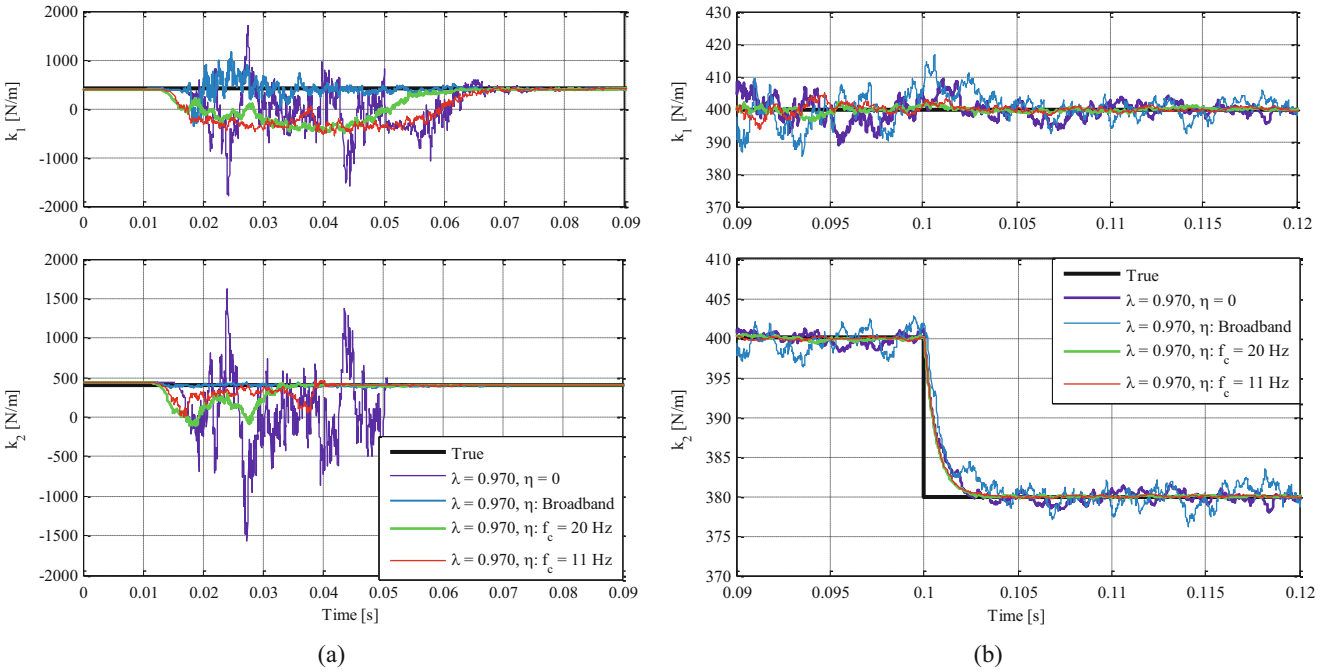

Fig. 16.7 Estimation results from the recursive least squares (RLS) estimator for varying additional inputs $\eta(t)$. (**a**) Estimations before and after the initial impulse. (**b**) Estimations during the 5% stiffness change. For all cases the forgetting factor is set to 0.970

Consider now adding an additional, stochastic input force $\eta(t)$ as in Eq. (16.21). Figure 16.6 shows the persistent excitation condition for different cases of $\eta(t)$ including broadband, Gaussian-distributed excitation to half the simulation's sampling rate (25 kHz), that excitation filtered with a low-pass filter of corner frequency 20 Hz, and the excitation filtered to 11 Hz. In all cases, $\eta(t)$ is given unit variance. All three added input forces create an improvement in the initial persistent excitation metric $\rho(t)$. The benefit of this increase initial excitation can be seen in the simulation results in Fig. 16.7. Initially the addition of a broadband η gives better robustness in the stiffness estimates than the impulse alone, but this broadband excitation causes more oscillations in the response later in the simulation during the parameter change. Filtering η results in slower initial convergence but better tracking during the stiffness change.

Figure 16.8 shows the NRMSE and the settling time for the connecting stiffness k_2 estimate using the recursive least squares (RLS) estimator. Results are shown with the additional force term set to zero ("$\eta = 0$" in the figure) and with added white noise filtered at 20 Hz ("η: $f_c = 20$ Hz" in the figure). The errors and settling times are considered before damage and after damage. Because of the random measurement noise and stochastic forcing terms in the simulations, NRMSE and settling times are averaged over five repetitions of the simulations at each condition. Error bars on the plots indicate two standard deviations above and below the mean.

In general, the additional force η reduces the NRMSE and the settling time. This extra force greatly reduces the error before damage occurs when there is 50 ms before the impact when the measurements would otherwise be only noise. This stochastic force introduces more variability in all of the simulation results. This variability in NRMSE decreases with increasing forgetting factors.

Larger forgetting factors generally decrease the NRMSE by making the estimates less influenced by noise. Before damage, the forgetting factor has little influence on the settling time during this initial period of high errors. After damage, there is only a noticeable increase in settling time for the 0.995 forgetting factor case. While none of the settling times in these examples are on the order of microseconds, these results do illustrate that adjusting the forgetting factor and introducing an additional force term can decrease parameter convergence times.

16.4.2 Extended Kalman Filter

Figure 16.9 shows the simulation results from the extended Kalman filter for the impulse only ($\eta = 0$) and with the additional stochastic force $\eta(t)$ filtered at 20 Hz. Here displacement measurements are used with a signal-to-noise ratio of 60 dB. The

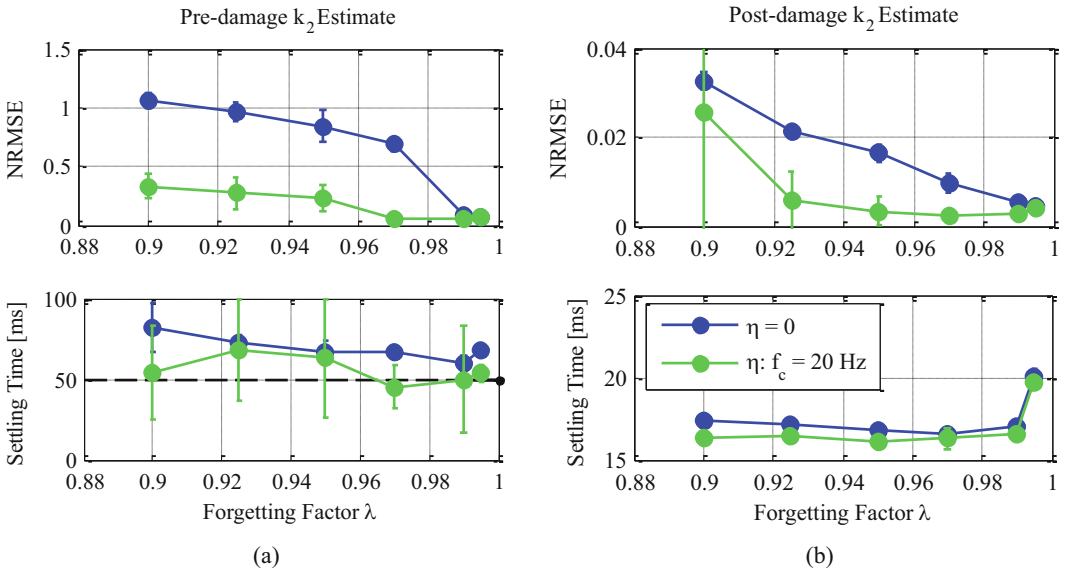

Fig. 16.8 Comparisons of the normalized root-mean-square error (NRMSE) and settling time for estimating the changing stiffness k_2 using the recursive least squares (RLS) estimator. (**a**) NRMSE and settling time before damage occurs. (**b**) NRMSE and settling time after damage. The legend in (**b**) applies to both (**a**) and (**b**)

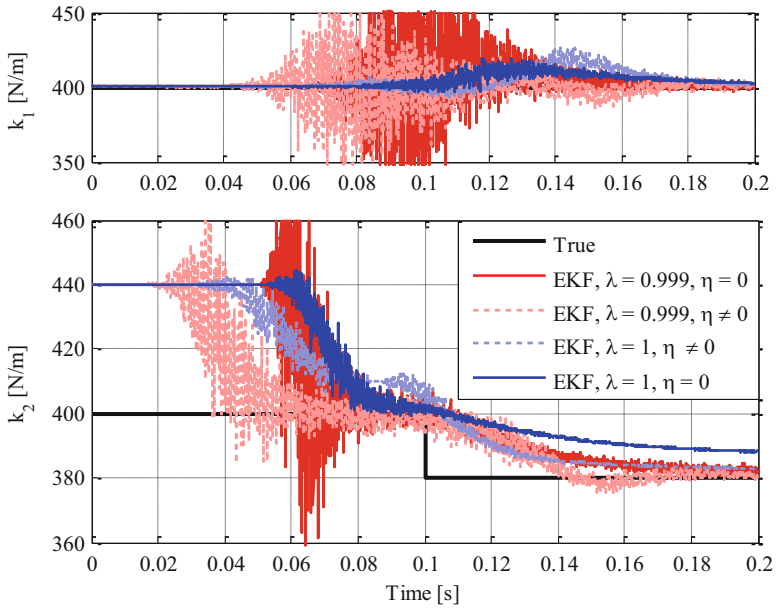

Fig. 16.9 Estimates of the stiffness values for the example system using the extended Kalman filter for different forgetting factors λ and with and without the additional stochastic force $\eta(t)$

standard extended Kalman filter is shown ($\lambda = 1$) beside one with a forgetting factor ($\lambda = 0.999$). Introducing $\eta(t)$ to the input reduces the initial convergence time both with and without the forgetting factor. The use of a forgetting factor improves overall convergence rate, but reduces the robustness to noise.

Table 16.1 lists the NRMSE for the EKF estimate of k_2, and Table 16.2 lists the settling time for the EKF estimate. The results compare the EKF with and without the stochastic force term filtered to 20 Hz. Note that the stiffness estimate does not settle within 1 N/m of the correct value before damage. Note also that the stiffness does not converge during the simulation time without the stochastic noise term and a forgetting factor of 1. As with the RLS method, the use of the additional force term reduces the NRMSE before damage during the initial parameter convergence. After damage occurs, the additional force term improves the average convergence times but introduces a large amount of variability in the settling time estimate. This

Table 16.1 Normalized root-mean-square error (NRMSE) for the EKF estimate of k_2 for the different conditions shown in Fig. 16.9 before and after damage. Two standard deviations above and below the mean are also listed. Note that the deviation in the simulation results is negligible when no stochastic force term is present

	Before damage		After damage	
	$\eta = 0$	$\eta \neq 0$	$\eta = 0$	$\eta \neq 0$
$\lambda = 0.999$	8.1%	(7.4 ± 1.3) %	1.3%	(1.1 ± 0.4) %
$\lambda = 1.000$	8.3%	(8.1 ± 2.1) %	2.2%	(2.0 ± 1.2) %

Table 16.2 Settling time for the EKF estimate of k_2 for the different conditions shown in Fig. 16.9 after damage. Two standard deviations above and below the mean are also listed. Note that the stiffness estimate does not settle to within the specified limit before damage occurs

	$\eta = 0$	η: $f_c = 20$ Hz
$\lambda = 0.999$	200 ± 2 ms	130 ± 80 ms
$\lambda = 1.000$	(Does not converge)	630 ± 360 ms

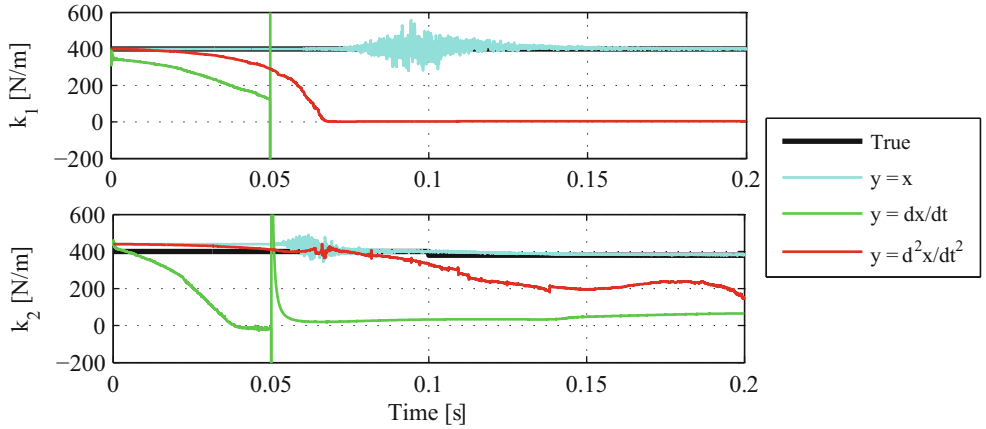

Fig. 16.10 Estimated stiffness values from the extended Kalman filter (EKF) using displacement (x), velocity (dx/dt), or acceleration (d^2x/dt^2) measurements. The forgetting factors λ is 0.999 and no additional stochastic force $\eta(t)$ is used

indicates that it may be useful to switch off the additional force term after a sufficiently large input force is applied to the system. Both NRMSE and convergence times are improved by using a forgetting factor. Note that the convergence times here are about one order of magnitude longer than those seen in the RLS method.

Finally, while results using displacement feedback to the observers show parameter convergence, the results are worse when using other types of measurements. Figure 16.10 shows the results using displacement, velocity, and acceleration measurements. The inability of the algorithm to converge illustrates that the type of measurement can have a role in the stability and observability of parameter estimates.

16.5 Conclusions and Future Work

There is a need for high rate state and parameter estimators for structural health monitoring and feedback control of complex systems. This paper illustrated some of the issues that are encountered in high rate parameter estimation and discussed methods of comparing and quantifying parameter error and convergence rates. A recursive least squares (RLS) estimator and an extended Kalman filter (EKF) were examined for estimating the stiffness values for an example, two degree of freedom system. Simulation results using a RLS technique illustrated the benefits of using a forgetting factor and ensuring persistent excitation. The forgetting factor allowed the estimator to more quickly adapt to parameter changes but at the expense of making the estimations more sensitive to measurement noise. Adding an additional, low-amplitude force term increased the initial persistent excitation metric and led to overall faster convergence times. Introducing forces on a structure before an external impact could allow the estimators to initially converge to the proper system parameters before damage occurs. It should also be noted that while only k_2 changed, the estimator may change both stiffness values in order to find the best parameters that solve the least squares problem in Eq. (16.11) as seen in Fig. 16.5. Care must be taken to ensure

this does not indicate a false state of damage in a structural health monitoring algorithm. Results from the EKF show the same benefits of a forgetting factor and an additional, persistent force term. The EKF results also show that the type of measurement (displacement, velocity, or acceleration) influenced the stability of parameter estimators with the displacement measurements providing the most accurate estimates.

The work presented here motivates the need to develop robust, adaptive observers with rapid state and parameter convergence. Future work will examine developing new, adaptive observers that incorporate forgetting factors and added stochastic input forces to reduce convergence times. In addition there is a need to examine the state and parameter observability of these systems to select the measurement locations and measurement types to best estimate particular system parameters. Simulation results here considered a two degree of freedom system with low natural frequencies. Future work will also consider the role of higher system natural frequencies and faster system dynamics on the ability of these estimators to track state and parameter changes.

Acknowledgements This material is based upon work supported by the Air Force Office of Scientific Research under award numbers FA9550-17RWCOR503 and FA9550-17-1-0131. Any opinions, findings, and conclusions or recommendations expressed in this material are those of the authors and do not necessarily reflect the views of the United States Air Force. Distribution A. Approved for public release; distribution unlimited (96TW-2017-0440).

References

1. Stein, C., Roybal, R., Tlomak, P., Wilson, W.: A review of hypervelocity debris testing at the Air Force Research Laboratory. Space Debris. **2**(4), 331–356 (2000). https://doi.org/10.1023/B:SDEB.0000030024.23336.f5
2. Hallion, R.P., Bedke, C.M., Schanz, M.V.: Hypersonic Weapons and US National Security, a 21st Century Breakthrough. Mitchell Institute for Aerospace Studies, Air Force Association, Arlington (2016)
3. Dodson, J., Inman, D.J., Foley, J.R.: Microsecond structural health montoring in impact loaded structures. In: Proc. Proceedings in SPIE, San Diego
4. Lowe, R., Dodson, J., Foley, J.: Microsecond prognostics and health monitoring. IEEE Reliability Society Newsletter. **60**, 1–5 (2014)
5. Kettle, R., Dick, A., Dodson, J., Foley, J., Anton, S.R.: Real-time detection in highly dynamic systems. In: Proc. IMAC XXXIV A Conference and Exposition on Structural Dynamics, Orlando
6. Hong, J., Laflamme, S., Cao, L., Dodson, J.: Variable input observer for structural health monitoring of high-rate systems. In: Proc. AIP Conference Proceedings, p. 07003
7. Hong, J., Laflamme, S., Dodson, J.: Variable input spce observer for structural health monitoring of high-rate system. In: Proc. Review of Progress in Quantitative Nondestructive Evaluation (QNDE)
8. Doebling, S., Farrar, C.R., Prime, M.B.: A summary review of vibration-based damage identification methods. Shock Vib. Dig. **30**, 91–105 (1998). https://doi.org/10.1177/058310249803000201
9. Yang, J.N., Lin, S., Huang, H., Zhou, L.: An adaptive extended Kalman filter for structural damage identification. Struct. Control. Health Monit. **13**(4), 849–867 (2006). https://doi.org/10.1002/stc.84
10. Yang, J.N., Pan, S., Huang, H.: An adaptive extended Kalman filter for structural damage identifications II: unknown inputs. Struct. Control. Health Monit. **14**(3), 497–521 (2007). https://doi.org/10.1002/stc.171
11. Åström, K.J., Witternmark, B.: Adaptive Control. Addison-Wesley Longman Publishing Co., Inc., Boston (1994)
12. Xia, Q., Roa, M., Ying, Y., Shen, X.: Adaptive fading Kalman filter with an application. Automatica. **30**(8), 1333–1338 (1994). https://doi.org/10.1016/0005-1098(94)90112-0

Chapter 17
Probabilistic Robustness Analysis of an Actively Controlled Structure that Operates in Harsh and Uncertain Environments

Christopher J. D'Angelo, Daniel G. Cole, and John C. Collinger

Abstract This work uses probabilistic robustness techniques to show how the stability margin of an uncertain controlled structure that operates in a harsh, potentially radioactive environment can be analyzed in order to find a less conservative destabilizing uncertainty perturbation. The uncertainty is quantified in terms of a measure on the size of the covariance matrix in a multivariate Gaussian distribution. This uncertainty is used to capture the aggregate effects on a structure's dynamic behavior due to material changes resulting from radiation embrittlement and mechanical fatigue. A probabilistic-robust full-state feedback $\mathcal{H}_\infty$ controller is synthesized for a low-dimensional structural model using a technique known as scenario-based probabilistic-robust synthesis. A probabilistic-robust stability margin is defined and extracted from a stability degradation function, demonstrating that a fourfold increase in the amount of uncertainty in the model can be tolerated if the designer is willing to concede a small probability that the actively-controlled structure may be unstable for certain system configurations.

Keywords Probabilistic robust control · Probabilistic stability margins · Uncertainty · $\mathcal{H}_\infty$ · Active vibration control

17.1 Introduction

Methods for designing controllers to handle unstructured uncertainty have been extensively studied and used in the literature [1]. Such robustness techniques are often overly conservative for two reasons: First, such approaches, which describe uncertainty as a norm bounded ball around a nominal plant, often do not account for the likelihood of plants within the uncertainty set. Second, unstructured uncertainty is often used to cover actual structured uncertainty, which may be too difficult to analyze. The result in both cases is that the resulting design must account for uncertainty that is not necessarily there and, hence, may sacrifice performance in order to achieve robustness.

These limitations have given rise to probabilistic robust techniques to analyze, design, and synthesize controllers. In probabilistic robust control (PRC), uncertainty is characterized using a probability density functions that more accurately describes the nature of uncertainty. An advantage of this approach is that one can characterize all types of uncertainty: real, complex, structured, and unstructured [1].

In this paper, we have designed and synthesized a full-state feedback $\mathcal{H}_\infty$ controller for structural vibration control using PRC. For synthesis, we have used a scenario-based approach [2]. In doing so, random parametric uncertainty is incorporated into the system model during controller synthesis. Additionally, a degradation function is formulated, and a probabilistic stability margin is defined. The degradation function describes the probability, as the amount of uncertainty in the model is increased, that the closed-loop system is stable. The probabilistic stability margin quantifies this amount relative to a nominal plant and nominal uncertainty model. This probabilistic approach is attractive for a two reasons:

1. It can be used in making decisions about the reliability of an active structural controller operating in a harsh environment, where the structure's behavior may change over time. The probabilistic stability margin can be used to define an upper limit for such changes. When exceeding such limits, it may be necessary to take an active controller offline or perform a redesign.

C. J. D'Angelo (✉) · D. G. Cole
Department of Mechanical Engineering and Materials Science, University of Pittsburgh, Pittsburgh, PA, USA
e-mail: cjd66@pitt.edu; dgcole@pitt.edu

J. C. Collinger
Naval Nuclear Laboratory, Bettis Atomic Power Laboratory, West Mifflin, PA, USA
e-mail: john.collinger@unnpp.gov

C. Niezrecki, J. Baqersad (eds.), *Structural Health Monitoring, Photogrammetry & DIC, Volume 6*,
Conference Proceedings of the Society for Experimental Mechanics Series, https://doi.org/10.1007/978-3-319-74476-6_17

2. By virtue of the way PRC allows system uncertainty to be expressed and quantified, actual laboratory data and engineering judgment can be used in capturing the structure's uncertainty more realistically. This will enable experimental data to be used to formulate uncertainty and subsequently used for controller synthesis and analysis.

Of particular interest for this effort, in the presence of radiation, structures that are subjected to significant temperature and pressure fluctuations experience material changes. Radiation embrittlement, for example, is a well-known phenomenon that causes structural resonances to drift to higher frequencies. At elevated temperatures, structural materials soften and creep; and, pressure and thermal excursions lead to material fatigue. All of these effects may lead to irreversible changes to the structure. Precisely capturing the aggregate effects and using this information during controller design can be difficult.

These changes and the resulting uncertainty can be addressed using PRC. Information about how the structure will be affected by the phenomena discussed above can be included in the design and synthesis process, leading to a controller that is probabilistically robust and better accounts for uncertainty than those resulting from conventional robust control [1].

17.2 State of the Art and Limitations

17.2.1 Robust Control

Controller design for uncertain dynamic systems gave rise to the field of robust control [3, 4]. Techniques such as μ-analysis/synthesis [5] were developed to handle control analysis and synthesis problems involving dynamic system uncertainty, where system uncertainty typically received some kind of norm bound [5, 6]. Even without consideration of structured or unstructured plant uncertainties, $\mathcal{H}_\infty$ control was found to be attractive due to the fact that stability margins could be guaranteed for this type of control approach, whereas linear quadratic approaches were lacking in their ability to provide a guaranteed stability margin [7].

Techniques like μ-synthesis are still very powerful synthesis tools for designing robust controllers for uncertain systems. Some drawbacks to tools like μ-synthesis are related to computational complexity and conservatism. Drawbacks related to computational complexity arise from the fact that algorithms used for μ-synthesis are only solvable in non-deterministic polynomial time (NP-hard), making their application to higher dimension problems difficult [8]. Design conservatism arises from norm-bounding the uncertainty—the designer implicitly treats all plant configurations in the uncertainty set as being equally likely to occur. In reality, especially for real, physical systems, some models in the uncertainty set are more likely to exist than others.

In response to some of the shortcomings and limitations to robust control, an alternative paradigm in robust control was developed in the early 1990s through work by Robert Stengel [9–11]. Stengel and colleagues began by analyzing the "stochastic robustness" of dynamic systems using Monte Carlo methods. Later, Stengel and other researchers conceived of design techniques for handling random system uncertainty [12, 13]. The field of PRC was born out of this research with subsequent researchers linking the rigors and descriptions of robust control to the ideas of stochastic robustness [1].

17.2.2 Probabilistic Robust Control of Structures

Probabilistic robust control has found recent application in the field of vibration control, but these applications take different control synthesis approaches and do not provide define or analyze stability margins for their closed-loop system designs. Some of this prior research will be discussed.

In the research by Guo [14], he focused on the development of a reliability method to robust controller synthesis, which built off of the FORM/SORM techniques for structural reliability [15]. His technique enables a relatively low-dimensional controller synthesis approach with "reliability index" defined in terms of the distance between the standard normal variables used to describe uncertainty in the model and the "failure surface", which is the point at which the system goes unstable. Although his approach provides some closed-form guarantees for the reliability of the controller for a system that has normally-distributed random variables, it does not define or discuss how stability margins can be extracted using his techniques.

The work by B. Scott May [16] applied PRC techniques to the reliable control of a civil structure, where control objectives were to minimize the probability of structural failure. May did not synthesize a probabilistic-robust $\mathcal{H}_\infty$ controller for an uncertain system, nor did he examine or provide definitions related to probabilistic robust stability margins.

The technical reports authored by Crespo and colleagues [17, 18] develop reliability-based controllers by searching for controller parameters that minimize the probability of violating performance requirements. To synthesize these controllers, they formulated and solved a multi-objective stochastic optimization problem, with these objectives specifying certain performance requirements for the system. Crespo's reliability-based approach did not approach controller synthesis as an $\mathcal{H}_\infty$ problem, which can be attractive for noise and vibration control problems. Similar to the research performed by Guo and May, Crespo and colleagues did not discuss or formulate an approach to quantifying the probabilistic stability margin.

The research reported here uses the scenario-based approach to probabilistic robust controller synthesis with a formulation specific to realizing a probabilistically robust full state feedback $\mathcal{H}_\infty$ controller [1, 2]. This type of probabilistic controller synthesis approach involves solving a semidefinite program with multiple linear matrix inequality (LMI) constraints, where the choice for number of LMI constraints bounds the probability that the controller will meet stability/performance requirements with confidence in this probability estimate. An a posteriori Monte Carlo evaluation is carried out for finding the probability that the closed-loop system will be stable for some nominal amount of random uncertainty used during controller synthesis. A stability degradation function is constructed and a probabilistic stability margin is defined using the stability degradation function. An approach for quantifying the amount of uncertainty in the system, along with how the probabilistic uncertainty can be increased for extracting a probabilistic stability margin, is presented alongside a numerical example in this work.

The approaches presented in this paper can be useful for designing and analyzing active controllers for structures where phenomena such as mechanical fatigue and radiation embrittlement are present. Probabilistic stability margins can aid in making decisions related to the need for controller re-tuning, adaptation, or decommissioning.

17.3 Methods & Approach

17.3.1 The Structural Model with Uncertainty

17.3.1.1 Uncertainty Model

The parametric uncertainty is characterized by the random variable Δ with a multivariate normal distribution,

$$f_\Delta(\delta_1, \ldots, \delta_p) = \frac{\exp\left(-\frac{1}{2}(\boldsymbol{\delta} - \boldsymbol{\mu})^T \Sigma^{-1}(\boldsymbol{\delta} - \boldsymbol{\mu})\right)}{2\pi^{p/2}|\Sigma|^{1/2}} \tag{17.1}$$

where the random vector $\delta = (\delta_1, \ldots, \delta_p)$ is a p-dimensional vector; the mean μ is p-dimensional vector; and the covariance matrix $\Sigma > 0$. In this paper, $p = 4$, $\mu = 0$. The nominal covariance matrix is $\Sigma_0 = 0.15I$. This is the design basis: the amount uncertainty for which a controller is designed. The magnitude of uncertainty characterized by the Frobenius norm of the covariance matrix; $\|\Sigma_0\|_F = 0.30$.

Since the composite effects of operating at high temperatures, pressures, and in the presence of radiation are assumed to principally affect the structural stiffness, and proportional damping is assumed, there is also uncertainty in the damping coefficients. The uncertainty affects the stiffness and damping matrices as follows:

$$\mathcal{K}_\Delta = \mathcal{K}_0 + \sum_{i=1}^{p} \mathcal{K}_i \delta_i, \qquad \delta \sim f_\Delta \tag{17.2}$$

$$\mathcal{C}_\Delta = \alpha\mathcal{M} + \beta\mathcal{K}_\Delta \qquad (\alpha = 10^{-3}, \beta = 4 \times 10^{-3}) \tag{17.3}$$

where $\mathcal{K}_0$ is the nominal stiffness matrix and $\mathcal{K}_i$ maps the ith uncertainty perturbations to the appropriate terms in $\mathcal{K}$. These matrices are given in section "Appendix: System Model". The coefficients α and β were chosen to create a lightly-damped, 3-degree-of-freedom, spring-mass-damper model. For the structural model shown in Fig. 17.1 and a nominal stiffness values of $k = 6\,\mathrm{N/m}$, the stiffness lies in the 3σ-range 4.84 to 7.16 N/m with probability 99.7%.

Results from the fields of stochastic computational mechanics and stochastic finite element methods have shown that the parametric probabilistic approach is effective at capturing both uncertainty in the low and mid-frequency range [19–21].

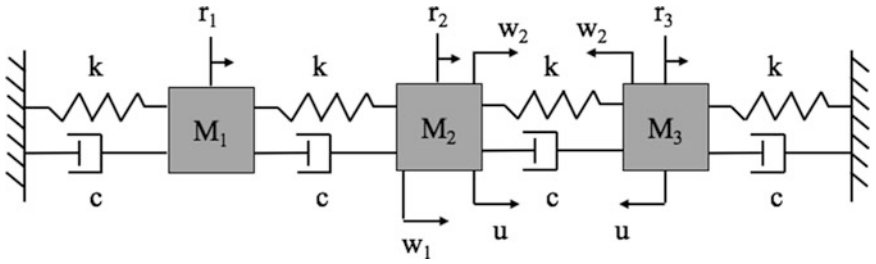

Fig. 17.1 Lumped spring-mass-damper model used in this analysis. Locations of disturbances (w_i) and control input (u) are indicated

17.3.1.2 Structural Model and Generalized Plant

To illustrate the concepts discussed in Sect. 17.1, we use the structure in Fig. 17.1. The equations of motion for this structure are

$$\mathcal{M}\ddot{r} + \mathcal{C}_\Delta \dot{r} + \mathcal{K}_\Delta r = \mathcal{D}_w w + \mathcal{D}_u u \tag{17.4}$$

where r is the absolute displacement, w is the disturbance, and u is the control input.

The generalized plant for this structural dynamic system is given by

$$P_\Delta : \begin{cases} \dot{x} = A_\Delta x + B_1 w \ \ + B_2 u \\ z = C_1 x + D_{11} w + D_{12} u \\ y = Ix \end{cases} \tag{17.5}$$

where the state is $x = \begin{bmatrix} r & \dot{r} \end{bmatrix}^T$, and the system matrices are

$$A_\Delta = \begin{bmatrix} 0 & I \\ -\mathcal{M}^{-1}\mathcal{K}_\Delta & -\mathcal{M}^{-1}\mathcal{C}_\Delta \end{bmatrix}, \quad B_1 = \begin{bmatrix} 0 \\ \mathcal{M}^{-1}\mathcal{D}_w \end{bmatrix}, \quad B_2 = \begin{bmatrix} 0 \\ \mathcal{M}^{-1}\mathcal{D}_u \end{bmatrix}. \tag{17.6}$$

The performance output z is chosen to meet certain design objectives by the choices for matrices C_1 and D_{12}; the pair (A_Δ, C_1) is observable. In this paper, these objectives are to minimize the following: (1) the effect that the disturbances have on the displacement of the third mass; (2) the effect that the disturbances have on the velocity of the second mass; and (3) the control effort. Numerical values for the system matrices given by Eqs. (17.2), (17.3), (17.4) and (17.5) are given in section "Appendix: System Model".

We are challenged with designing a controller for a system with the eigenvalue distribution shown in Fig. 17.2. It is important to realize that the distribution of poles is not uniform, and we must develop tools that account for the probabilistic nature of the uncertainty.

17.3.2 Controller Synthesis

17.3.2.1 $\mathcal{H}_\infty$ Controller Synthesis

Techniques like $\mathcal{H}_\infty$ for synthesizing active controllers possess intuitive attractiveness in their application to sound and vibration control problems. Often active control objectives and goals are specified so that sound or vibration limits not exceed specified thresholds across the frequency band. For the generalized plant in (17.5), the objective is to find the feedback gain, K, for the control law, $u = Ky$, that ensures magnitude of the transfer function matrix

$$G(j\omega) = (C_1 + D_{12}K)(sI - (A + B_2K))^{-1}B_1 + D_{11} \tag{17.7}$$

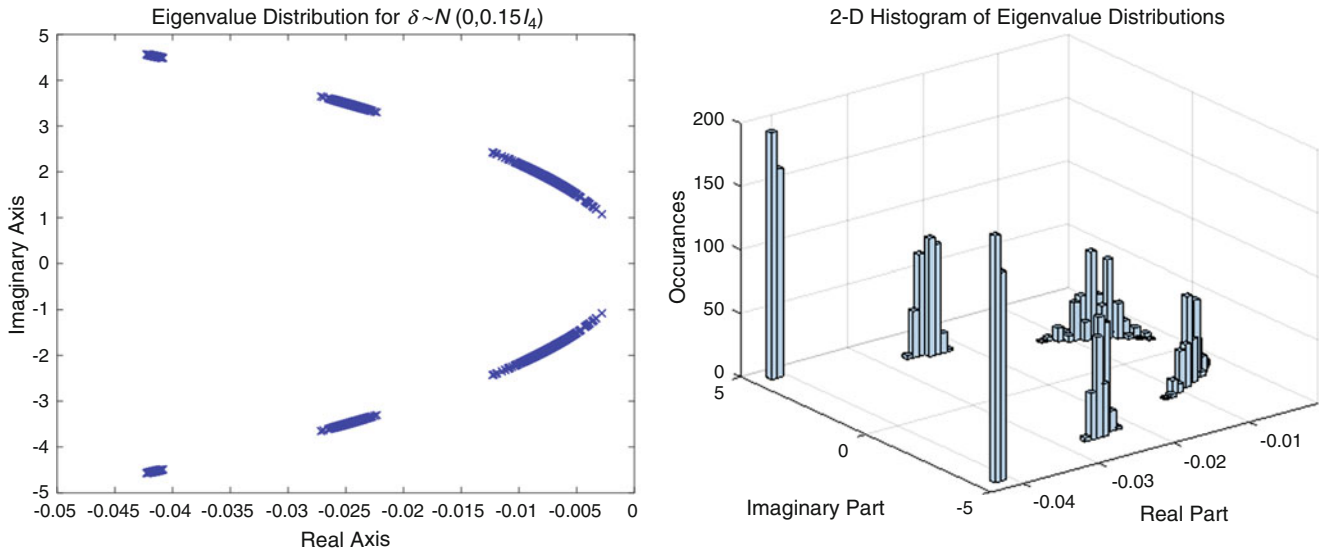

Fig. 17.2 Eigenvalue distributions for the uncertain structure

is below some threshold γ. This objective can be easily formulated as an ∞-norm criteria, where for a linear time invariant system the system's ∞-norm is defined to be

$$\|G\|_\infty = \sup_\omega \bar{\sigma}\left(G(j\omega)\right) \tag{17.8}$$

Thus, the ∞-norm is the peak of the controlled structure's frequency response function (FRF) matrix. The objective is then to choose a controller so that this peak is small. There exists a controller

$$K = YQ^{-1} \tag{17.9}$$

such that

$$\|G\|_\infty < \gamma \tag{17.10}$$

provided the linear matrix inequality (LMI)

$$\begin{bmatrix} AQ + QA' + B_2Y + Y'B_2' & Q, C_1' + Y'D_{12}' & B_1 \\ C_1Q + D_{12}Y & -\gamma^2 I & D_{11} \\ B_1' & D_{11}' & -I \end{bmatrix} < 0, \quad \text{and} \quad Q > 0,\ Y \text{ free} \tag{17.11}$$

has a solution [22, 23]. In this paper, we choose $\gamma = 100$, a value that is below the open-loop ∞-norm of the plant.

17.3.2.2 Controller Synthesis Using Scenario-Based Design

The true plant is one from the uncertainty set. Conventional $\mathcal{H}_\infty$, when used for robust controller synthesis, designs controllers with equal probability in the uncertainty set. For our problem, the plants within the uncertainty set have corresponding probability density f_Δ, and conventional $\mathcal{H}_\infty$ tools are not appropriate. In order to design probabilistic-robust full-state feedback $\mathcal{H}_\infty$ controller, we synthesized the controller using the scenario-based approach in PRC. A cursory overview of the scenario-based approach is provided. More details about the scenario-based design approach in PRC can be found in the literature [1, 2].

In the scenario based approach, one begins by generating N scenarios of the uncertain plant, P_Δ^k, chosen from the uncertainty set; this is equivalent to choosing A_Δ^k. Each of these instances is cast into the full-state feedback $\mathcal{H}_\infty$ LMI constraints.

$$\begin{bmatrix} A_\Delta^k Q + Q A_\Delta^{k\prime} + B_2 Y + Y' B_2' & Q, C_1' + Y' D_{12}' & B_1 \\ C_1 Q + D_{12} Y & -\gamma^2 I & D_{11} \\ B_1' & D_{11}' & -I \end{bmatrix}_k < 0 \quad \text{for} \quad k = 1, \ldots, N; \quad \text{and} \quad Q > 0, \; Y \text{ free}, \tag{17.12}$$

Instead of having two constraints as in Eq. (17.11), there are $N+1$ constraints. Using convex optimization techniques [23, 24], this LMI is solved with a search for Y and Q that meet all $N+1$ constraints, yielding a controller as defined in Eq. (17.9).

Naturally, the question arises as to how to choose N. A key result by Tempo et al. [1] (Corollary 2.1) establishes that if N is chosen so that

$$N \geq \frac{2}{\epsilon}\left(\ln\frac{1}{\beta} + n_\theta\right) \tag{17.13}$$

then with confidence $(1-\beta)$, one finds a controller that meets the objective with probability $(1-\epsilon)$.

The quantity n_θ corresponds to the number of free controller parameters. The free parameters in the search are Y is $1 \times n$ and Q is symmetric $n \times n$; thus $n_\theta = n + \frac{1}{2}n(n+1)$. For this problem, $n = 6$ and $n_\theta = 27$. For $N = 360$ and $\beta = 5\%$ (95% confidence), $\epsilon = 16.7\%$ and the controller will meet performance specifications 83.3% of the time.

17.4 Results & Discussion

17.4.1 The Controller

A probabilistic-robust controller was found to exist for the uncertainty and performance requirements described in Sect. 17.3.2.2

$$K = \begin{bmatrix} -640.9 & 25.1 & 1103.9 & -801.8 & -957.7 & -801.5 \end{bmatrix} \tag{17.14}$$

As a measure of performance, we can compare the open and closed-loop performance for the nominal plant without uncertainty.

The performance of the probabilistic-robust controller on all 360 plant instances used during synthesis is shown in Fig. 17.3. The open-loop response across each channel for the nominal plant (no uncertainty) is shown in Table 17.1.

17.4.2 The Probability of Stability

To evaluate stability of the controlled system, it is no longer sufficient to consider guarantees of stability for the nominal system or for all plants in the uncertainty set. Because the uncertainty set includes some inherent probability, we must think probabilistically when evaluating the stability of the controller for the uncertain plant. Mathematically, we can describe this as

$$\Pr(\text{stable}) = \int_\Delta \text{stable}\,(A_\Delta + B_2 K | \Delta) f_\Delta \, d\Delta, \quad \text{for } K \text{ fixed}. \tag{17.15}$$

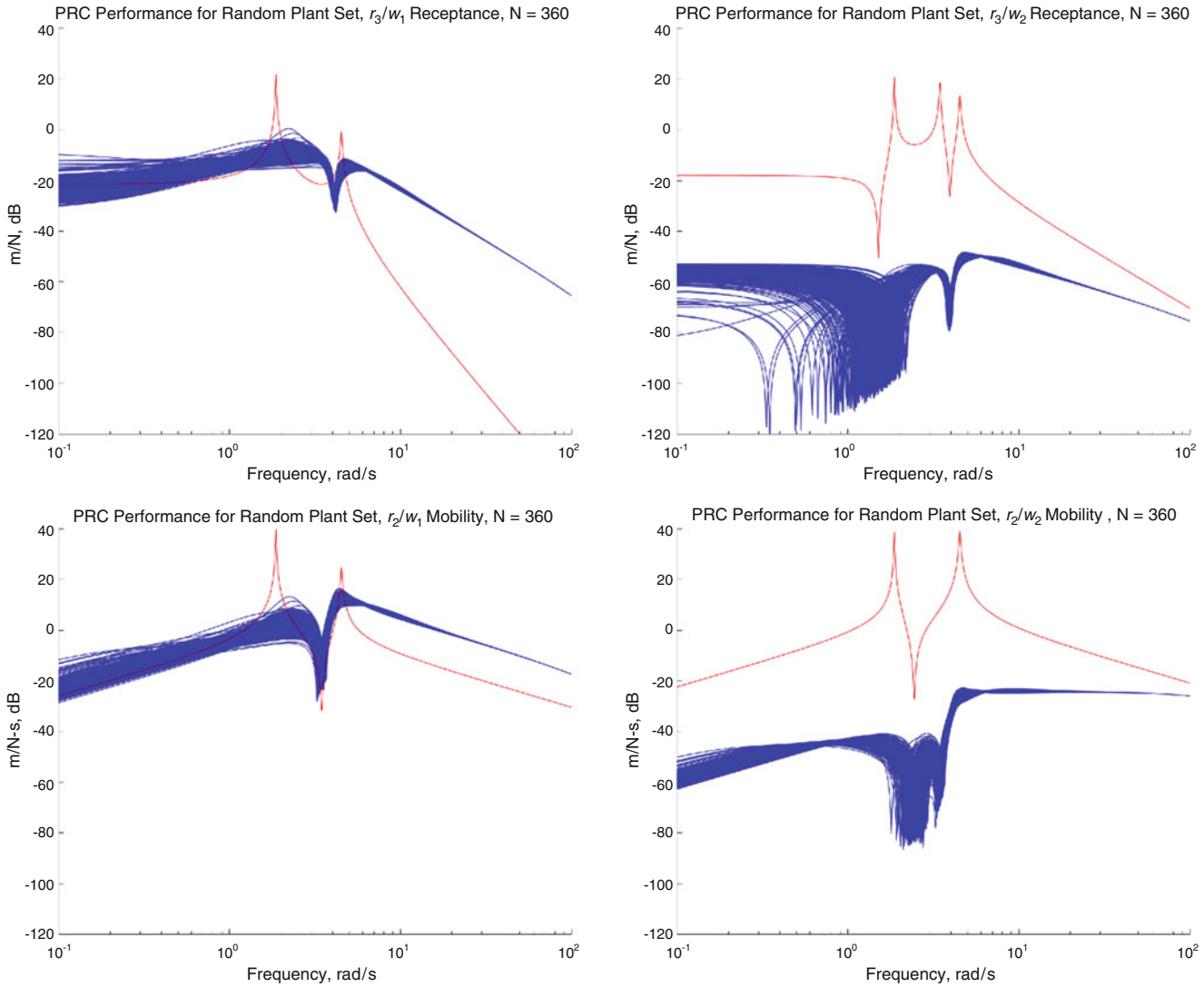

Fig. 17.3 Probabilistic robust $\mathcal{H}_\infty$ controller performance across all disturbance (w) performance output (z) channels. The open-loop response for the nominal plant is shown as well

Table 17.1 Probabilistic robust $\mathcal{H}_\infty$ controller performance

Plant	Controller	Performance	
Nominal	Open-loop	133.7	42.5 dB
Nominal	Closed-loop	6.98	16.9 dB
Net improvement		19.1	25.6 dB

The stable() function returns one if all eigenvalues of the argument have negative real part and zero otherwise. However, evaluating this integral is clearly impractical, so we must resort to estimating it using Monte Carlo techniques. To do this, we generate $\hat{N}$ samples and evalute the stability of each for the fixed K

$$\text{stable}\left(A_\Delta^k + B_2 K\right) \quad \text{for} \quad k = 1, \ldots, \hat{N}, \tag{17.16}$$

generating an estimate of the probability of stability

$$\widehat{\Pr}(\text{stable}) = \frac{1}{\hat{N}} \sum_{k=1}^{\hat{N}} \text{stable}\left(A_\Delta^k + B_2 K\right) \quad \text{for } K \text{ fixed.} \tag{17.17}$$

The probability of stability test then amounts to evaluating whether or not this probability estimate is greater than some desired level. The number $\hat{N}$ is chosen such that the magnitude of the error in the estimate is acceptable to the designer. We can establish, with some specified confidence, that the error in our estimate is within some range of the true probability by using Chernoff bounds [1], defined as follows: given any $\zeta \in (0, 1)$ and $\xi \in (0, 1)$, if

$$\hat{N} \geq \frac{1}{2\zeta^2} \ln \frac{2}{\xi} \tag{17.18}$$

then

$$\Pr\left(\left|\widehat{\Pr}(\text{stable}) - \Pr(\text{stable})\right| < \zeta\right) \geq 1 - \xi. \tag{17.19}$$

In this work, we choose an error bound $\zeta = 0.2\%$ and confidence parameter $\xi = 0.07\%$. This results in a requirement that $\hat{N} \geq 9.95 \times 10^5$, thus, we chose $\hat{N} = 10^6$. The estimate of the probability of stability was calculated to be $\widehat{\Pr}(\text{stable}) = 99.98\%$, and with probability 99.93%, this estimate is within 0.2% of the true probability of stability for our chosen $\hat{N}$.

17.4.3 The Probabilistic Stability Margin

It is apparent that the probability of stability of the closed-loop system is directly tied to the amount of uncertainty. For a specific controller, increasing uncertainty would degrade control objectives, e.g, stability and performance. This deterioration is quantified in the degradation function, an idea that comes from Tempo et al. [1] and associated works. The degradation function describes how the probability of a control objective changes as the amount of uncertainty is increased in the system.

In this paper, we define the stability degradation function as

$$\text{degrade}(a) = 1 - \widehat{\Pr}\Big(\text{ stable } (A_\Delta + B_2 K | \Sigma = aI)\Big) \quad \text{for } K \text{ fixed.} \tag{17.20}$$

The stability degradation function for the uncertain structure of this paper is shown in Fig. 17.4. The uncertainty in the structure is scaled by $\Sigma = aI$. The uncertainty can be quantified by the Frobenius norm of the covariance matrix, $\|\Sigma\|_F$. It is easily seen that the probability increases as $\|\Sigma\|_F = 2a$ increases.

Since our probabilistic thinking about stability requires us to associate a probability with stability, for any fixed controller there is an uncertainty that corresponds to a certain probability.

$$\begin{aligned} \text{degrade}(a_1) = \pi_1 \Rightarrow\ a_1 = \text{degrade}^{-1}(\pi_1) \\ \text{degrade}(a_0) = \pi_0 \Rightarrow\ a_0 = \text{degrade}^{-1}(\pi_0). \end{aligned} \tag{17.21}$$

We can thus define the probabilistic stability margin (PSM) as the change in uncertainty that takes the probability of being unstable from π_0 to π_1

$$\text{PSM} = a_1 - a_0 \tag{17.22}$$

In Fig. 17.4, we see that for

$$\pi_1 = 5.0\,\% \quad \Rightarrow \quad \text{PSM} = 0.596 - 0.150 = 0.446 \tag{17.23}$$

Thus, with the stipulation that the probabilistic robust controller may be unstable for 5% of system configurations, this is nearly a fourfold increase in the amount of uncertainty that the closed-loop system can tolerate. Furthermore, this implies that if the structural stiffness parameters lie in the 3σ range 3.68 to 8.32 N/m, the controller will remain stable 95.0% of the time.

A designer can define an increased probability of instability π_1 that they are willing to accept in exchange for greater uncertainty. Engineers or operators can now make decisions regarding how long active vibration controllers should remain in operation before re-tuning or decommissioning. In harsh environments where structures are subjected to radiation and experience mechanical fatigue, uncertainty in structure parameters will inevitably increase over time.

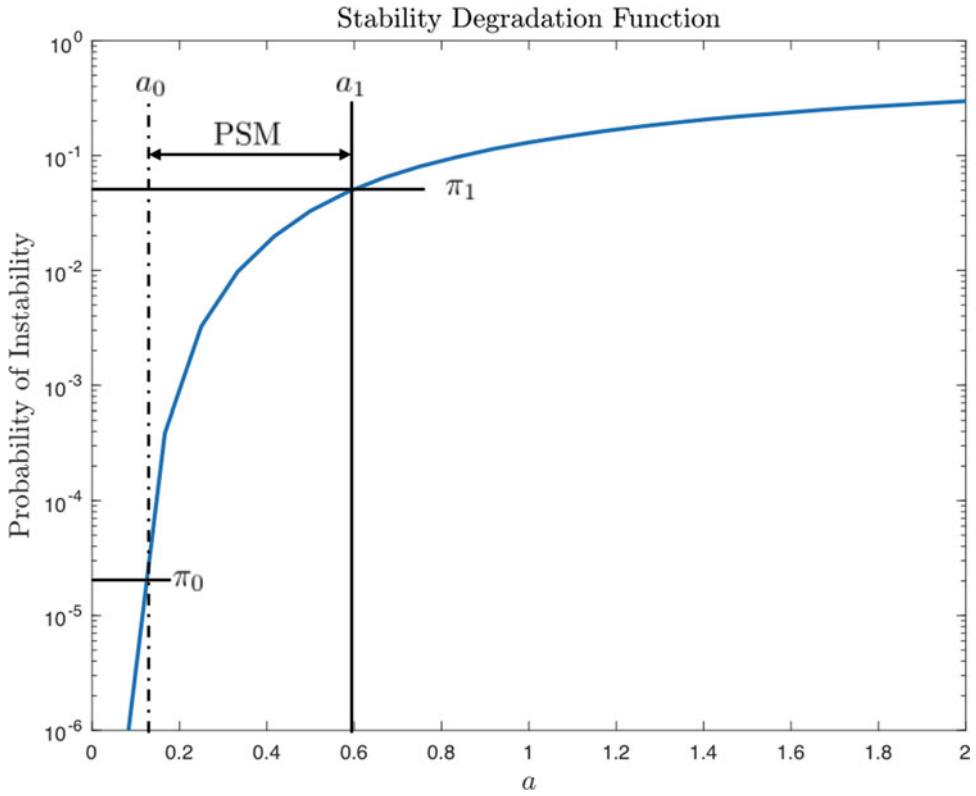

Fig. 17.4 The degradation function for the uncertain structural system. Also shown is the stability margin that is possible

17.5 Conclusion

In this paper, a probabilistic-robust $\mathcal{H}_\infty$ controller has been designed for an uncertain structure. Random parametric uncertainty in the structure's stiffness, and damping, arose from the fact that it could be operating in a harsh environment. In order to capture uncertainty in the low-mid frequency range, uncertainty was described by normally-distributed affine perturbations to the stiffness and damping matrices of the structure.

The controller was synthesized using LMI's, and the probabilistic-robust controller was found using the scenario-based approach, which finds a single fixed controller that meets the LMI criteria for N scenarios. The number of scenarios N is specified to ensure a priori probability bounds on performance and confidence in the estimated performance generated by the scenario-based approach. Closed-loop performance and stability is verified using a posteriori Monte Carlo evaluations.

The notion of probability of stability was introduced. We then defined a degradation function and the probabilistic robust stability margin, and showed how this margin can be used to determine an increase in the amount of uncertainty that the controller can tolerate. For the scenario presented, this was nearly a fourfold increase in uncertainty.

The approach and tools presented may find use in certain critical applications. In applications where structures are exposed to a harsh environment—like high temperatures, high pressures, or radiation—or experience harsh mechanical fatigue, the uncertainty in structural behavior inevitably increases over time. An informed decision, based on a probabilistic safety assessment of the active system, can be made by operators about how long an active controller should remain in operation before the chance that a loss of performance or stability becomes too great.

Appendix: System Model

- The uncertain system description given by Eqs. (17.2), (17.3), and (17.4):

$$\mathcal{M} = \begin{bmatrix} 1 & 0 & 0 \\ 0 & 1 & 0 \\ 0 & 0 & 1 \end{bmatrix}, \quad \mathcal{C}_0 = \begin{bmatrix} 0.049 & -0.024 & 0 \\ -0.024 & 0.049 & -0.024 \\ 0 & -0.024 & 0.049 \end{bmatrix}, \quad \mathcal{K}_0 = \begin{bmatrix} 12 & -6 & 0 \\ -6 & 12 & -6 \\ 0 & -6 & 12 \end{bmatrix}$$

- The $\mathcal{K}_i$ matrices of the structural uncertainty model (17.2):

$$\mathcal{K}_1 = \begin{bmatrix} 1 & 0 & 0 \\ 0 & 0 & 0 \\ 0 & 0 & 0 \end{bmatrix}, \quad \mathcal{K}_2 = \begin{bmatrix} 1 & 1 & 0 \\ 1 & 1 & 0 \\ 0 & 0 & 0 \end{bmatrix}, \quad \mathcal{K}_3 = \begin{bmatrix} 0 & 0 & 0 \\ 0 & 1 & 1 \\ 0 & 1 & 1 \end{bmatrix}, \quad \mathcal{K}_4 = \begin{bmatrix} 0 & 0 & 0 \\ 0 & 0 & 0 \\ 0 & 0 & 1 \end{bmatrix}.$$

- The matrices B_1, B_2, C_1, D_{11}, and D_{12}:

$$B_1 = \begin{bmatrix} 0 & 0 & 0 \\ 0 & 0 & 0 \\ 0 & 0 & 0 \\ 0 & 0 & 0 \\ 1 & 3 & 0 \\ 0 & -3 & 0 \end{bmatrix}, \quad B_2 = \begin{bmatrix} 0 \\ 0 \\ 0 \\ 0 \\ 1 \\ -1 \end{bmatrix}, \quad C_1 = \begin{bmatrix} 0 & 0 & 1 & 0 & 0 & 0 \\ 0 & 0 & 0 & 0 & 3 & 0 \\ 0 & 0 & 0 & 0 & 0 & 0 \end{bmatrix}, \quad D_{11} = \begin{bmatrix} 0 & 0 & 0 \\ 0 & 0 & 0 \\ 0 & 0 & 0 \end{bmatrix}, \quad D_{12} = \begin{bmatrix} 0 \\ 0 \\ 1 \end{bmatrix}.$$

Acknowledgements This research was performed under appointment to the Rickover Fellowship in Nuclear Engineering.

References

1. Tempo, R., Calafiore, G., Dabbene, F.: Randomized Algorithms for Analysis and Control of Uncertain Systems with Applications, 2nd ed. Springer, London (2013)
2. Calafiore, G., Campi, M.: The scenario approach to robust control design. IEEE Trans. Autom. Control **51**(5), 742–753 (2006)
3. Zhou, K., Doyle, J.C.: Essentials of Robust Control, 1st ed. Prentice Hall, Upper Saddle River, New Jersey (1999)
4. Green, M., Limebeer, D.J.: Linear Robust Control, 1st ed. Dover Publications, Mineola, New York (2012)
5. Young, P.M., Newlin, M.P., Doyle, J.: μ analysis with real parametric uncertainty. In: 30th Conference on Decision and Control, pp. 1251–1256 (1991)
6. Doyle, J., Packard, A., Zhou, K.: Review of LFTs, LMIs, and μ. In: Proceedings of the 30th IEEE Conference on Decision and Control, vol. 2, pp. 1227–1232 (1991)
7. Doyle, J.C.: Guaranteed margins for LQG regulators. In: IEEE Trans. Autom. Control **23**(4), 756–757 (1978)
8. Blondel, V.D., Tsitsiklis, J.N.: A survey of computational complexity results in systems and control. Automatica **36**(9), 1249–1274 (2000)
9. Ray, L.R., Stengel, R.: Application of stochastic robustness to aircraft control systems. J. Guid. Control. Dyn. **14**(6), 1251–1259 (1991)
10. Ray, L.R., Stengel, R.F.: A Monte Carlo approach to the analysis of control system robustness. Automatica **29**(1), 229–236 (1993)
11. Marrison, C.I., Stengel, R.: Stochastic robustness synthesis applied to a benchmark control problem. Int. J. Rob. Nonlinear Control **5**(1), 13–31 (1995)
12. Marrison, C., Stengel, R.: Design of robust control systems for a hypersonic aircraft. J. Guid. Control. Dyn. **21**(1), 58–63 (1998)
13. Marrison, C.I., Stengel, R.F.: Robust control system design using random search and genetic algorithms. English **42**(6), 835–839 (1997)
14. Guo, S.-X.: An efficient reliability method for probabilistic h-infinity robust control of uncertain linear dynamic systems. J. Vib. Control **21**(15), 2946–2958 (2014)
15. Ditlevsen, O., Madsen, H.O.: Structural Reliability Methods, 1st ed. Wiley, Chichester (2007)
16. May, B., Beck, J.L.: Probabilistic control for the active mass driver benchmark structural model. Earthq. Eng. Struct. Dyn. **27**(11), 1331–1346 (1998)
17. Crespo, L.G., Kenny, S.P.: Robust control design for systems with probabilistic uncertainty. Technical report NASA/TP?2005?213531, NASA (2005)
18. Crespo, L.G., Kenny, S.P.: Reliability-based control design for uncertain systems. J. Guid. Control. Dyn. **28**(4), 1–30 (2005)
19. Soize, C.: A comprehensive overview of a non-parametric probabilistic approach of model uncertainties for predictive models in structural dynamics. Sound Vib. **288**(3), 623–652 (2005)

20. Stefanou, G.: The stochastic finite element method: past, present and future. Comput. Methods Appl. Mech. Eng. **198**(9–12), 1031–1051 (2009)
21. Schuëller, G.I.: Computational stochastic mechanics – recent advances. Comput. Struct. **79**(22–25), 2225–2234 (2001)
22. Gahinet, P., Apkarian, P.: A linear matrix inequality approach to $\langle_\infty$ control. Int. J. Rob. Nonlinear Control **4**(4), 421–448 (1994)
23. Boyd, S., El Ghaoui, L., Feron, E., Balakrishnan, V.: Linear Matrix Inequalities in System and Control Theory, vol. 15. SIAM, Philadelphia, Pennsylvania (1994)
24. Grant, M.C., Boyd, S.P.: The CVX Users' Guide. Technical report release 2.1, CVX research (2015)

Chapter 18
Implementation of Piezoelectric Shape Sensors Using Digital Image Correlation

Jason Tran and Jayant Sirohi

Abstract A practical procedure of implementing shape sensors for full-field deformation sensing of a structure is demonstrated in this extended abstract. The sensors are constructed using a piezoelectric film material which is bonded to the surface of a beam structure. The electrical outputs of the sensors are then calibrated such that the modal coordinates of the beam displacement can be measured. Calibration of the sensors is performed by using beam displacement data from high-speed 3D digital image correlation (DIC). Operational modal analysis is used to estimate mode shapes and to extract the modal coordinates from the DIC data. The shape sensor is then implemented by calibrating sensor voltages to the extracted modal coordinates. This extended abstract presents the procedure and results of this methodology on a beam instrumented with rectangular piezoelectric sensors of arbitrary length.

Keywords Digital image correlation · Piezoelectric · Shape Sensor · Modal Analysis · Smart Material

18.1 Introduction

Shape sensors can be used to enable in situ, full-field measurements on the deformation of structures. One example of an application is the measurement of in-flight deflections of an aircraft wing. Using a modal shape sensing approach, only a few sensors are necessary to accurately reconstruct the full-field displacement. In the literature, the use of smart materials to fabricate the sensors is popular because the sensors can be made to measure distributed strains so that signal to noise ratios are high [1]. The distributed sensors can be arbitrarily shaped, and some approaches have demonstrated that modal filtering can be achieved if the sensor is fabricated in a specific shape [2]. Although modal filtering is attractive, the specific shapes can be difficult to implement due to the precision of manufacturing required. The sensors used in this paper are a simple rectangular shape which may be more easily manufactured.

There is a large amount of literature which studies the use of smart materials for shape sensors, but relatively few works actually validate the reconstructed displacements by the sensors against a measured value of displacement. This is in part due to the difficulty of calibrating the sensor output to the desired physical quantity. The specified mechanical constants from manufacturers come in a wide range and the distributed nature of the sensors make it difficult to compare against traditional discrete measurements such as strain gages. This paper addresses the difficulty of calibrating the shape sensors by taking advantage of full-field displacement measurements from digital image correlation (DIC).

Using the modal approach to shape sensing means that only a few sensors are needed for accurate displacement reconstruction, but this will require that sensors are calibrated to modal coordinate rather than the physical displacements measured by DIC. Therefore, mode shapes are estimated from a modal vibration experiment using high-speed 3D DIC, and modal coordinates are extracted from the DIC displacement data. Finally, with both shape sensor voltage output and modal coordinates measurements, the shape sensors can be calibrated so that arbitrary deformations can be reconstructed. The presented example in this paper is of a beam structure with rectangular piezoelectric elements.

J. Tran (✉) · J. Sirohi
The University of Texas at Austin, Department Aerospace Engineering and Engineering Mechanics, Austin, TX, USA
e-mail: jasontran@utexas.edu

C. Niezrecki, J. Baqersad (eds.), *Structural Health Monitoring, Photogrammetry & DIC, Volume 6*,
Conference Proceedings of the Society for Experimental Mechanics Series, https://doi.org/10.1007/978-3-319-74476-6_18

18.2 Calibration Procedure Applied to Beam Shape Sensors

A beam structure is used to demonstrate the calibration procedure for shape sensors. The beam structure used is made from carbon fiber and has a total of six rectangular sensors of various lengths bonded to the surface as shown in Fig. 18.1. The charge output from the sensors is conditioned using a charge amplifier circuit. The beam is excited using a shaker which the beam is directly mounted onto. The experimental setup used for digital image correlation in the modal vibration test is shown in Fig. 18.2. Throughout all tests, sensor voltages and displacements from digital image correlation are measured simultaneously.

The calibration procedure can be shortly summarized as follows: (1) Estimate the mode shapes of the structure, (2) Extract modal coordinates from measured DIC displacements, (3) Use a least squares solution to calibrate sensor voltages to modal coordinates. Finally, the modal coordinates as estimated by the shape sensors can be used to reconstruct the displacement shape of the structure.

In order to estimate the mode shapes of the beam, a modal vibration experiment is performed. A random shaker input voltage signal is created and processed using a low-pass filter so that the excitation signal only contains energy in the first two modes. The natural excitation technique (NExT) and eigensystem realization algorithm (ERA) are then used to estimate mode shapes using measured displacements from DIC [3]. With the mode shapes known the modal coordinates can be extracted by solving the modal expansion equation at all times

$$\{w_{DIC}\} = [\Phi_{DIC}]\{\eta_{DIC}\}$$

where $\{w_{DIC}\}$ is a M x 1 vector of the out of plane displacements as measured at M points by DIC, $[\Phi_{DIC}]$ is a M x N matrix of estimated mode shapes where N is the number of mode shapes, and $\{\eta_{DIC}\}$ is a N x 1 vector of modal coordinates to be solved for. Here $M \gg N$, because only a few modes are necessary to reconstruct the displacement to good accuracy. In the beam experiment $M = 1000$ while $N = 2$, thus the system is an overdetermined and may be easily solved at all times.

With the modal coordinates known at all times, the sensor outputs can be calibrated. The goal is to calculate a calibration matrix $[C]$ such that the following equation can be used to convert sensor voltage to modal coordinates

$$\{\eta_{sensor}\} = [C]\{V_{sensor}\}$$

Fig. 18.1 A beam with rectangular piezoelectric elements (3 elements on each side)

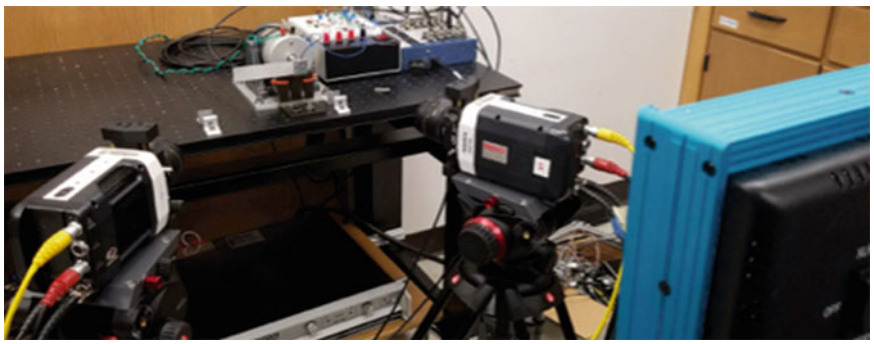

Fig. 18.2 Experimental setup for modal vibration testing with DIC

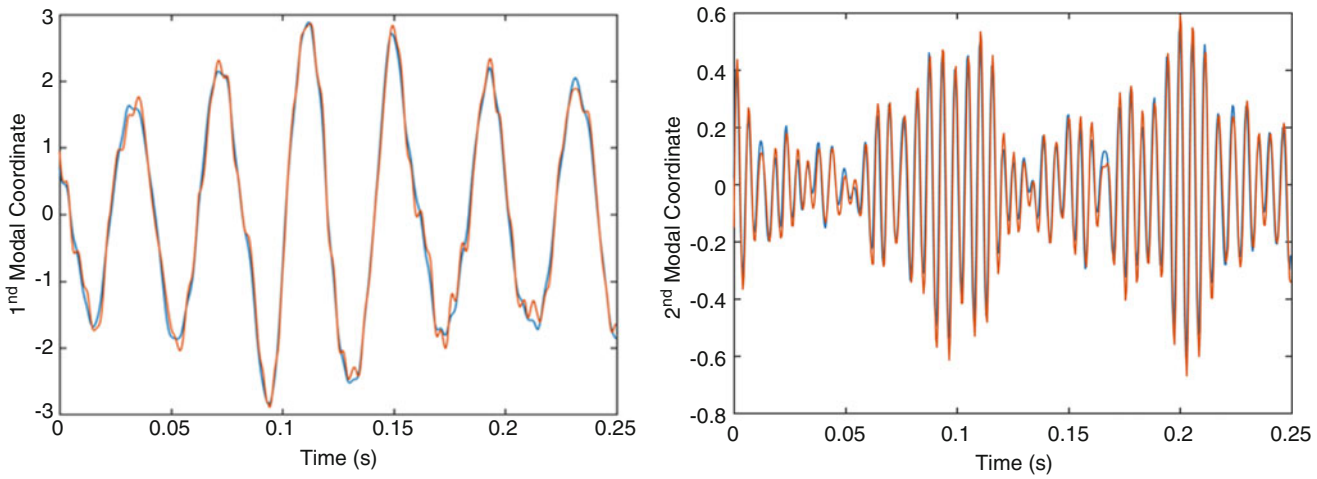

Fig. 18.3 Comparison of modal coordinates as measured by DIC (blue) and by calibrated shape sensors (orange)

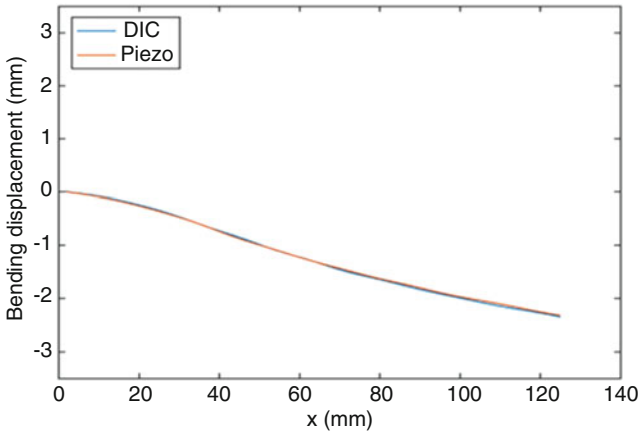

Fig. 18.4 Comparison of displacement measured by DIC versus reconstruction by calibrated shape sensor at a point in time

where $\{\boldsymbol{\eta}_{sensor}\}$ is a vector of modal coordinates as estimated by the sensor at point in time and $\{\boldsymbol{V}_{sensor}\}$ is a vector of sensor voltage measurements a point in time. The calibration matrix $[\boldsymbol{C}]$ would be of size N x P where P is the number of different sensors used. In general, $P > N$, so that the instrumented beam is made robust against failure of a few sensors. To calculate the matrix $[\boldsymbol{C}]$, an intermediate matrix $[\boldsymbol{D}]$ is built by using the modal coordinates from DIC and sensor voltage measurements from a calibration case. The $[\boldsymbol{D}]$ matrix is built row by row by solving

$$\{\boldsymbol{V}_{sensor}\}_i = [\boldsymbol{\eta}_{DIC}]\,\{\boldsymbol{D}\}_i \qquad i = \mathbf{1}, \ldots, \boldsymbol{P}$$

where $\{\boldsymbol{V}_{sensor}\}_i$ is a vector of sensor i voltage at all times, $[\boldsymbol{\eta}_{DIC}]$ is a matrix which contains modal coordinates from all the modes throughout time, and $\{\boldsymbol{D}\}_i$ is a vector containing the $i^{'}th$ row of matrix $[\boldsymbol{D}]$. The pseudoinverse of matrix $[\boldsymbol{D}]$ is then used to find matrix $[\boldsymbol{C}]$ so that sensor voltage outputs can be directly used to estimate modal coordinates. With the modal coordinates and mode shapes, beam displacements can be calculated. Figure 18.3 demonstrates that modal coordinate estimated by DIC and shape sensors are comparable for a beam undergoing random excitation. Figure 18.4 compares displacements directly measured by DIC versus displacements reconstructed by the shape sensor at a point in time. The results indicate that this calibration method of implementing shape sensors is able to achieve measurements which are comparable to DIC. The calibration method is generic and may be applied to structures other than beams. The challenge associated with implementing the shape sensors on more complex structures is the placement of piezoelectric sensors so that all the desired modes are sensed. The authors are applying the method to a plate structure which is undergoing both bending and twisting deformation.

References

1. Baz, A., Poh, S., Gilheany, J.: A multi-mode distributed sensor for vibrating beams. J. Sound Vib. **165**, 481–495 (1993)
2. Lee, C.-K., Moon, F.C.: Modal sensors/actuators. J. Appl. Mech. **57**, 434–441 (1990)
3. Caicedo, J.M.: Practical guidelines for the natural excitation technique (NExT) and the eigensystem realization algorithm (ERA) for modal identification using ambient vibration. Exp. Tech. **35**, 52–58 (2010)

Chapter 19
Variable Amplitude Fatigue Testing Apparatus and Its Dynamical Characterization

Hewenxuan Li and David Chelidze

Abstract A modified version of variable amplitude fatigue testing rig suitable for studying the effects of crack breathing phenomenon under variable *R*-ratios is presented. This system is intended to investigate the interaction between fatigue damage evolution and structural dynamics, and apply the acquired understanding to practical fatigue life prediction. Generalized frequency response function, sine-sweep, and restoring force surface methods were used to identify and characterize nonlinearities, and estimate the corresponding parameters. A simple, two-degrees-of-freedom model development and experimentally validation are also presented.

Keywords Dynamical fatigue testing · Nonlinear system identification · Restoring force surface

19.1 Introduction

Variable amplitude fatigue testing rig [2] in Nonlinear Dynamics Laboratory at University of Rhode Island is modified to investigate the effects of crack breathing phenomenon. The layout of the contact pins between inertial mass blocks and notched beam specimen has been changed to four symmetrical contacts from the previous three-point implementation [2]. This testing rig uses inertial forces to load the specimen and it allows reconfigurations to adapt various specimen sizes, changes in structural components and instrumentation. It is designed to be used as a flexible platform to study the interaction between structural dynamics and fatigue crack propagation.

For the current investigation, zero mean stress at the tip of the crack is of main interest. In order to make sure the tip of the crack undergoes such stress field at its equilibrium position, a more streamlined and robust air preparation system was implemented to give identical pressure inside of the two pneumatic cylinders and to maintain it at a target value during the test. Moreover, this pneumatic layout can be changed easily for fatigue tests at any *R*-ratios by adding another electric proportional regulator to the pneumatic line.

19.2 Experimental Approach

Because of these modifications made to the test rig, the dynamics of the system can undergo a considerable change. Therefore, the characterization and modeling of the testing rig has to be reevaluated to design further fatigue experiments. The prior testing has identified the nonlinear features of the system [2, 5], and thus, we need to reevaluate out system using nonlinear system identification. We focus on the detection, characterization of nonlinearity, and parameter estimation of the system. There are variety of nonlinear identification methods used in practice. However, there are still no standard methodologies use for specific systems [3, 6]. In our case, the test for homogeneity or frequency response function overlay (FRFO) [4] has been applied to the detection of nonlinearity, which tests amplitude-dependent frequency of motion for nonlinear systems [1]. During the modal analysis, a beam specimen without initial notch has been used to remove the influence of the damage on the system identification. Then, the *restoring force surface* (RFS) method was utilized to non-parametrically characterize the observed nonlinearity [7, 8].

H. Li · D. Chelidze (✉)
Mechanical, Systems and Industrial Engineering Department, University of Rhode Island, Kingston, RI, USA
e-mail: hewenxuan_li@my.uri.edu

C. Niezrecki, J. Baqersad (eds.), *Structural Health Monitoring, Photogrammetry & DIC, Volume 6*,
Conference Proceedings of the Society for Experimental Mechanics Series, https://doi.org/10.1007/978-3-319-74476-6_19

19.3 New Mechanical Layout

As a modified version of the previous layout [2] is shown in Fig. 19.1. In the current design, we mainly altered the load configuration from three-point to four-point contact. In this way, the crack tip can experience cyclic opening and closure (which is also called the crack breathing phenomenon) under various excitation scenarios. As fatigue crack propagates, the structural parameters will change accordingly, which in turn will alter the loads on the crack. Therefore, we can study the mutual interaction between the changes in structural parameters and fatigue evolution. The core of this testing rig is the slip table which is driven by a LDS electromagnetic shaker. The specimen is one-side notched beam to focus test on stage II fatigue. It is pin-pin supported on the slip table. Two identical mass blocks, which are actuated linearly by two identical pneumatic cylinders, are pushed toward the beam to exert inertial force on the initiated crack. The preload forces between the mass blocks and the specimen are now controlled by a electric proportional regulator which can maintain the pneumatic pressure within 5% of the interested pressure level. Redundant parts of the previous air preparation system have been replaced by a simpler design. This provides a much more stable performance during the dynamic testing. In order to keep a zero mean load on the crack tip, pressure in the pneumatic cylinders need to be identical at all time.

19.4 Experimental Results

From the frequency response function overlay in Fig. 19.2, the peak of the first mode moves slightly toward the low frequency as the input excitation level increases. This is an indication of softening spring stiffness. Meanwhile, the amplitude of the FRF proportionally increases with the excitation level. This indicates nonlinear damping in the testing rig [1]. In order to get more insight into the nature of the system, the RFS characterization method has been used to investigate the nonlinear behavior. The system was exited by band limited white gaussian noise with different input levels. Two sets of data have been used for the surface reconstruction. One set was acquired under the same clamping pressure with varying forcing amplitudes, the other was established under the same forcing amplitude with increasing clamping pressures. From the slice views of the reconstructed force surfaces (Fig. 19.3), a softening spring nonlinearity as well as stick-slip hysteresis can be observed, and this phenomenon gets prominent with increasing either the input excitation or the clamping pressure to the beam specimen. This trend indicates the nonlinear stiffness can be a result of the increasing pneumatic stiffness of the air inside of the cylinders. From the force-velocity slice overlay, the frictional damping gets more prominent while the pressure or excitation level increases. This can be described as a combination of viscous and Coulomb damping.

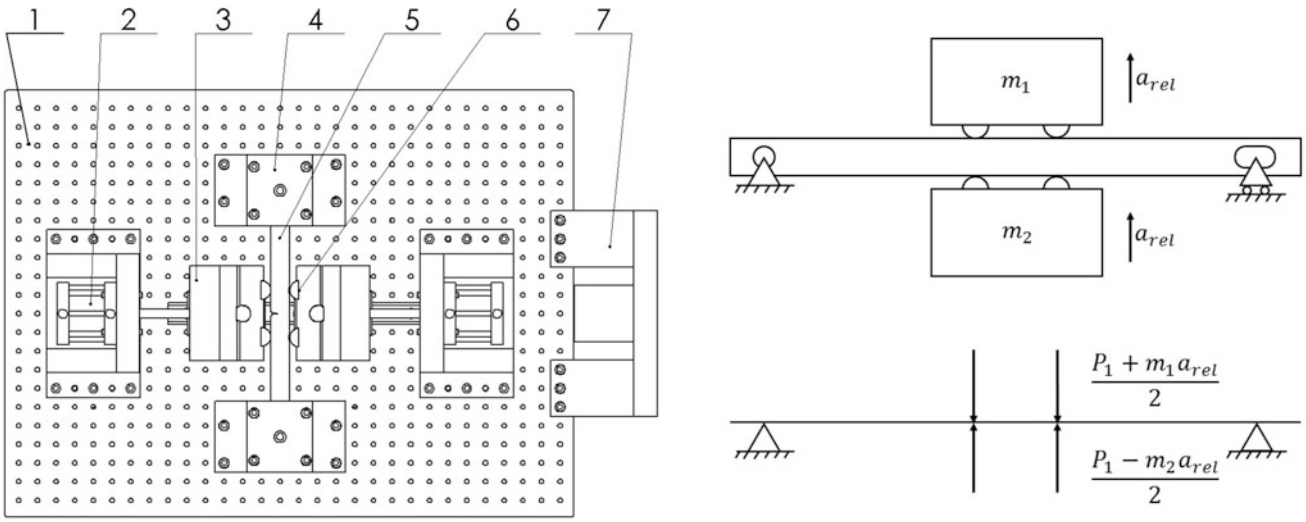

Fig. 19.1 Left: Schematics of the current layout of the slip table: 1. Slip table; 2. Pneumatic cylinder(s); 3. Mass block(s); 4. Beam support(s); 5. Specimen; 6. Contact(s); and 7. Connector to the shaker. Right: Current layout of the contacts

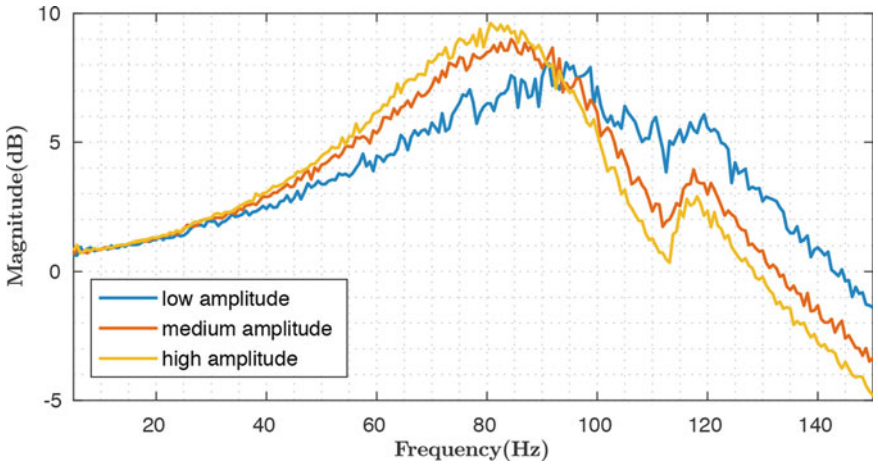

Fig. 19.2 Frequency response function overlay

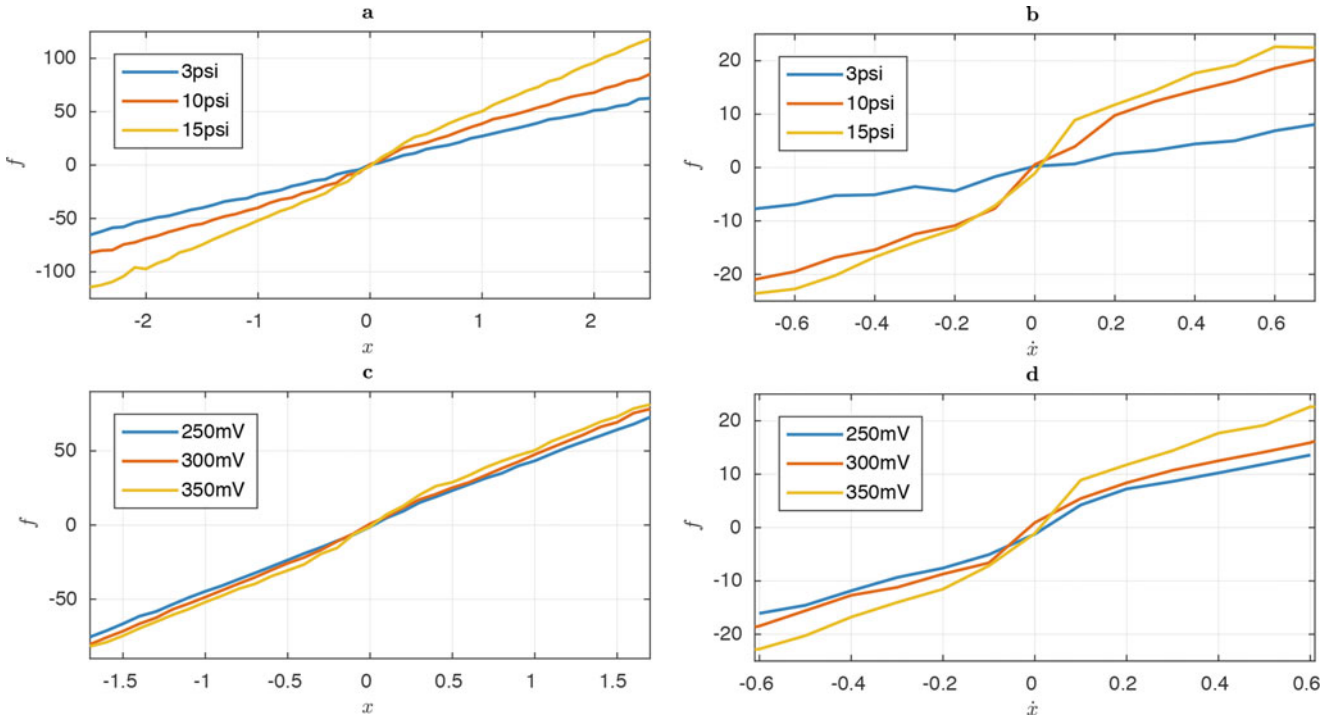

Fig. 19.3 (**a**) RFS force-displacement slice overlay under the same shaker input. (**b**) RFS force-velocity slice overlay under the same shaker input. (**c**) RFS force-displacement slice overlay under the same clamping pressure. (**d**) RFS force-velocity slice overlay under the same clamping pressure

References

1. Allemang, R.J., Brown, D.L., Rost, R.W.: Experimental Modal Analysis and Dynamic Component Synthesis. Volume 2. Measurement Techniques for Experimental Modal Analysis. Technical report, Department of Mechanical and Industrial Engineering, Cincinnati University, OH (1987)
2. Falco, M., Liu, M., Nguyen, S.H., Chelidze, D.: Nonlinear system identification and modeling of a new fatigue testing rig based on inertial forces. J. Vib. Acoust. **136**(4), 041001 (2014)
3. Kerschen, G., Worden, K., Vakakis, A.F., Golinval, J.-C.: Past, present and future of nonlinear system identification in structural dynamics. Mech. syst. signal process. **20**(3), 505–592 (2006)
4. Newland, D.E.: An introduction to random vibrations, spectral & wavelet analysis. Courier Corporation (2012)
5. Nguyen, S.H., Falco, M., Liu, M., Chelidze, D.: Different fatigue dynamics under statistically and spectrally similar deterministic and stochastic excitations. J. Appl. Mech. **81**(4), 041004 (2014)

6. Noël, J.-P., Kerschen, G.: Nonlinear system identification in structural dynamics: 10 more years of progress. Mech. Syst. Signal Process. **83**, 2–35 (2017)
7. Worden, K.: Data processing and experiment design for the restoring force surface method, part I: integration and differentiation of measured time data. Mech. Syst. Signal Process. **4**(4), 295–319 (1990)
8. Worden, K: Data processing and experiment design for the restoring force surface method, part II: choice of excitation signal. Mech. Syst. Signal Process. **4**(4), 321–344 (1990)

Chapter 20
An Efficient Likelihood-Free Bayesian Computation for Model Selection and Parameter Estimation Applied to Structural Dynamics

A. Ben Abdessalem, N. Dervilis, D. Wagg, and K. Worden

Abstract Model selection is a challenging problem that is of importance in many branches of the sciences and engineering, particularly in structural dynamics. By definition, it is intended to select the most plausible model among a set of competing models, that best matches the dynamic behaviour of a real structure and better predicts the measured data. The Bayesian approach is based essentially on the evaluation of a likelihood function and is arguably the most popular approach. However, in some circumstances, the likelihood function is intractable or not available even in a closed form. To overcome this issue, likelihood-free or approximate Bayesian computation (ABC) algorithms have been introduced in the literature, which relax the need of an explicit likelihood function to measure the degree of similarity between model prediction and measurements. One major issue with the ABC algorithms in general is the low acceptance rate which is actually a common problem with the traditional Bayesian methods. To overcome this shortcoming and alleviate the computational burden, a new variant of the ABC algorithm based on an ellipsoidal nested sampling technique is introduced in this paper. It has been called ABC-NS. This paper will demonstrate how the new algorithm promises drastic speedups and provides good estimates of the unknown parameters. To demonstrate its practical applicability, two illustrative examples are considered. Firstly, the efficiency of the novel algorithm to deal with parameter estimation is demonstrated using a moving average process based on synthetic measurements. Secondly, a real structure called the VTT benchmark, which consists of a wire rope isolators mounted between a load mass and a base mass, is used to further assess the performance of the algorithm in solving the model selection issue.

Keywords Model selection · Structural dynamics · Likelihood-free Bayesian computation · Moving average process · Wire rope isolators

20.1 Introduction

Many branches of the sciences and engineering, including structural dynamics involve a choice between a set of models. This is quite challenging, mainly when a large set of competing models with different numbers of parameters are available. In practice, one may assume a set of plausible models and then estimate the evidence associated to each one using a sophisticated statistical tool. The Bayesian approach is one of the most popular techniques to deal with model selection and parameter estimation issues. Arguably, the most popular algorithm in this class of methods is the one proposed by Green and called Reversible-Jump Markov chain Monte Carlo (RJ-MCMC), readers can go for more details about the RJ-MCMC in [1] and for an extensive review of the different methods to [2]. The Bayesian method requires the definition of a likelihood function; however, in some circumstances, the likelihood function is computationally intractable or not available. To overcome this shortcoming, a class of methods called likelihood-free or approximate Bayesian computation (ABC) algorithms have been proposed in the literature. ABC has gained popularity in recent years owing to its easy implementation, flexibility and good performance. It has been applied in a wide range of applications and recently in structural dynamics [3–6]. The most popular variants are the ABC-MCMC [7] and ABC-SMC [8]. Those algorithms can be applied when it is possible to generate data from the model, offering the possibility to make Bayesian inference relying only on an appropriate choices of summary statistics. Despite their numerous advantages and popularity, the ABC algorithms suffer from a difficulty in maintaining a

A. Ben Abdessalem (✉)
LARIS, EA, 7315, Angers University, Angers, France
e-mail: anis.ben-abdessalem@univ-angers.fr

N. Dervilis · D. Wagg · K. Worden
Dynamics Research Group, Department of Mechanical Engineering, University of Sheffield, Sheffield, UK

C. Niezrecki, J. Baqersad (eds.), *Structural Health Monitoring, Photogrammetry & DIC, Volume 6*,
Conference Proceedings of the Society for Experimental Mechanics Series, https://doi.org/10.1007/978-3-319-74476-6_20

reasonable acceptance rate over the populations. In the framework of this paper, a novel ABC algorithm based on an efficient ellipsoidal sampling method [9, 10] is proposed to enhance the capability of the ABC algorithm to deal with parameter estimation and model selection issues. To demonstrate the efficiency of the algorithm, two illustrative examples in structural dynamics have been proposed. The proposed examples will show that the parsimony principle (i.e., simpler models are automatically preferred unless a more complicated model provides a significantly better fit to the data) is naturally embedded in the ABC-NS algorithm. Moreover, by employing a nested sampling technique, the ABC algorithm can be substantially accelerated, offering the possibility to consider a relatively large number of competing models.

The paper is organised as follows. Section 20.2 will shortly go through the basics of the Bayesian paradigm for parameter estimation and model selection and will introduce the novel algorithm. Sections 20.3 and 20.4 are devoted to numerical and experimental examples and forms the core of the paper. Section 20.5 concludes the paper.

20.2 Bayesian Inference

20.2.1 Bayesian Method for Parameter Estimation

In this section, a brief introduction to the Bayesian and approximate Bayesian methods is given. In the Bayesian method, the posterior probability density, $p(\theta|u)$ given observed data u and a model $\mathcal{M}$, can be computed using Bayes' Theorem:

$$p(\theta|u) = \frac{p(\theta)\mathcal{L}(u|\theta)}{\int_\theta p(\theta)\mathcal{L}(u|\theta)\mathrm{d}\theta} \propto p(\theta)\mathcal{L}(u|\theta) \tag{20.1}$$

where $p(\theta)$ is the prior probability of θ and $\mathcal{L}(u|\theta)$ is the likelihood function. The denominator is a normalising constant.

However, as mentioned earlier, explicit forms for likelihood functions are rarely available. The ABC methods approximate the likelihood by evaluating the discrepancy between the observed data and the data generated by a simulation using a given model, yielding an approximate form of Bayes' Theorem:

$$p(\theta|\Delta(u,u^*) < \varepsilon) \propto p(\theta)p\left(\Delta(u,u^*) < \varepsilon|\theta\right) \tag{20.2}$$

where $u^* \sim f(\cdot|\theta)$ are the simulated data, $\Delta(\cdot)$ is a discrepancy metric, and $\varepsilon > 0$ is a tolerance threshold (when ε tends towards 0, the approximated posterior distribution is a good approximation of the true posterior distribution).

20.2.2 Bayesian Method for Model Selection

In model selection, usually two or more competing models exist and may support the data u. Assume that k candidate models, $\mathcal{M}_j, j = 1, \ldots, k$, are under consideration, each with associated unknown parameters, θ_j. Here one would like to quantify the relative support from the data for each candidate model. Bayes' Theorem can be applied to compute the posterior probability associated to each candidate model:

$$p(\mathcal{M}_j|u) = \frac{p(u|\mathcal{M}_j)p(\mathcal{M}_j)}{\sum_r p(u|\mathcal{M}_r)p(\mathcal{M}_r)} \tag{20.3}$$

where $p(u|\mathcal{M}_j)$ is the posterior probability of $\mathcal{M}_j$ and $p(\mathcal{M}_j)$ is the prior probability of $\mathcal{M}_j$, in most cases, one assigns equal prior probabilities to each candidate model.

20.2.3 ABC-NS Implementation

In this section, a detailed description of the novel ABC algorithm is given for parameter estimation. The ABC-NS algorithm broadly works following the same scheme as the ABC-SMC algorithm in [8]. The main novelties are in (i) the way of sampling, (ii) the weighting technique adopted from [11] and (iii) instead of dropping one particle per iteration, a proportion

of particles is dropped based on the assigned weights, which speeds-up the algorithm without compromising the precision on the posterior estimates. The iterative process for parameter estimation is detailed in Algorithm 1. The algorithm starts by generating N particles from the prior satisfying the constraint $\Delta(u, u^*) < \varepsilon_1$ (here, u for observed data, u^* for simulated data and ε_1 is the first tolerance value defined by the user). The accepted particles are then weighted (see, Step 9) and the next tolerance threshold is defined based on the discrepancy values ranked in descending order (highest on top, see, step 11) as the $(\alpha_0 N)$th value where α_0 is a proportion of dropped particles defined by the user. Then, one assigns a weight of zero to the dropped particles. After that, the weights of the remaining particles are normalised. From the remaining particles, one selects $\beta_0 N$ particles based on the updated weight values, where β_0 is a proportion of particles the so-called "alive" particles. The alive particles are then enclosed in an ellipsoid in which the mass center μ_1 and covariance matrix $\mathcal{C}_1$ are estimated based on the values of those particles; one denotes this ellipsoid by $\mathcal{E}_1 = (\mu_1, \mathcal{C}_1)$. The generated ellipsoid could be enlarged by a factor f_0 to ensure that the particles on the borders are inside. It should be noted that ellipsoidal sampling was firstly proposed in [12] to improve the efficiency of the nested sampling algorithm which has been widely used for Bayesian inference, mainly in cosmology [13]. Finally, the population is replenished by resampling $(1 - \beta_0)N$ particles inside the enlarged ellipsoid and a re-weighting step is carried out. The procedure is repeated until a stopping criterion defined by the user is met. It should be noted that for model selection, the same scheme shown in Algorithm 1 is followed by considering the candidate models as additional parameters. Thus, one treats the pair $(\mathcal{M}_j, \theta^{(j)})$ with $\mathcal{M}_j$ as a candidate model and $\theta^{(j)}$ its vector of unknown parameters. For a given $(\mathcal{M}_j, \theta^{(j)})$, the pair is accepted or rejected based on a discrepancy value. At the end of the algorithm, the model probability for $\mathcal{M}_j$ is approximated using Eq. (20.4).

$$p(\mathcal{M}_j|u^*) \approx \frac{\text{Accepted particles for } \mathcal{M}_j}{\text{Total number of particles } N} \tag{20.4}$$

In the considered examples, the tuning parameters used to run the ABC-NS algorithm are selected as follows: the number of samples is set to 1000, α_0, β_0 and f_0 are set to 0.3, 0.6 and 1.1, respectively.

20.3 Moving Average Process

In this section, one demonstrates the efficiency of the ABC-NS algorithm to deal with parameter estimation (or model calibration). One considers a moving average (MA) process defined by:

$$y_\ell = e_\ell + \sum_{i=1}^{d} \theta_i e_{l-i} \tag{20.5}$$

where e_ℓ is an independently and identically distributed (iid) sequence of a standard Gaussian $\mathcal{N}(0, 1)$; d and ℓ are set to 2 and 1000, respectively.

Denote by $y = [y_1, \ldots, y_l, \ldots, y_\ell]$ the observed data. The objective is to illustrate the ability of the algorithm to sample from the ABC posterior relying on available data and an appropriate choice of summary statistics. Figure 20.1 shows a series of data from a moving average model of order 2 denoted by MA(2). In this example, the quadratic distance between the $d = 2$ first autocovariances is taken as a metric to measure the degree of similarity between simulated and observed data, as in [14]:

$$\Delta(\eta(x), \eta(y)) = \sum_{q=1}^{d} (\tau_{y,q} - \tau_{x,q})^2 \tag{20.6}$$

where the terms $\tau_{y,q}$ and $\tau_{x,q}$ are the autocovariances of y and x (x is the simulated data given a candidate (θ_1, θ_2)), respectively, which are used as summary statistics. They are obtained as $\tau_{y,q} = \sum_{k=q+1}^{\ell} y_k y_{k-q}$ and $\tau_{x,q} = \sum_{k=q+1}^{\ell} x_k x_{k-q}$, respectively.

To avoid unnecessary difficulties, a standard identifiability condition is imposed on this model (see, [14] for further details). In this case of $d = 2$, this condition is fulfilled when the explored space is delimited by imposing the following constraints on the input parameters:

$$-2 < \theta_1 < 2; \quad \theta_1 + \theta_2 > -1; \quad \theta_1 - \theta_2 < -1 \tag{20.7}$$

Algorithm 1 ABC-NS SAMPLER

Require: u: observed data, $\mathcal{M}(\cdot)$: model, $\varepsilon_1, N, \alpha_0, \beta_0, f_0$

set $t = 1$
for $i = 1, \ldots, N$ **do**
  repeat
    Sample θ^* from the prior distributions $p(\cdot)$
    Simulate u^* using the model $\mathcal{M}(\cdot)$
  until $\Delta(u, u^*) < \varepsilon_1$
  set $\Theta_i = \theta^*$, $e_i = \Delta(u, u^*)$
end for
Associate a weight to each particle: $\omega_i \propto \frac{1}{\varepsilon_1}\left(1 - (\frac{e_i}{\varepsilon_1})^2\right)$
Sort e_i in descending order and store them in e^t.
Define the next tolerance threshold $\varepsilon_2 = e^t(\alpha_0 N)$
Drop particles with $\Delta(u, u^*) \geq \varepsilon_2$, $\underset{(1-\alpha_0)N}{\omega_{j=1:\alpha_0 N}} = 0$
Normalise the weights such that $\sum_{i=1} \omega_i = 1$
Select $\mathcal{A}^t = \beta_0 N$ particles from the remaining based on the weights
Define the ellipsoid by its centre of the mass and covariance matrix $\mathcal{E}_t = \{\mu_t, \mathcal{C}_t\}$
Enlarge the ellipsoid by f_0 ▷ For simplicity the same notation for the updated ellipsoid is kept
for $t = 2, \ldots, T$ **do**
  for $j = 1, \ldots, (1 - \beta_0)N$ **do**
  repeat
    Sample one particle θ^* inside $\mathcal{E}_{t-1}$
    Simulate u^* using the model $\mathcal{M}(\cdot)$
  until $\Delta(u, u^*) < \varepsilon_t$
  set $\Theta_j = \theta^*$, $e_j = \Delta(u, u^*)$
  end for
    Store the new particles in $\mathcal{S}_t$
    Obtain the new particle set, $\mathcal{N}_{new} = [\mathcal{A}_{t-1}; \mathcal{S}_t]$ with their correspondent distance values e^t
    Sort e^t and define $\varepsilon_{t+1} = e^t(\alpha_0 N)$
    Associate a weight to each particle as in step (9)
    Define the new set of selected particles $\mathcal{A}^t$ as in step (14)
    Update the ellipsoid hyperparameters using $\mathcal{A}^t$, $\mathcal{E}_t = \{\mu_t, \mathcal{C}_t\}$ ▷ The enlargement factor is kept constant
end for

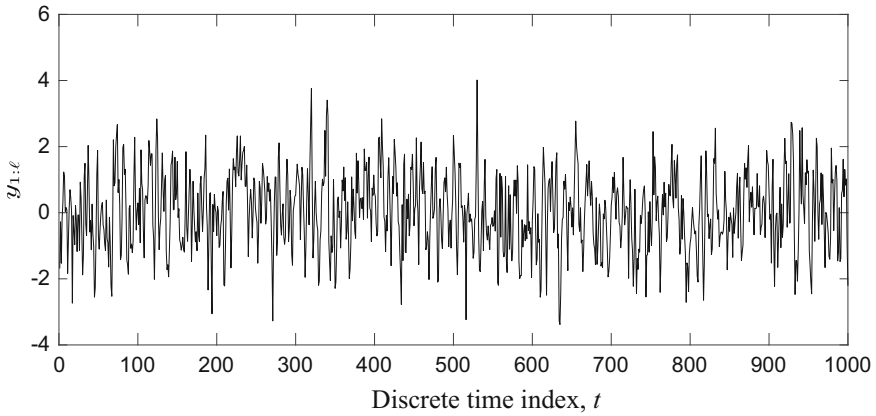

Fig. 20.1 Simulated data from moving average model MA(2) with $(\theta_1, \theta_2) = (0.6, 0.2)$

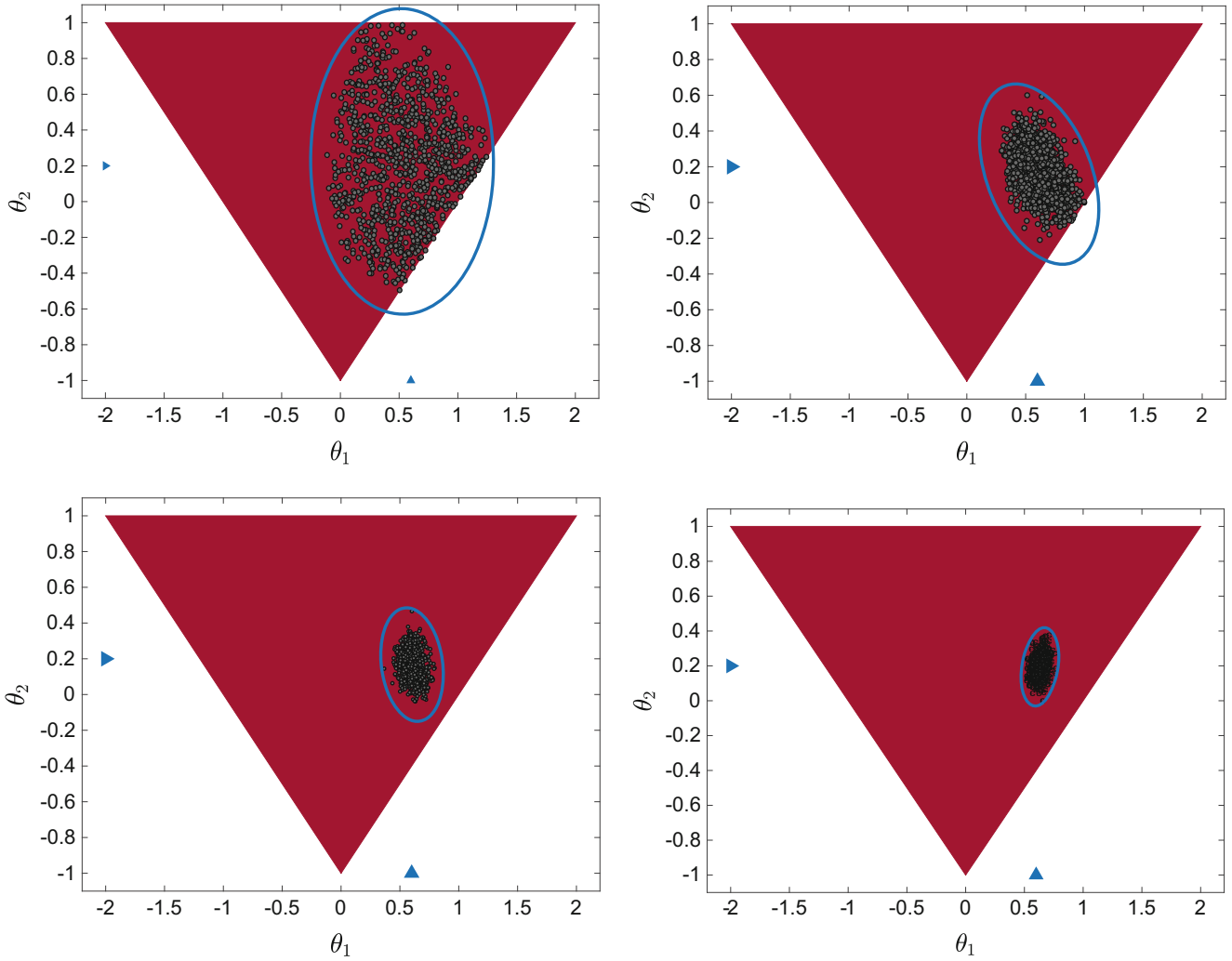

Fig. 20.2 Evolution of the particles distribution over some selected populations, the triangle in red delimits the input space, the blue triangles are the true values

One uses synthetic data for y by generating it from Eq. (20.5) considering $\theta_{true} = (0.6, 0.2)$. The numerical simulation can now be performed using the ABC-NS algorithm with the hyperparameters given in Sect. 20.2.3. From Fig. 20.2, one can see the evolution of the sample distribution over some selected populations for different tolerance threshold values (from left to right, the tolerance values are equal to $\varepsilon_{up-l} = 6.043 \times 10^5$, $\varepsilon_{up-r} = 6.544 \times 10^4$, $\varepsilon_{down-l} = 1.002 \times 10^3$, $\varepsilon_{down-r} = 0.178$) enclosed in an ellipsoid. The histograms of the particles at the last population are shown in Fig. 20.3 from where one can see that those histograms are well peaked around the true values. Table 20.1 shows the statistics of the posterior estimates, one can see that the posterior estimates are well estimated from the last population with reduced uncertainty.

20.4 Example 2: Characterisation of the Dynamics of a Wire Rope Isolator Using ABC-NS

20.4.1 Experimental Set-Up

The second example consists of characterising the dynamics of a wire rope isolator (WRI) used for vibration isolation. WRIs have found a vast number of application in medical equipment and military hardware to mention just a few, due to their superior performance for the isolation of impact and vibration. However, the dynamical properties of mechanical isolators are typically nonlinear and these characteristics are seldom well defined, which may cause problems for the design

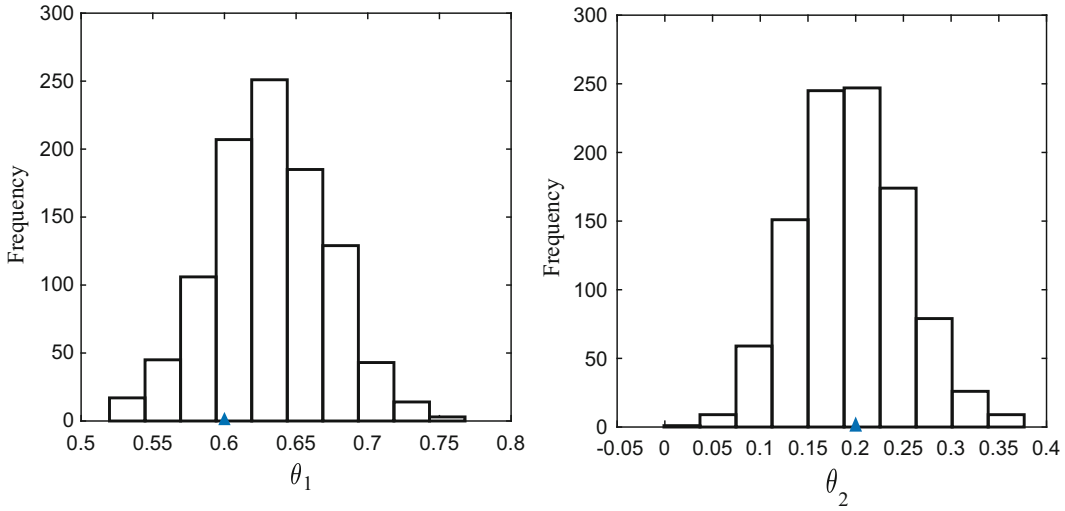

Fig. 20.3 Histograms of the MA(2) model parameters

Table 20.1 Statistics of the posterior estimates for the MA(2) model

Parameter	Mean value	Std. dev.	Quantiles	
			2.5%	97.5%
θ_1	0.6318	0.04044	0.5522	0.7115
θ_2	0.1942	0.0569	0.0871	0.3108

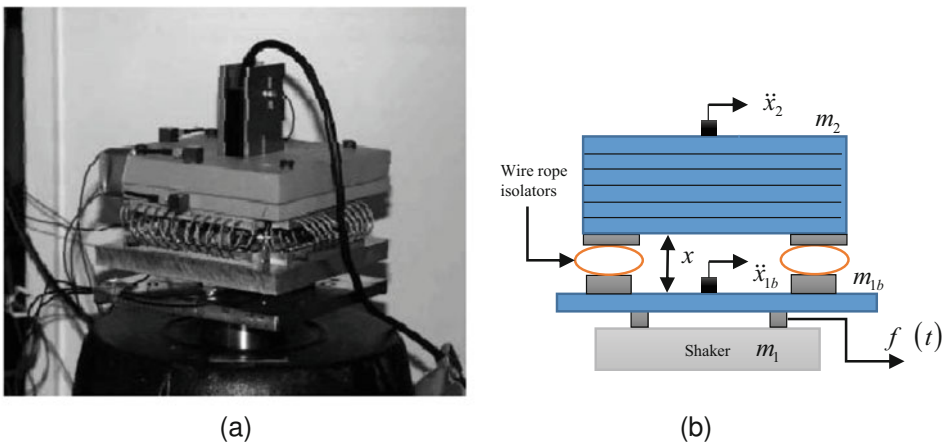

Fig. 20.4 (**a**) Experimental set-up: configuration of the experiment, (**b**) schematic illustration of the dynamical system under consideration

calculations and computer simulations. The system considered in this paper has been proposed within the framework of the European COST Action F3 working group in "Identification of non-linear systems" [15]. The aim of this benchmark was to identify the dynamic properties of resilient mounts used for vibration isolation in industrial applications using different methods. Figure 20.4a shows the experimental set-up of the WRI mounted between a load mass m_2 and a base mass m_{1b} while Fig. 20.4b is a schematic illustration. The applied excitation is produced by an electro-dynamic shaker and corresponds to a white noise sequence, low-pass filtered at 400 Hz. The motion and forces experienced by the isolators are measured; in particular, the acceleration responses $\ddot{x}_2$ and $\ddot{x}_{1b}$ of the load mass and bottom plate, the applied f and the relative displacement x_{12} between the top and bottom plates. For more details concerning the experimental set-up and the methods presented for the identification of the system, the reader is referred to the following references [16–19].

In this Benchmark, 5 excitation amplitude levels have been considered, varying from 0.5 to 8 Volts. In the present work, one is interested in the experimental data obtained for an excitation amplitude equal to 4 Volts. Figure 20.5a shows the relative displacement while Fig. 20.5b shows the inertial force versus the relative displacement. From Fig. 20.5b, one may

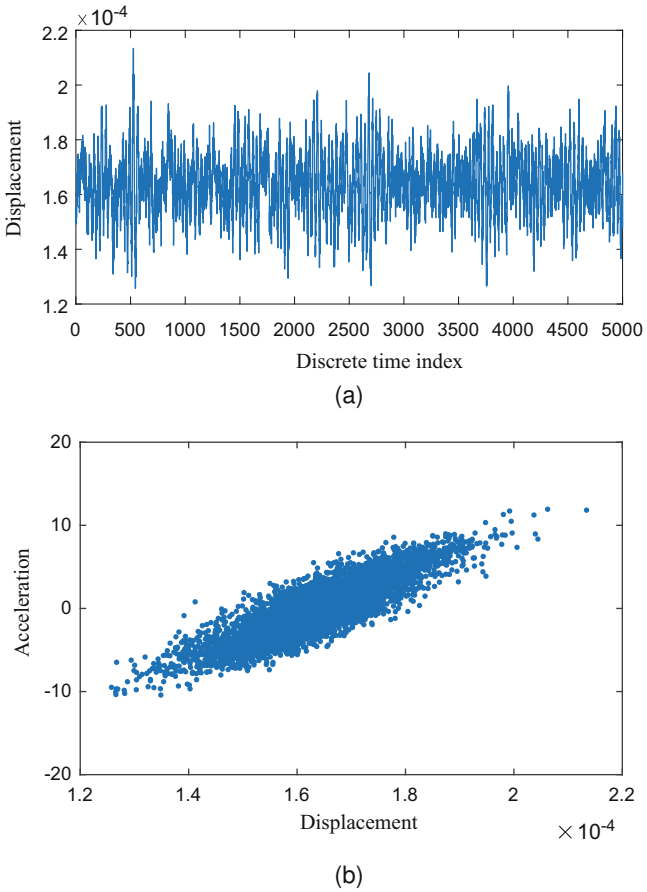

Fig. 20.5 (**a**) Displacement, (**b**) inertial force versus relative displacement under an excitation amplitude of 4 Volts

observe a hysteretic behaviour of the WRI. This leads one to select the popular Bouc-Wen model as a competing model. The model has been used previously in similar problems in [20, 21].

20.4.2 Selection of the Competing Models

The general single-degree-of-freedom (SDOF) hysteretic system described in the terms of Wen [22], is represented below:

$$m\ddot{y} + g(y, \dot{y}) + z(y, \dot{y}) = f(t) \tag{20.8}$$

where $g(y, \dot{y})$ is the polynomial part of the restoring force, $z(y, \dot{y})$ is the hysteretic part and $f(t)$ is the excitation force, m is the mass, and the polynomial part of the restoring force is assumed to be linear given by the following equation:

$$g(y, \dot{y}) = c\dot{y} + ky \tag{20.9}$$

The hysteretic component is defined by Wen [22] via the additional equation of motion:

$$\dot{z} = \begin{cases} -\alpha|\dot{y}|z^n - \beta\dot{y}|z^n| + A\dot{y}, & \text{for } n \text{ odd} \\ -\alpha|\dot{y}|z^{n-1}|z| - \beta\dot{y}|z^n| + A\dot{y}, & \text{for } n \text{ even} \end{cases} \tag{20.10}$$

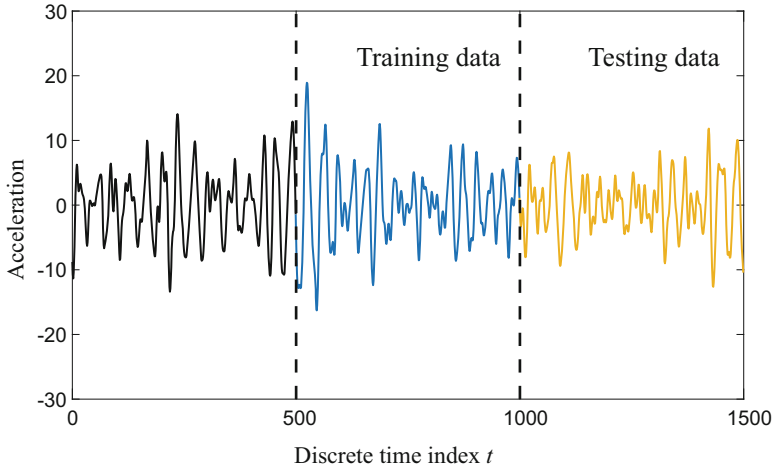

Fig. 20.6 Training and testing data sets using an excitation amplitude of 4 Volts

The parameters α, β and n govern the shape and the smoothness of the hysteresis loop. It should be noted that the equations offer a simplification from the point of view of parameter estimation, in that the stiffness term in Eq. (20.9) can be combined with the $A\dot{y}$ term in the state equation for z. The reader can refer to [23] for full details.

A set of competing models have been proposed to capture the dynamics of wire rope isolators. First, although the problem is nonlinear, a linear model is considered at the aim to analyse the behaviour of the algorithm. Then, four models based on the Bouc-Wen model have been defined by varying n in the equations of motion from 1 to 4. In total, five competing models are considered and denoted by:

$$\mathcal{M}_1 : m\ddot{y} + c\dot{y} + Ay = f(t) \tag{20.11}$$

$$\mathcal{M}_{2:5} : \text{Eqs.}(8) - (10), n = 1 : 4 \tag{20.12}$$

After selecting a set of competing models, one aims to determine the most likely model among the competing ones by estimating the evidence associated to each one based on the available data. The data set contains 1000 samples representing a short recording period of the acceleration of the top plate. The data set is split into training data (from 501 to 1000) and testing data (from 1001 to 1500) as shown in Fig. 20.6. It should be noted that the transient part (from 0 to 500) has been ignored to reduce the effect of initial conditions.

For the implementation of the ABC-NS algorithm, the same set of hyperparameters used previously is kept. Here, one considers the case where there is no prior information preferring some models over the other, so the prior is $p(\mathcal{M}_{i=1:5}) = \frac{1}{5}$. In this example, the tolerance threshold sequence is adaptively defined as mentioned in Algorithm 1. The normalised mean square error (MSE) given by Eq. (20.13) is selected as a metric to measure the discrepancy between the observed and simulated data. Finally, the stopping criterion chosen here is when the difference between two consecutive tolerance thresholds is less than 10^{-5}.

$$\Delta(u^*, u) = \frac{100}{n\sigma_{u^*}^2} \sum_{i=1}^{n} \left(u_i^* - u_i\right)^2 \tag{20.13}$$

where n is the size of the training data, $\sigma_{u^*}^2$ is the variance of the observed acceleration; u^* and u are the observed and simulated accelerations given by the model, respectively.

20.4.3 Results and Discussion

Figure 20.7 shows the model posterior probabilities over some selected populations. One can see that the algorithm converges to $\mathcal{M}_2$. From the same figure, one can see that at higher tolerance values, the algorithm tends to select the linear model (see, the posterior probabilities at populations 7, 13 and 22 for example). This tendency shows that the parsimony principle is

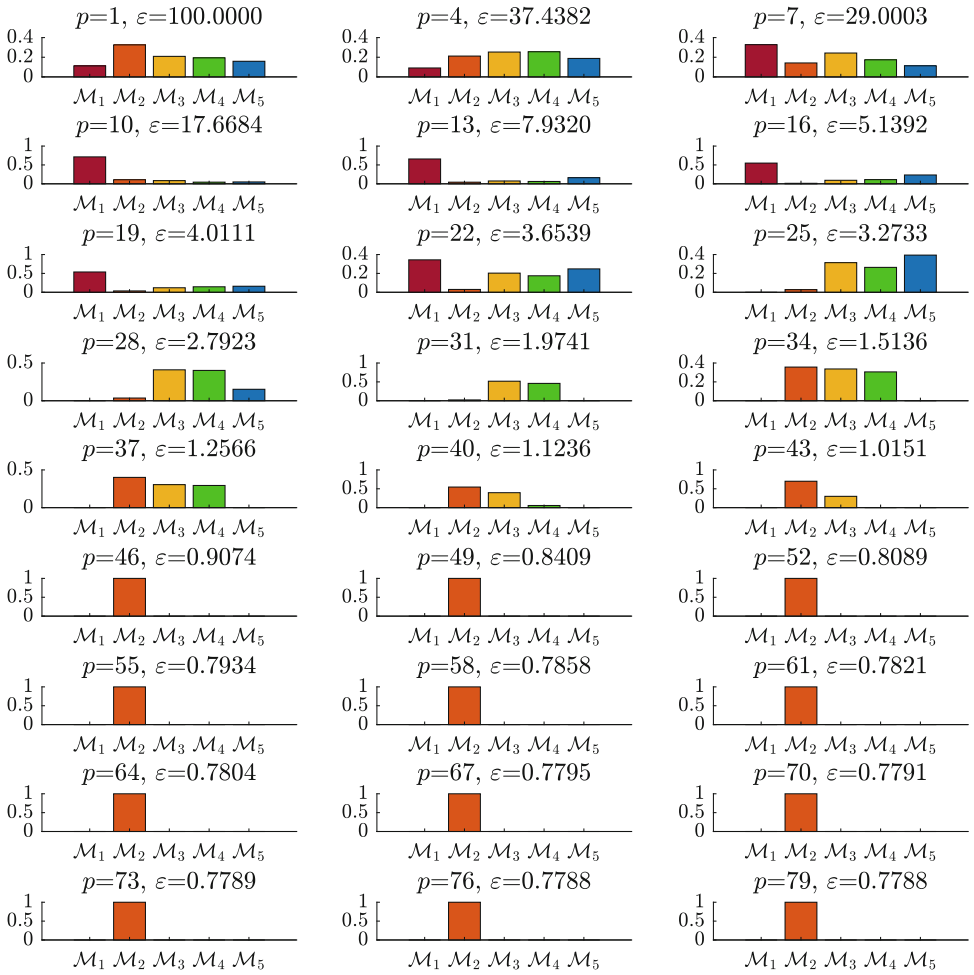

Fig. 20.7 Model posterior probabilities over some selected populations using an excitation amplitude of 4 Volts

naturally embedded in the ABC-NS algorithm. Although, the system is nonlinear, the algorithm tries first to favour simpler models in an automatic way, while in the classical methods for model selection based on the estimation of an information criterion, a penalty term is defined to enforce parsimony. The ABC-NS algorithm switches to a more complex model only when those models are more accurate. Figure 20.8 shows the histograms of the selected model parameters obtained at the last population as the mean values shown with red triangles.

Using the selected model with the posterior estimates from the last population, one can make predictions. Figure 20.9 shows the model predictions on the training and testing data sets. As one can see, the predicted results match satisfactorily with the experimental results, which means that the selected model captures perfectly well the dynamics of the WRI. The normalised MSE values on the training and testing data sets are equal to 0.77 and 0.63, respectively, indicating an excellent fit.

To check if the choice of the best model is dependent on the training data, a new simulation is performed using a longer time series. The same tendency using a short time series has been observed and the algorithm finishes by converging to $\mathcal{M}_2$ (the results are not shown to simplify presentation). Therefore, it becomes obvious that model $\mathcal{M}_2$ is the model with the best predictive ability among the competing models.

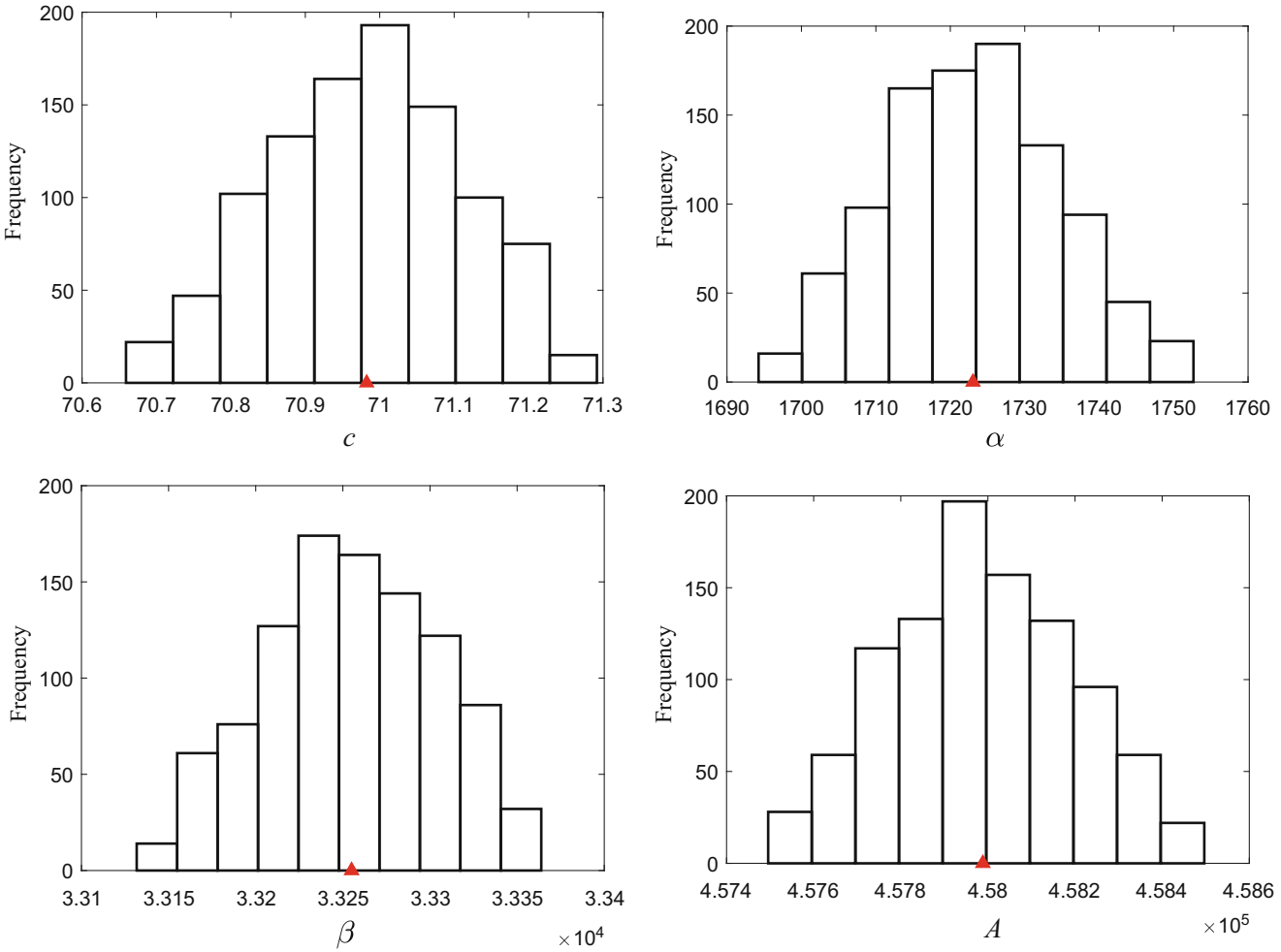

Fig. 20.8 Histograms of the model parameters

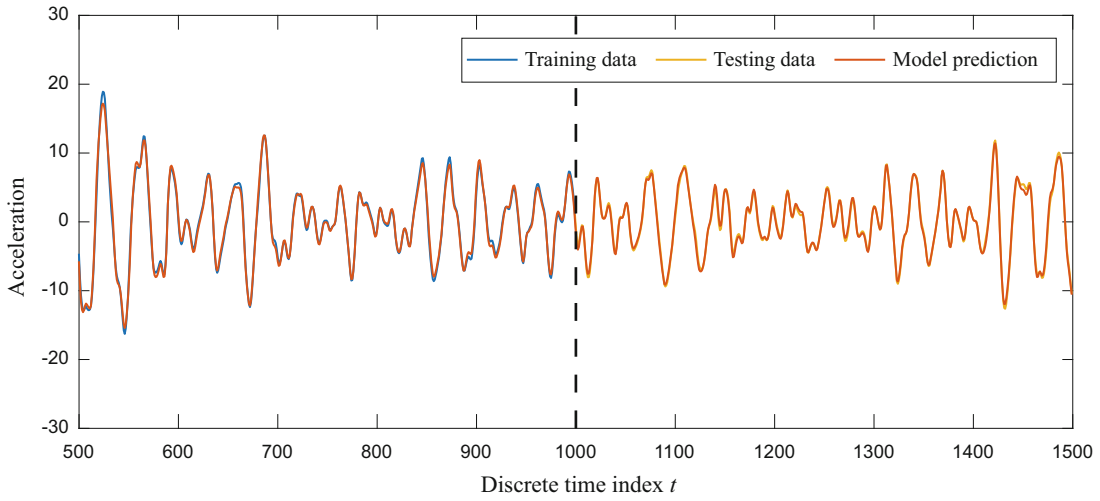

Fig. 20.9 Model predictions on training and testing data sets

20.5 Conclusions

A novel algorithm named ABC-NS, for parameter estimation and model selection based on an ellipsoidal nested sampling has been developed. The efficiency and robustness of the novel algorithm to deal with parameter estimation and model selection issues in structural dynamics has been demonstrated through two examples: a moving average process and a wire rope isolator. It has been shown that the algorithm is a promising alternative, offering the possibility to make Bayesian inference for complex systems based on the selection of an appropriate summary statistics. The algorithm is able to provide a good estimation of the unknown parameters within a reasonable computational requirement. In addition, it makes a comparison between a set of competing models with different dimensionality in an automatic way, as the parsimony principle is naturally embedded in the ABC-NS algorithm. The efficiency of the novel ABC algorithm to deal with more challenging scenarios using different kinds of features and metrics from either the time domain or the frequency domain will be investigated in an upcoming work.

Acknowledgements The support of the UK Engineering and Physical Sciences Research Council (EPSRC) through grant reference no. EP/K003836/1 is greatly acknowledged.

References

1. Green, P.J.: Reversible jump Markov chain Monte Carlo computation and Bayesian model determination. Biometrika **82**(4), 711–732 (1995)
2. Vehtari, A., Ojanen, J.: A survey of Bayesian predictive methods for model assessment, selection and comparison. Stat. Surv. **6**, 142–228 (2012)
3. Ben Abdessalem, A., Dervilis, N., Wagg, D., Worden, K.: Identification of nonlinear dynamical systems using approximate Bayesian computation based on a sequential Monte Carlo sample. In: International Conference on Noise and Vibration Engineering, Leuven, 19–21 Sept 2016
4. Ben Abdessalem, A., Worden, K., Dervilis, N., Wagg, D.: Recent advances in approximate Bayesian computation methodology: application in structural dynamics, ENL Workshop, Bristol, 2017
5. Ben Abdessalem, A., Dervilis, N., Wagg, D., Worden, K.: ABC-NS: a new computational inference method applied to parameter estimation and model selection in structural dynamics. Conference: 23 Congrès Français de Mécanique, Lille, May 2017
6. Ben Abdessalem, A., Dervilis, N., Wagg, D., Worden, K.: Model selection and parameter estimation in structural dynamics using approximate Bayesian computation. Mech. Syst. Signal Process. **99**, 306–325 (2018)
7. Marjoram, P., Molitor, J., Plagnol, V., Tavare, S.: Markov chain Monte Carlo without likelihoods. Proc. Natl. Acad. Sci. USA **100**, 15324–15328 (2003)
8. Toni, T., Welch, D., Strelkowa, N., Ipsen, A., Stumpf, M.P.H.: Approximate Bayesian computation scheme for parameter inference and model selection in dynamical systems. J. R. Soc. Interface **6**, 187–202 (2009)
9. Skilling, J.: Nested sampling. In: Fischer, R., Preuss, R., Toussaint, U.V. (eds.), American Institute of Physics Conference Series, pp. 395–405 (2004)
10. Skilling, J.: Nested sampling for general Bayesian computation. Bayesian Anal. **1**(4), 833–860 (2006). http://doi.org/10.1214/06-BA127
11. Beaumont, M.A., Zhang, W., Balding, D.J.: Approximate Bayesian computation in population genetics. Genetics **162**(4), 2025–2035 (2002)
12. Mukherjee, P., Parkinson, D., Liddle, A.R.: A nested sampling algorithm for cosmological model selection. ApJ **638**, L51 (2006)
13. Feroz, F., Hobson, M.P., Bridges, M.: MultiNest: an efficient and robust Bayesian inference tool for cosmology and particle physics. Mon. Not. R. Astron. Soc. **398**(4), 1601–1614 (2009)
14. Marin, J.M., Pudlo, P., Robert, C.P., Ryder, R.J.: Approximate Bayesian computational methods. Stat. Comput. **22**, 1167–1180 (2012)
15. Technical Report, COST Action F3, VTT Technical Research Centre of Finland (1999)
16. Juntunen, M., Linjama, J.: Presentation of the VTT benchmark. Mech. Syst. Signal Process. **17**(1), 179–182 (2003)
17. Kerschen, G.: On the model validation in non-linear structural dynamics. Thèse de doctorat, Université de Liège (2002)
18. Kerschen, G., Worden, K., Vakakisc, A.F., Golinval, J.C.: Past, present and future of nonlinear system identification in structural dynamics. Mech. Syst. Signal Process. **20**, 505–592 (2006)
19. Peifer, M., Timmer, J., Voss, H.U.: Non-parametric identification of non-linear oscillating systems. J. Sound Vib. **267**, 1157–1167 (2003)
20. Demetriades, G.F., Constantinou, M.C., Reinhorn, A.M.: Study of wire rope systems for seismic protection of equipment in buildings. Eng. Struct. **15**(5), 321–334 (1993)
21. Constantinou, M.C., Tadjbakhsh, I.G.: Hysteretic dampers in base isolation: random approach. J. Struct. Eng. **111**(4), 705–721 (1985)
22. Wen, Y.: Method for random vibration of hysteretic systems. ASCE J. Eng. Mech. Div. **102**(2), 249–263 (1976)
23. Worden, K., Hensman, J.J.: Parameter estimation and model selection for a class of hysteretic systems using Bayesian inference. Mech. Syst. Signal. Process. **32**, 153–169 (2012)

Chapter 21
Investigation on the Performance of a Velocity Feedback Control Unit for Structural Vibration Control: Theory and Experiments

S. Camperi, M. Ghandchi-Tehrani, and S. J. Elliott

Abstract A valuable solution for structural vibration control of lightly damped systems, subjected to random disturbance, is to provide active damping by generating a control force proportional to the local velocity of the structure. It has been shown in the literature that an optimal feedback gain exists, at which the kinetic energy of the structure is minimised. Furthermore, other studies have shown that the minimisation of the kinetic energy can be approximated with the maximisation of the power absorbed by the control unit, reducing the amount of information required for the estimation of the performance of the control system. In this paper the reduction of flexural vibration on a plate by means of a local velocity feedback control, with a collocated inertial actuator and sensor pair, is considered. The performance of the control unit is investigated both numerically and experimentally, in terms of the kinetic energy of the structure and the power absorbed by the control unit. The influence of the frequency range considered in the assessment of the performance is analysed. In particular, the equivalence between the minimisation of the kinetic energy and the maximisation of the power absorbed is investigated, as a crucial step into the design of a self-contained locally tunable control unit.

Keywords Active control · Velocity feedback · Structural vibration · Inertial actuator · Power absorption

21.1 Introduction

Vibration in lightly damped structures can be effectively reduced through active damping [1]. In such a control system, the actuator-sensor pair is collocated, and a local velocity feedback signal is generated, proportional to the absolute velocity of the structure.

In order to assess the performance of the control system, the global level of vibration may be considered, through the measurement of the kinetic energy of the structure. In particular, for lightly damped panels, a minimum in the kinetic energy exists, and for further increase of the feedback gain a pinning condition is approached [2]. Therefore, the tuning of the feedback gain can be performed by minimising the kinetic energy of the structure.

Alternatively, the local power absorbed by the control unit from the structure may be considered [2, 3], which does not require any information about the structure, and enables the design of a self-contained modular unit. However, in order to guarantee the reduction of structural vibration, the two tuning methods need to be compared.

Zilletti et al. [4] proved analytically the equivalence of the two tuning methods for a single-degree-of-freedom structure case. Other studies [2, 5] have shown that the two optimisations are almost equivalent when a plate is considered, and the actuator dynamics is not included. However, the influence of the frequency range, i.e. the number of structural modes taken into account, in the extent of the equivalence between the minimisation of the kinetic energy and the maximisation of the power absorbed has not been specifically addressed yet.

In this paper, the performance of a local velocity feedback control unit for the reduction of flexural vibration on a rectangular plate is investigated both theoretically and experimentally, in terms of the kinetic energy of the structure and the power absorbed. The control unit consists of an accelerometer and a current-driven collocated inertial actuator. In the second section, a mathematical model is introduced, in which the problem is approached from a typical vibration point of view, and the plate response is analysed in the frequency domain. The dynamic behaviour of the inertial actuator is described in terms of impedances, and its influence on the stability of the feedback control loop is investigated.

In the third section, numerical results are shown, and the influence of the frequency range of integration is evaluated. Finally, in the fourth section, a comparison between the analytical and the experimental results is carried out.

S. Camperi (✉) · M. Ghandchi-Tehrani · S. J. Elliott
Institute of Sound and Vibration Research, University of Southampton, Southampton, UK
e-mail: sc4r14@soton.ac.uk

C. Niezrecki, J. Baqersad (eds.), *Structural Health Monitoring, Photogrammetry & DIC, Volume 6*,
Conference Proceedings of the Society for Experimental Mechanics Series, https://doi.org/10.1007/978-3-319-74476-6_21

21.2 Mobility-Impedance Mathematical Model

In this section a mathematical model is formulated in order to investigate the stability of the feedback control loop, as well as the performance of the control unit in terms of the kinetic energy of the structure and the power absorbed. The system consists of a structure, on which an inertial actuator is mounted. A current proportional to the local velocity of the structure drives the actuator, as shown in Fig. 21.1a.

The system dynamics is described through the concept of mobilities and impedances, in which the control unit is coupled with the structure.

The structure is a rectangular aluminium plate fully clamped, already used in previous studies [6, 7], whose physical parameters are summarised in Table 21.1.

The velocity $\dot{w}_s$ at any point of the structure with respect to a point force f, can be written, in the frequency domain, as

$$\dot{w}_s = Y_{sp} f_p, \tag{21.1}$$

in which Y_{sp} is the point mobility of the structure at the position s, with respect to the point p. The point mobility can be modelled according to its modal components, as the summation of the first N resonant terms $\sum_{n=1}^{N} j\omega\phi_{n,s}\phi_{n,p}/[m_n(\omega_n^2 - \omega^2 + j2\zeta_n\omega_n\omega)]$, in which ϕ_n are the eigenfunctions for a clamped rectangular plate [8].

The inertial actuator consists of a moving magnet surrounded by a coil, and thus can generate a control force on the structure when externally excited by (i) a base velocity $\dot{w}$ from the structure, or (ii) an external current i. Therefore, it is convenient to write the control force f_c as [9, 10]

$$f_c = -Z\dot{w} + Ti, \tag{21.2}$$

in which Z and T are, respectively, the passive and active impedances of the actuator.

Since active control concerns the low frequency range, the components of the actuator can be assumed to be rigid in the frequency range of interest, and thus the transducer can be described as a single degree of freedom system, with passive impedance

$$Z = jm_b\omega + \frac{jm\omega(k + jc\omega)}{k + jc\omega - m\omega^2}, \tag{21.3}$$

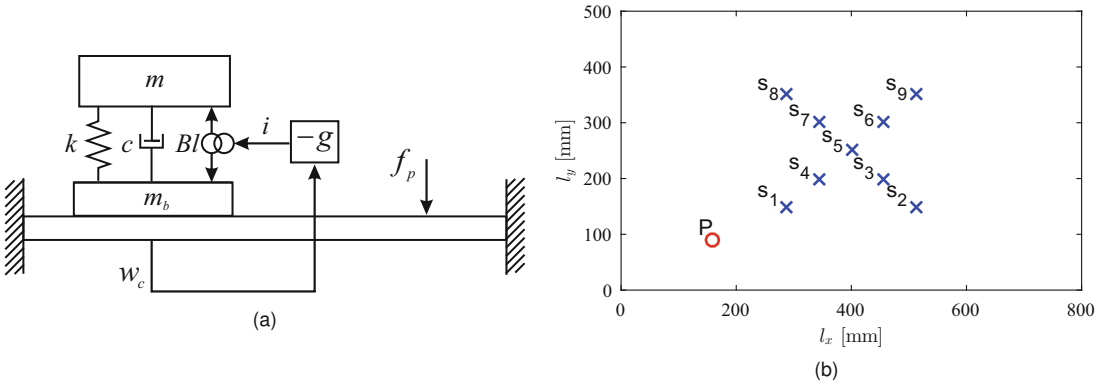

Fig. 21.1 Schematic representation of (**a**) a local feedback control with an inertial actuator, and (**b**) the sensors and primary position P on the plate

Table 21.1 Geometry and physical parameters of the plate

Parameter	Value		
Dimensions	$l_x \times l_y$	800×500	mm^2
Thickness	h	2	mm
Density	ρ	2720	kg/m^3
Young's modulus	E	7×10^{10}	N/m^2
Poisson ratio	ν	0.33	
Internal damping ratio	ζ	1%	

Table 21.2 Physical properties of the inertial actuator Micromega® IA01

Parameter	Value		
Moving mass	m	32	g
Base mass	m_s	53	g
Natural frequency	f_n	8.7	Hz
Damping ratio	ζ	0.4	
Voice coil coefficient	Bl	1.6	N/A

and active impedance

$$T = \frac{-mBl\omega^2}{k + jc\omega - m\omega^2}. \tag{21.4}$$

The inertial actuator considered is the Micromega® IA01, whose physical properties are listed in Table 21.2.

When the inertial actuator is mounted on the structure, both the primary force and the control force act on the plate. Thus Eq. (21.1) can be rewritten as

$$\dot{w}_s = Y_{sp} f_p + Y_{ss} f_c, \tag{21.5}$$

in which Eq. (21.2) can be implemented, obtaining

$$\dot{w}_s = Y_{sp} f_p - Y_{ss} Z \dot{w}_s + Y_{ss} Ti. \tag{21.6}$$

The coupling between the structure and the inertial actuator can be treated separately with respect to the passive and active impedance of the actuator. Because both Y_{ss} and Z have positive real part at any frequency, the passive coupling between the actuator and the structure is unconditionally stable. Therefore, to simplify the notation, the mobility Y' of the structure coupled with the passive actuator can be defined as $Y'_{sp} = Y_{sp}/(1 + Y_{ss}Z)$, and Eq. (21.6) can be rewritten as

$$\dot{w}_s = Y'_{sp} f_p + Y'_{ss} Ti. \tag{21.7}$$

In order to reduce vibration, active damping can be generated by providing a current proportional to the local velocity of the structure to the actuator. The closed-loop velocity of the structure, when the local velocity feedback is implemented, is

$$\dot{w}_s = \frac{Y'_{sp}}{1 + Y'_{ss} Tg} f_p, \tag{21.8}$$

in which g is the velocity feedback gain.

Although the sensor and the actuator are collocated, and thus the mobility Y'_{ss} has positive real part, the active impedance T shows a drop in phase of 180° below its resonance. For this reason, the open-loop transfer function $Y'_{ss}T$ has negative real part below the actuator resonance [11], and, according to the Nyquist Criterion, an upper limit on the feedback gain value can be determined, above which the system becomes unstable.

Finally, the performance of the control unit can be assessed in terms of reduction of kinetic energy, and power absorbed by the control unit.

For a random, continuous and ergodic process, the time-averaged kinetic energy $\bar{K}_e$ can be evaluated as [5, 12]

$$\bar{K}_e = E[K_e(t)] \approx \frac{m}{2} \sum_{i=1}^{9} \frac{1}{2\pi} \int_{-\infty}^{\infty} |\dot{w}_i|^2 d\omega, \tag{21.9}$$

in which $E[\ \ ]$ is the expectation operator, and the kinetic energy of the structure is approximated as summation of the structure velocity at 9 measuring positions, avoiding nodal lines relative to the first structural modes, as shown in Fig. 21.1b and summarised in Table 21.3.

Table 21.3 Primary and sensors position

Position	(l_x, l_y) [mm]
Primary	(160, 90)
s_1	(286, 150)
s_2	(514, 150)
s_3	(457, 200)
s_4 (control position)	(343, 200)
s_5	(400, 250)
s_6	(457, 300)
s_7	(343, 300)
s_8	(286, 350)
s_9	(514, 350)

Similarly, the power absorbed by the control unit from the structure can be written as the product between the local velocity of the structure and the control force

$$\bar{P} = E[P(t)] = E[f_c \dot{w}_s] \approx \frac{1}{2\pi} \int_{-\infty}^{\infty} \Re\{Z + Tg\} |\dot{w}_s|^2 d\omega. \tag{21.10}$$

21.3 Feedback Gain Optimisation

In this section, the performance of the active control is investigated. First the effect of the feedback loop on the structure resonances is analysed in the frequency domain. Secondly the optimisation of the feedback gain is performed, with respect to the kinetic energy and the power absorbed.

In order to be consistent with the experimental results obtained in the next section, the accelerometers have been included into the model, and modelled as simple point mass, as their first natural resonance is much larger than the frequency range of interest in this study.

The assessment of the maximum stable gain is omitted, as it has already been largely discussed in other studies [9, 11]. The conditional stability of the control system can be determined according to the Nyquist Criterion: in the open-loop transfer function, a phase-shift of 180° occurs at the actuator resonance because of the coupling between the driving-point mobility of the plate and the active impedance of the actuator.

Once the maximum stable gain is determined, the influence of the feedback gain on the performance of the control system can be investigated.

Figure 21.2 shows the effect of the active control on the kinetic energy and the power absorbed, in the frequency domain.

As the feedback gain increases, active damping is introduced in the structure, which reduces the first structural resonances, as shown in Fig. 21.2a. However, for further increase of the feedback gain, a new peak rises at low frequencies, and eventually approaches to infinite amplitude at the actuator resonance, when the feedback gain reaches the maximum stable gain. At the same time, for large values of feedback gain, a pinning condition is approached, in which the boundary conditions of the plate change, and new resonances occur at higher frequencies.

A similar behaviour can be noticed in the power absorbed by the control unit from the structure, as show in Fig. 21.2b. When the feedback gain is zero, the actuator behaves passively, and the power absorbed presents well separated peaks corresponding to the resonances of the structure. However, increasing the feedback gain, active damping is introduced into the structure. As a result, the resonance peaks are reduced in magnitude, but the overall power absorbed is generally increased. Finally, the power absorbed below the actuator resonance is negative because of the shift in phase in the active impedance, and therefore the power is injected into the structure in this frequency range [13].

In order to better investigate the influence of the feedback gain on the reduction of vibration into the structure, the time-averaged values can be considered according to Eqs. (21.9) and (21.10). However, the integrals in the frequency domain, in general, cannot be solved analytically, and thus numerical integration is required. The numerical integration depends on the frequency step size, and on the maximum frequency f_{max} considered. The frequency step size has to be chosen small enough to guarantee the convergence of the integration, and in this study has to be set equal to 0.2 Hz.

The influence of the maximum frequency of integration f_{max} on the estimation of the time-averaged values is shown in Fig. 21.3.

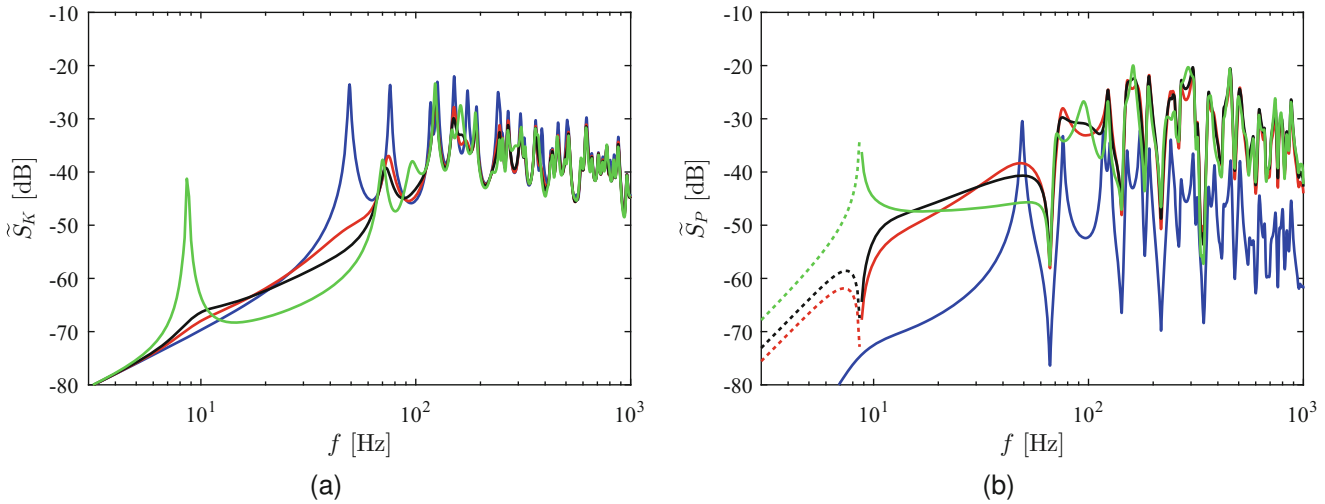

Fig. 21.2 Power Spectral Densities of (**a**) the kinetic energy of the structure, and (**b**) the power absorbed by the control unit from the structure, with the feedback gain g equal to the 0% (blue), 17% (red), 30% (black), and 100% (green) of the maximum stable gain. Dotted lines correspond to negative power absorbed

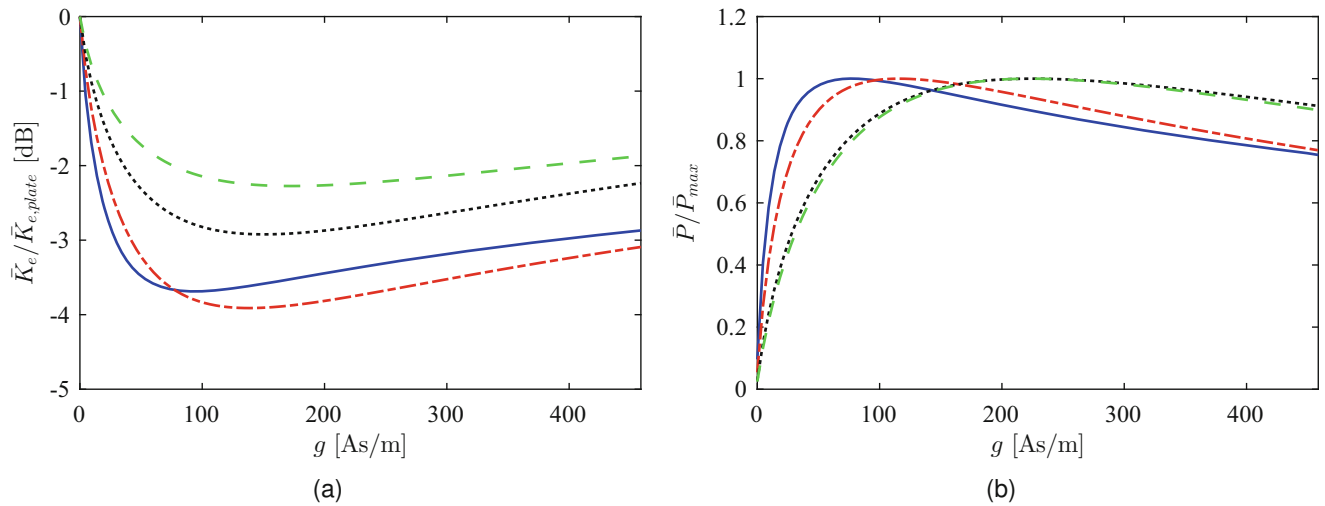

Fig. 21.3 Time-averaged (**a**) kinetic energy and (**b**) power absorbed with respect to the feedback gain, for different frequency ranges of integration from 0 to: 150 Hz (solid blue line), 250 Hz (dash-dotted red line), 500 Hz (dotted black line), 1 kHz (dashed green line)

Figure 21.3a shows the time-averaged kinetic energy with respect to the feedback gain for different values of f_{max}. For any frequency range of integration considered, as the feedback gain increases, the time-averaged kinetic energy is reduced up to a minimum. However, for large values of feedback gain, the time-averaged kinetic energy rises again because of the approaching to (i) a pinning condition of the plate, and (ii) the instability at the actuator resonance.

However, the amount of reduction obtained depends on the frequency range on integration considered. For small values of f_{max}, only the first structural resonances are accounted for, on which the active control is particularly effective, and thus a large reduction of time-averaged kinetic energy is obtained. However, as the frequency range of integration is increased, high order structural modes, which cannot be controlled, are included in the integration.

As a result, the presence of a stable minimum in the time-averaged kinetic energy becomes less clear as the frequency range of integration is increased. This poses a constraint on the design of a self-tuning algorithm [12] capable of adjust the value of the feedback gain in such a way that the time-averaged kinetic energy is minimised. Such constraint is related to the convergence of the algorithm, which requires the gradient of the time-averaged kinetic energy to be large.

A similar analysis can be carried out for the time-averaged power absorbed by the control unit from the structure. For small values of feedback gain, the power absorbed depends only on the passive coupling between structure and actuator. However, as the feedback gain increases, active damping is introduced into the structure, and more power is absorbed. A

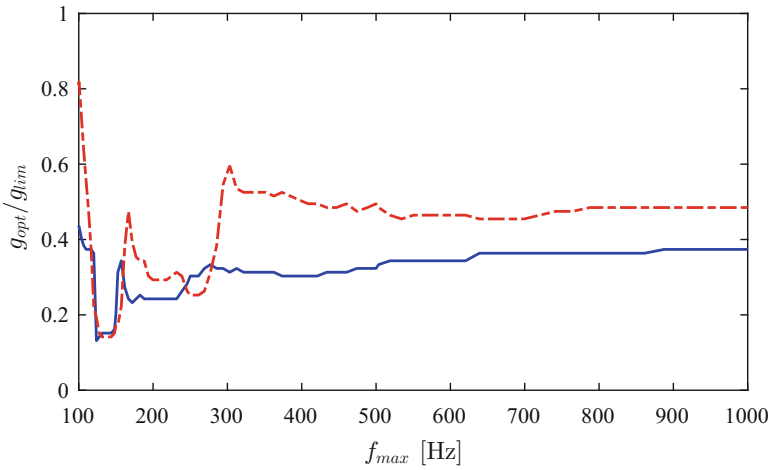

Fig. 21.4 Optimal gain for different frequency ranges of integration minimising the kinetic energy (solid blue), and maximising the power absorbed (dash-dotted red)

maximum can be noticed in the time-averaged power absorbed, and for further increase of the feedback gain the power absorbed reduces, with a behaviour similar to the one observed in the time-averaged kinetic energy.

To conclude, the influence of the frequency range on the optimal feedback gains, which minimise the time-averaged kinetic energy and maximise the time-averaged power absorbed is investigated in Fig. 21.4.

For small values of f_{max}, the optimal gains strongly depends on the structural modes considered in the time average. However, as f_{max} increases, the optimal gains approaches a constant value. This is due to the fact that the high frequency range is included, in which the dynamic response of the structure is mostly determined by its non-resonant terms, because of the increase of the plate modal density. Finally, the optimal gain which maximises the power absorbed, occurs at larger values than the one minimising the kinetic energy of the structure. However, it is important to notice that the maximisation of the power absorbed corresponds to a reduction of kinetic energy, which is less than 1 dB worse than the minimum of the kinetic energy, for any frequency range of integration considered. Therefore the maximisation of the power absorbed can be considered as an alternative way of tuning the feedback gain of the control unit as long as a frequency range, in which the feedback control is effective, has been considered.

21.4 Experiment Setup and Results

The parameters introduced in Sect. 21.2, and used in the simulation in Sect. 21.3, refer to actuators commercially available, and to a structure specifically designed [7] and available in the laboratory, shown in Fig. 21.5. The structure consists of a rectangular aluminium plate clamped to a mounting system, with bending modes well above the frequency range of interest. The whole structure is fixed on a large concrete block to avoid low frequency whole body vibration.

The primary excitation is generated by a LDS V200 shaker, and an EDVECO 2312 force sensor is mounted between the shaker and the plate to measure the force transmitted. The velocity of the plate is measured through nine B&K 4507B004 accelerometers.

The control loop, as well as the acquisition of the nine acceleration signals, and the generation of the primary excitation are all performed through a dSPACE® DS1103 PPC Control Board, running with a sampling frequency of 16 kHz, which is configured through the dSPACE ControlDesk® and Matlab Simulink® software.

The control unit consists of an accelerometer, digital filtering and integration in order to obtain the velocity signal, and an analogical power amplifier and anti-aliasing filter to generate a control current signal for the inertial actuator. The control unit has been already fully characterised in a previous study on a different plate[13], and with a similar procedure it can be found experimentally that the gain margin, on this structure, is 68.69.

The plate is excited with a random broadband excitation up to 300 Hz, and different values of feedback gain are implemented.

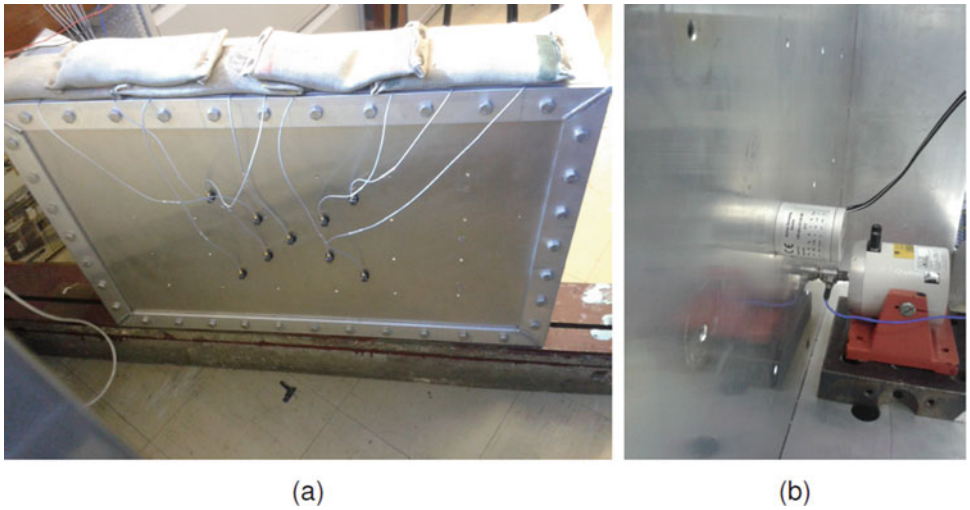

Fig. 21.5 Experimental set-up

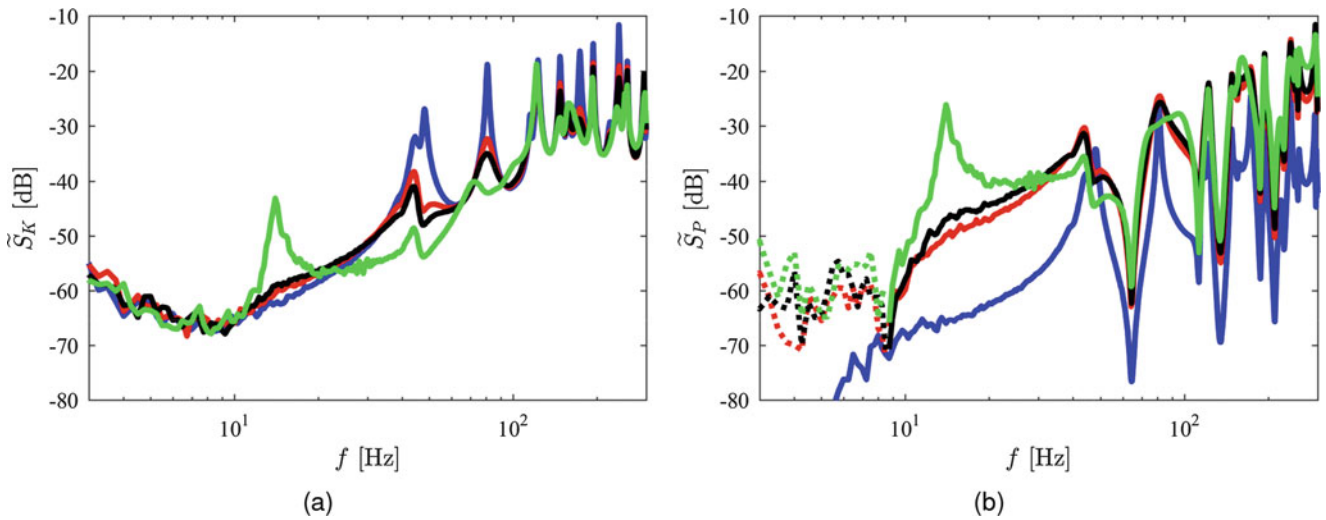

Fig. 21.6 Measured Power Spectral Densities of (**a**) the kinetic energy of the structure, and (**b**) the power absorbed by the control unit from the structure, with the feedback gain g equal to the 0% (blue), 20% (red), 30% (black), and 90% (black) of the maximum stable gain. Dotted lines correspond to negative power absorbed

Figure 21.6 shows the measurements in the frequency domain, for different values of velocity feedback gain. The Power Spectral Density of the kinetic energy, shown in Fig. 21.6a, is obtained as summation of the absolute value of the measured point mobilities at the sensors positions, in such a way that the results are consistent with the analytical ones shown in Sect. 21.3.

The measurements are in good agreement with the analytical results, both in magnitude and in resonant frequencies, with the first structural resonances reducing as the feedback gain increases. However, a second peak at 45 Hz can be noticed close to the first structural resonance due to the coupling of the structure with the shaker. Finally, at low frequencies, below 10 Hz, the increase in general level is attributed to (i) the vibration from the floor, and (ii) the digital integrator amplifying the sensor noise.

The power absorbed is measured as product of the velocity at the control position, and the control force generated by the actuator. In order to reduce the number of sensors required, the control force is estimated from the measurement of the structure velocity, through a digital filter, which reproduces the active and passive impedances of the actuator, according to Eq. 21.2.

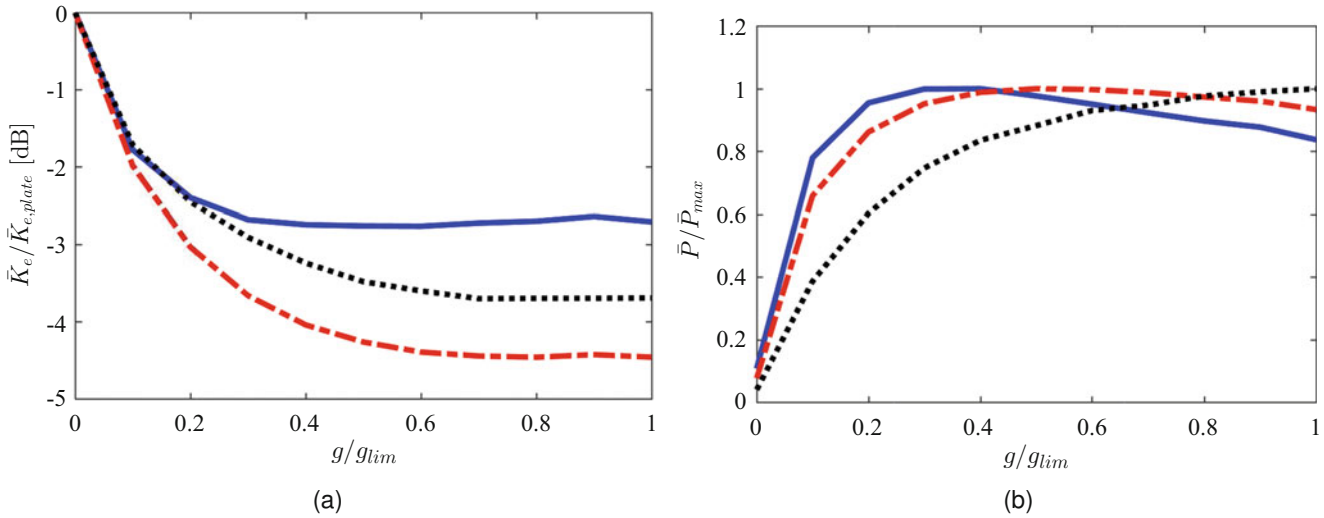

Fig. 21.7 Measured time-averaged (**a**) kinetic energy and (**b**) power absorbed with respect to the feedback gain, for different frequency ranges of integration from 0 to: 150 Hz (solid blue line), 250 Hz (dash-dotted red line), and 300 Hz (dotted black line)

As it can be noticed in Fig. 21.6b, the measured power absorbed matches with the analytical results at almost every frequency. Below the natural frequency of the inertial actuator, the power absorbed is negative when the active control is introduced into the system. This means the control unit puts energy into the structure at these frequencies.

Finally, the time-averaged values, obtained from Eqs. (21.9) and (21.10) for different frequency ranges of integration, are shown in Fig. 21.7.

The time-averaged kinetic energy changes depending on the frequency range considered, and the measured reduction of vibration is in good agreement with the analytical results. As the frequency range of integration is increased, the curves move up, and the performance of the control system reduces. However, the experimental results are different in a number of aspects. In particular, for any frequency range of integration, the time-averaged kinetic energy does not increase when the minimum is reached, and instead it levels off. This is probably due to the noise at low frequencies, and the consequent inaccuracy into the measurement of the actuator resonance approaching the instability.

For similar reasons, the time-averaged kinetic energy measured up to 150 Hz seems to be in contradiction with the theoretical results. This is due to the fact that reducing the frequency range of integration, the influence of the noise at low-frequencies in the time-average increases, and has the same effect observed when high frequencies are included in the average.

In the time-averaged power absorbed a better agreement between measured and analytical results can be noticed with respect to the kinetic energy, as outlined in Fig. 21.7b. This is because the magnitude of the noise at low frequencies is small compared to the measured power absorbed at higher frequencies, and thus a better estimation of the power absorbed can be carried out.

21.5 Conclusions

In this paper, the performance of an active feedback control for structural vibration has been investigated both numerically and experimentally.

The coupling between the structure and the control unit has been modelled through the concept of impedances and mobilities, and the conditional stability of the system has been analysed.

The performance of the control system has been defined in terms of the kinetic energy of the structure and the power absorbed by the control unit. A minimum in the kinetic energy with respect to the feedback gain almost corresponds to a maximum in the power absorbed. However, these two optima depends on the frequency range of integration.

In order to properly tune the feedback gain of the control unit with respect to the performance, only the first few resonances, in which the control is effective, have to be taken into account. For larger frequency ranges of integration, which include uncontrolled resonances, the effectiveness of the control reduces, and the optimal gain cannot be clearly determined.

Future work will focus on the real-time estimation of the performance of the control unit, and the design of a self-tuning algorithm.

Acknowledgements This research work was supported by the European Commission as "Marie Sklodowska-Curie Fellowship for Early Stage Research" program through the "Initial Training Network" (ITN) within the seventh framework project (FP7) "Advanced Training and Research in Energy Efficient Smart Structures" (ANTARES) (Grant Agreement 606817).

References

1. Preumont, A.: Vibration Control of Active Structures: An Introduction. vol. 179. Springer Science & Business Media, Dordrecht (2011)
2. Elliott, S., Zilletti, M., Gardonio, P.: Self-tuning of local velocity feedback controllers to maximise power absorption. In: Recent Advances Structural Dynamics: Proceedings of the X International Conference, 12pp. University of Southampton (2010)
3. Zilletti, M., Elliott, S.J., Rustighi, E.: Optimisation of dynamic vibration absorbers to minimise kinetic energy and maximise internal power dissipation. J. Sound Vib. **331**(18), 4093–4100 (2012)
4. Zilletti, M., Gardonio, P., Elliott, S.J.: Optimisation of a velocity feedback controller to minimise kinetic energy and maximise power dissipation. J. Sound Vib. **333**(19), 4405–4414 (2014)
5. Gardonio, P., Miani, S., Blanchini, F., Casagrande, D., Elliott, S.: Plate with decentralised velocity feedback loops: power absorption and kinetic energy considerations. J. Sound Vib. **331**(8), 1722–1741 (2012)
6. Baumann, O.N., Elliott, S.J.: An experiment comparing centralised and decentralised control using inertial actuators. In: ForumAcusticum (2005)
7. Baumann, O.N., Elliott, S.J.: The stability of decentralized multichannel velocity feedback controllers using inertial actuators. J. Acoust. Soc. America **121**(1), 188–196 (2007)
8. Leissa, A.W.: Vibration of Plates. Technical Report. OHIO STATE UNIV COLUMBUS (1969)
9. Rohlfing, J., Elliott, S., Gardonio, P.: Feedback compensator for control units with proof-mass electrodynamic actuators. J. Sound Vib. **331**(15), 3437–3450 (2012)
10. Elliott, S.J., Zilletti, M.: Scaling of electromagnetic transducers for shunt damping and energy harvesting. J. Sound Vib. **333**(8), 2185–2195 (2014)
11. Elliott, S., Serrand, M., Gardonio, P.: Feedback stability limits for active isolation systems with reactive and inertial actuators. J. Vib. Acoust. **123**(2), 250–261 (2001)
12. Zilletti, M., Elliott, S.J., Gardonio, P.: Self-tuning control systems of decentralised velocity feedback. J. Sound Vib. **329**(14), 2738–2750 (2010)
13. Camperi, S., Ghandchi-Tehrani, M., Elliott, S.J.: Experimental maximisation of the power absorbed by an inertial actuator for structural vibration control. In: 24th International Congress on Sound and Vibration (ICSV24), p. 8 (2017)

Chapter 22
Experimental Implementation of a Nonlinear Feedback Controller for a Stroke Limited Inertial Actuator

M. Dal Borgo, M. Ghandchi Tehrani, and S. J. Elliott

Abstract This research consists of theoretical and experimental studies of a stroke limited inertial, or proof mass, actuator used in active vibration control. Traditionally, inertial actuators are used with velocity feedback controllers to reduce structural vibrations. However, physical limits, such as stroke saturation, can affect the behaviour and the stability of the control system. In fact, stroke saturation results in impulse like excitations, which are transmitted to the structure that is liable to damage. Moreover, the shocks produced by the impacts are in phase with the velocity of the structure. This produces an input force, which reduces the overall damping and eventually leads to limit cycle oscillations and the instability of the system. This paper examines the experimental implementation of a nonlinear feedback controller to avoid collisions of the proof mass with the actuator's end stops, hence preventing the instability of the system due to stroke saturation. Firstly, the nonlinear behaviour of the stroke limited inertial actuator is reported. This allows identifying the stroke length of the proof mass. Secondly, the nonlinear feedback controller is presented, which acts as a second loop alongside the velocity feedback control loop. The main purpose of the nonlinear feedback controller is to increase the damping of the actuator when the poof mass gets close to the end stops. Finally, the experimental implementation of the nonlinear controller is investigated and a comparison in terms of performance and stability of the control system is made when both the feedback loops or only the velocity feedback loop are present.

Keywords Inertial actuator · Stroke saturation · Limit cycle oscillations · Velocity feedback · Nonlinear feedback

22.1 Introduction

Previous research has established the importance of active devices to control vibrations of lightweight and flexible structures [1–7]. A considerable amount of literature has also been published on the use of electromagnetic inertial, or proof mass, actuators as active forcing devices in velocity feedback controllers [2, 5, 7–13]. A velocity feedback controller consists of an electromagnetic actuator attached to a structure, a collocated sensor of vibration (usually an accelerometer) and a controller, which feeds back the velocity of the structure to the actuator. In fact, velocity feedback controllers are capable to add a certain quantity of viscous damping into the structure reducing its level of vibration mainly at the low frequency structure's resonances. An inertial actuator consists of a magnetic proof mass, a voice coil and a suspension, which connects the proof mass to a casing. An input current to the inertial actuator generates the control force on the structure by reacting against the proof mass, which starts to accelerate [7]. The main concern using inertial actuators in a velocity feedback loop is that their internal dynamics affect the feedback control system, which turns to be only conditionally stable [14]. In fact, there exists a maximum feedback gain, over which the system becomes unstable [8, 15, 16]. Moreover, most studies in this area have not dealt with nonlinear models of actuators, limiting them to work in restricted operating conditions. The most important nonlinearity encountered by the authors that can affect the dynamic behaviour of an inertial actuator is a saturation phenomenon of the force that can be generated on a structure [17]. The limitation of the force delivered by the actuator can be due to a saturation of the power electronics, hence the maximum current fed to the actuator [17, 18]. Also, it can be due to the finite stroke length between the end stops within the actuator casing, hence the maximum displacement achievable for the proof mass [19–25]. A combination of these two limitations results in a limited region of linear operation for the inertial actuator, over which linear relationships between input and output no longer exist. The limit on the force that is given by the current saturation, whose dynamic is flat over the whole frequency range, is indeed a limitation on the temperature and heating of the actuator. As it is well described in Refs. [15, 16], an increase in the input power to the actuator's coil

M. Dal Borgo (✉) · M. Ghandchi Tehrani · S. J. Elliott
Institute of Sound and Vibration Research, University of Southampton, Hampshire, UK
e-mail: M.Dal-Borgo@soton.ac.uk; mdb2g15@soton.ac.uk; M.Ghandchi-Tehrani@soton.ac.uk; S.J.Elliott@soton.ac.uk

C. Niezrecki, J. Baqersad (eds.), *Structural Health Monitoring, Photogrammetry & DIC, Volume 6*,
Conference Proceedings of the Society for Experimental Mechanics Series, https://doi.org/10.1007/978-3-319-74476-6_22

would produce a temperature rise of its components. The maximum current is given by the maximum temperature rise, which does not lead to demagnetisation of the proof mass caused by passing the Curie temperature (for most of permanent magnets is about 80°C), when the atoms of the material deviate from the magnetic alignment. An ultimate limit is then given by the melting temperature of the wire insulation, which is about 150°C for common materials [16]. The force limit due to stroke saturation appears to be an effective limit at low frequencies, instead. In fact, the spectrum of this limitation is proportional to the frequency squared. This two phenomena can be seen as two separated regions in the spectrum of the force generated by the actuator: below the saturation cut off frequency ω_s, where the limitation of the blocked force is given by stroke saturation; and above the saturation cut off frequency, where the limit is given by the power electronics saturation. In this paper, we focus our attention onto the nonlinearity due to the stroke limits. The displacement saturation phenomenon in inertial actuators has been investigated in Refs. [8, 22–24, 26–28]. Indeed the implication of stroke saturation is not the only limitation on the amount of force available from the actuator. If the proof mass is driven against its end stops, hence saturating in the displacement, large shocks are imparted to the actuator casing and to the structure, and damage may result. Moreover, this phenomenon is undesirable in terms of the stability of the closed loop control system, because it can reduce the stability margin, and in fact, enhance the level of vibration [23]. It has also been observed experimentally that this problem affects systems with multiple actuators and local velocity controllers [14]. In this case, the instability in one loop leads to instability in all the other loops [14]. Hence, the dynamic behaviour of inertial actuators is not always well described by a linear mathematical model [8, 15–25], and the nonlinearity should be considered.

This paper explores the experimental implementation of a nonlinear feedback controller, which is able to increase the safe operating region of an inertial actuator in a velocity feedback loop for the purpose of reducing the vibration of a cantilever beam. Firstly, the nonlinear behaviour of the inertial actuator is reported from a previous nonlinear identification study [25]. Secondly, a mathematical model of the nonlinear proof mass actuator attached to a single degree of freedom structure is derived and the stability of the nonlinear system is analysed. Then, the nonlinear feedback control law is presented, aiming to prevent the instability of the system caused by stroke saturation. Finally, the experimental implementation of such a controller is discussed and the outcomes of the nonlinear controller tested under different scenarios are investigated.

22.2 System Model

The cross section with the main parts of a classical inertial actuator are shown in Fig. 22.1. This device comprises a magnetic proof mass, an electrical winding, a suspension and an outer casing. The current flowing through the coil generates the control force to the structure (to which the inertial actuator is attached) and is equal but in opposite direction to the reaction force on the proof mass [7].

The displacement saturation in inertial actuators has been investigated in Refs. [8, 22–24, 26–28]. Moreover, previous studies by the authors have shown how to experimentally characterise and identify the nonlinearities in inertial actuators [25]. The findings are briefly reported here for the purpose of introducing the motivation and formulation for the next sections of the paper. The inertial actuator of Fig. 22.1 can be modelled as a single degree of freedom (SDOF) system with a general nonlinear passive connection to the structure and an active force generator acting between the structure and the proof mass. Considering the inertial actuator attached to a rigid and blocked mass, the equation of motion of the proof mass results,

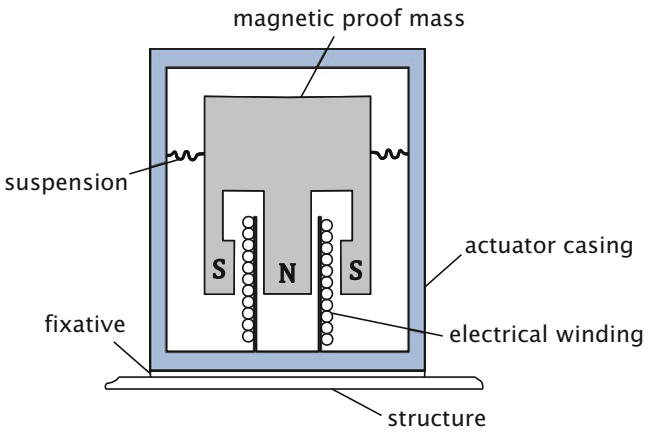

Fig. 22.1 Schematic of the inertial actuator in cross section

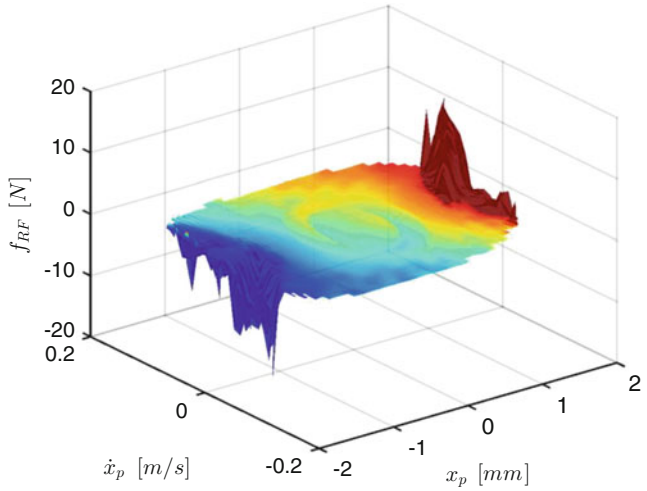

Fig. 22.2 3D plot of the restoring force surface of the stroke limited inertial actuator versus the proof mass displacement and velocity

$$m_p\ddot{x}_p(t) + f_{RF}\left(\dot{x}_p, x_p\right) = (Bl)i_a(t), \tag{22.1}$$

where m_p is the actuator's proof mass, $\ddot{x}_p(t)$ the proof mass displacement, (Bl) the transduction coefficient of the electromechanical conversion, and $i_a(t)$ the current flowing through the coil. The term $f_{RF}\left(\dot{x}_p, x_p\right)$ is the restoring force of the proof mass, hence the force that brings the proof mass to its equilibrium position. In this case, the restoring force describes the general nonlinear passive connection between the proof mass and the ground. Experimental work on a Micromega Dynamics IA-01, whose documentation can be found in Ref. [29], has been carried out in order to characterise its nonlinear behaviour. The restoring force $f_{RF}\left(\dot{x}_p, x_p\right)$ of this actuator is derived by exciting the system with a sine sweep in frequency and measuring the force at the base, which is given by

$$f_b(t) = -m_p\ddot{x}_p(t). \tag{22.2}$$

Knowing the value of the proof mass m_p and of the transduction coefficient (Bl) permits to calculate the restoring force of the actuator by rearranging the terms in Eq. (22.1). Moreover, the acceleration of the proof mass $\ddot{x}_p(t)$ can be calculated by using Eq. (22.2) and then the velocity and displacement derived by filtering and integrating the acceleration signal. The restoring force data points are then averaged on a velocity and displacement grid, in order to create a uniform surface that describes the nonlinear dynamics. Figure 22.2 shows the restoring force surface for the Micromega Dynamics IA-01 inertial actuator, versus the velocity and displacement of the proof mass.

The actuator is strongly nonlinear, as can be observed in Fig. 22.2. In fact, for displacements between -1.25 and 1.25 mm the restoring force is a plane tilted by constant coefficients along the velocity and displacement axes. However, for larger displacements the restoring force suddenly changes, which means that the proof mass has reached the end stops and it is not allowed to move any further. The nonlinear model of the connection between the proof mass and the structure is obtained assuming that the restoring force is given by a summation of an elastic force, which depends only on the displacement and a damping force, which depends only on the velocity of the proof mass [30, 31]. Hence,

$$f_{RF}\left(\dot{x}_p, x_p\right) = f_{RF,v}\left(\dot{x}_p\right) + f_{RF,d}\left(x_p\right), \tag{22.3}$$

where $f_{RF,v}\left(\dot{x}_p\right)$ is the damping force, which contributes to the total restoring force and $f_{RF,\,d}(x_p)$ is the elastic force, which contributes to the total restoring force. The two contributions are derived by Fig. 22.2 taking a section of the restoring force at displacements close to zero ($|x_p| \cong 0$) for the damping force $f_{RF,v}\left(\dot{x}_p\right)$ and velocities close to zero ($\left|\dot{x}_p\right| \cong 0$) for the elastic force $f_{RF,\,d}(x_p)$. The results are shown in Fig. 22.3a, b, where the scattered blue points are the experimental data and the dashed red lines show the identified model. In particular, Fig. 22.3a shows the elastic component of the restoring force versus the displacement of the proof mass. The clearance between the two actuator's end stops can be identified, which results to be $x_0 = 1.25$ mm for each side. Moreover, a piecewise linear model has been fitted to the experimental data, in order to capture the non-smooth nature of this nonlinearity. On the other hand, the damping component of the restoring force has been fitted with a linear model, as shown in Fig. 22.3b.

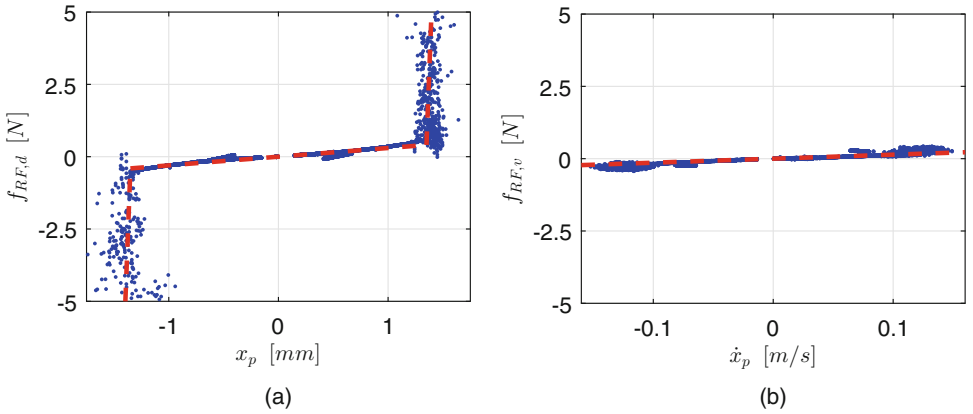

Fig. 22.3 (**a**) Elastic component of the restoring force of the stroke limited inertial actuator versus the proof mass displacement; (**b**) damping component of the restoring force of the stroke limited inertial actuator versus the proof mass velocity; the scattered blue dots indicate the experimental data, while the dashed red lines display the fitted nonlinear model

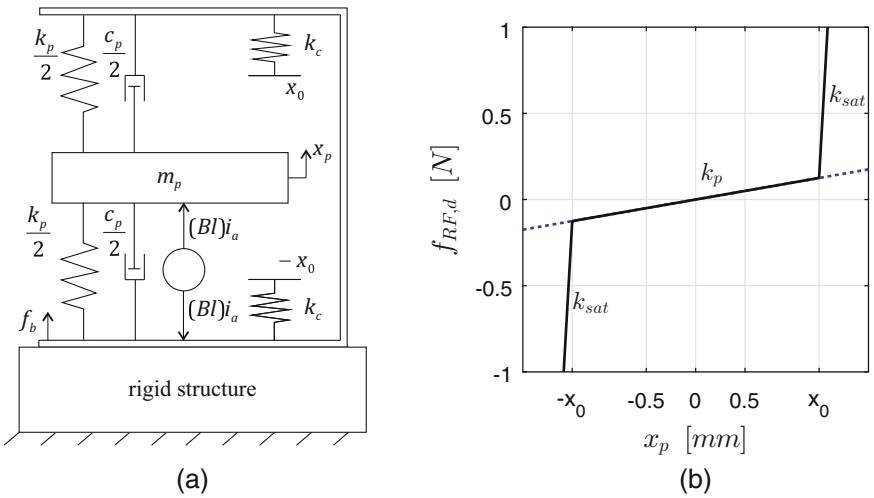

Fig. 22.4 (**a**) A lumped parameter model of the inertial actuator with stroke limits; (**b**) restoring force plot for the underlying linear actuator (dotted blue line) and the nonlinear actuator (solid black line)

The resulting nonlinear mechanical model of the inertial actuator is shown in Fig. 22.4a, where it is mounted on a rigid structure. The equation of motion of the proof mass (22.1) can be rewritten as,

$$m_p\ddot{x}_p(t) + c_p\dot{x}_p + f_{RF,d}\left(x_p\right) = (Bl)i_a(t), \tag{22.4}$$

where, c_p represents the damping coefficient of the suspension. Moreover, for brevity $f_{RF,d}(x_p)$ will be called the nonlinear restoring force of the actuator. Since the stiffness varies depending on the value of the displacement x_p, the impact, or end stop, stiffness is given by the parameter k_c, and the stiffness parameter related to the suspension is given by k_p. In this way, the model can be seen as a linear SDOF system for displacements lower than the stroke length, and as a nonlinear system with a hardening stiffness, when stroke saturation occurs. Considering the model of Fig. 22.4a, the overall stiffness for displacements exceeding the stroke length is $k_{sat} = k_p + k_c$. In general, the restoring force for such a model can be written as,

$$f_{RF,d}\left(x_p\right) = \begin{cases} k_{sat}\left(x_p - x_0\right) + k_p x_0 & x_p > x_0 \\ k_p x_p & \left|x_p\right| \leq x_0 \\ k_{sat}\left(x_p + x_0\right) - k_p x_0 & x_p < -x_0 \end{cases} \tag{22.5}$$

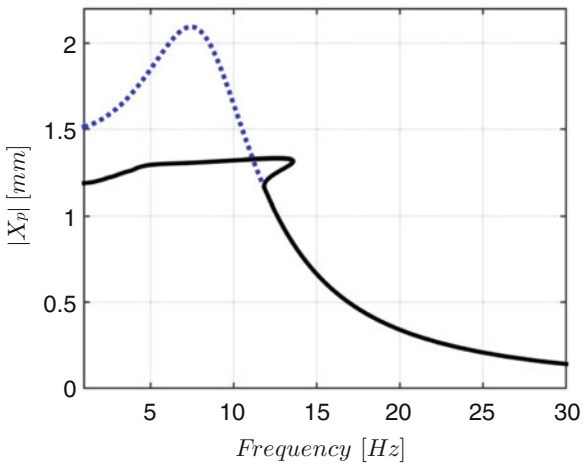

Fig. 22.5 Comparison between the underlying linear frequency response function (dotted blue line) and the nonlinear frequency response curve (solid black line)

Equation (22.5) is also represented in Fig. 22.4b for two values of the impact stiffness k_c. It should be noted that if the impact stiffness $k_c = 0$, the system becomes linear.

A comparison between the nonlinear model and the underlying linear model of the inertial actuator can be done in frequency domain, using the harmonic balance method (HBM), which permits to find the periodic solutions of Eq. (22.4). The method is explained in detail by Detroux et al. in [32] where the periodic solution has been approximated considering several harmonics in the response signal. In fact, to better understand the nonlinear behaviour of the stroke limited inertial actuator, the computation of higher order nonlinear frequency response curves is required, since the non-smooth nonlinearity activates higher harmonics. Simulation analysis involving the computation of periodic solutions are performed using the NI2D software for this study. The mathematical derivation of this approach can be found in Refs. [31–33]. Figure 22.5 shows the comparison between the nonlinear frequency response curve (NFRC) obtained computing the periodic solutions up to the 15th harmonic for the nonlinear model of the inertial actuator and the frequency response function (FRF) of the underlying linear model of the inertial actuator, in a frequency range from 2 to 30 Hz and an amplitude excitation of 0.14 N, corresponding to a current $i_a = 0.0875A$.

It can be observed that the resonance frequency is higher in the nonlinear model than in the underlying linear one. This is due to the hardening behaviour of the nonlinearity. However, the amplitude of the resonance peak for the nonlinear system is lower than the peak of the underlying linear system. In fact, the nonlinear system is constrained within the stroke limits, which do not permit the proof mass to move any further. This results in the NFRC becoming particularly skewed towards higher frequency with respect to the linear FRF. This can be a threat when the inertial actuator is used in a velocity feedback loop, as an increase in the actuator's resonance frequency can lead to a decrease of the stability margin of the controller.

Figure 22.6 shows the lumped parameter model of a SDOF structure connected to the nonlinear inertial actuator previously described. The SDOF, also referred to single-input single-output (SISO) system, would represent the first resonance of a real structure. The proof mass m_p is coupled to the structural mass m_s via the actuator suspension parameters $\kappa(x_r)$ and c_p. Stroke saturation dynamics is, therefore, represented by a piecewise linear stiffness $\kappa(x_r)$, which is shown by the black solid line of Fig. 22.4b, where the variable x_p is replaced by x_r. The structural mass is connected to the ground via the stiffness and damping parameters k_s and c_s, respectively. The absolute displacement of the structure is denoted as x_s. Hence, the relative displacement is defined as,

$$x_r = x_p - x_s. \tag{22.6}$$

The structure is subject to the external, or primary, force f_e, and the control, or secondary, force due to the actuator transducer $(Bl)i_a$. L is the inductance and R the resistance associated with the actuator's coil. The current in the actuator coil is defined as i_a, while the voltage at its terminals is defined as e_a.

The structure's velocity signal $\dot{x}_s$ is multiplied by a fixed gain h_s and fed back to the actuator input current i_a. This forms the linear velocity feedback control loop (VFC). Alongside the VFC, a nonlinear feedback controller (NLFC) has been added, which is defined as a nonlinear function of the relative displacement and velocity $\Psi\,(x_r, \dot{x}_r)$ and can be included or excluded using a switching device. Hence, the simulation results with and without the NLFC can be compared. The dynamics of the system described above can be expressed in a state space form as follow,

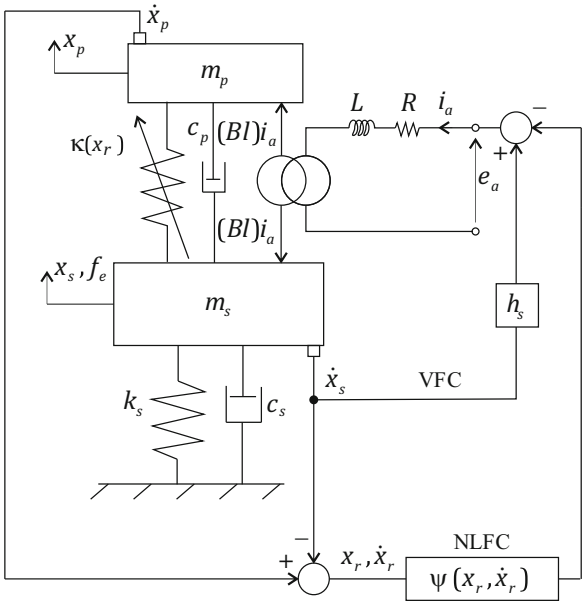

Fig. 22.6 A lumped parameter model of the nonlinear actuator, structure, velocity feedback controller (VFC) and nonlinear feedback controller (NLFC)

Table 22.1 Table of model parameters

Property	m_s (kg)	k_s (N/m)	c_s (Ns/m)	m_p (kg)	k_p (N/m)	c_p (Ns/m)	Bl (N/A)	k_{sat} (N/m)	x_0 (mm)	ω_p (Hz)	ω_s (Hz)
Value	0.05	5000	0.32	0.032	100	1.4	1.6	$10^2 k_p$	1.25	8.9	50.3

$$\begin{cases} \dot{\mathbf{y}} = \mathbf{A}(\mathbf{y})\,\mathbf{y} + \mathbf{B}_e f_e - \mathbf{B}_a (Bl) i_a \\ z = \mathbf{C}\mathbf{y} \end{cases}, \tag{22.7}$$

where $\mathbf{y}$ is the state vector comprising of the displacements and velocities of the structural and proof masses. $\mathbf{A}(\mathbf{y})$ is the system matrix, which includes the nonlinear model of the stiffness. $\mathbf{B}_e$ and $\mathbf{B}_a$ are the input matrices for the external and control forces, respectively. If only the VFC loop is considered, the output of the system z is defined as $z = \dot{x}_s$. Hence, for a fixed gain of the VFC, the input current to the actuator coil becomes,

$$i_a = h_s z. \tag{22.8}$$

If the NLFC loop is also implemented, the output of the system becomes a vector defined as $\mathbf{z} = \{\dot{x}_s \;\; \dot{x}_r\}^T$. The time series data are simulated using Simulink® ODE4 solver with fixed time-step sampled at 20 kHz. The parameters used in the simulations for the system shown in are reported in Table 22.1.

22.3 Velocity Feedback Control and Stability Analysis: Theoretical Results

In the following part of this section, the NLFC is not included in the feedback loop. Hence, the system under study comprises the SDOF structure, the nonlinear actuator and the VFC. The stability of the VFC for the underlying linear system can be calculated from the Nyquist plot of the open loop FRF [10, 13, 23]. Applying this approach to the system of Fig. 22.6 described by the parameters given in Table 22.1 gives a maximum feedback stable gain of,

$$h_{s,\max} = 42. \tag{22.9}$$

However, including the nonlinearity in the model of the actuator will change significantly the stability of the VFC, as discussed in Ref. [34]. The stability of the VFC for the nonlinear system can be verified in time domain by analysing the impulse response of the system for increasing gains. Figure 22.7a shows the time series of the proof mass, structure and

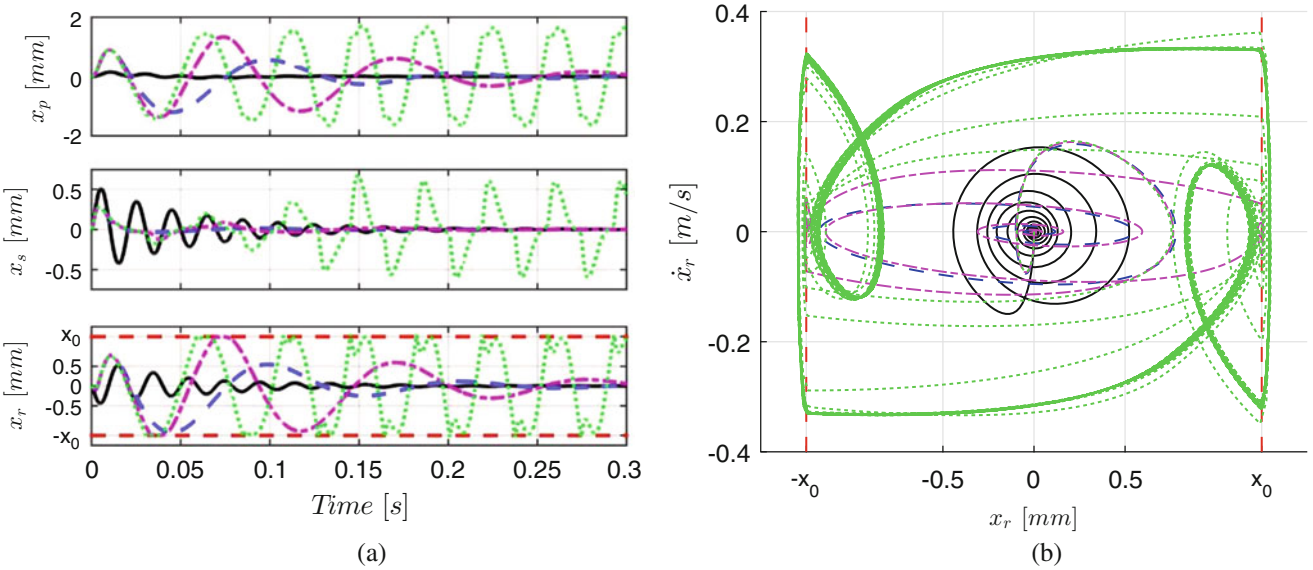

Fig. 22.7 (**a**) Time series of the response of the system to an initial impulse for several values of h_s; (**b**) phase portrait of the response of the system to an initial impulse for several values of h_s

relative displacements, respectively, due to an impulse at time 0 with a magnitude of 10 N. The black solid line shows the response of the system without control. As the feedback gain is increased to 35% of $h_{s,\,\max}$ (blue dotted line), the response of the system to the same impulse shows that the vibration of the structural mass is significantly reduced, while the vibration of the proof mass is increased. However, the proof mass does not collide with the end stops. A further increase of the feedback gain to the value of 45% of $h_{s,\,\max}$ (magenta dash-dotted line) causes the relative displacement to overshoot the allowed stroke length, hence an impulse like excitation is imparted to the structure. However, after two impacts this behaviour decays away. Applying a slightly bigger feedback gain of 50% of $h_{s,\,\max}$ (green dotted line) results in an unstable system. It should be noted that the feedback gain that causes the nonlinear system to go unstable ($h_s = 50\ \%\ h_{s,\,\max}$) is much lower than the one predicted with the linear analysis for the underlying linear model of the system, as reported in Ref. [34]. When the control system becomes unstable, limit cycle oscillations are observed, as shown in Fig. 22.7b. In this figure, the phase portrait of the relative coordinate is displayed for the same simulation conditions of Fig. 22.7a. It can be seen that an increase in the feedback gain rises the possibility of collisions with the end stops. From the time simulation shown in Fig. 22.7a, b the amplitude and frequency of the limit cycle oscillation can be derived in the case of $h_s = 1/2 h_{s,\,\max}$ (green dotted line). In fact, the maximum amplitude of the relative displacement results to be 1.29 mm. The frequency of the limit cycle can be calculated from the time series of Fig. 22.7a considering the zero crossing of the signal. It follows that the frequency of the limit cycle is 27.6 Hz, which is higher than the frequency of the instability for the underlying linear system (about the natural frequency of the actuator ω_p). Hence, the instability of the VFC at lower feedback control gains than those predicted by the linear analysis is caused by the limit cycle oscillation of the nonlinear actuator [23, 24, 34, 35].

22.4 Nonlinear Feedback Control: Theoretical Results

The study of the previous section motivates for the development of a nonlinear controller, whose aim is to prevent the destabilisation of the feedback loop due to stroke saturation. There have been several studies with different approaches that attempted to solve this problem. In fact, a first and crude solution is to switch off the VFC in case stroke saturation is detected [24, 36, 37]. The system then becomes passive, as no more power is supplied to the actuator, and it stabilises. Eventually, one can set that after a certain period of time, the VFC switches on again, until the next stroke saturation is detected. Of course, this solution negates all the benefits of the VFC and the performance is severely reduced. Another idea is the so-called "error governor", which is a penalty function on the velocity feedback gain [38] and many studies have successfully implemented this approach [39–43]. Basically, the controller decreases the velocity feedback gain of a certain amount if the proof mass is approaching the end stops. Also in this case the performance of the VFC is reduced. In this paper, the authors are considering a different approach. As discussed in Ref. [44], if to the system of Fig. 22.6 a relative velocity feedback controller (using

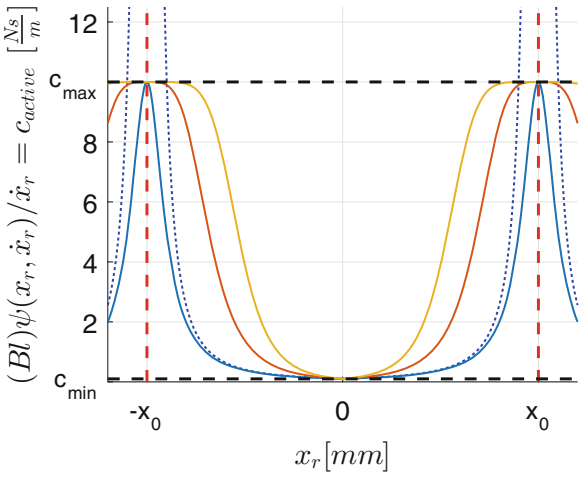

Fig. 22.8 Control action of the proposed NLFC law. The dotted blue line displays the control law of Eq. (22.10) for $b = 0$ and $n = 1$; the solid lines represent the control law in which b is calculated imposing a minimum ($c_{\min}$) and a maximum ($c_{\max}$) in the control action; the blue solid curve shows the NLFC for $n = 1$, the red solid curve for $n = 2$ and the yellow solid curve for $n = 3$

the relative velocity signal $\dot{x}_r$) were used instead of the VFC, the closed loop FRF would have been unconditionally stable and any large feedback gain could have been applied. However, the relative velocity feedback (RVFC) aims to reduce the vibration between the structure and the proof mass and it is of no use to damp the vibration of the structure itself. Hence, [44] proposed to use a combination of the VFC and RVFC. The tuning of the two feedback gains is a trade-off between stability and performance of the controller. Later on, other researchers dealt with the stroke saturation phenomenon using a nonlinear feedback controller function of the relative proof mass displacement [17]. This nonlinear feedback controller acts as a second loop alongside the VFC as shown in Fig. 22.6. In this paper we merge this two ideas into a novel NLFC, whose control law is,

$$\psi\left(x_r, \dot{x}_r\right) = \frac{n_r \dot{x}_r}{\left(x_0 - |x_r|\right)^{2n} + b}. \tag{22.10}$$

where n_r is the feedback gain of the nonlinear controller, b is a function limitation parameter and n is an exponent parameter. Basically, Eq. (22.10) increases the damping of the inertial actuator as the proof mass approaches the end stops. In fact, as the relative displacement of the proof mass gets close to the stroke limit, the denominator term of Eq. (22.10) reduces, hence the current proportional to the relative proof mass velocity increases. A graphical representation of the control action $((Bl)\psi\left(x_r, \dot{x}_r\right)/\dot{x}_r)$ is shown in Fig. 22.8. The dotted blue plot of Fig. 22.8 shows the case in which the parameter $b = 0$ and $n = 1$ in Eq. (22.10).

It can be seen that for low values of the displacement the added active damping to the actuator is almost zero. As the displacement approaches the stroke limits, the nonlinear controller increases the active damping of the actuator. In such a configuration, the input current to the actuator's coil becomes,

$$i_a = h_s \dot{x}_s - \frac{n_r \dot{x}_r}{\left(x_0 - |x_r|\right)^2}. \tag{22.11}$$

Applying Eq. (22.11) can yield the current to take very large values with dangerous and impractical implications, as shown in Fig. 22.8 by the dotted blue plot. Hence, a saturation limit on the maximum control action has to be set. The active damping added to the actuator can be derived from Eq. (22.10) as,

$$c_{active}\left(x_r\right) = \frac{(Bl)\psi\left(x_r, \dot{x}_r\right)}{\dot{x}_r} = \frac{(Bl)n_r}{\left(x_0 - |x_r|\right)^{2n} + b}. \tag{22.12}$$

Then we force the control action to be bounded between a minimum active damping $c_{active}(0) = c_{\min}$ that is reached when the proof mass is centred within the casing and a maximum active damping $c_{active}(x_0) = c_{\max}$ that is reached when the proof mass saturates in stroke. From this consideration, the parameters b and n_r can be calculated. Assuming $x_r = 0$ and $b \ll x_0$, the parameter n_r can be calculated from Eq. (22.12) as,

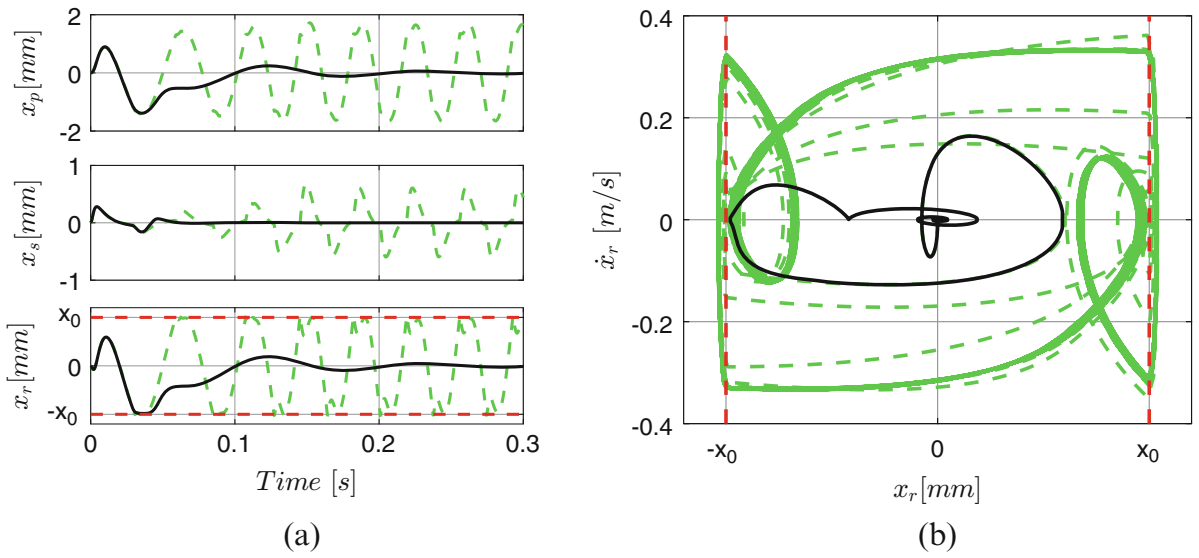

Fig. 22.9 Time history and phase portrait of the response of the system to an initial impulse for $h_s = 1/2h_{s,\max}$; the dashed green line shows the response using the VFC loop only (NLFC switched off); the solid black line shows the response using both the VFC and the NLFC loops (NLFC switched on). (**a**) Time histories; (**b**) phase portrait

$$c_{\min} \equiv c_{active}(0) = \frac{(Bl)n_r}{x_0^{2n}} \quad \Rightarrow \quad n_r = \frac{c_{\min}x_0^{2n}}{n_r}. \tag{22.13}$$

Similarly, assuming $x_r = x_0$, the parameter b can be calculated from Eq. (22.12) as,

$$c_{\max} \equiv c_{active}\,(x_0) = \frac{(Bl)n_r}{b} \quad \Rightarrow \quad b = \frac{(Bl)n_r}{c_{\max}}. \tag{22.14}$$

The solid lines in Fig. 22.8 are graphical representations of the control action in which Eqs. (22.13) and (22.14) have been used. In particular the blue, red and solid curves show the NLFC for the exponent parameter $n = 1, 2, 3$, respectively. It can be seen that increasing the exponent parameter n increases the active damping of the actuator on a bigger range of displacements. This can be beneficial for the stability of the system, but can be detrimental for the performance of the VFC. Time simulation studies are carried out to assess the performance of the NLFC. In particular a comparison with the VFC is made. Figure 22.9 shows the time histories and the phase portraits of the system with a feedback gain $h_s = 1/2h_{s,\max}$ and excited by an impulse at time 0 with a magnitude of 10 N.

In this scenario the system goes unstable if the NLFC is turned off. Implementing the NLFC described by Eq. (22.10) yields the proof mass to avoid the contact with the end stops, as the relative velocity goes to zero before the actuator saturates and the system remains stable. Of course, the stability of the nonlinear system does not depend only on the value of the velocity feedback gain h_s, but also on the magnitude of the excitation P, as reported in Ref. [34]. Therefore, a parametric study has been carried out in order to investigate the potential benefits of the NLFC over different scenarios. In particular, the stability of the system has been evaluated for each value of P and h_s, and in two different testing conditions: the VFC loop is implemented with the NLFC switched off, and both the VFC and NLFC are implemented. For each scenario, the operating region of the inertial actuator is defined as,

$$OR\,(P, h_s) = \left\{ (P, h_s) | \max_{t\to\infty} |x_r(t)| < x_0 \right\}, \tag{22.15}$$

where the sets of (P, h_s) inside the operating region are those in which the system is stable and the inertial actuator is adding damping to the structure. The results of the parametric study are shown in Fig. 22.10. The green area delimited by the dotted black line in Fig. 22.10 shows the safe operating region when the VFC is implemented. It can be seen that the nonlinearity in the inertial actuator severely reduces the stability of the system for large values of the excitation or the feedback gain. It should be noted that for low value of excitation, the operating region reaches the 100% of $h_{s,\max}$. This is because the system does not reach the end stops, hence it behaves linearly and the maximum feedback gain calculated with the Nyquist criterion

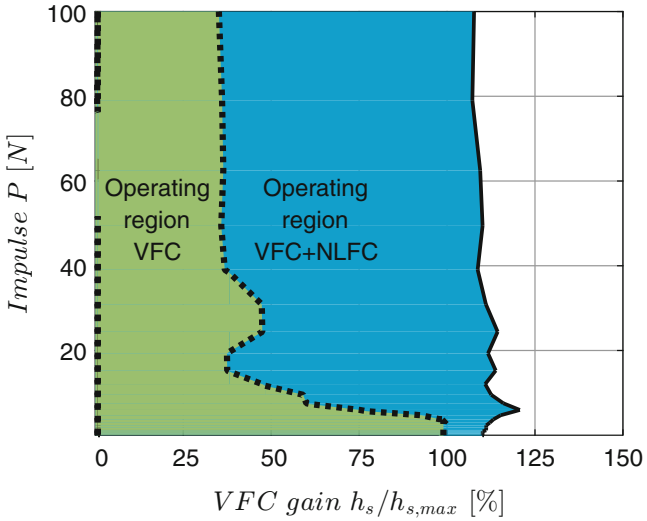

Fig. 22.10 Comparison between the safe operating regions of the inertial actuator as function of the amplitude of the impulse excitation P and of the velocity feedback gain h_s. The green area delimited by the dotted black line displays the safe operating region if only the VFC is implemented; the blue area delimited by the solid black line shows the safe operating region if both the VFC and NLFC are implemented

is the correct one. However, as soon as the excitation value is increased, the maximum gain that can be fed to the actuator without reaching the instability quickly drops down. Repeating the same parametric study, but including the NLFC in the system, produces a completely different result. This is shown in Fig. 22.10 with the blue area delimited by the solid black line. In this case, the area covered by the operating region of the actuator using both VFC and NLFC is bigger than the area of the VFC only. Hence, the added NLFC loop increases the safe operating region of the inertial actuator. Moreover, the maximum gain that can be fed to the actuator overshoots $h_{s,\,\max}$. This is because, even for low excitations, the NLFC increases the damping of the actuator. Thus, a bigger velocity feedback gain can be used before the system gets unstable.

22.5 Nonlinear Feedback Control: Experimental Implementation and Results

This section examines the experimental implementation of the VFC and NLFC loops for the vibration reduction of the first mode of a cantilever beam using the stroke limited inertial actuator presented in Sect. 22.2. The experimental set-up is shown in Fig. 22.11. It consists of an aluminium cantilever beam and a control unit attached at the nodal point of the second mode of the beam. This is because the experimental set-up aim to control only the first mode of the beam. The control unit comprises the Micromega Dynamics IA-01 inertial actuator, a B&K accelerometer (type 4375V) and a PCB Piezotronics 208C01 ICP force sensor. The external excitation is given by a Dytran Dynapulse 5800B3 S/N 6160 roving hammer instrumented with a medium stiff Delrin tip (127-6250P). The acceleration signal passes through a B&K charge amplifier (type 2635) before entering the acquisition system. The acquisition and control system are performed using a dSPACE 1103 PPC Controller Board, which also does the analogue-to-digital (ADC) and digital-to-analogue (DAC) conversions. The sampling rate of the digital system has been set at $f_s = 10$ kHz. All the measurements are then recorded by ControlDesk Next Generation software on a PC workstation. The control signal from the dSPACE passes through a low pass analogue filter with a cut off frequency at 4 kHz before entering the Micromega Dynamics voltage driven current amplifier PR-052-01-04-03 and then the inertial actuator. The parameters of the test rig are given in Table 22.2 for the beam and control unit, and in Table 22.1 for the inertial actuator.

The same approach of the theoretical study of Sect. 22.3 has been considered for the experimental study. Firstly, the open loop FRF has been measured in order to obtain the gain margin of the VFC. Consequently, the VFC closed loop response has been measured for several excitation levels and velocity feedback gains.

Finally, the test campaign has been repeated with the implementation of the NLFC discussed in Sect. 22.4, alongside the VFC. The stability of the VFC is analysed using the Nyquist criterion for the open loop FRF $L(j\omega) = h_s Y_{cc}(j\omega)$, where $Y_{cc}(j\omega)$ is the driving point mobility [45]. The control gain h_s is set to unity and the actuator is driven by a broadband white noise current. This results in the open loop FRF shown by the polar plot in Fig. 22.12. It can be seen that the locus of the

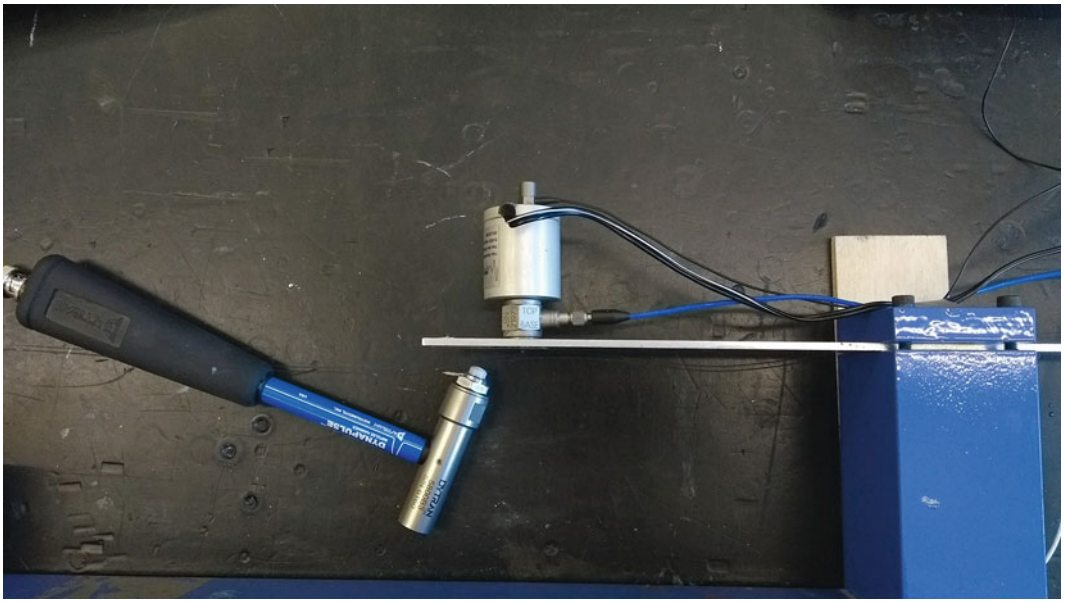

Fig. 22.11 Experimental test rig for the VFC and NLFC of the beam using a stroke limited inertial actuator

Table 22.2 Parameters of the cantilever beam and the control unit

Property	l_{beam} (mm)	b_{beam} (mm)	h_{beam} (mm)	m_{acc} (kg)	$m_{base,act}$ (kg)	$m_{force,gauge}$ (kg)
Value	175	25	3	0.005	0.053	0.023

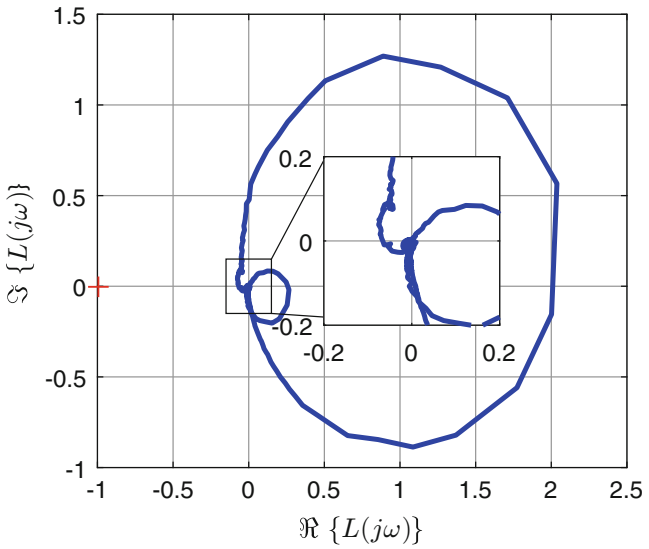

Fig. 22.12 Nyquist plot of the measured open loop FRF with a control gain $h_s = 1$

Nyquist intersects the negative real axis at a distance $\delta = 0.068$, which corresponds to a gain margin of $g_m = 1/\delta = 14.7$. As a result, the maximum velocity feedback gain that can be applied to the system without driving it unstable is $h_{s,\,\max} = 14.7$.

The VFC and NLFC are then implemented as follow. The acceleration signal from the accelerometer at the control point c is acquired by the dSPACE. The controller applies then a high pass filter with a cut off frequency of 2 Hz to the signal, which is consequently integrated using the trapezoidal rule to obtain the velocity at the control point $\dot{x}_c$. The velocity of the structure at the control point is then amplified by a fixed feedback gain h_s. The amplified signal is then fed to the actuator. This constitutes the VFC. The NLFC instead has been designed according to Eq. (22.10) to have $c_{\min} = 0.5\,\text{Ns/m}$, $c_{\max} = 100\,\text{Ns/m}$ and $n = 1$.

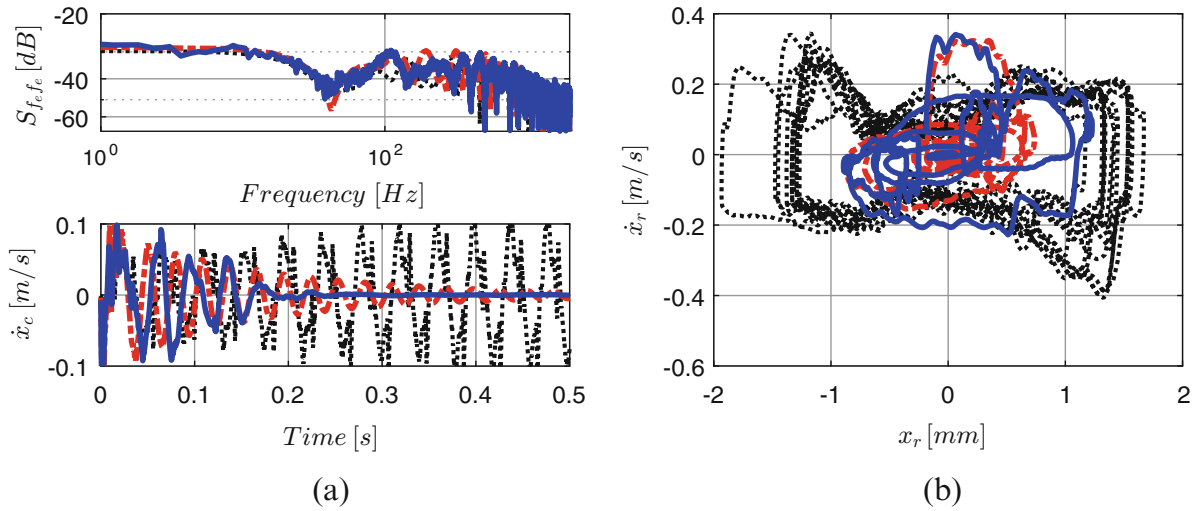

Fig. 22.13 (**a**) Power spectral density of the excitation force and time history of the velocity signal at the control point; (**b**) phase portrait of the relative proof mass displacement and velocity. Dashed red lines represent the response for the uncontrolled scenario; dotted black lines represent the response with the NLFC switched off and $h_s = 42\,\%\,h_{s,\,\max}$; solid blue lines represent the response with the NLFC switched on and $h_s = 42\,\%\,h_{s,\,\max}$

In this case, the signal of the force cell, which corresponds to the control force f_c has been high pass filtered, as well as the acceleration signal $\ddot{x}_c$, with a second order Butterworth high pass with a cut off frequency of 2 Hz. The relative proof mass acceleration has been calculated as,

$$\ddot{x}_r = \frac{f_c - m_c \ddot{x}_c}{m_p}, \tag{22.16}$$

where $m_c = m_{acc} + m_{base,\,act} + m_{force,\,gauge}$ is the total attached mass at the control point. The relative proof mass velocity and displacement are then derived by high pass filtering and integrating the acceleration signal in the same way as it has been discussed for the structure's velocity signal. Then, the NLFC input signal to the inertial actuator is calculated in real time using Eq. (22.10). A comparison among the uncontrolled scenario (passive system), the VFC system and the VFC plus NLFC system has been done and the results are reported in Fig. 22.13. For the comparison between the two control strategies, the system has been excited by an impulse at the free end of the beam using the instrumented hammer. A fixed control gain h_s is implemented for each test case, starting from the uncontrolled scenario and increasing its value until instability is reached. Each acquisition lasts 5 s after the hammer triggering. An interesting result is displayed in Fig. 22.13. This figure compares the uncontrolled case (dashed red lines) with the VFC case using $h_s = 42\,\%\,h_{s,\,\max}$ (dotted black lines) and with the VFC plus NLFC case also with $h_s = 42\,\%\,h_{s,\,\max}$ (solid blue lines). Figure 22.13a shows the power spectral density of the excitation force and the time history of the velocity at the control point. Figure 22.13b instead shows the phase plane of the relative proof mass displacement and velocity. It can be seen that in the uncontrolled case, the vibration of the structure dies out, but only after a certain period of time. Also, the trajectory of the proof mass starts to orbit until it eventually decays to zero. Implementing the VFC and assuming a feedback gain $h_s = 42\,\%\,h_{s,\,\max}$ leads the system to instability for the same level of excitation of the uncontrolled case. In fact, the trajectory of the proof mass is fixed on a limit cycle as predicted by the theoretical analysis of Sect. 22.4. If the NLFC is also implemented, under the same conditions of level of excitation and velocity feedback gain, the system will remain stable. This can be observed in both the time history of the structure's velocity and in the trajectory of the proof mass. The theoretical parametric study performed in Sect. 22.4, has been repeated here for the experimental analysis. In this case the beam has been excited with three different level of excitation, namely: low (below 20 N), medium (between 20 and 30 N) and high (above 30 N). For each level of excitation, the test has been repeated increasing the velocity feedback gain from the uncontrolled case to $h_{s,\,\max}$. The parametric study has been conducted firstly with the VFC loop only and secondly with both the VFC and NLFC in order to compare the operating regions of the inertial actuator with the two different control strategies. The results are shown in Fig. 22.14, where the red asterisks are the experimental data points in which the VFC is stable, and the blue squares are the experimental data points in which the VFC plus NLFC is stable.

The data points of the two control strategies defines the operating region of the inertial actuator that is highlighted by the green area delimited by the dashed red line for the VFC strategy and by the blue area delimited by the solid blue line for the

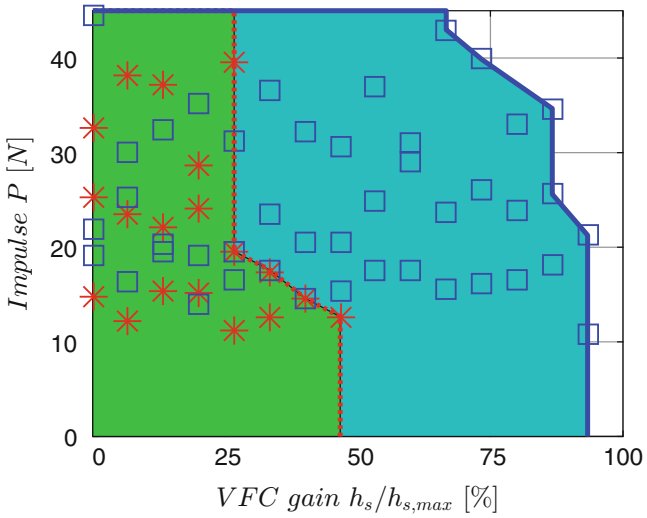

Fig. 22.14 Comparison between the safe operating regions of the inertial actuator as function of the amplitude of the impulse excitation P and of the velocity feedback gain h_s. The green area delimited by the dotted red line displays the safe operating region if only the VFC is implemented (the experimental data is shown by the red star points); the blue area delimited by the solid blue line shows the safe operating region if both the VFC and NLFC are implemented (the experimental data is shown by the blue square points)

VFC plus NLFC strategy. Hence, the main finding of the experimental study is that the added NLFC loop is able to increase the safe operating region of the inertial actuator.

22.6 Conclusions

In this paper, a nonlinear feedback controller has been presented to avoid stroke saturation. Firstly, the mathematical model of the nonlinear inertial actuator has been derived, where the nonlinearity has been modelled by a piecewise linear stiffness. Simulation studies in frequency domain have been carried out using the harmonic balance method. It turned out that the nonlinear inertial actuator behaves significantly different compared to the underlying linear model. In particular, the resonance frequency of the inertial actuator increases as the amplitude of the excitation increases, due to the hardening nonlinearity. Secondly, the theoretical implementation of a stroke limited inertial actuator within a velocity feedback loop to control a single degree of freedom structure has been investigated. The stability for the nonlinear system operating in velocity feedback control has been analysed using the time series and phase portrait analysis. It emerged that the maximum feedback gain that leads the nonlinear system to instability is consistently lower than the one predicted by the linear analysis, where the nonlinear element is neglected. This motivated the development of a nonlinear controller. A nonlinear feedback control law, which operates as a second loop alongside the classical velocity feedback, has been presented and analysed. Basically, the nonlinear controller increases the damping of the inertial actuator as the proof mass approaches the end stops, whereas it takes negligible values as the proof mass moves clear from the displacement constraints. A test rig consisting of a cantilever beam with a control unit attached to the free end has been considered for the experimental investigation of the nonlinear controller. The implementation of the nonlinear control law has been discussed and the results of the tests has been presented for the beam being controlled and excited under several scenarios. In particular the two control approaches (VFC and VFC plus NLFC) has been compared under several excitation levels and velocity feedback gains. For each test the stability of the system has been assessed. It has been shown both theoretically and experimentally that the nonlinear feedback controller is able to increase the safe operating region of the actuator. Hence, larger feedback gains can be used or larger impulse excitations can be withstood without leading the system to instability if this controller is used alongside the VFC. Future work will be related on the estimation of the relative proof mass displacement in order to reduce the sensor number and the added mass to the structure.

Acknowledgements The authors gratefully acknowledge the European Commission for its support of the Marie Curie program through the ITN ANTARES project (General Agreement 606817). The results presented in this paper were partly obtained using the NI2D software developed by the Space Structures and Systems Laboratory (S3L), University of Liège.

References

1. Meirovitch, L.: Dynamics and Control of Structures. Wiley, New York (1990)
2. Fuller, C.C., Elliott, S.J., Nelson, P.A.: Active Control of Vibration. Academic Press, San Diego, CA (1996)
3. Elliott, S.J.: Signal Processing for Active Control. Academic Press, London, UK (2001)
4. Inman, D.J.: Vibration with Control. Wiley, Chichester, UK (2006)
5. Fahy, F., Gardonio, P.: Sound and Structural Vibration: Radiation, Transmission and Response, 2nd edn. Elsevier Science, Oxford, UK (2007)
6. Wagg, D.J., Neild, S.A.: Nonlinear Vibration with Control: For Flexible and Adaptive Structures. Springer, Dordrecht (2010)
7. Preumont, A.: Vibration Control of Active Structures: An Introduction. Springer, Dordrecht (2011)
8. Gardonio, P., Díaz, C.G.: Downscaling of proof mass electrodynamic actuators for decentralized velocity feedback control on a panel. Smart Mater. Struct. **19**(2), 025004 (2010)
9. Rohlfing, J., Gardonio, P., Elliott, S.J.: Base impedance of velocity feedback control units with proof-mass electrodynamic actuators. J. Sound Vib. **330**(20), 4661–4675 (2011)
10. Rohlfing, J., Elliott, S.J., Gardonio, P.: Feedback compensator for control units with proof-mass electrodynamic actuators. J. Sound Vib. **331**(15), 3437–3450 (2012)
11. Díaz, C.G., Paulitsch, C., Gardonio, P.: Smart panel with active damping units. Implementation of decentralized control. J. Acoust. Soc. Am. **124**(2), 898–910 (2008)
12. Díaz, C.G., Paulitsch, C., Gardonio, P.: Active damping control unit using a small scale proof mass electrodynamic actuator. J. Acoust. Soc. Am. **124**(2), 886–897 (2008)
13. Paulitsch, C., Gardonio, P., Elliott, S.J.: Active vibration control using an inertial actuator with internal damping. J. Acoust. Soc. Am. **119**(4), 2131–2140 (2006)
14. Baumann, O.N., Elliott, S.J.: The stability of decentralized multichannel velocity feedback controllers using inertial actuators. J. Acoust. Soc. Am. **121**(1), 188–196 (2007)
15. Paulitsch, C., Gardonio, P., Elliott, S.J., Sas, P., Boonen, R.: Design of a lightweight, electrodynamic, inertial actuator with integrated velocity sensor for active vibration control of a thin lightly-damped panel. In: Proceedings of ISMA 2004: International Conference on Noise and Vibration Engineering, Leuven, pp. 239–253, 20–22 Sept 2004
16. Paulitsch, C.: Vibration control with electrodynamic actuators. Institute of Sound and Vibration Research, Ph.D. Thesis, University of Southampton (2005)
17. Zvonar, G.A., Lindner, D.K., Borojevic, D.: Nonlinear control of a proof-mass actuator to prevent stroke saturation. In: Dynamics and Control of Large Structures; Proceedings of the 8th VPI&SU Symposium, Blacksburg, pp. 37–48, 6–8 May 1991
18. Lindner, D.K., Zvonar, G.A., Borojevic, D.: Limit cycle analysis of a nonlinear controller for a proof-mass actuator. In: AIAA Dynamics Specialists Conference, Dallas, pp. 585–594, 16–17 Apr 1992
19. Lindner, D.K., Celano, T.P., Ide, E.N.: Vibration suppression using a proofmass actuator operating in stroke/force saturation. J. Vib. Acoust. Trans. ASME. **113**(4), 423–433 (1991)
20. Lindner, D.K., Zvonar, G.A., Borojevic, D.: Performance and control of proof-mass actuators accounting for stroke saturation. J. Guid. Control Dyn. **17**(5), 1103–1108 (1994)
21. Lindner, D.K., Zvonar, G.A., Borojevic, D.: Nonlinear control of a proof-mass actuator. J. Guid. Control Dyn. **20**(3), 464–470 (1997)
22. Scruggs, J., Lindner, D.: Optimal sizing of a proof-mass actuator. In: 40th Structures, Structural Dynamics, and Materials Conference, St. Louis, 12–15 Apr 1999
23. Baumann, O.N., Elliott, S.J.: Destabilization of velocity feedback controllers with stroke limited inertial actuators. J. Acoust. Soc. Am. **121**(5), EL211–EL217 (2007)
24. Wilmshurst, L.I.: Analysis and control of nonlinear vibration in inertial actuators. Institute of Sound and Vibration Research, Ph.D. Thesis, University of Southampton (2015)
25. Dal Borgo, M., Ghandchi Tehrani, M., Elliott, S.J.: Dynamic analysis of nonlinear behaviour in inertial actuators. In: 13th International Conference on Motion and Vibration Control (MOVIC 2016) and the 12th International Conference on Recent Advances in Structural Dynamics (RASD 2016), Southampton, 012027, 4–6 July 2016
26. Politansky, H., Pilkey, W.D.: Suboptimal feedback vibration control of a beam with a proof-mass actuator. J. Guid. Control Dyn. **12**(5), 691–697 (1989)
27. Wilmshurst, L.I., Ghandchi Tehrani, M., Elliott, S.J.: Nonlinear vibrations of a stroke-saturated intertial actuator. In: 11th International Conference on Recent Advances in Structural Dynamics (RASD 2013), Pisa, 1–3 July 2013
28. Wilmshurst, L.I., Ghandchi Tehrani, M., Elliott, S.J.: Nonlinear identification of proof-mass actuators accounting for stroke saturation. In: Proceedings of ISMA 2014: International Conference on Noise and Vibration Engineering, Leuven, pp. 209–223, 15–17 Sept 2014
29. Micromega Dynamics: Active damping devices and inertial actuators. http://www.micromega-dynamics.com/download/category/4-active-damping-device.html (2016). Accessed 10 Jun 2016
30. Worden, K.: Data-processing and experiment design for the restoring force surface method, part 1: integration and differentiation of measured time data. Mech. Syst. Signal Process. **4**(4), 295–319 (1990)
31. Worden, K., Tomlinson, G.R.: Nonlinearity in Structural Dynamics: Detection, Identification and Modelling. Institute of Physics, Bristol (2000)
32. Detroux, T., Renson, L., Masset, L., Kerschen, G.: The harmonic balance method for bifurcation analysis of large-scale nonlinear mechanical systems. Comput. Meth. Appl. Mech. Eng. **296**, 18–38 (2015)
33. Pavlov, A., van de Wouw, N., Nijmeijer, H.: Frequency response functions and Bode plots for nonlinear convergent systems. In: Proceedings of the 45th IEEE Conference on Decision and Control, San Diego, pp. 3765–3770, 13–15 Dec 2006
34. Dal Borgo, M., Ghandchi Tehrani, M., Elliott, S.J.: Nonlinear control and stability of a stroke limited inertial actuator in velocity feedback. In: 9th European Nonlinear Dynamics Conference ENOC2017, Budapest, 25–30 June 2017

35. Dal Borgo, M., Ghandchi Tehrani, M., Elliott, S.J.: Dynamic analysis of two nonlinear inertial actuators in active vibration control. In: 27th International Conference on Noise and Vibration Engineering (ISMA2016), Leuven, 19–21 Sept 2016
36. Wilmshurst, L.I., Ghandchi Tehrani, M., Elliott, S.J.: Active control and stability analysis of flexible structures using nonlinear proof-mass actuators. In: IX International Conference on Structural Dynamics (Eurodyn 2014), Porto, pp. 1571–1578, 30 June – 2 July 2014
37. Wilmshurst, L.I., Ghandchi Tehrani, M., Elliott, S.J.: Preventing of stroke saturation in inertial actuators using a detection scheme. In: The 21st International Congress on Sound and Vibration (ICSV21), Beijing, 13–17 July 2014
38. Gilbert, E.G., Tan, K.T.: Linear systems with state and control constraints: the theory and application of maximal output admissible sets. IEEE Trans. Automat. Contr. **36**(9), 1008–1020 (1991)
39. Díaz, I.M., Pereira, E., Reynolds, P.: Integral resonant control scheme for cancelling human-induced vibrations in light-weight pedestrian structures. Struct. Control Health Monit. **19**(1), 55–69 (2012)
40. Díaz, I.M., Reynolds, P.: On-off nonlinear active control of floor vibrations. Mech. Syst. Signal Process. **24**(6), 1711–1726 (2010)
41. Hudson, E.J., Reynolds, P., Nyawako, D.S.: Active vibration control of a multi-panel floor area. In: Structures Congress 2014, Boston, pp. 2500–2511, 2014
42. Noormohammadi, N., Reynolds, P.: Experimental investigation of dynamic performance of a prototype hybrid tuned mass damper under human excitation. In: Active and Passive Smart Structures and Integrated Systems 2013, San Diego, 10–14 Mar 2013
43. Rohlfing, J., May, T., Walter, L., Millitzer, J.: Self-tuning velocity feedback control for a time varying structure using a voltage driven electrodynamic inertial mass actuator. In: 27th International Conference on Noise and Vibration Engineering (ISMA2016), Leuven, 19–21 Sept 2016
44. Inman, D.J.: Control/structure interaction: effects of actuator dynamics. In: Dynamics Specialists Conference, Structures, Structural Dynamics, and Materials, Long Beach, pp. 507–533, 5–6 Apr 1990
45. Gardonio, P., Brennan, M.J.: Mobility and impedance methods in structural dynamics. In: Fahy, F. (ed.) Advanced Applications in Acoustics, Noise and Vibration, pp. 389–447. Taylor and Francis, London (2004)

Chapter 23
Bio-inspired Nonlinear Control of Artificial Hair Cells

Sheyda Davaria, V. V. N. Sriram Malladi, and Pablo A. Tarazaga

Abstract The human auditory mechanism can detect sound frequencies ranging from 20 Hz to 20 kHz, over a broad pressure range of 0–120 dB SPL due to its nonlinear amplification performed by the cochlea. Sound waves travel through the ear canal, eardrum and the three bones of the middle ear. The last bone of the middle ear (stapes) pushes on the oval window and creates propagating waves in the cochlea. Each of the sound frequency components excites a specific location along the basilar membrane when it travels through the cochlea. These are then coupled to the hair cells, which apply their nonlinear compressibility and amplification behavior to improve sound detection. These functions of the cochlea are the inspiration to design more sensitive and capable sensors.

The primary objective of this work is to mimic the nonlinear amplification of cochlea by developing piezoelectric based active artificial hair cells (AHCs). By examining models of the biological cochlea, a nonlinear feedback control law is designed which applies the appropriate forcing conditions to the beam to amplify or suppress vibrations initially induced by an external stimulus. To achieve this goal, a two degree of freedom model of the AHCs is created. Control laws are then applied to the system to mimic the phenomenological active nonlinear functions of the outer hair cells seen in the mammalian cochlea and to improve the ability of a single AHC to work for more than one frequency.

Keywords Active artificial hair cell · Nonlinear amplification · Feedback control · Cochlea · Piezoelectric material

23.1 Introduction

In [1–4], Joyce et al., developed a control law that eliminates the linear damping of the system and introduces a cubic damping into the system of equations to drive the response of the system to a Hopf bifurcation. It is observed that the cochlea works similar to a system tuned to a Hopf bifurcation [5–8]. In Joyce et al.'s work, the model was assumed to be a single degree of freedom model of a piezoelectric cantilever beam. The nonlinear control law determined the feedback voltage to the piezoelectric actuator based on the response of the SDOF model. Such a closed-loop system was able to simulate the nonlinear amplification seen in the mammalian cochlea [9]. However, the nonlinear amplification of the AHC developed by Joyce et al., is limited to frequencies close to the first natural frequency (single frequency sensor). As a result, to have a wider bandwidth system, the need of an array of AHCs, each limited to a single frequency is sought. It is desirable to expand the ability of each AHC to work for more than one frequency, thus, a novel multiple degrees of freedom (MDOF) approach is considered in this study.

In the present study, a two degree of freedom model of the beam is considered. The response of the beam to a base excitation passes through two filters separately, a low pass and a bandpass filter. The filtered response is then used as feedback for two controllers to introduce cubic damping at multiple frequencies as an attempt to move to MDOF hair cell mimicry.

23.2 Modeling

The aluminum beam modeled in this study is clamped at one end and free at the other end. A base excitation input is used as the external excitation to the system. A pair of piezoelectric actuators are bonded to the clamp end of the beam to control the system. A schematic picture of the beam is shown in Fig. 23.1. The beam is length L, width w_b and thickness $2t_b$ and

S. Davaria (✉) · V. V. N. Sriram Malladi · P. A. Tarazaga
Vibration, Adaptive Structures, and Testing Laboratory, Department of Mechanical Engineering, Virginia Tech, Blacksburg, VA, USA
e-mail: sheydada@vt.edu

C. Niezrecki, J. Baqersad (eds.), *Structural Health Monitoring, Photogrammetry & DIC, Volume 6*,
Conference Proceedings of the Society for Experimental Mechanics Series, https://doi.org/10.1007/978-3-319-74476-6_23

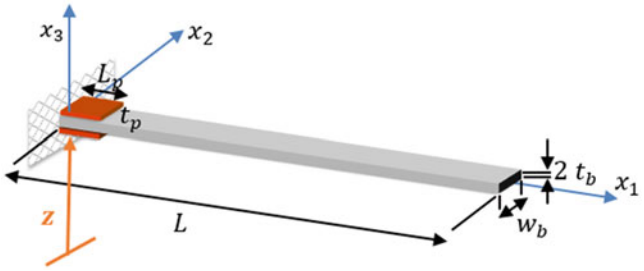

Fig. 23.1 Schematic picture of the beam with piezoelectric actuators

Table 23.1 The model parameters of the beam and piezoelectric actuators

Properties	Beam		Piezoelectric actuator	
Young modulus (GPa)	$C^E_{b_{11}}$	71.1	Y_p	30.336
Density (kg/m^3)	ρ_b	2700	ρ_p	7800
Length (m)	L	0.5	L_p	0.04
Width (m)	w_b	0.025	w_p	0.025
Thickness (mm)	$2t_b$	3.2	t_p	0.4
d_{31} (C/N)			-180×10^{-12}	

Table 23.2 The parameters used in two degree of freedom model

$w_1\left(\frac{\text{rad}}{\text{s}}\right)$	ζ_1	$\beta_{1V}\left(\frac{\text{kg}^{1/2}\text{m}}{\text{s}^2\text{V}}\right)$	$\beta_{1z}\left(\text{kg}^{\frac{1}{2}}\right)$	$w_2\left(\frac{\text{rad}}{\text{s}}\right)$	ζ_2	$\beta_{2V}\left(\frac{\text{kg}^{1/2}\text{m}}{\text{s}^2\text{V}}\right)$	$\beta_{2z}\left(\text{kg}^{\frac{1}{2}}\right)$
69.450	0.05	−0.001	0.255	431.773	0.05	0.006	−0.143

the piezoelectric actuator is length L_p, and thickness t_p with the width equal to the beam's width. It is excited in the vertical direction x_3 and the base acceleration is $\ddot{z}$.

The parameters of the beam and the piezoelectric actuators are listed in Table 23.1. These will be used for simulation purposes.

A finite element model of the beam with piezoelectric actuators is developed. The equations were then transformed into the modal domain in order to decouple the system of equations and break the model into modal equations. The model is then reduced to only the first two modes and the nonlinear control law is then applied to the first two modal equations. The decoupled set of the equations of motion are,

$$(\ddot{r}_1) + 2\zeta_1 w_1 \dot{r}_1 + w_1^2 r_1 = \beta_{1v} V + \beta_{1z}\ddot{z}, \tag{23.1}$$

$$(\ddot{r}_2) + 2\zeta_2 w_2 \dot{r}_2 + w_2^2 r_2 = \beta_{2v} V + \beta_{2z}\ddot{z}, \tag{23.2}$$

where, V is the control voltage supplied to the piezoelectric actuators, $\ddot{z}$ is the base acceleration in the form of $\ddot{z} = Z\ \sin(\Omega t)$, where Z is the acceleration amplitude and Ω is the excitation frequency, ζ_1 and ζ_2 are damping ratios of the first and second mode respectively, w_1 and w_2 are the corresponding natural frequencies, β_{1V} and β_{2V} are control influence terms on the first and second mode, and β_{1z} and β_{2z} are force influence terms. The values of all the coefficients used in the present study are tabulated in Table 23.2.

The equations of the motion (23.1) and (23.2) were used to develop a state space model of the system with $\dot{r}_1$ and $\dot{r}_2$ as feedback to the controller. A Simulink model is created based on the state space model and implements the filters and control laws. Both of the filters are designed such that the bandwidth of the filtered velocities lies in the frequency bandwidth of the first two natural frequencies of the beam. The low pass filter is a fourth order Butterworth filter with a corner frequency of 200 rad/s (31.83 Hz) and the band pass filter is a sixth order Butterworth filter with pass band edge frequencies of 220 rad/s (35.01 Hz) and 1000 rad/s (159.15 Hz). The response of the system is the velocity, $\dot{u}_t$, at the tip of the beam which is approximated by $\dot{u}_t = s_1\dot{r}_1 + s_2\dot{r}_2$, where s_1 and s_2 are the mode participation factor of the first and second mode on the tip velocity. These coefficients are calculated using the inverse of the transformation from the physical to the modal domain and are equal to $-6.14418\ \text{kg}^{-1/2}$ and $-6.12068\ \text{kg}^{-1/2}$, respectively (Fig. 23.2).

In the present work, the control law developed in Ref. [1] for SDOF system is extended to a two DOF system. Therefore, the control voltage applied to the piezoelectric systems is a summation of frequency bandwidth limited voltage signals $V1$ and $V2$. The control signal ($V1$) is in the form of $V1 = \frac{1}{\beta_{1V}}\left(\frac{\alpha_{11}}{s_1}\dot{u}_{t1} - \frac{\alpha_{31}}{s_1^3}\dot{u}_{t1}^3\right)$, where $\dot{u}_{t1}$ is the low-pass filtered velocity. Also, a band pass filter around the second natural frequency of the system is used and the control signal of $V2 = \frac{1}{\beta_{2V}}\left(\frac{\alpha_{12}}{s_2}\dot{u}_{t2} - \frac{\alpha_{32}}{s_2^3}\dot{u}_{t2}^3\right)$ is created, where $\dot{u}_{t2}$ is the velocity of the tip filtered by the bandpass filter. The coefficients

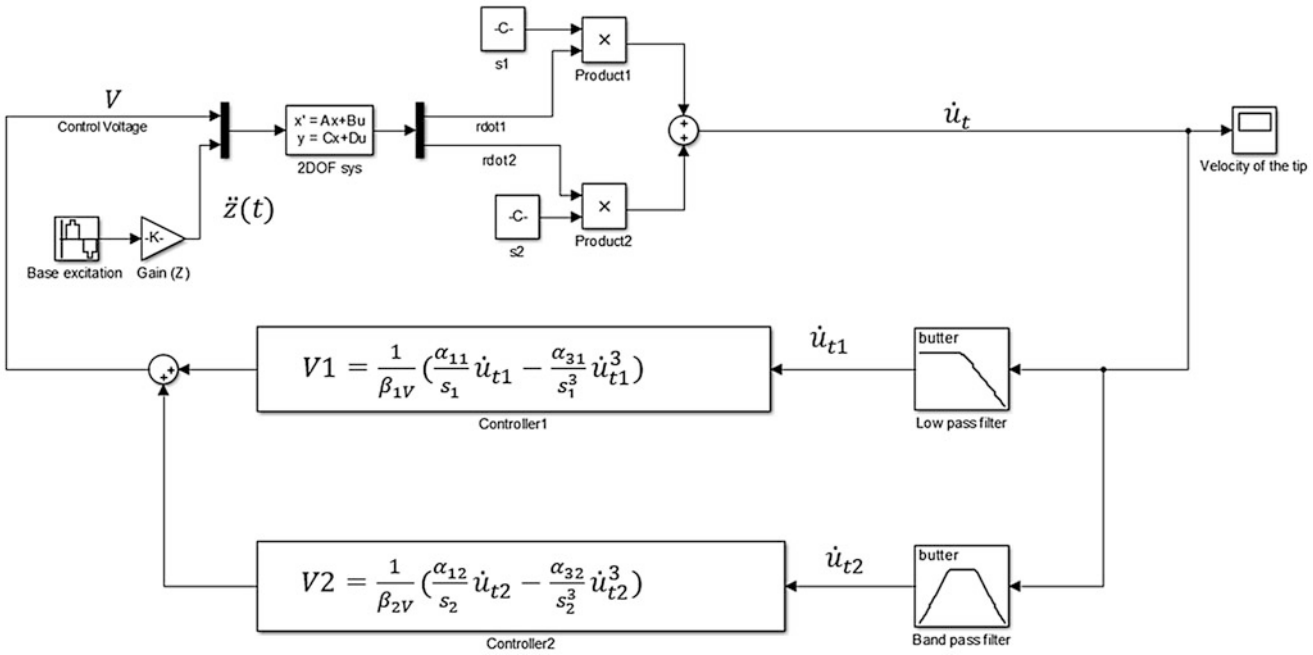

Fig. 23.2 Simulink model of the controlled system

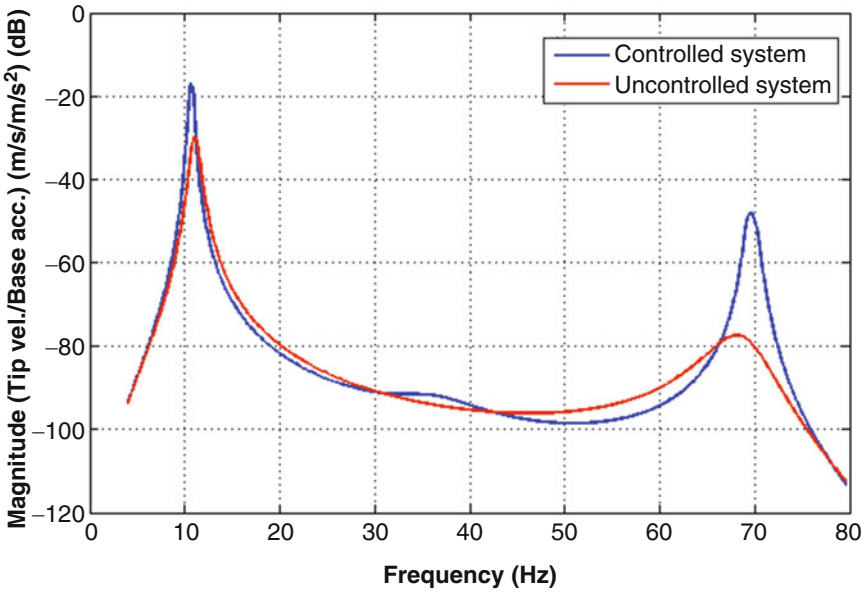

Fig. 23.3 Controlled system with two controllers

α_{11} and α_{12} are chosen to be $2\zeta_1 w_1$ and $2\zeta_2 w_2$ to remove the linear damping of the first and second mode, respectively. The cubic damping gains (α_{31} and α_{32}) are selected based on the dynamics of the system.

23.3 Results

The base excitation of the beam is simulated as a stepped sine signal in the frequency range of 20 $\left(\frac{\text{rad}}{\text{s}}\right)$ (3.18 Hz) to 500 $\left(\frac{\text{rad}}{\text{s}}\right)$ (79.57 Hz) with an amplitude of 0.2 m/s^2. The two degree of freedom linear system (without filters and controllers) is also excited using the same input. Frequency response function (FRF) of the uncontrolled and controlled systems with $\alpha_{31} = 10^4 \left(\frac{\text{s}}{\text{m}^2\text{kg}}\right)$ and $\alpha_{32} = 10^6 \left(\frac{\text{s}}{\text{m}^2\text{kg}}\right)$ is presented in Fig. 23.3.

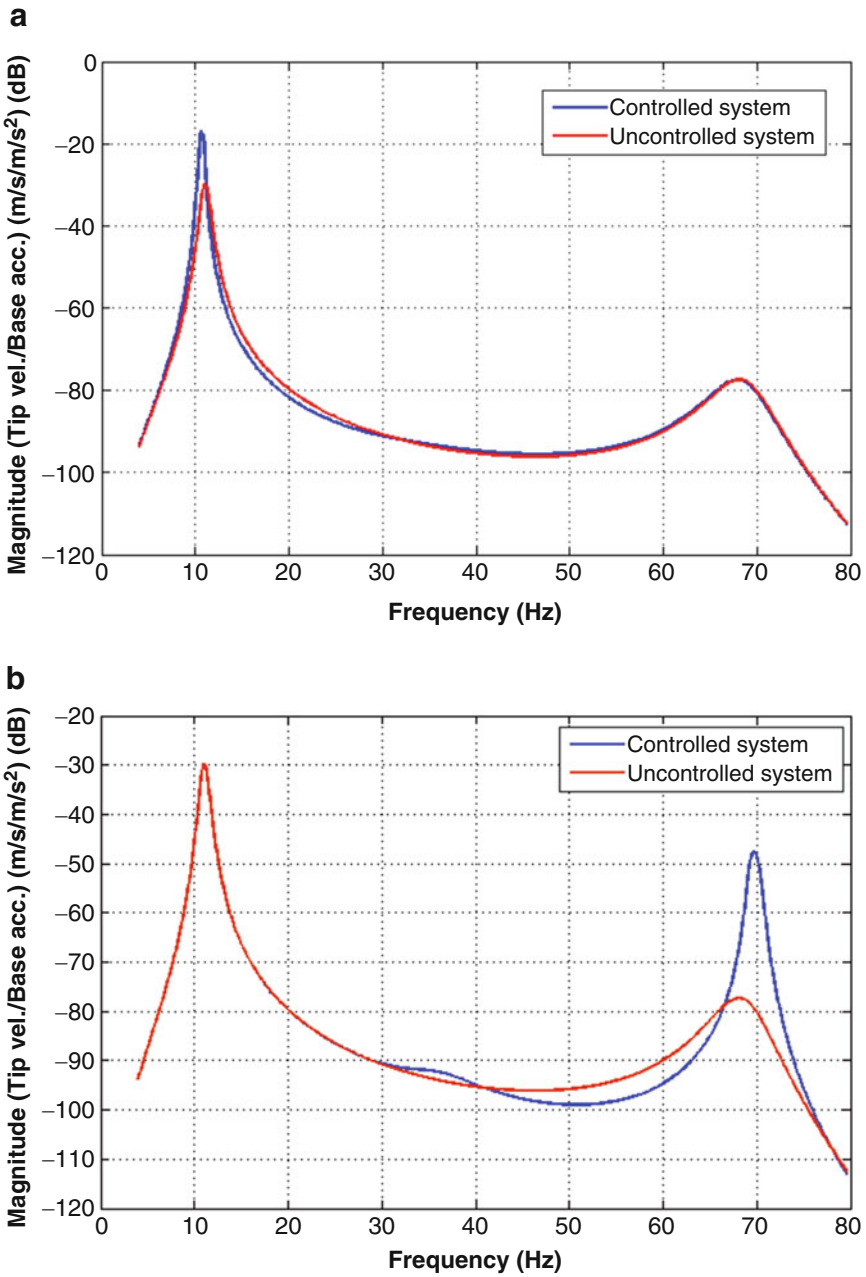

Fig. 23.4 FRF of the controlled system with (**a**) controller only on the first mode, (**b**) controller only on the second mode

In this figure, the controller, amplifies the response of the system close to the first and second natural frequencies. Additionally, the control law can also be applied such that only one of the two natural frequencies show nonlinear amplification. To further illustrate this, Fig. 23.4a shows the FRF of the system with only the first controller (V_1) and Fig. 23.4b shows the results by only having the second controller (V_2). In summary, each of the controllers only affects the response close to the corresponding natural frequency as expected.

The nonlinear effect of the control law is easily seen when the amplitude of the base excitation is varied. Figure 23.5 shows the nonlinear effect of changing the base acceleration amplitude (Z) on the FRF of the system close to each of the natural frequencies. In Fig. 23.5a, the response is compressed nonlinearly for the 1, 2 and 4 m/s^2 input accelerations, while it is amplified for the lower input levels. Figure 23.5b shows that the response is compressed for $Z = 4$ m/s^2 close to the second natural frequency and it is amplified for the other cases.

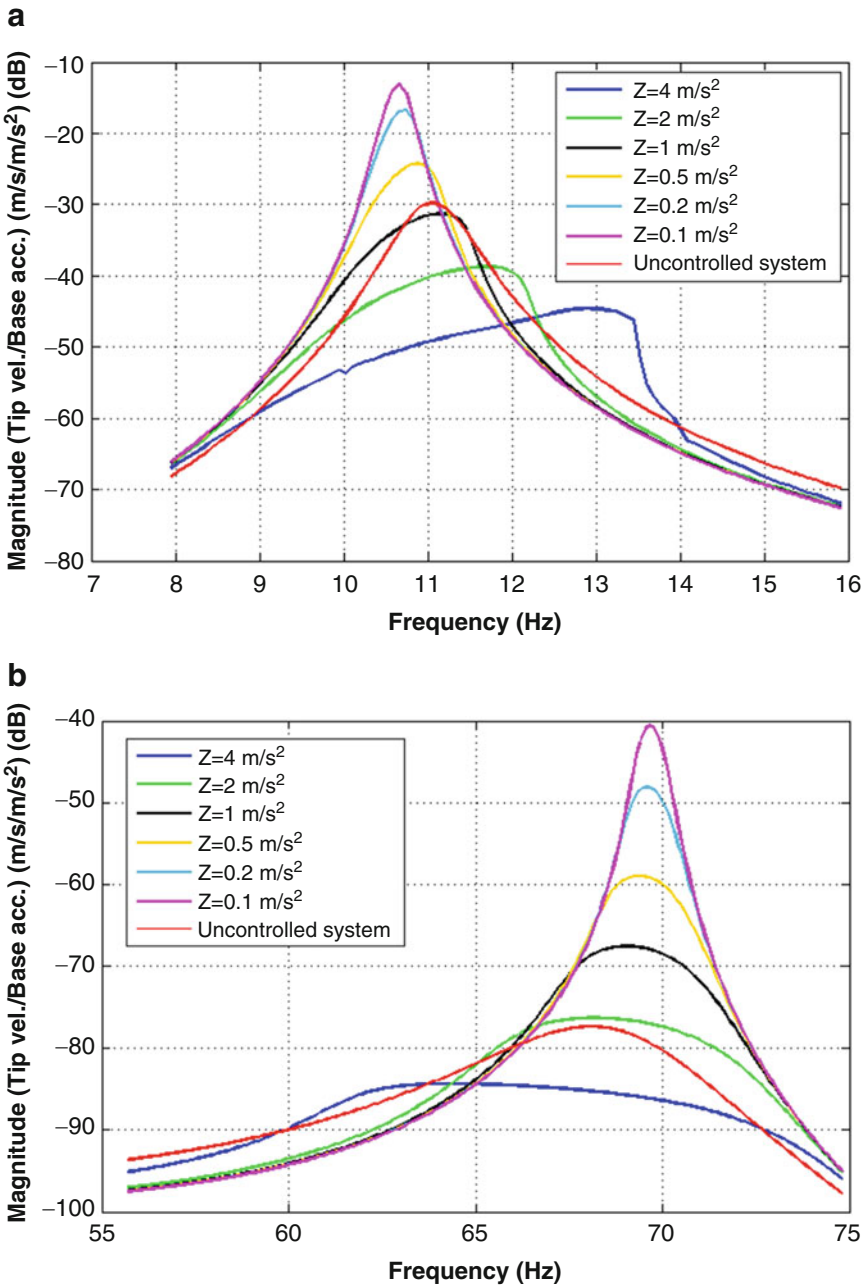

Fig. 23.5 Frequency response functions of the system due to changing the input amplitude (**a**) close to the first natural frequency, (**b**) close to the second natural frequency

23.4 Conclusion

In this study, a piezoelectric-based sensor inspired by the nonlinear behavior of the hair cells of the mammalian cochlea was designed. Inspired by the motion of the cochlear hair cells, an AHC was modeled as a beam excited by a base acceleration. For sensing and amplifying a broad range of frequencies, two controllers were used to remove the linear damping of the first and second mode and also used to add a nonlinear damping to the system close to the natural frequencies of the AHC. Comparison between the simulation results of the linear and nonlinear systems showed that the amplitude of the response close to each of the natural frequencies can be controlled without affecting the response close to the other natural frequencies. Also, it is concluded that exciting the system with different levels of the input show the nonlinear amplification function of the system.

Acknowledgement The authors would like to acknowledge the generous support from the National Science Foundation (NSF) (Grant No.1604360) which provided the funding for this project. Any opinions, findings, and conclusions or recommendations expressed in this material are those of the author(s) and do not necessarily reflect the views of the National Science Foundation.

The authors would also like to acknowledge the support received through the John R. Jones III Faculty Fellowship.

References

1. Joyce, B.S., Tarazaga, P.A.: Developing an active artificial hair cell using nonlinear feedback control. Smart Mater. Struct. **24**(9), 094004 (2015)
2. Joyce, B.S., Tarazaga, P.A.: Mimicking the cochlear amplifier in a cantilever beam using nonlinear velocity feedback control. Smart Mater. Struct. **23**(7), 075019 (2014)
3. Joyce, B.S., Tarazaga, P.A.: Active artificial hair cells using nonlinear feedback control. In: ASME 2014 Conference on Smart Materials, Adaptive Structures and Intelligent Systems, V002T06A002-V002T06A002 (2014)
4. Joyce, B.S., Tarazaga, P.A.: Artificial cochlear hair cells using active piezoelectric materials. In: ASME 2013 Conference on Smart Materials, Adaptive Structures and Intelligent Systems, V002T06A002-V002T06A002 (2013)
5. Martignoli, S., van der Vyver, J.J., Kern, A., Uwate, Y., Stoop, R.: Analog electronic cochlea with mammalian hearing characteristics. Appl. Phys. Lett. **91**(6), 064108 (2007)
6. Eguíluz, V.M., Ospeck, M., Choe, Y., Hudspeth, A.J., Magnasco, M.O.: Essential nonlinearities in hearing. Phys. Rev. Lett. **84**(22), 5232–5235 (2000)
7. Szalai, R., Champneys, A., Homer, M., Maoiléidigh, D., Kennedy, H., Cooper, N.: Comparison of nonlinear mammalian cochlear-partition models. J. Acoust. Soc. Am. **113**(1), 323–336 (2013)
8. Hudspeth, A.J., Julicher, F., Martin, P.: A critique of the critical cochlea: hopf—a bifurcation—is better than none. J. Neurophysiol. **104**(3), 1219–1229 (2010)
9. Robles, L., Ruggero, M.A.: Mechanics of the mammalian cochlea. Physiol. Rev. **81**(3), 1305–1352 (2001)

Chapter 24
Transient Excitation Suppression Capabilities of Electromagnetic Actuators in Rotor-Shaft Systems

Nitish Sharma, Shivang Shekhar, and Jayanta Kumar Dutt

Abstract Impulsive forces cause sudden variations in dynamic systems and may result in fatal damage to the system especially in turbines where the whole system is enclosed inside a casing with very small clearance between the blades and the casing. Electromagnetic actuators have been known to apply non-contact electromagnetic force on a rotor- shaft section preventing rotor-shaft vibrations. This work attempts to investigate the comparison of two different control laws in controlling the vibrations caused by noises such as sudden flow rate change, blade loss, or excitations occurring due to seismic vibrations. A rotor-shaft system is developed within a simulation framework which includes an actuator placed away from the bearings. Literature shows the use of conventional PD (Proportional Derivative) control law which is equivalent to a 2-element support model. This work novels the 3-element viscoelastic support model, which is found to offer better vibration mitigation abilities in terms of controlling transient excitations. Preliminary theoretical simulation using linearized expression of electromagnetic force and the accompanying example show good reduction in transverse response amplitude, postponement of instability caused by viscous form of rotor internal damping.

Keywords Electromagnetic actuator · 3-Element viscoelastic model · Blade loss · Earthquake excitation · Active control

24.1 Introduction

In any rotor shaft system, vibration control plays a vital role in evaluating the performance of the system. The most common source of excitation is the residual unbalance which can be handled by precise balancing and other passive control actions. Various works by Lund, Dutt-Nakra, Dutt-Toi [1–4] and many more have shown how providing passive support damping can be efficient in reducing rotor response and increasing the Stability Limit Speed (SLS) of rotors. References [2–4] have shown that viscoelastic supports perform better than conventional PD controller.

Active Magnetic Bearings (AMBs) as well as actuators are increasingly used in high speed industrial machines such as compressors, turbines, and pumps [5]. Both AMB and actuator share same electro-magnetic properties, but actuator does not support the load of the rotor system and just provides actuation. In our analysis, we are considering an actuator which provides the control action against the unbalanced forces (excitations) in the system.

Das et al. [6] showed how efficient a PD control law used in an electromagnetic actuator can work when compared to an uncontrolled Lalanne's rotor [7] shown in Fig. 24.1. Further building on this work, Shekhar et al. [8] showed a comparison between a conventional PD and 3-element viscoelastic control laws to generate electromagnetic actuator force for vibration control of rotor-shaft system. It was found that 3-element control law provides better Stability limit speed and lower amplitude vibrations against the unbalance mass which excites the system at the operating frequency.

In this work, impulsive noises in the form of blade loss, flow rate change, and the multi-frequency excitations in the form of earthquake have been considered. In Ref. [8], it was shown that almost at all the operating speeds 3-element control law provides more negative real part of the eigenvalues signifying better transient properties. This claim has been supported concretely in the present work as transient response died earlier in case of 3-element control law when compared to 2-element control law.

N. Sharma (✉) · S. Shekhar · J. K. Dutt
Department of Mechanical Engineering, I.I.T, Delhi, India
e-mail: jkdutt@mech.iitd.ernet.in

C. Niezrecki, J. Baqersad (eds.), *Structural Health Monitoring, Photogrammetry & DIC, Volume 6*,
Conference Proceedings of the Society for Experimental Mechanics Series, https://doi.org/10.1007/978-3-319-74476-6_24

24.2 System Details

24.2.1 Electromagnetic Actuator and Its Control Laws

As shown in Fig. 24.1 at node 8, Electromagnetic actuators in two radial directions are used for controlling the vibration of the system, thereby making it a system of 4 poles. Following Schweitzer et al. [5], the force for the actuator is given by

$$F_{mag}(t) = -\frac{k_M i(t)^2}{l_g^2} \quad \text{where } k_M = \frac{\mu_0 A_p N^2}{4} \tag{24.1}$$

In Eq. (24.1), μ_0 is the absolute permeability of free air, A_p is the pole face area, N is the number of coil turns, i(t) is instantaneous current and l_g is the nominal air gap. For complete derivation of this part of the work, readers are referred to Ref. [5]. Linearized equivalent for force expression about the operating point can be given by Eq. (24.2). This expression highlights the importance of low deviations under operating conditions for any kind of Model Predictive Control or active control. This is certainly a limitation with 2-element control law and suggests the use of a viscoelastic law as done in current work.

$$F_{mag}(t) = K_i i(t) + K_s x(t) \tag{24.2}$$

where $K_i = 4k_{mag}\frac{i_0}{g_0^2}$ and $K_s = -4k_{mag}\frac{i_0^2}{g_0^3}$

24.2.2 Comparison of Control Laws

Figure 24.2 represents the current control model of the actuator. The type of suspension characteristics given by the control action is governed by the transfer function between the current and the error signal e(t). The error signal is taken between the reference air gap r(t) and the instantaneous air gap x(t) between the rotor and the actuator pole faces, as picked up by a proximity sensor in each direction. It should be noted that 2-element control law is similar to a PD controller while a 3-element model corresponds to a lead compensator where the 'D' action becomes high-frequency band limited which helps in attenuating noises better [8].

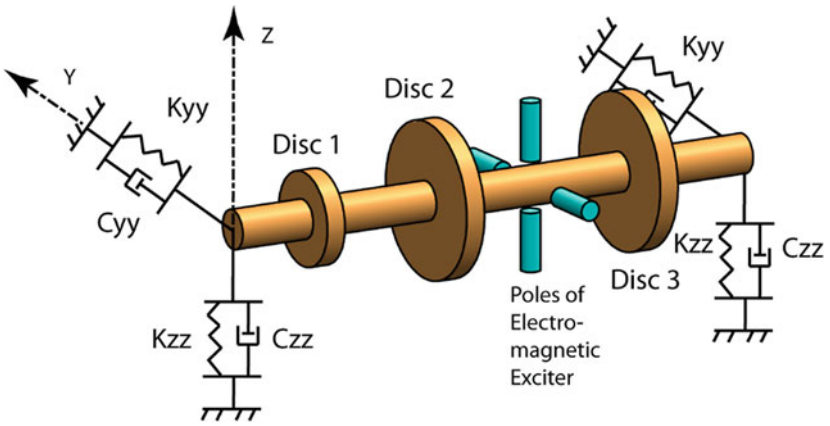

Fig. 24.1 Schematic diagram of Lalanne's rotor-bearing system with electromagnetic exciters

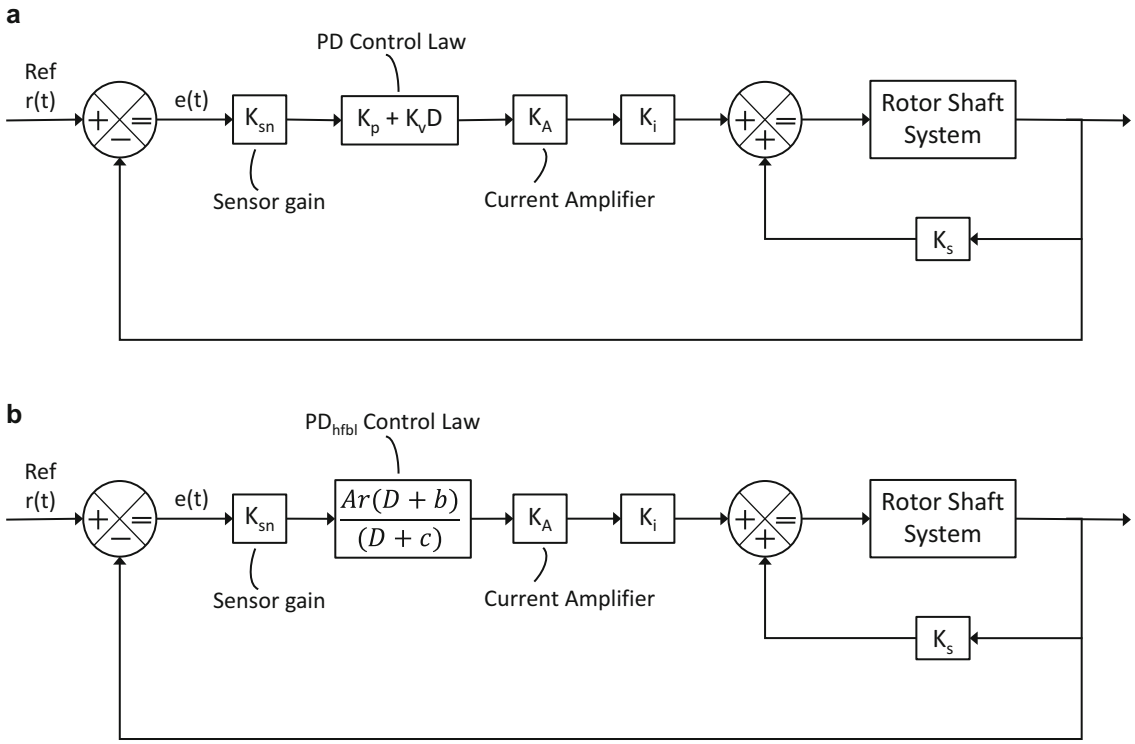

Fig. 24.2 (**a**) Block-diagram showing 2-element control action along each direction. (**b**) Block-diagram showing 3-element control action along each direction

24.2.3 Finite Element Modelling of Rotor Shaft System

Finite element modelling of a rotor shaft system is well addressed in literature [6, 8]. Following the analysis given in Ref. [8], the rotor-bearing system is subdivided into three types of elements, viz rotor-shaft, rotor-disc and bearing, as usual. Further building on [6], the shaft is modelled using 2-noded Rayleigh beam finite element with 4 degrees of freedom per node. Distributed mass, moment of inertia, gyroscopic effect and viscous form of internal material damping are considered along with the direct bending stiffness of the shaft.

Equation (15) of Ref. [6] can be re-written as:

$$[\mathrm{M}]_{(\mathrm{nxn})}\left\{\ddot{\delta}\,(\mathrm{t})\right\} + [\mathrm{C}]_{(\mathrm{nxn})}\left\{\dot{\delta}\,(\mathrm{t})\right\} + [\mathrm{K}]_{(\mathrm{nxn})}\{\delta\,(\mathrm{t})\} = \{\mathrm{Q}\,(\mathrm{t})\}_{(\mathrm{nx1})} \tag{24.3}$$

where 'n' denotes the degrees of freedom after applying the boundary conditions, δ is the displacement vector, 'M' denotes the inertia matrix, 'C' and 'K' matrices denote respectively the coefficients to velocity and displacement vectors and 'Q' denotes the vector of nodal forces. Individually, all the terms can be expanded as follows:

$[\mathrm{M}] = [\mathrm{M_T}] + [\mathrm{M_R}]$; where $[\mathrm{M_T}]$ and $[\mathrm{M_R}]$ the translatory and rotary mass matrix respectively.
$[\mathrm{C}] = [\mathrm{C_b}] + \eta_V[\mathrm{K_B}] - \Omega[\mathrm{G}]$; where $[\mathrm{C_b}]$ is the contribution of bearing damping, η_V is the viscous internal damping coefficient, $[\mathrm{K_B}]$ stands for direct bending stiffness, Ω is the operating speed and [G] defines the gyroscopic matrix.
$[\mathrm{K}] = [\mathrm{K_b}] + \eta_V\Omega[\mathrm{K_C}] + [\mathrm{K_B}]$; where $[\mathrm{K_b}]$ is the contribution of bearing stiffness, $[\mathrm{K_C}]$ is the circulatory stiffness matrix.

Now, for the present work, a comparison of different control laws is achieved by modifying the exciter stiffness and damping matrices as given in Ref. [8].

Therefore, for the control action the equation of motion, i.e. Eq. (24.3) may be written conveniently as

$$[\mathrm{M}]\left\{\ddot{\delta}\right\} + \left[\mathrm{K^*}\,(\mathrm{D})\right]\{\delta\} = \{\mathrm{Q}\} \tag{24.4}$$

In the above [K*(D)] is the matrix coefficient to the displacement vector '{δ}', where the elements of matrix K* are in general functions of D; the matrix coefficient $[K^*(D)] = [K] + [C]\,D$ for the PD control law and $\frac{ArK_AK_i(D+b)}{(D+c)} + K_s$ for the 3-element controller. It is important to note that the total matrix equation of motion in case of 3-element control law become third order when operated by (D + c) present in the denominator [8].

24.2.4 Mathematical Modelling of Blade Loss

Among various excitations involved in the rotor shaft systems, sudden loss in mass like blade breakage forms one of the serious threats to the system as it leads to impulsive forces leading to sudden change in angular as well as linear velocity of the system leading to transient as well as steady state vibrations. Such transient response can cause fatal damage to the system especially in the case of turbines in which the whole system is enclosed inside a casing and a very small clearance is provided between the blades and the casing.

Importance of blade loss dynamics for the consideration in the design of rotor-bearing system has been highlighted in few works. For example, Kirk and Hibner [9], Alam and Nelson [10] presented simulated results on blade-loss-dynamics of the rotor. Further, Das et al. [11], showed the implementation of actuator (PD controller) proposed in Ref. [6] for controlling blade loss vibrations in Jeffcott rotor. Working on the similar guidelines along with taking inspiration from [8], a comparative study of 2-element controller and 3-element controller has been performed on Lalanne's rotor.

24.2.4.1 Dynamics of Rotor Shaft System with Blade Loss

Figure 24.3 shows the change in the position of the centre of mass of the disc before and after the blade loss. It is safe to model the blade loss as the instantaneous change giving rise to impulsive forces in the system. Effect of blade loss on the system can be attributed in two phases.

- Change in centre of mass leading to changed steady state response. Let us consider a disc that has a mass unbalance $m * e$, with total mass of the disc m placed at a distance of e from the axis of rotation at a phase angle of γ. Due to loss in mass m_b of blade placed at r_b with initial phase angle of γ_b, effective mass of $m - m_b$ can be considered placed at e' with a phase γ' which can be written as follows:

$$e' = \frac{1}{(m - m_b)}\sqrt{(me)^2 + (m_b r_b)^2 - 2mem_b r_b \cos(\gamma - \gamma_b)} \tag{24.5}$$

$$\gamma' = \tan^{-1}\left(\frac{me\sin\gamma - m_b r_b \sin\gamma_b}{me\cos\gamma - m_b r_b \cos\gamma_b}\right) \tag{24.6}$$

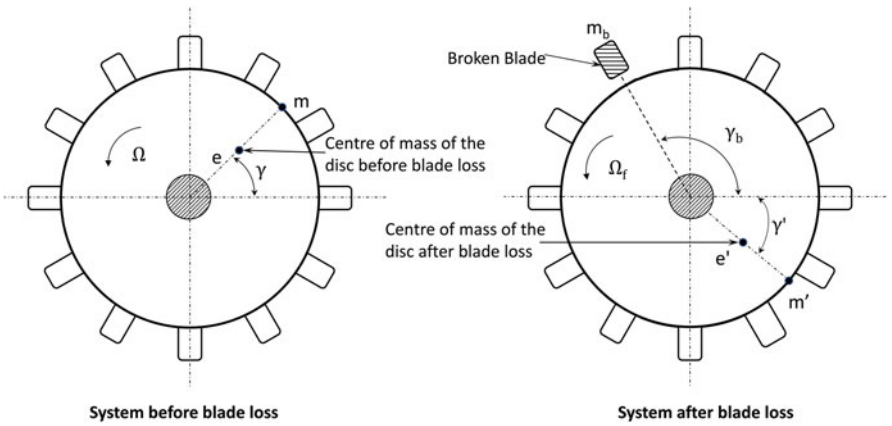

Fig. 24.3 System before and after the blade breakage [11]

- Instantaneous change in linear and angular velocity of the system which can be found by linear and angular momentum balance. As blade loss is an instantaneous process, system's stiffness as well as damping forces don't change significantly before and after the event.

  Considering a disc of radius r with a mass unbalance **me**, with total mass of the disc m placed at a distance of e from the axis of rotation at a phase angle of γ. Due to loss in mass m_b of blade placed at r_b with initial phase angle of γ_b, effective mass of $m - m_b$ can be considered placed at e' with a phase γ'. J_p is moment of inertia of the system about the axis of rotation. So, for a disc rotating with angular velocity of Ω at any time t following set of equations can be set up by considering angular and linear momentum are conserved. All the factors have been defined in the attached appendix. Simulated results for the effect of blade loss and vibration control with both the controllers have been presented in Sect. 24.3.3.

$$\begin{bmatrix} a_{11} & a_{12} & a_{13} & a_{14} & a_{15} \\ a_{21} & a_{22} & 0 & 0 & a_{25} \\ a_{31} & 0 & a_{31} & a_{34} & 0 \\ 0 & 0 & 0 & 1 & 0 \\ 0 & 0 & 0 & 0 & 1 \end{bmatrix} \begin{Bmatrix} \Omega_f \\ \dot{u}_f \\ \dot{v}_f \\ \dot{\Phi}_f \\ \dot{\varphi}_f \end{Bmatrix} = \begin{Bmatrix} b_1 \\ b_2 \\ b_3 \\ b_4 \\ b_5 \end{Bmatrix} \tag{24.7}$$

24.3 Simulated Results and Discussion

A three-disc rotor-shaft system which includes Lalanne's rotor, shown in Fig. 24.1, has been used. This is kept the same as in Ref. [8] for the sake of comparison among the control laws. The details of parameters of the rotor shaft system can be found in Ref. [6] and has been omitted here for the sake of brevity.

24.3.1 Sudden Change in Flow Rate

During the working of a turbine, pressure can't be maintained at a constant value. Pressure change in turn leads to fluctuation in mass flow rate. Flow rate fluctuations further leads to sudden change in operating speed. Flow rate change as such does not pose any serious transverse noises directly to the system but can lead to further complications (not shown here) like blade loss and blade misalignment).

In some adverse cases like steam hammer, it can lead to rupture of the pipes and adversely changes the dynamics of the system. In this analysis, only effect due to the mass flow rate fluctuations has been taken to be on the operating speed. In this work, the 10% change in the operating speed due to sudden change in the mass flow rate has been considered. This change has been assumed to take place in 25° of rotation in case of a 5000-rpm rotor.

Figure 24.4a shows the response when there is decrease in mass flow rate such that it leads to 10% decrease in operating speed. Similarly Fig. 24.4b is for 10% increase in operating speed. From Fig. 24.4, it can be easily seen that both the 2-element and 3-element control laws are performing quite satisfactory. Flow rate change is not as fatal as other noises in turbines as the working fluids are largely low-density fluids. It can be of importance when the working fluid is dense like water as the operating speed change will be more in high density fluids. Nevertheless, these results show the benefits of using a 3-element control law as compared to 2-element as the steady state accumulated error in 3-element control law case is approximately half as compared to conventional 2-element control law. Further, the transient behaviour is much better in 3-element control law. High frequency components have much lower magnitude compared to 2-element case.

24.3.2 Earthquake Excitations

Earthquakes are a major source of seismic noise, consisting mostly surface waves. These types of vibrations are commonly categorized under Gaussian white noise making them impossible to be handled by any passive controller.

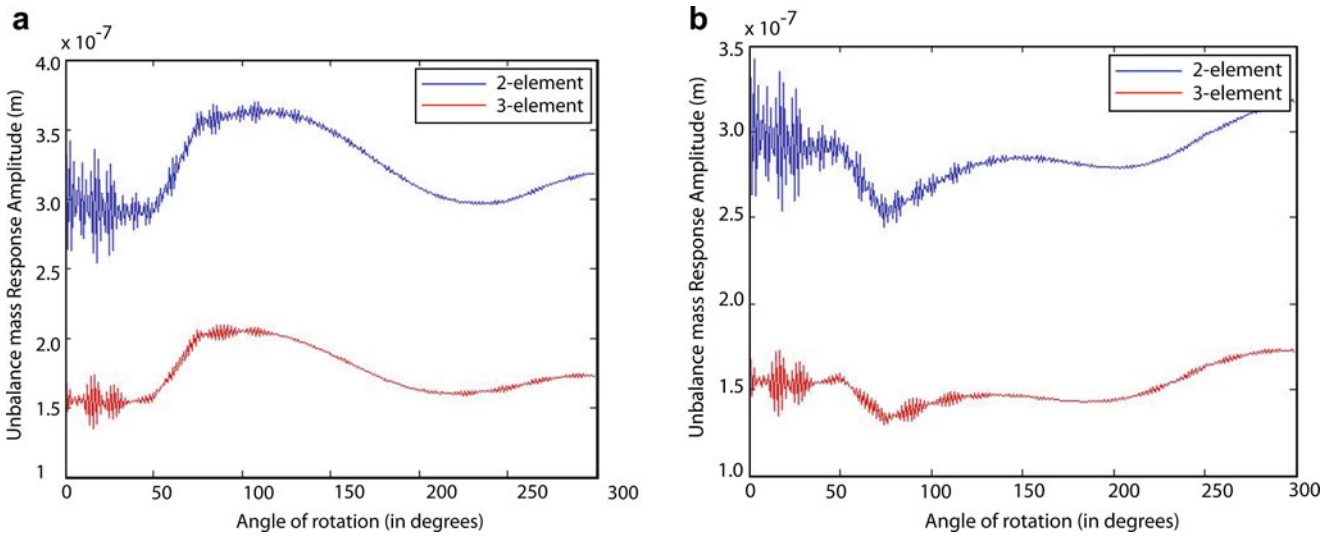

Fig. 24.4 (**a**) Response of the system due to 10% increase in operating speed. (**b**) Response of the system due to 10% decrease in operating speed

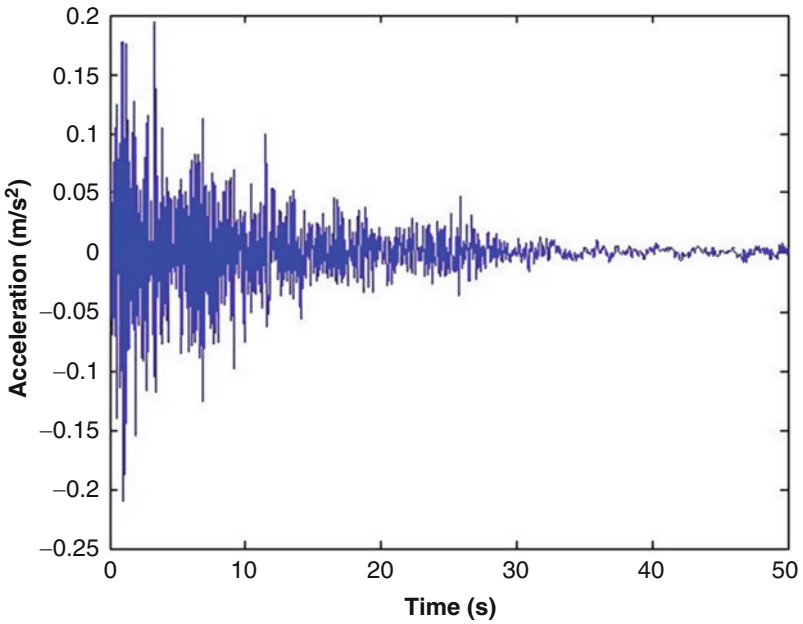

Fig. 24.5 El Centro 1940 earthquake acceleration data

In this work, the earthquake acceleration data from the El Centro earthquake has been used for simulations. Figure 24.5 shows the acceleration data of the earthquake. As evident from the figure, in the current work, earthquake has been modeled as a transient phenomenon. Forces have been applied at the bearing nodes and transient response is simulated for the full system like [12]. Response has been simulated for excitations caused by the earthquake. 2-element and 3-element control laws are efficient in controlling the response as shown in Fig. 24.6. As expected, the 3-element control law is much better in reducing the vibrations also evident from the more negative real eigenvalue components depicting better transient response.

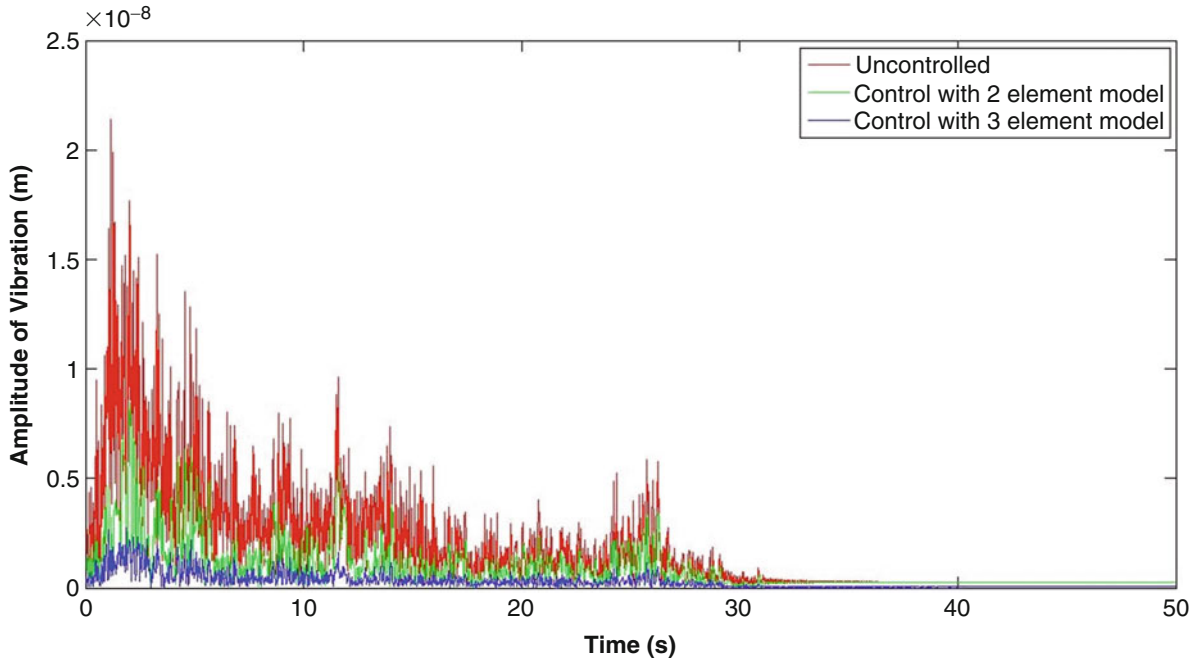

Fig. 24.6 Comparison of response due to earthquake excitations with different controller models

Table 24.1 Two cases of blade breakage

Case	Disc number	Mass of blade (kg)	Initial phase angle (degrees)	Radius of centre of mass of the blade (m)
1	1	0.02	90	0.1
2	2	0.03	118	0.16

24.3.3 Blade Loss

In any typical turbine, blades (90 in number) constitute about 10% of the total mass of the disc. Though a single blade comprises a small portion of the total momentum of the system, impulsive nature of the force of blade loss can lead to large amplitude vibrations if not kept under control. Table 24.1 shows the three different cases considering blade loss from one disc at a time. Mass of the blade is taken proportional to its disc diameter and phase angle is the initial phase angle with respect to the mass unbalance which have been selected randomly.

Figure 24.7a shows the transient response (maximum amplitude throughout the rotor) of the system at 5000 rpm for the first case. Maximum fluctuation in case of 3-element control law is around ¼ times that of 2-element. Also, the steady state error is much lesser in 3-element control law as compared to 2-element control law. Similarly, in Fig. 24.8a for case 2, it can be seen that 3-element control law is performing marginally better than the 2-element control law.

Figures 24.7b and 24.8b show the fluctuating component of the response. In this as well, 3-element is performing better than 2-element. Response settles down faster in 3-element as compared to 2-element control law. Both the results support the better energy extracting capabilities of the viscoelastic model as compared to PD controller as highlighted in Refs. [3, 4, 8].

24.4 Conclusions

In the current work, an electromagnetic actuator, at a plane away from conventional bearing planes, is used which is effective in suppressing sudden excitations as reported in already existing literature. Transient excitations are simulated using the cases of blade loss, sudden change in flow rate and seismic excitations. For the blade loss case and earthquake excitation cases, simulations show better performance by the 3-element control law. For the flow rate case, both the 2-element and 3-element control laws are comparable. However, even in this case, the modified controller is more promising. Overall, it can be concluded that using a viscoelastic form of current-control law for the electromagnetic actuator, better transient excitation

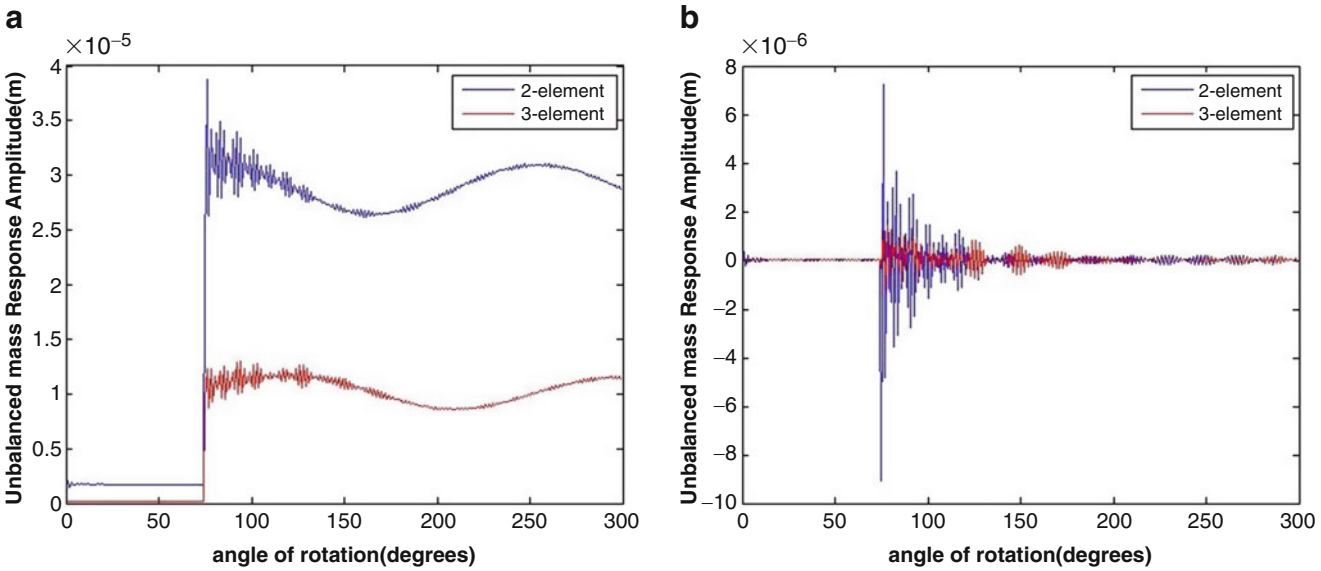

Fig. 24.7 (**a**) Transient response comparison between 2-element and 3-element at 5000 rpm with blade breakage at disc 1. (**b**) Fluctuation comparison between 2-element and 3-element at 5000 rpm with blade breakage from disc 1

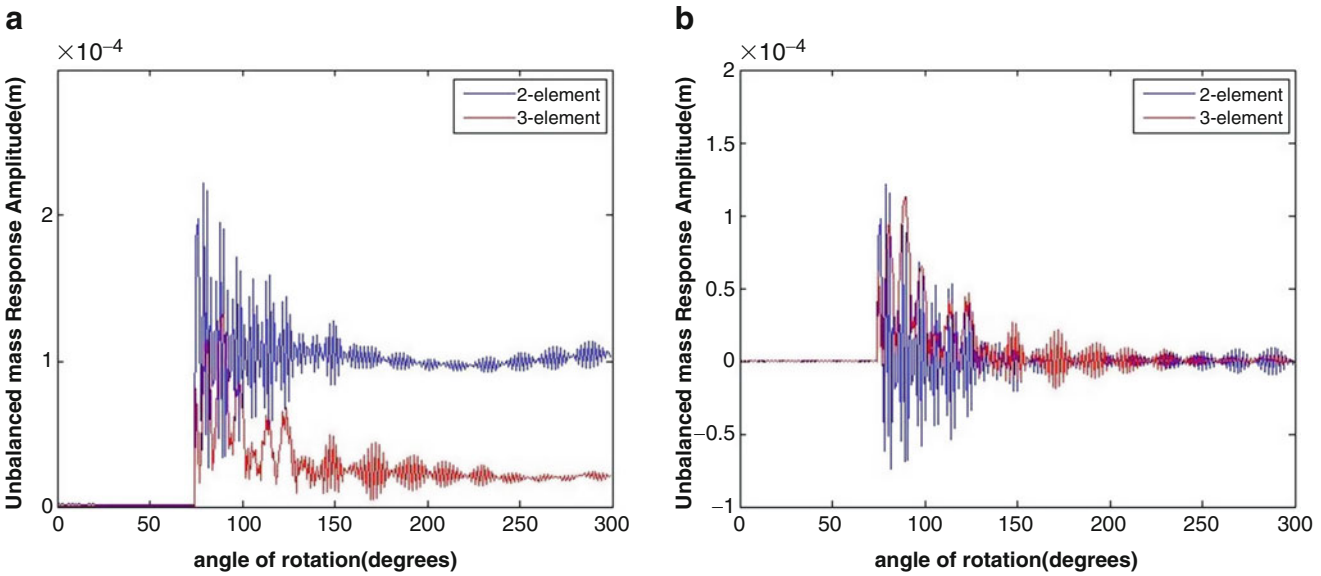

Fig. 24.8 (**a**) Transient response comparison between 2-element and 3-element at 5000 rpm with blade breakage at disc 2. (**b**) Fluctuation comparison between 2-element and 3-element at 5000 rpm with blade breakage from disc 2

suppression capabilities is observed. In some cases, however, the difference between the 2-element (PD) and 3-element control law is not significant. However, in all cases, the proposed control law has better vibration damping characteristics. Therefore, the study inspires the use of higher order control laws for improvement of system's transient response. It will be interesting to analyze the control effort for these control laws as their order is increased. The authors [8] reported comparable magnitudes in control effort and hence it can be used as an optimization criterion. However, this is not included in the scope of current work.

Appendix

System of Eq. (24.7) has been derived using conservation of linear and angular momentum in each direction [11]. Of course, there is no change in linear velocity along the axis of the rotor. That can be assumed to be constant and equal to zero. All the factors are defined as follows:

$$\begin{bmatrix} a_{11} & a_{12} & a_{13} & a_{14} & a_{15} \\ a_{21} & a_{22} & 0 & 0 & a_{25} \\ a_{31} & 0 & a_{31} & a_{34} & 0 \\ 0 & 0 & 0 & 1 & 0 \\ 0 & 0 & 0 & 0 & 1 \end{bmatrix} \begin{Bmatrix} \Omega_f \\ \dot{u}_f \\ \dot{v}_f \\ \dot{\Phi}_f \\ \dot{\varphi}_f \end{Bmatrix} = \begin{Bmatrix} b_1 \\ b_2 \\ b_3 \\ b_4 \\ b_5 \end{Bmatrix}$$

where,

$$a_{11} = J_{pf} + (m - m_b)\, e' \left\{ r - e \cos\left(\gamma' - \gamma\right) \right\}$$

$$a_{12} = (m - m_b) \left\{ e' \sin\left(\Omega t + \gamma'\right) - e \sin\left(\Omega t + \gamma\right) \right\}$$

$$a_{13} = (m - m_b) \left\{ e' \cos\left(\Omega t + \gamma'\right) - e \cos\left(\Omega t + \gamma\right) \right\}$$

$$a_{14} = e' \sin\phi$$

$$a_{15} = e' \sin\psi$$

$$a_{21} = -e' \sin\left(\Omega t + \gamma'\right)$$

$$a_{31} = e_f \cos\left(\Omega t + \gamma_f\right)$$

$$\begin{aligned} b_1 = {} & \Omega \left[J_p + m\,(r - e)\, r + m_b r_b \left\{ r_b - e \cos\left(\gamma_b - \gamma\right) \right\} \right] \\ & + m_b \left\{ \left(r_b \sin\left(\Omega t + \gamma_b\right) - e \sin\left(\Omega t + \gamma_b\right) \right) \right\} \dot{y} \\ & - m_b \left\{ \left(r_b \cos\left(\Omega t + \gamma_b\right) - e \cos\left(\Omega t + \gamma_b\right) \right) \right\} \dot{z} \end{aligned}$$

$$b_2 = \dot{u} + \frac{\Omega}{m - m_b} \left[m_b r_b \sin\left(\Omega t + \gamma_b\right) - m_e \sin\left(\Omega t + \gamma\right) \right]$$

$$b_3 = \dot{v} - \frac{\Omega}{m - m_b} \left[m_b r_b \cos\left(\Omega t + \gamma_b\right) - m_e \cos\left(\Omega t + \gamma\right) \right]$$

$$b_4 = \dot{\phi}$$

$$b_5 = \dot{\psi}$$

References

1. Lund, J.W.: The stability of an elastic rotor in flexible damped supports. ASME J. Appl. Mech. **32**, 911–922 (1965)
2. Dutt, J.K., Nakra, B.C.: Stability of rotor shaft systems with viscoelastic support. J. Sound Vib. **153**(1), 89–96 (1992)
3. Dutt, J.K., Nakra, B.C.: Stability characteristics of rotating systems with journal bearings on viscoelastic supports. Mech. Mach. Theory. **31**(6), 771–779 (1996)
4. Dutt, J.K., Toi, T.: Rotor vibration reduction with polymeric sectors. J. Sound Vib. **262**(4), 769–793 (2003)
5. Schweitzer, G., Maslen, E.H., Bleuler, H., Cole, M., Keogh, P., Larsonneur, R., Nordmann, R., Okada, Y., Traxler, A.: Magnetic Bearings: Theory, Design and Application to Rotating Machinery, pp. 167–220, 251–290, 319–380. Springer (2009)
6. Das, A.S., Dutt, J.K., Nighil, M.C., Irretier, H.: Vibration control and stability analysis of rotor-shaft system with electromagnetic exciters. Mech. Mach. Theory. **43**, 1295–1316 (2009)
7. Lalanne, M., Ferraris, G.: Rotor Dynamics Prediction in Engineering, 2nd edn, pp. 125–132. Wiley (1998)
8. Shekhar, S., Sharma, N., Roy, H.K., Das, A.S., Dutt, J.K.: Vibration control of rotor shaft systems using electromagnetic actuator. In: Proceedings of 9th International Conference on Rotor Dynamics, IFTOMM, Milan, Sept 2014
9. Kirk, R.G., Hibner, D.H.: A note on blade loss dynamics of rotor-bearing systems. ASME J. Eng. Ind. **98**, 497–504 (1976)
10. Alam, M., Nelson, H.D.: A blade loss response spectrum for flexible rotor dynamics. ASME J. Eng. Gas Turbine Power. **107**, 197–504 (1985)
11. Das, A.S., Dutt, J.K., Irretier, H.: Active control of a Jeffcott rotor vibration due to blade loss. In: Proceedings of 9th International Conference on Vibrations in Rotating Machinery, IMechE, Exeter, Sept 2008
12. Sharma, P., Gupta, S., Das, A.S., Dutt, J.K.: Active vibration control of flexible rotor-shaft system subject to earthquake. In: Proceedings of the ASME 2012 International Mechanical Engineering Congress & Exposition IMECE 2012, Houston, 9–15 Nov 2012

Chapter 25
Active Vehicle Suspension with a Weighted Multitone Optimal Controller: Considerations of Energy Consumption

Waldemar Rączka, Marek Sibielak, and Jarosław Konieczny

Abstract Vibration reduction is a significant problem in the design and construction of vehicle suspensions (Lozia and Zdanowicz, IOP Conf Ser Mater Sci Eng 148:12014, 2016; Konieczny et al., J Low Freq Noise Vib Act Control 32:81–98, 2013). Passive semi-active and active methods are used in order to reduce vibrations. Considerations related to active and semi-active vibration reduction and the influence of disturbances on such objects can be found in many publications. In the case of these systems, the aim is always to find a compromise between their efficiency and energy consumption. The control law for such systems is usually determined as a solution to the optimisation problem with quadrant quality indicator. Energy limitation is taken into account by selection coefficients of the weighting matrix associated with the control signals vector. The efficiency of vibration reduction is able to be improved in the entire useful frequency range of the system operation but this generally results in an increase in the demand for external energy. An additional problem in the case of vehicle suspensions includes the need for increased vibration reduction for selected frequencies. This is related to the internal vibration frequencies of the driver's internal organs. The paper presents the synthesis of a weighted multitone optimal controller (WMOC) for an active vibration reduction system. The control signal in this case is determined on the basis of the identified sinusoidal disturbances vector. The vibration transmissibility function and the energetic indicators for the active suspension were determined while taking note of nonlinearities occurring in the actual vehicle. The analysis of energy indicators (e.g. energy, maximum power) is presented, depending on the level of vibration reduction efficiency. The results were compared with analogous linear-quadratic regulator (LQR).

Keywords Active suspension · Optimal control · WMOC · SUV · Suspension control

25.1 Control System with WMOC Controller

The WMOC (the WMOC is fully described in Refs. [3, 4]) controller determines optimal control signals only for sinusoidal components with frequencies $\omega_1, \ldots, \omega_{n_w}$. Having considered this, in case of the remaining frequencies the amplitude characteristics of the closed system remains unchanged. The control signal in the WMOC controllers is generated based on the state variables and the sinusoidal components of the disturbing signal (25.2). In order to calculate $u_*^{(j)}(t)$ components of the control signal, it is necessary to determine the sinusoidal component vectors $w(t)$ and the $w_\omega(t)$ vector (25.3) in real time. In the applied method $w_j(t)$ signals are identified in the time interval $\left[t - T_I^{(j)}, t\right]$ (where $T_I^{(j)}$ is the identification time and t is present moment of time) on the basis of the formulas (25.4)

$$K_j = -\left(B_u^T\left(-i\omega_j I_n - A_s^T\right)^{-1} Q\left(i\omega_j I_n - A_s\right)^{-1} B_u + R_j\right)^{-1} \cdot \\ \cdot B_u^T\left(-i\omega_j I_n - A_s^T\right)^{-1} Q\left(i\omega_j I_n - A_s\right)^{-1} B_w^{(j)} \tag{25.1}$$

$$u_*^{(j)}(t) = \mathrm{Re}\left(K_j\right) w_j(t) + \mathrm{Im}\left(K_j\right) w_{\omega,j}(t) \tag{25.2}$$

$$w_\omega(t) = \left(\alpha_1 \sin\left(\omega_1 t + \varphi_1 + \frac{\pi}{2}\right), \ldots, \alpha_{n_w} \sin\left(\omega_{n_w} t + \varphi_{n_w} + \frac{\pi}{2}\right)\right)^T \tag{25.3}$$

W. Rączka (✉) · M. Sibielak · J. Konieczny
AGH University of Science and Technology, Department of Process Control, Krakow, Poland
e-mail: waldemar.raczka@agh.edu.pl

C. Niezrecki, J. Baqersad (eds.), *Structural Health Monitoring, Photogrammetry & DIC, Volume 6*,
Conference Proceedings of the Society for Experimental Mechanics Series, https://doi.org/10.1007/978-3-319-74476-6_25

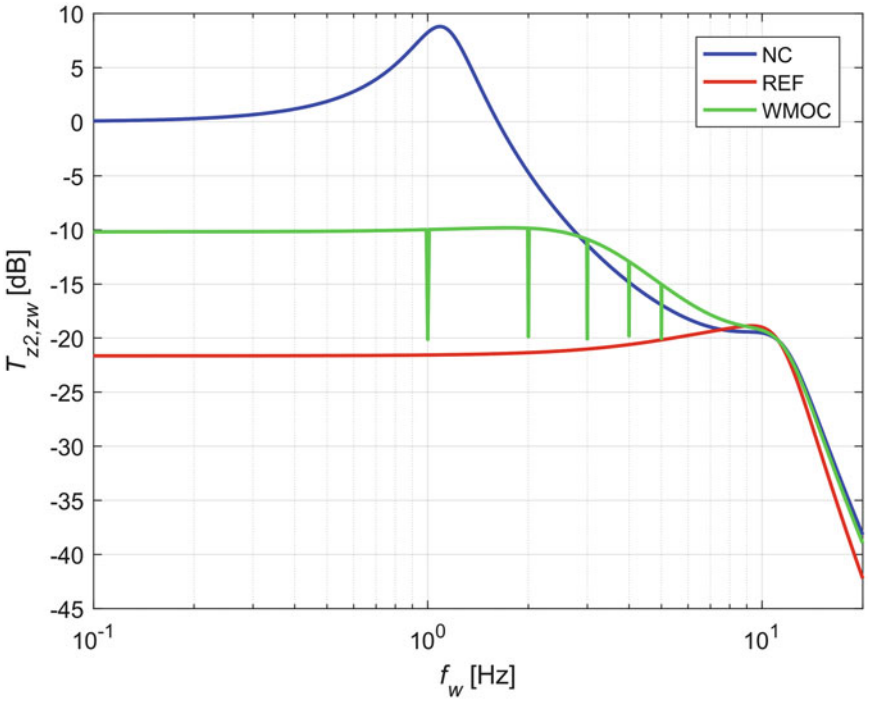

Fig. 25.1 Vibration transmission functions for suspension with no controller (NC), REF controller and WMOC controller

$$
\begin{aligned}
w_{\alpha}^{(j)}(t) &= \frac{1}{T_I^{(j)}} \int\limits_{t-T_I^{(j)}}^{t} w(s)\sin\left(\omega_j\left(s-t+T_I^{(j)}\right)\right) ds \\
w_{\beta}^{(j)}(t) &= \frac{1}{T_I^{(j)}} \int\limits_{t-T_I^{(j)}}^{t} w(s)\cos\left(\omega_j\left(s-t+T_I^{(j)}\right)\right) ds \\
w_j(s) &= w_{\alpha}^{(j)}(t)\sin\left(\omega_j s\right) + w_{\beta}^{(j)}(t)\cos\left(\omega_j s\right) \;\; dla\; s \in \left[t-T_I^{(j)}, t\right]
\end{aligned}
\tag{25.4}
$$

The identification times $T_I^{(j)}$ of individual components can be chosen independently of j. In practice, they are determined as the multiple of the identified $w_j(t)$ component period. The signals $w_j(t)$, $w_{\omega,j}(t)$ for the present moment of time t are determined on the basis of formulas (25.5).

$$
\begin{aligned}
w_j(t) &= w_{\alpha}^{(j)}(t)\sin\left(\omega_j T_I^{(j)}\right) + w_{\beta}^{(j)}(t)\cos\left(\omega_j T_I^{(j)}\right) \\
w_{\omega,j}(t) &= w_{\alpha}^{(j)}(t)\sin\left(\omega_j T_I^{(j)} + \frac{\pi}{2}\right) + w_{\beta}^{(j)}(t)\cos\left(\omega_j T_I^{(j)} + \frac{\pi}{2}\right)
\end{aligned}
\tag{25.5}
$$

The tests were carried out for the active parallel suspension with WMOC control. The model of this suspension is 2-DOF. The Reference controller (REF) was determined using the LQR method. It was assumed that the determined controllers are to guarantee vibration reduction below −10 dB over the entire frequency range. Additionally, it was assumed that for arbitrarily selected frequencies (1, 2, 3, 4, 5 Hz), the vibration reduction should be greater and be at a level of at least −20 (dB). The vibration transfer functions for the designed controllers and the open loop feedback system are shown in Fig. 25.1. In the case of a reference controller, the need to provide vibration reduction of −20 dB for additional frequencies resulted in a necessity to increase the efficiency of vibration reduction over the entire frequency range to the level of −20 dB.

Figure 25.2 shows the comparison of the average energy $E_{s,\,avg}$ taken from the external power source for the WMOC controller and the reference controller. In the frequency range between 1.9 and 10.6 Hz, $E_{s,\,avg}$ takes negative values. For the WMOC controller in the frequency range between 1.9 and 10.6 Hz, $E_{s,\,avg}$ takes negative values, except for the specific frequencies of 3, 4 and 5 Hz. Taking this into consideration, the use of an efficient energy recovery system would allow for the reduction of vibrations at −10 dB level without an external power supply. The vibration transfer values for frequencies of 1, 2, 3, 4 and 5 Hz are below −20 dB. Therefore, the values $E_{s,\,avg}$ for these frequencies are greater than zero.

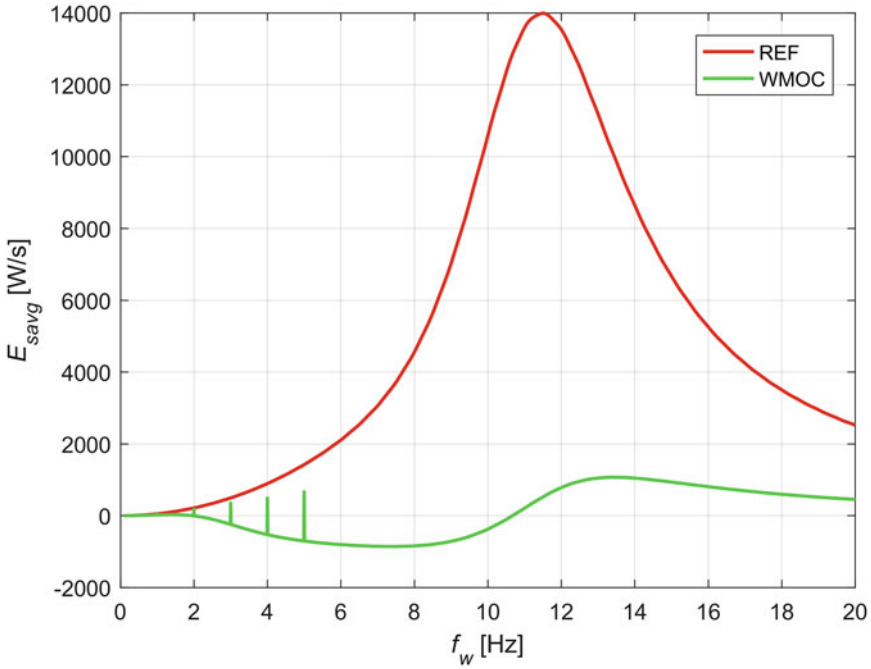

Fig. 25.2 Average energy consumed by the active suspension with the WMOC and the REF controllers

Conclusions based on the $E_{s,\,avg}$ analysis indicate the possibility of a significant reduction in energy use in the case of active suspension when using an energy recovery system; however, the construction of such systems is still being researched. The WMOC controller improves the vibration transfer function for selected frequencies while taking note of energy limitations. The control signal generated by the WMOC controller for these frequencies is optimal, making it possible to improve the vibration transmission function while limiting the amplitude of the force generated by the actuator element. The use of the WMOC controller allowed for reducing the requirements concerning the power generated by the actuator element compared to LQR controller when the assumed requirements regarding the vibration transfer function are met. The WMOC controller allowed for limiting the power consumption from external power sources, resulting in its reduced dimensions and price.

Acknowledgements This work was supported by National Centre for Research and Development of Poland (research project No. PBS3/B6/27/2015).

References

1. Lozia, Z., Zdanowicz, P.: Optimization of damping in the passive automotive suspension system with using two quarter-car models. IOP Conf. Ser. Mater. Sci. Eng. **148**, 12014 (2016)
2. Konieczny, J., Kowal, J., Raczka, W., Sibielak, M.: Bench tests of slow and full active suspensions in terms of energy consumption. J. Low Freq. Noise Vib. Act. Control. **32**, 81–98 (2013)
3. Tang, G.-Y., Gao, D.-X.: Approximation design of optimal controllers for nonlinear systems with sinusoidal disturbances. Nonlinear Anal. Theory Methods Appl. **66**, 403–414 (2007)
4. Sibielak, M., Raczka, W., Konieczny, J., Kowal, J.: Optimal control based on a modified quadratic performance index for systems disturbed by sinusoidal signals. Mech. Syst. Signal Process. **64–65**, 498–519 (2015)

Chapter 26
Sliding Mode Controller for Vehicle Body Roll Reduction Using Active Suspension System

Jarosław Konieczny, Marek Sibielak, and Waldemar Rączka

Abstract In many designs of vehicle suspension anti-roll bars are used for body roll reduction (Cronjé and Els, J Terramechanics 47:179–189, 2010; Her et al., IFAC Proc. 2013. https://doi.org/10.3182/20130904-4-JP-2042.00152). Such solutions are used in compact cars (C-segment), mid-size cars (D-segment), mid-size luxury car (E-segment) and even sports cars (S-segment). Antiroll bars are torsion bars connecting both sides of car suspension and they are connected with suspension arms. When car wheels move in vertical direction these torsion bars are twisted. Increasing torsional stiffness of front or rear suspension is the main role of sway bars. The use of these rods reduces tilting of the body while riding at high speed when the tilt of a car body is caused by the centrifugal force acting on the car. This force compress suspension spring with one side of the car, and extends on the other. The torque generated by the torsion bars reduce the difference in springs suspension. It reduces the compression of springs on one side of a car and extension on the other. Reduction of car body tilt improving handling and road holding and therefore improve safety. Antiroll bars also allow for the reduction of lateral vibrations caused by road roughness. During straight driving on equal road surface or under the same excitation of the wheels, the stabilizer doesn't work. During overcoming high road irregularities, the force acting on one of a wheel is transferred to the other via the bar. Antiroll bars also allow for the reduction of lateral vibrations caused by road inequalities. This causes unwanted oscillations. This effect is more noticeable if angle stiffness of the stabilizer is higher. In order to avoid such phenomena, active anti-roll bars are used. The most commonly used solutions are two-part active disconnect anti-roll bar or just active antiroll bar. In case of a two-part disconnectable anti-roll bar a hydraulic actuator connected to the ends of the roll bars usually is used. In such case, wheels work independently of each other so that the reactions from one wheel are not transferred to the other. If necessary, the stabilizer is connected by means of an actuator and works just like the classic one. In an active stabilizer a hydraulic actuator connected to the ends of the antiroll rods usually is used. Controlling the pressure or flow rates of the oil gives wide possibilities for acting actively on the anti-swaying of the vehicle.

Keywords Active suspension · Active-roll bar · Sliding controller · SUV · Suspension control

26.1 Control System with Sliding Mode Controller

The system under consideration in this paper is a fully-active suspension of a half car. The solution is based on hydraulic actuators as active force generators used for improving driving comfort and safety. Instead of introducing additional actuators in the form of active anti-roll bar, it was decided to add additional functionality to an active suspension control algorithm taking into account body rolling of the vehicle. For this purpose a sliding mode controller (SMC) was used. Figure 26.1 shows the calculation scheme of the suspension model of a vehicle. Parameters of the model are calculated based on the characteristics of a real SUV suspension. Hydraulic actuators [3] have been modeled with regard to servo-valve dynamics and compressibility of used liquid (26.1).

$$\begin{aligned} \dot{P}_{rjk} &= u_{rjk} l \propto C_d \sqrt{\frac{P_z - \text{sign}(u_{rjk}) P_{rjk}}{\rho}} - \propto A_{\propto} \vartheta \left(\dot{z}_{sjR} - \dot{z}_{wjk} \right) - \propto C_{tm} P_{rjk} \\ \tau \dot{u}_{rjk} &= -u_{r_{jk}} + k_{sv} u_{sjk} \end{aligned} \tag{26.1}$$

J. Konieczny (✉) · M. Sibielak · W. Rączka
AGH University of Science and Technology, Department of Process Control, Krakow, Poland
e-mail: koniejar@agh.edu.pl

C. Niezrecki, J. Baqersad (eds.), *Structural Health Monitoring, Photogrammetry & DIC, Volume 6*,
Conference Proceedings of the Society for Experimental Mechanics Series, https://doi.org/10.1007/978-3-319-74476-6_26

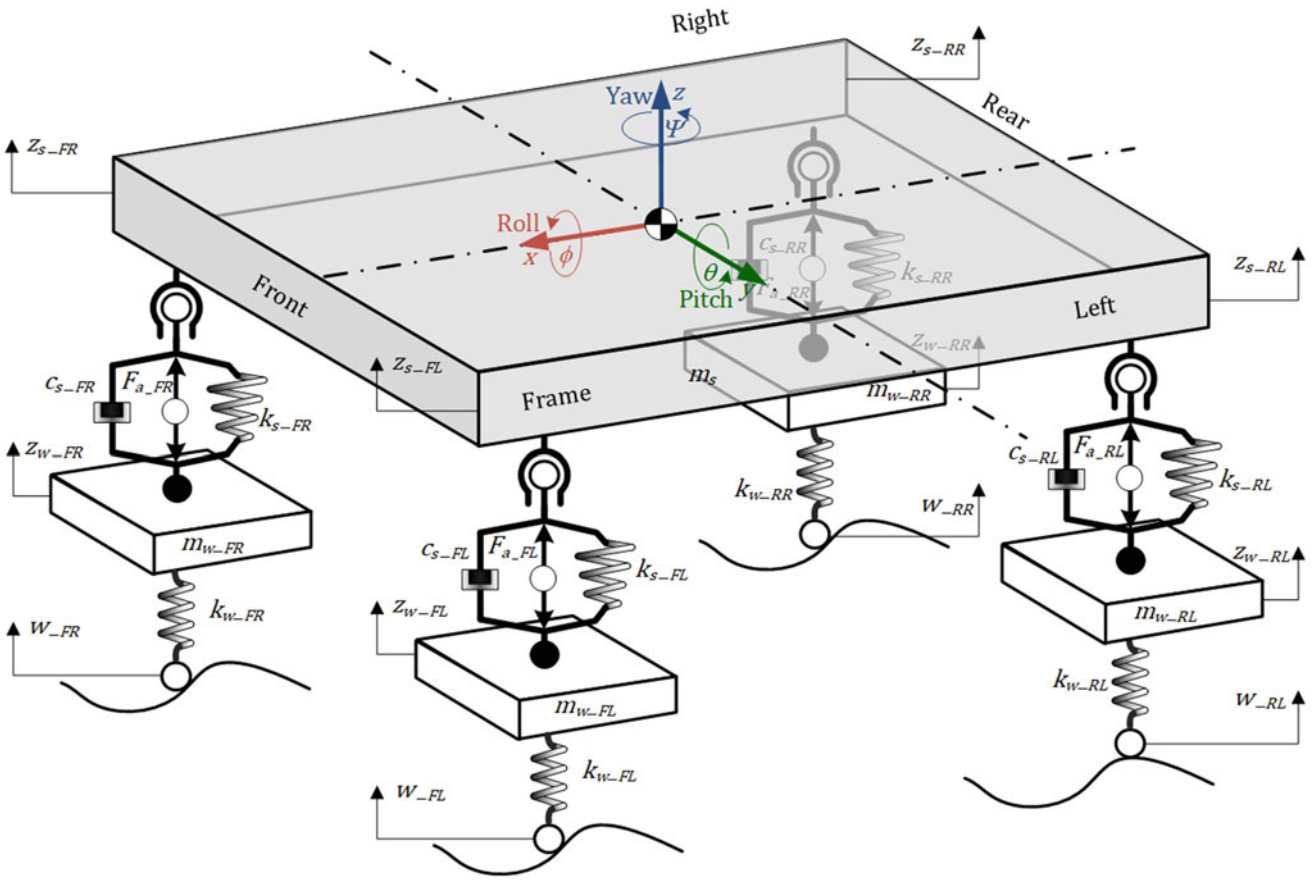

Fig. 26.1 Suspension diagram of the vehicle

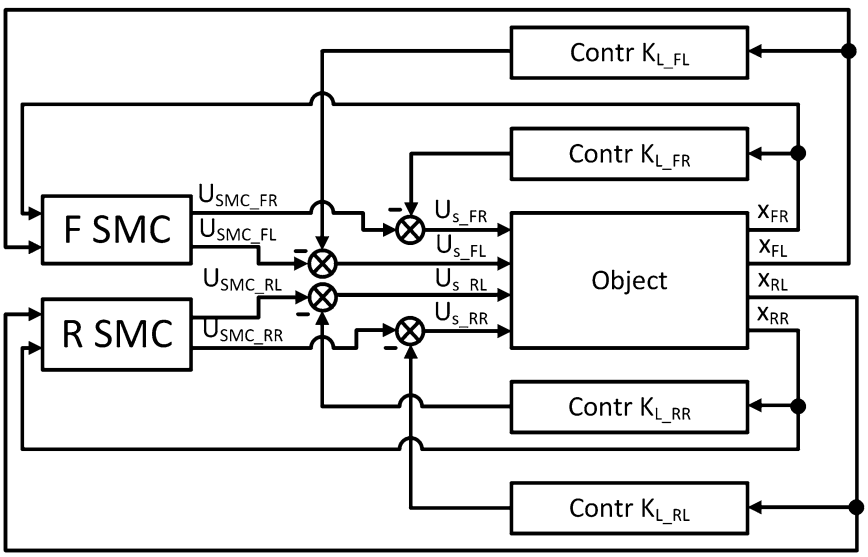

Fig. 26.2 Scheme diagram of the control system

In Eq. (26.1) the pressure differences between the cylinder chambers, the servo valve sliders displacements, the servo-valve control voltages are designated respectively P_{r_jk}, u_{r_jk}, u_{s_jk} [4].

The Fig. 26.2 shows the structure of the SMC. The purpose of the controllers K_{L_jR}, K_{L_jL} is reduction to provide vertical vibration for each of the columns.

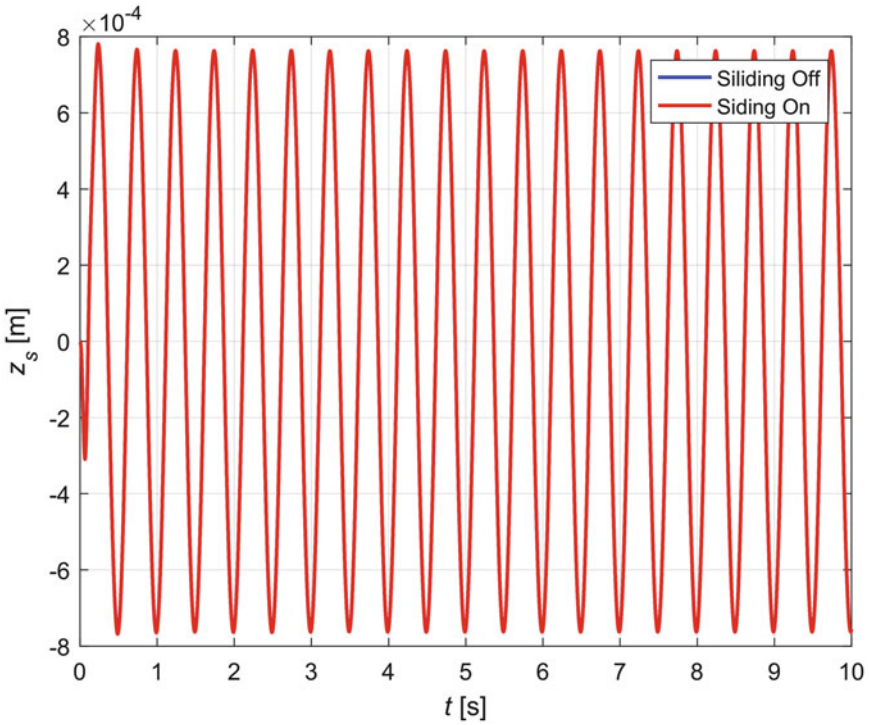

Fig. 26.3 Vertical displacement of the geometric

The SMC is applicated to reduce the rolling of the vehicle. The K_{L_jR}, K_{L_jL} controllers are designed so that the vibration reduction in the entire frequency band is less than -18 (dB). During designing the controllers, energy constraints were considered and sliding surface of sliding mode controller is defined by Eq. (26.2).

$$s\left(\varphi, \dot{\varphi}, u_{rjP}, u_{rjL}\right) = c_1\varphi + c_2\dot{\varphi} + 0,5\left(u_{rjP} - u_{rjL}\right) \tag{26.2}$$

Figures 26.3 and 26.4 show the vertical displacement of the geometric center of the vehicle and the body roll of the vehicle with the sliding controller switched on and switched off. As the road excitation, sinusoidal signals have been used. They are phase shifted between themselves with $\pi/2$. The amplitudes of excitation were $A = 0.01$ (m), while the frequencies were $f = 2$ (Hz). Figure 26.6 shows that the sliding mode controller has no influence on the vertical displacements reductions as was assumed, while the body roll was reduced eightfold.

Figure 26.5 shows the time waveform of the function $s\left(\varphi, \dot{\varphi}, u_{rjP}, u_{rjL}\right)$ which defines the sliding surface. In the case of a excitation of amplitude $A = 0,01$ (m), the system trajectories were on the sliding surface. While in the case of a excitation of amplitude $A = 0.03$ (m), the trajectories of the system reached the sliding surface at a time of about 0, 1 (s). The effect was related to the fact that the control signals generated by the sliding mode controller reached the maximum permissible values (Fig. 26.6). Control signal of the left-hand column reached saturation at times 0, 01, 0, 2 (s).

26.2 Conclusions

In this paper authors used sliding mode control law as a master controller for active suspension actuators of the off-road vehicle. The use of the proposed sliding controller solution enabled the roll reduction of the vehicle. The proposed method allows the independent synthesis of the controllers responsible for the reduction of vertical vibration and roll of the vehicle. Considered in the paper system is a full-active suspension with hydraulic actuators for improving driving comfort and safety. Instead of introducing additional actuators in the form of the active anti roll bars, it was decided to enrich the suspension control algorithm with additional functionality for roll compensation. For this purpose, sliding mode control is used.

Acknowledgments This work was supported by National Centre for Research and Development of Poland (research project No. PBS3/B6/27/2015).

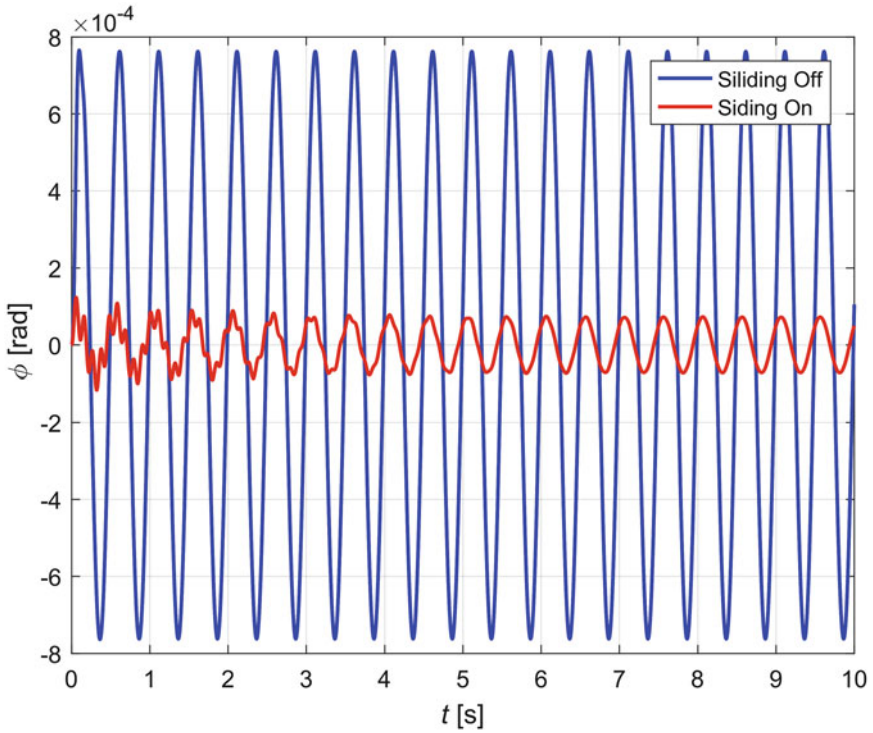

Fig. 26.4 Body roll of the vehicle center of the vehicle

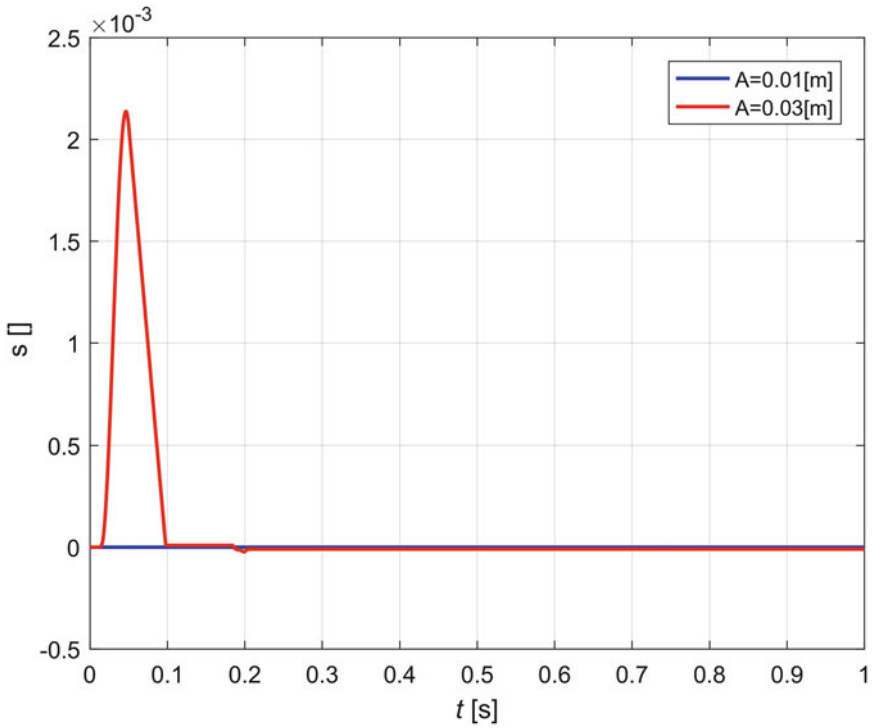

Fig. 26.5 Function describing sliding surfaces

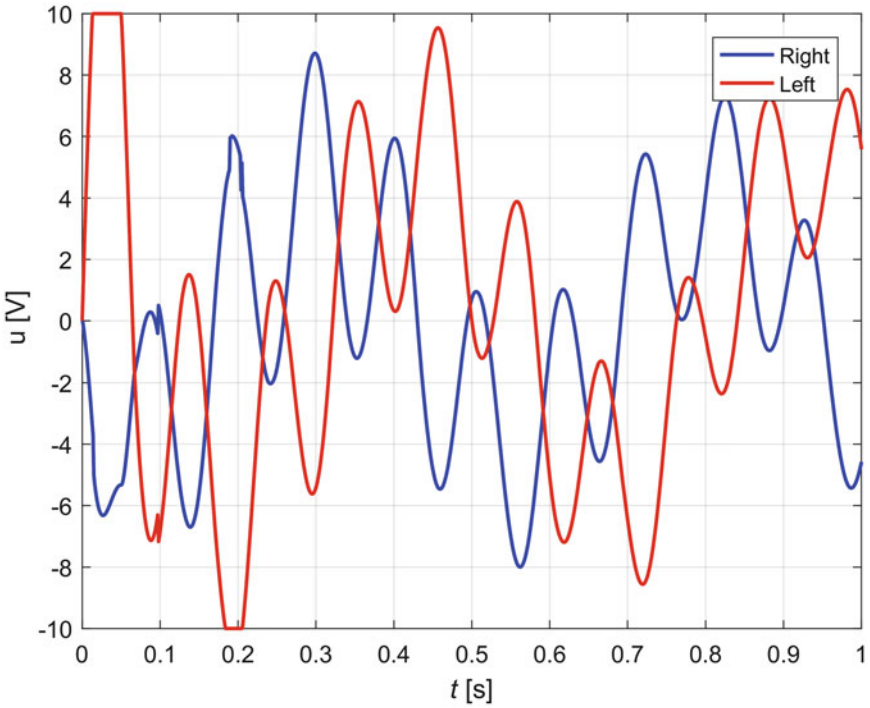

Fig. 26.6 Control signals of left and right columns generated by the sliding controller

References

1. Cronjé, P.H., Els, P.S.: Improving off-road vehicle handling using an active anti-roll bar. J. Terramechanics. **47**, 179–189 (2010)
2. Her, H., Yi, K., Suh, J., Kim, C.: Development of integrated control of electronic stability control, continuous damping control and active anti-roll bar for vehicle yaw stability [Internet]. IFAC Proc. Vol. IFAC. Available from: https://doi.org/10.3182/20130904-4-JP-2042.00152 (2013)
3. Konieczny, J., Kowal, J., Raczka, W., Sibielak, M.: Bench tests of slow and full active suspensions in terms of energy consumption. J. Low Freq. Noise Vib. Act. Control. **32**, 81–98 (2013)
4. Sibielak, M., Konieczny, J., Kowal, J., Raczka, W., Marszalik, D.: Optimal control of slow-active vehicle suspension—results of experimental data. J. Low Freq. Noise Vib. Act. Control. **32**, 99–116 (2013)

Chapter 27
Applying Concepts of Complexity to Structural Health Monitoring

Brian M. West, William R. Locke, Travis C. Andrews, Alex Scheinker, and Charles R. Farrar

Abstract The process of implementing a damage detection strategy for aerospace, civil, and mechanical engineering infrastructure is referred to as structural health monitoring (SHM). The SHM method complements traditional nondestructive evaluation by extending these concepts to online, *in situ*, system monitoring on a more global scale. For long term SHM, the output is periodically updated information that provides details on the continual deterioration of a system. After severe events, SHM is used for short term rapid condition screening and aims to provide reliable, near real-time information on structural integrity. The hypothesis of this paper is that structural degradation increases the complexity of a system, and that SHM can be used to detect this change over both long and short-term periods. Various measures of complexity were investigated, including Shannon and spectral entropies of accelerometer readings for real time damage detection and gradient measures for image-based corrosion detection. It was concluded that different measures of complexity were more appropriate for varying types of damage, i.e. spectral entropy was more appropriate for identifying cracks in a structure, while Shannon entropy was more appropriate for identifying corrosion on a plate.

Keywords Complexity · Damage detection · Shannon entropy · Spectral entropy · Structural health monitoring

27.1 Introduction

Structural Health Monitoring (SHM) is a method for monitoring damage in aerospace, civil, and mechanical infrastructure systems. SHM is being adapted in some aerospace and mechanical engineering systems and to a lesser extent in civil engineering systems, but regardless of the application the lack of convincing validation demonstrations and associated demonstrations of positive rate-of-return on investment continue to limit the transition of SHM research to practice [14]. Various methods of damage detection have been explored through electromagnetic, radiographic, and vibration-based experiments, but most have only been proven to work in laboratory environments and are not yet practical for real-world usage [1, 15, 16]. The inclusion of SHM as part of an asset monitoring strategy for current and future aerospace, civil and mechanical infrastructure would enable remote, continuous monitoring of structural integrity to better detect damage and implement more informed life-cycle management strategies. Regardless of the application, there are four integral steps related to the development of an effective SHM system that build off one another. First, an operation evaluation defines the damage to be detected. Next, appropriate sensing hardware is selected to properly detect the anticipated type of damage. Features used to assess damage are then extracted from the data. Lastly, a statistical model for feature discrimination is built to classify whether the structure is damaged [14]. In this study, focus is placed on selecting features that best identify and quantify damage using the concept of signal and image complexity.

Previous studies have defined complexity by various means over time [3] and definitions have evolved as more robust data processing techniques have been developed. These definitions range from the number of components in a system,

B. M. West
Department of Mechanical and Aerospace Engineering, Missouri University of Science and Technology, Rolla, MO, USA

W. R. Locke
Glenn Department of Civil Engineering, Clemson University, Clemson, SC, USA

T. C. Andrews
Department of Mechanical and Aerospace Engineering, University of Florida, Gainesville, FL, USA

A. Scheinker · C. R. Farrar (✉)
Los Alamos National Laboratory, Los Alamos, NM, USA
e-mail: farrar@lanl.gov

C. Niezrecki, J. Baqersad (eds.), *Structural Health Monitoring, Photogrammetry & DIC, Volume 6*,
Conference Proceedings of the Society for Experimental Mechanics Series, https://doi.org/10.1007/978-3-319-74476-6_27

to probabilities of component states and the extent of interconnections between components [4, 5]. Complexity has also been defined through pattern recognition, but tends to be subjective based on each observer's perspective [6]. For the purposes of this paper, complexity in SHM refers to how damage makes a system more unpredictable. Damage causes various forms of complexity to arise. Geometric complexity is introduced when damage creates cracks, which increases the number of edges and faces in a structure. Material complexity, traditionally defined on a microstructural level, pertains to the voids and dislocations caused by damage. Information complexity is seen when damage introduces nonlinearities to a system, increasing the variations in kinematic responses to a given excitation. Similar to the concept of "damage," the idea of complexity is relative and to meaningfully quantify complexity, two or more states must be compared to each other.

Research in SHM has shown that various entropy measures can be used as methods for quantifying the changes in complexity caused by damage. Wimarshana et al. used wavelet transforms to amplify signal irregularities so that sample entropy could be used to better quantify the complexity of bi-linear responses of cantilever beams caused by fatigue cracks. It was stated that, for a given system, higher complexity in a dynamic response corresponded to higher entropy [7]. Approximate entropy in rotary machines was used to identify deterioration of rolling-element bearings. Because of damage to the bearings, the approximate entropy increased on the order of 200% [8]. Lin and Liang used multi-scale and multi-scale cross-sample entropies in SHM to analyze the ambient vibration of a structure. Using multi-scale entropy, the damage condition of a structure was able to be assessed with an accuracy of 63.4%. Cross-sample entropy detected the location of damage with an accuracy of 86.6% [9]. In another study, generalized local entropy, found to be resilient to noise, detected crack damage in cantilever beams using the first and second mode shapes [10]. Castro et al. detected damage in carbon fiber reinforced polymer plates using spectral entropy (SE). The researchers stated that the SE increased or decreased depending on the location of damage relevant to the location of monitoring and required further evaluation to relate the SE to the magnitude of damage. An issue with this study was that variation in the SE was not monotonic and was believed to be caused by improper experimental design or damage representation [11].

In this paper, two measures of complexity, Shannon entropy and spectral entropy, were investigated to determine a potential method for identifying crack and corrosion damage for SHM. It is proposed that increases in complexity result from increases in geometric and informational uncertainty, caused by damage and/or the introduction of nonlinearities to a system. The experiments conducted include a modal analysis of a scale model four-story frame structure and an optical evaluation on an aluminum plate. The frame structure was damaged by implementing breathing cracks at various locations using a bumper mechanism. Random excitations were applied at the base of the structure and acceleration data was recorded at a central node on each floor. An analysis of the outputs was performed in the time and frequency domains to measure changes in Shannon and spectral entropies, respectively. The aluminum plate was locally exposed to an electrolytic bath to introduce varying magnitudes of corrosion. Optical images of corrosion were compared with uncorroded locations by identifying non-uniformities in color distributions via gray-scale gradient differences. Pixels were grouped together in cells and averaged to reduce noise from lighting variations. The Shannon entropies for each cell were measured and the variations in magnitudes across each image were compared.

27.2 Entropy

In 1948, Claude E. Shannon introduced the concept of informational entropy, where he defined "Shannon" entropy as the shortest length of an information chain required to losslessly describe a data set. More complex data sets require longer chains to describe them and thus correspond to higher Shannon entropy values [12]. Shannon entropy is calculated by obtaining a signal, placing the amplitudes into bins to create a histogram, normalizing the histogram to create a probability density function (PDF), and inputting those probabilities into Eq. 27.1 to yield a scalar entropy value, $H(A)$ [12]. Spectral entropy is another quantification of the information that applies the Shannon entropy calculation to the power spectral density (PSD) of a signal. Both Shannon and spectral entropies are used as measures of complexity in this study.

$$H(A) = -\sum_{i=1}^{n} p_i \log_2 (p_i) \tag{27.1}$$

To properly compare baseline and damaged states, global bounds were established for measured data sets and PSDs. Entropy was found to change with the number of bins. For consistency, 100 bins were used for all PDFs. A convergence

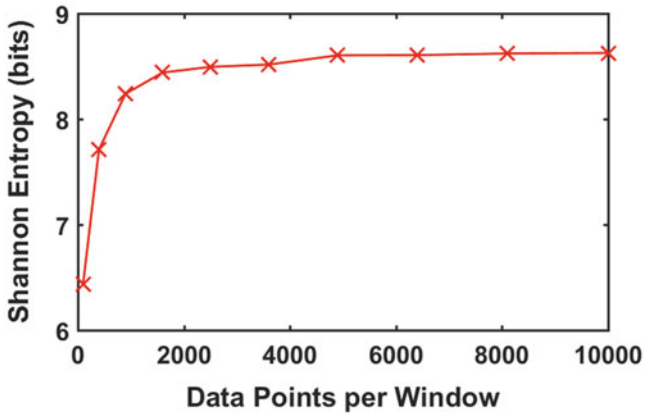

Fig. 27.1 Convergence study of entropy as window size increases

Table 27.1 Shannon entropy of coin toss outcomes

Trial	Heads	Tails	Entropy (bits)
1	50	50	1.0000
2	75	25	0.8113
3	100	0	0.0000

study found a Shannon entropy calculation of random, normally distributed numbers, required a minimum of approximately 5000 data points to converge on a consistent entropy value. For this reason, all entropy calculations were performed using 8192 data points (Fig. 27.1).

Further insight into Shannon entropy can be found by analyzing the outcomes of multiple coin flip trials. In each trial a coin is flipped 100 times. One trial is a fair coin toss where half of the outcomes are heads and half are tails. Another trial is a biased coin where 75% of the outcomes are heads and 25% are tails. A third trial has a coin with heads on both sides, having a guaranteed outcome. Shown in Table 27.1, the fair coin has the most uncertainty and therefore has the highest entropy. The biased coin is more predictable and has a lower uncertainty and entropy. For the two-headed coin, the outcome is certain and has an entropy of zero.

27.3 Frame Analysis

27.3.1 Numerical Models

Nonlinear and linear numerical models of a four-story frame structure, shown in Fig. 27.2, were created to test the hypothesis that damage changes the complexity of a structure. Using MATLAB, the frame was modeled as a two-dimensional shear-building with lumped masses at every floor, approximating the stiffness between floors using Euler-Bernoulli beam theory. The Euler-Bernoulli equation of motion for a beam, Eq. 27.2, was used to model the response of the structure to a random excitation force. Physical properties for the structure can be seen in Table 27.2.

$$\mathbf{M}\ddot{\mathbf{x}} + \mathbf{C}\dot{\mathbf{x}} + \mathbf{K}\mathbf{x} = \mathbf{F} \tag{27.2}$$

The global stiffness, **K**, and mass, **M**, matrices were approximated using the physical characteristics of the structure. The damping matrix, **C**, was estimated using previous research measurements and Rayleigh damping [10]. The force, **F**, was a random excitation signal applied at various locations depending on the experiment. Nodal displacement, velocity and acceleration vectors were respectively represented by $\ddot{\mathbf{x}}$, $\dot{\mathbf{x}}$, and **x**. Newmark-Beta average acceleration numerical integration was used to solve the equation of motion for the unknown kinematic responses of the structure [13]. Dynamic responses of the system were simulated at 1 kHz over 163.84 s.

The nonlinear springs shown in Fig. 27.3 were modeled as elements with bilinear stiffness to imitate a propagating, breathing crack. For a cracked element, a relative displacement threshold was set between adjacent floors to define a transition

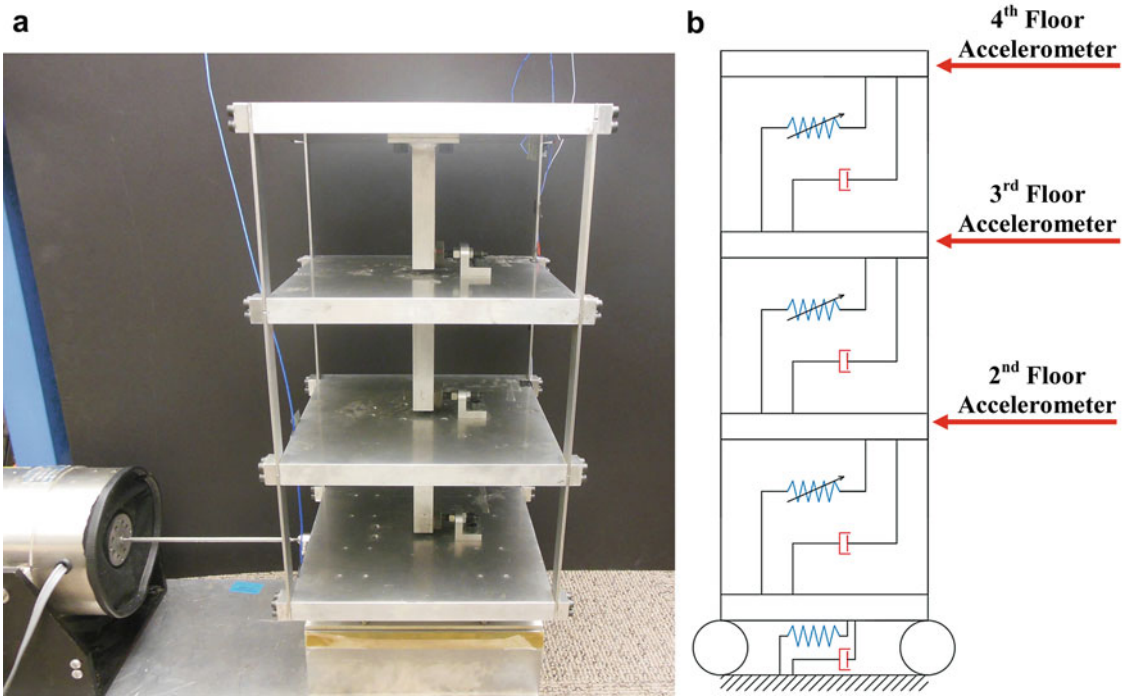

Fig. 27.2 Frame structure with bumper-column system (left). Free body diagram of nonlinear frame structure (right)

Table 27.2 Physical properties of shear-frame

Variable	Parameter (unit)	Value
Lc	Column length (m)	0.177
m	Lumped mass (kg)	6.2792
E	Modulus of elasticity (GPa)	69
I	Moment of inertia (m^4)	7.8125×10^{-9}
ζ	Damping ratio (%)	0.03

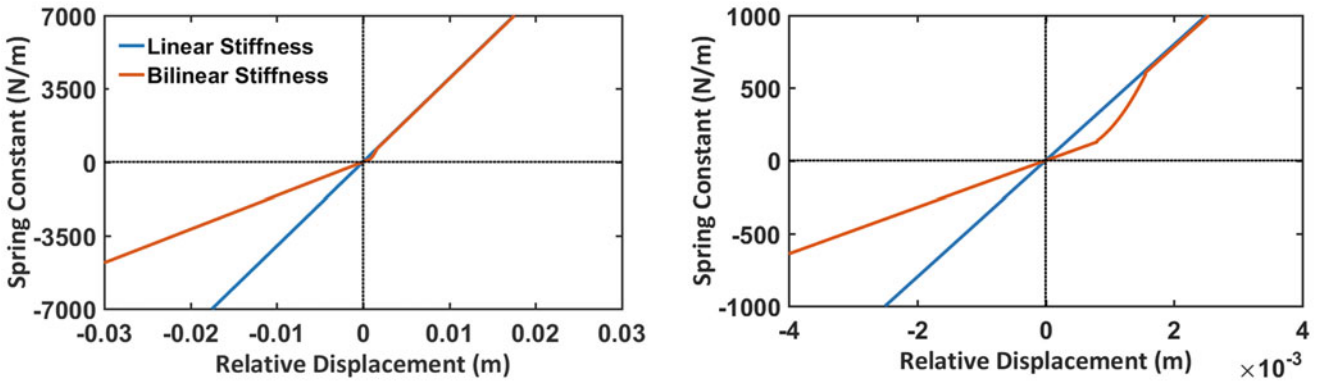

Fig. 27.3 Nonlinear stiffness of cracked member

stage between reduced and nominal stiffness, representing the opened and closed states of a crack, respectively. Over time, the opened stiffness of the region was reduced, simulating the reduction of cross-sectional area from the propagation. These states are displayed in Fig. 27.3. For the first 80 s of the simulation, column stiffness was held nominal. After 80 s the bilinear stiffness was introduced. To excite the structure, a random excitation with a root mean square (RMS) magnitude of 95 N was applied at the first floor. Spectral entropy was calculated for a moving window of 8192 acceleration samples for four different damage states.

Table 27.3 Experimental design matrix

Test	Bumper A	Bumper B	Bumper C
1	N	N	N
2	D	N	N
3	N	D	N
4	N	N	D
5	D	D	D

D damaged, *N* not damaged

To identify the effects of linear damage on a structure's complexity, damage was introduced after 80 s by linearly reducing the stiffness until 20% of the nominal stiffness remained. As with the nonlinear model, a random excitation with an RMS magnitude of 95 N was applied at the first floor, and Shannon and spectral entropies were calculated for a moving window of 8192 acceleration samples for four different damage states.

27.3.2 Experimental Model

An aluminum four-story frame structure, shown in Fig. 27.2, had an interior bumper-column system between each floor to imitate a breathing crack. There was a gap of approximately 0.25 mm between the bumper and column when a floor was treated as damaged, and the bumper system was completely removed when a floor was treated as undamaged. A design matrix for locations of damage in each test is found in Table 27.3. The structure was supported with four linear bearings spanned across two parallel rails. An electrodynamic shaker applied a normally-distributed random excitation with an RMS value of 95 N to the bottom floor of the structure. A PCB 208C03 force transducer collected the input force at the connection between the shaker's stinger and the side face of the bottom floor. Three PCB 352C22 single-axis accelerometers were placed on the opposite side of the structure, on the upper three floors, to collect acceleration data, see right side Fig. 27.2. Measurements and excitations were performed at a sample rate of 8192 Hz for a duration of 24 s. Acceleration data was used to calculate Shannon and spectral entropy values for each damage state.

27.3.3 Results and Discussion: Nonlinear Numerical and Experimental Models

The results of the numerical study are shown in Fig. 27.4. When cracking was introduced at a specific location, a sudden increase in spectral entropy was observed at the adjacent floors, with the exception of floor 1. This increase was attributed to the introduction of harmonics into the frequency response. Entropy continued to increase as the crack(s) propagated. Larger increases in entropy were observed for floors located immediately above damage. When cracks were introduced between all floors, the largest increase in spectral entropy was observed throughout the structure. From these observations, it was concluded that changes in spectral entropy can be used to detect the presence of damage and potentially quantify degrees of structural degradation. Furthermore, the location of damage can be identified based on which floors experience an increase in spectral entropy. Floor 1 entropy had a larger magnitude and variance because the acceleration response was dominated by the excitation force. The dominating force caused the acceleration response of floor 1 to be insensitive to changes in damage. From this result, it was determined that precaution should be taken when introducing excitation forces to avoid masking damage. For this reason, the entropy values for floor 1 were excluded in the remainder of the analysis.

To validate the above conclusions, entropy changes from the numerical model were compared to those of the physical model when crack(s) were introduced in the same manner. Figure 27.5a, b show the entropy values of floors 2, 3, and 4 from the numerical and experimental models for comparable magnitudes of damage, respectively.

It was found that the experimental entropy changes, shown in Fig. 27.5b, had similar trends to the entropy changes predicted in the numerical simulation in Fig. 27.5a. When crack(s) were introduced, floors adjacent to damaged supports saw an increase in entropy, validating previous conclusions from the simulation. Dissimilarities between the models were attributed to subjective approximations of damping, boundary conditions, and crack-based nonlinearities. Imperfections within the shaker may have also contributed to deviations in observed trends. Given more time, the numerical models would have been refined to better match the physical structure; however, for the purpose of this study, the similar trends indicated that the model was sufficient and confirmed the hypothesis that damage does increase the complexity of a system as quantified by spectral entropy.

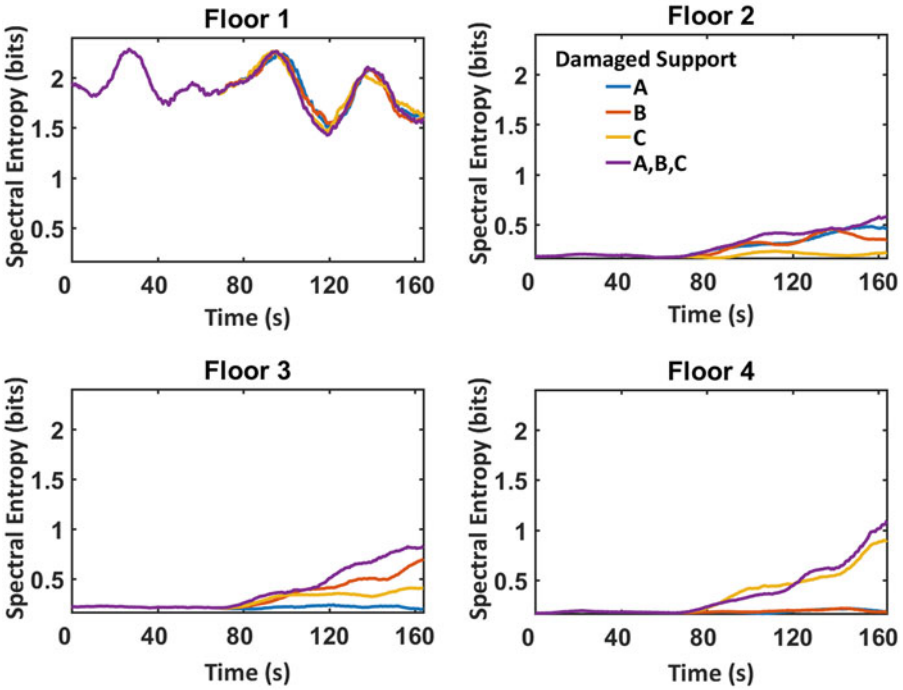

Fig. 27.4 Nonlinear numerical model of propagating, breathing crack introduced at 80 s

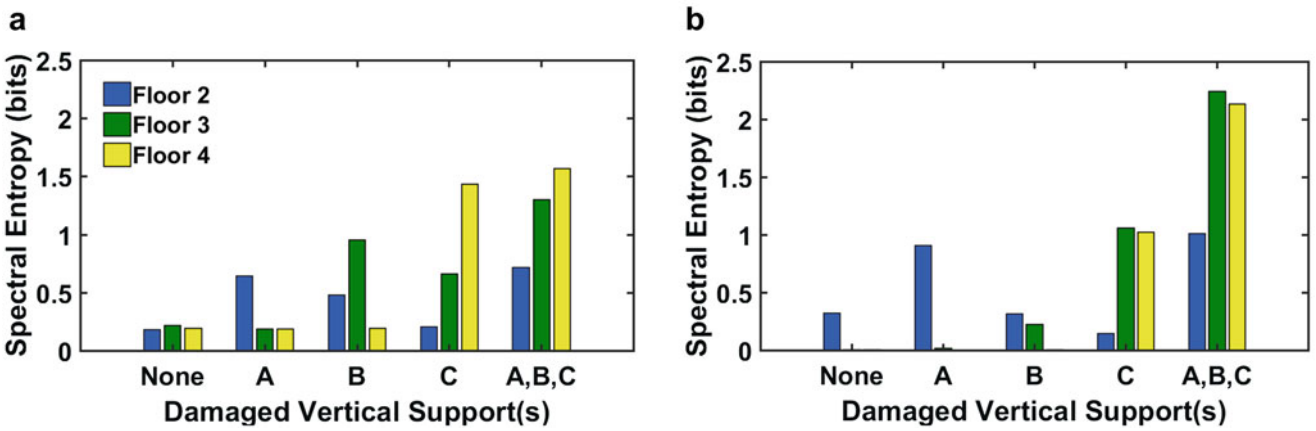

Fig. 27.5 (**a**) Spectral entropy of nonlinear numerical model. (**b**) Spectral entropy of experimental model

27.3.4 Results and Discussion: Linear Numerical Model

Figure 27.6 shows spectral entropy was unaffected by linear reductions in column stiffness. This was expected because even though frequency and modal properties of the structure may have been altered by reductions in column stiffness, the structure itself did not become more complex. Studies have shown that the same shifts in properties can be observed due to environmental effects, such as temperature, without damage being present [2].

Physical degradation in structural stiffness can result from reductions in material cross-sections caused by corrosion with the structure still exhibiting linear response characteristics. The results in Fig. 27.6 would then seem to contradict the statement that damage causes an increase in system complexity. However, it was also noted that different measure will be needed to assess complexity associated with different forms of damage. To evaluate the change in geometric complexity caused by corrosion, an image processing method was used as described in Sect. 27.4.

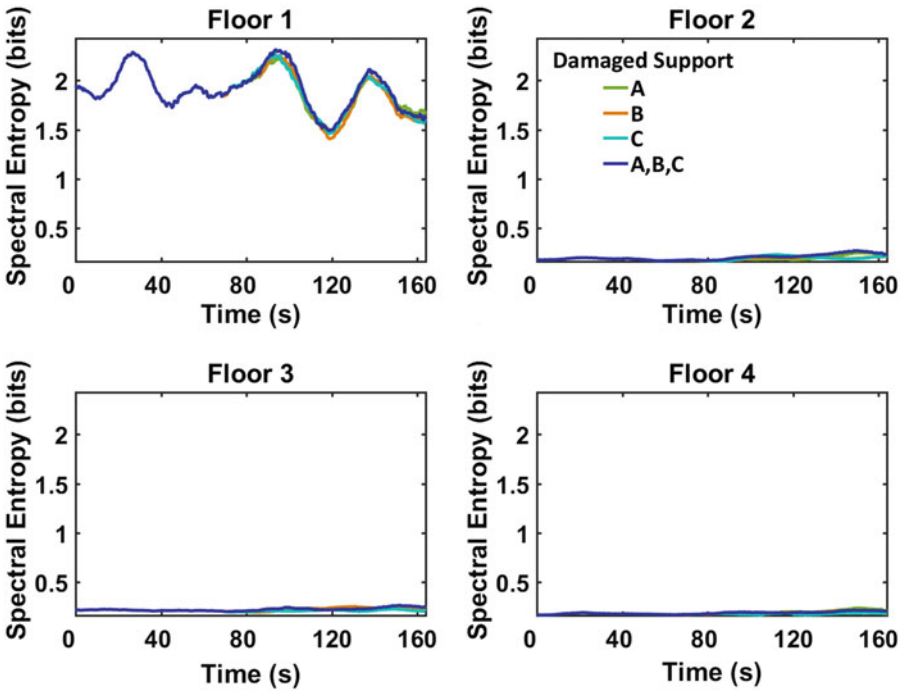

Fig. 27.6 Spectral entropy of floors 1–4 as element stiffness reduced by 80%

27.4 Corroded Plate Imaging

27.4.1 Experimental Procedure

An aluminum plate, shown in Fig. 27.7, was exposed to an electrolytic brine solution at several localized regions to induce varied magnitudes of corrosion. Figure 27.8 shows each localized region of corrosion and a baseline uncorroded region that were photographed using a Sony A7 camera mounted on a tripod. The tripod was fixed at a distance of 50 cm from the aluminum plate to assure consistency across images. Black poster boards surrounded the plate to reduce noise from nonuniform lighting. Different camera filters were evaluated to see if noise from lighting could be reduced. Sets of ten images were taken with the filters at each corrosion location; the lights in the room were kept on for five images and turned off for five images to test how well the filters performed under different lighting conditions. Gradient sums of corroded and uncorroded grayscale images for each filter and lighting conditions were gathered into probability density functions and compared for misidentification likelihood.

From Fig. 27.9, it was determined that the Soft Focus "High" filter, which is a high-pass imaging filter, had little variance in gradient sums across damage states, preventing misidentification of corroded and uncorroded images. The filter also proved acceptable for both lighting conditions, making it potentially effective for helping detect real world corrosion, which is why it was selected for this project. Image gradient values were input into Eq. 27.1 and a single entropy value was calculated for each photograph. As seen in Fig. 27.10, the entropy within a given damage state had little variability, with the overall max relative standard deviation being 0.84%. Increases in entropy of 23%, 28% and 30% were observed when comparing corrosion regions B, C and D to uncorroded region A, respectively. It was concluded that these trends in entropy reflected increases in geometric complexity, and could be used to potentially quantify the severity of corrosion.

To further evaluate the severity of corrosion within an image, a localized entropy calculation was performed. Filtered images were divided into square cells comprised of 8100 pixels each. Gradient values of each cell were input into Eq. 27.1 to calculate local entropy values. These values were then reconstructed into a lower-resolution image that showed specific locations of damage and further reduced noise from the pre-processed image. Figure 27.11 shows corroded images represented with locally calculated entropy. Moving from image A to D, entropy increased in the background as well as in localized regions of corrosion. It can be seen in image D that fine surface flaws including thin scratches were detected. This sensitivity shows the potential to identify minor defects before propagation occurs.

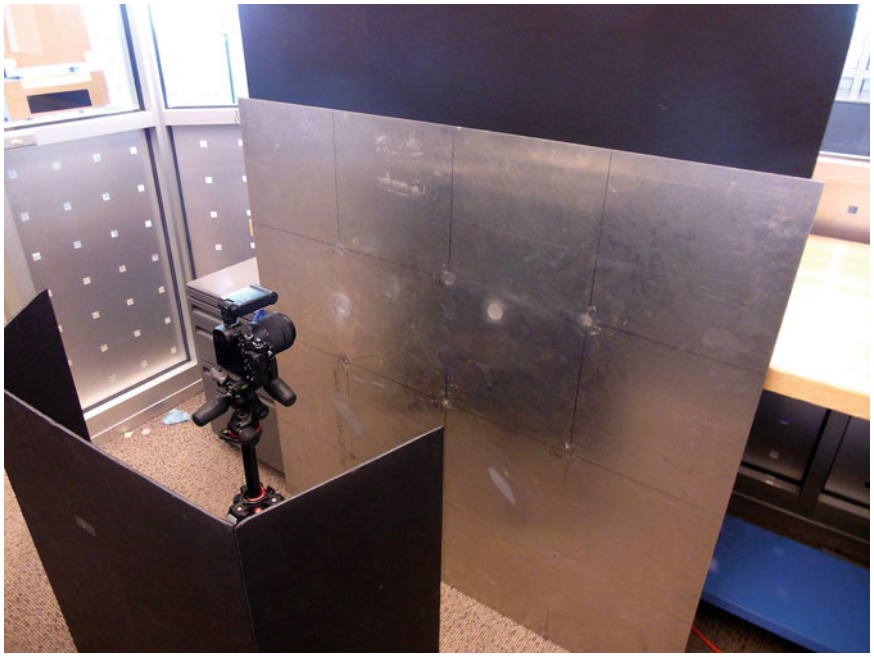

Fig. 27.7 Photographing regions of corroded aluminum plate

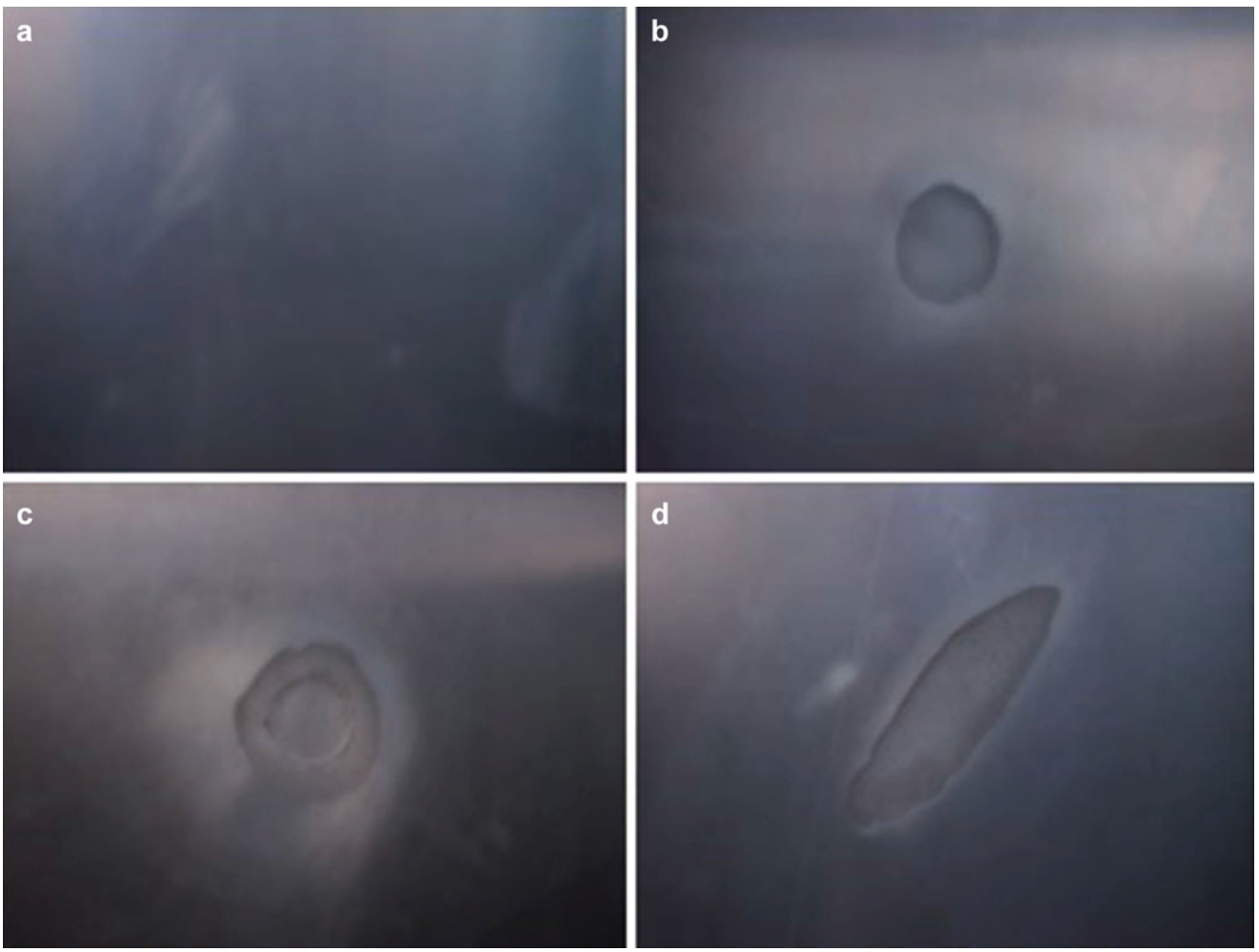

Fig. 27.8 Different degrees of corrosion. Corrosion levels are based on the surface area of corrosion. (**a**) no area of corrosion, (**b**) smallest area of corrosion, (**c**) medium area of corrosion, (**d**) highest area of corrosion

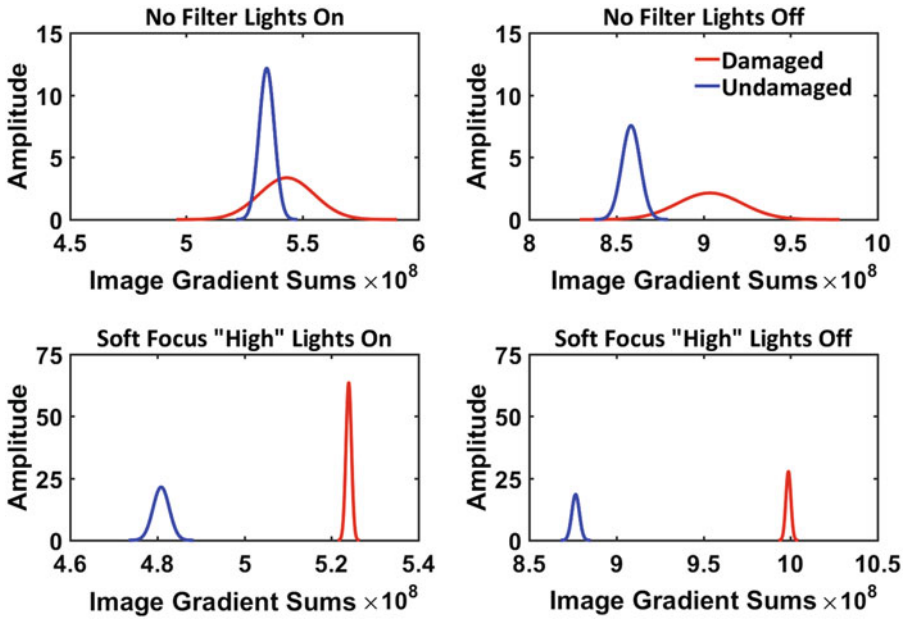

Fig. 27.9 Probability density functions for different filters and lighting conditions

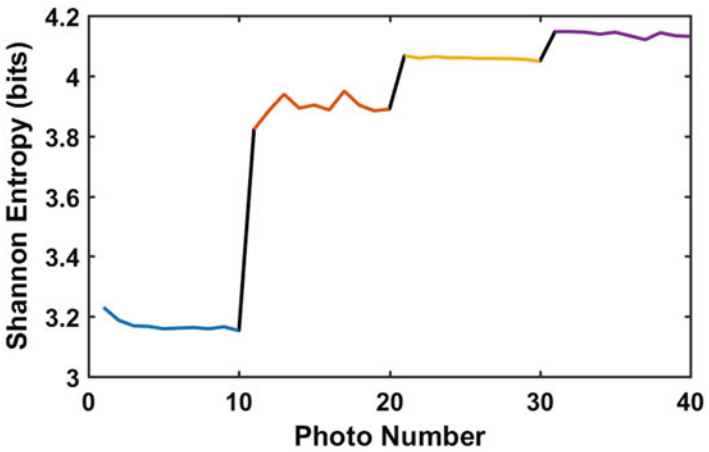

Fig. 27.10 Shannon entropy of ten soft focus "high" filtered images for each damage case

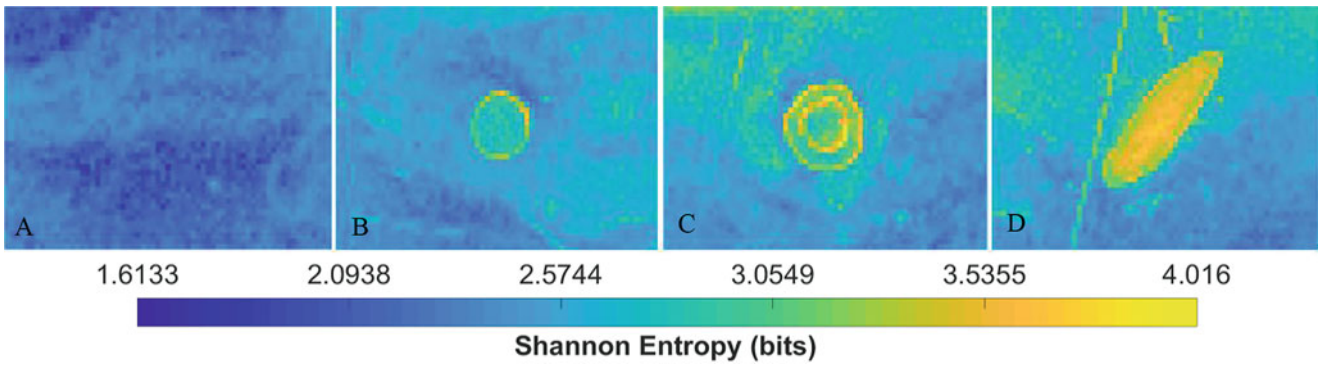

Fig. 27.11 Localized complexity values at different corrosion levels. (**a**) uncorroded, (**b**) small corrosion, (**c**) medium corrosion, (**d**) high corrosion

In summary, increases in Shannon entropy were observed when comparing corroded regions to the uncorroded region. When entropy was calculated on a cellular basis, localized increases in entropy were observed in corroded areas. These results show increases in geometric complexity caused by corrosion can be observed and quantified on a broad and localized scale, further confirming the hypothesis that damage increases complexity.

27.5 Conclusion

In this project, focus was placed on applying the concept of complexity to identify damage within a system. It was hypothesized that damage increases the complexity of a system and different damage types may require different measures of complexity to be detected. Two measures of complexity, Shannon and spectral entropy, were investigated to quantify damage caused by cracking and corrosion. A nonlinear numerical model of a four story frame structure was simulated and validated with experimental results. When damage was initiated in the structure in the form of a breathing crack, an increase in spectral entropy was observed on floors adjacent to the damage location(s), with the exception of the floor of excitation. From this observation, it was concluded that increases in spectral entropy can successfully be used to detect and locate damage on floors where excitations are not directly applied. In a linear numerical model, spectral entropy was not sensitive to damage caused by reductions in column stiffness. This result was expected because a change in stiffness does not necessarily correspond to a change in informational complexity. However, a reduction in stiffness could be caused by corrosion, potentially resulting in changes in *geometric* complexity. To account for this change, an image processing technique was implemented to quantify the change in geometric complexity caused by varying degrees of corrosion on an aluminum plate. Sums of grayscale color gradients for images, captured using various camera filters and lighting conditions, were compared to identify specific filter and lighting combinations that were resilient to light noise and effective at edge detection. The soft focus “high” filter with minimal light was the optimal combination selected for measuring the complexity of subject plate regions. Damage was classified using whole-image and cell-based Shannon entropy calculations of grayscale color gradients. When comparing corroded regions to the uncorroded region, increases in Shannon entropy were observed. The proposed hypothesis that damage increases the complexity of a system and that different damage types may require different measures of complexity to be detected held true for all conducted experiments.

In future work, different types of test structures and damage types should be evaluated to determine if the hypothesis holds true for other situations/conditions. Additionally, other measures of complexity need to be assessed to identify the best method for quantifying various types of damage. Studies should also be conducted to determine how resilient measures of complexity are to operational and environmental variabilities, e.g. variations in the types of excitation force or temperature effects. Because there is currently no principled approach for selecting damage sensitive features in SHM, future work should focus on developing a more systematic procedure that is based on the concept of complexity and that relies less on engineering judgement.

References

1. Doebling, S.W., Farrar, C.R., Prime, M.B., Shevitz, D.W.: Damage identification and health monitoring of structural and mechanical systems from changes in their vibration characteristics: a literature review. Los Alamos National Laboratory (LANL), No. LA-13070-MS (1996)
2. Farrar, C., Doebling, S., Straser, E., Cornwell, P.: Variability of modal parameters measured on the Alamosa Canyon Bridge. In: XV International Modal Analysis Conference (1997)
3. Lloyd, S.: Measures of complexity: a nonexhaustive list. IEEE Control Syst. Mag. **21**(4), 7–8 (2001)
4. Min, B.K., Chang, S.H.: System complexity measure in the aspect of operational difficulty. IEEE Trans. Nucl. Sci. **38**(5), 1035–1039 (1991)
5. Jung, W.S., Cho, N.Z.: Complexity measures of large systems and their efficient algorithm based on the disjoint cut set method. IEEE Trans. Nucl. Sci. **43**(4), 2365–2372 (1996)
6. Lopez-Ruiz, R., Mancini, H.L., Calbet, X.: A statistical measure of complexity. Phys. Lett. A. **209**(5–6), 321–326 (1995)
7. Wimarshana, B., Wu, N., Wu, C.: Identification of breathing cracks in a beam structure with entropy. In Nondestructive Characterization and Monitoring of Advanced Materials, Aerospace, and Civil Infrastructure 2016. **9804**, 980425-01–980425-16 (2016)
8. Yan, R., Gao, R.X.: Approximate entropy as a diagnostic tool for machine health monitoring. Mech. Syst. Signal Process. **21**(2), 824–839 (2007)
9. Lin, T.K., Liang, J.C.: Application of multi-scale (cross-) sample entropy for structural health monitoring. Smart Mater. Struct. **24**(8), 085003 (2015)
10. Yang, Z., Chen, X., Jiang, Y., He, Z.: Generalised local entropy analysis for crack detection in beam-like structures. Nondestruct. Test. Eval. **29**(2), 133–153 (2014)
11. Castro, E., Moreno-García, P., Gallego, A.: Damage detection in CFRP plates using spectral entropy. Shock Vib. **2014**, 1–8 (2014)

12. Shannon, C.E.: A mathematical theory of communication. ACM SIGMOBILE Mob. Comput. Commun. Rev. **5**(1), 3–55 (2001)
13. Huebner, K.H., Dewhirst, D.L., Smith, D.E., Byrom, T.G.: The Finite Element Method for Engineers, no. 3. Wiley, New York (2008)
14. Farrar, C.R., Worden, K.: An introduction to structural health monitoring. Philos. Trans. R. Soc. Lond. A Math. Phys. Eng. Sci. **365**(1851), 303–315 (2007)
15. Hellier, C.J.: Handbook of Non-destructive Evaluation, no. 2. McGraw-Hill, Boston (2012)
16. Farrar, C.R., Worden, K.: Structural Health Monitoring: A Machine Learning Approach. John Wiley and Sons Ltd, Chichester (2013)